Exploiting Photoisomerization: Spectroscopy on a Carotenoid Sensor and Retinal Proteins

---

Im Fachbereich Physik der Freien Universität Berlin eingereichte Dissertation zur Erlangung des Grades eines Doktors der Naturwissenschaft (Dr. rer. nat.)

vorgelegt von

David Ehrenberg

Berlin, März 2020

Erster Gutachter	Prof. Dr. Joachim Heberle
Zweiter Gutachter	Prof. Dr. Ana-Nicoleta Bondar
Tag der Disputation:	10. Dezember 2020

Parts of this thesis have been already published in:

Schnedermann, C., Muders, V., **Ehrenberg, D.**, Schlesinger, R., Kukura, P. & Heberle, J. Vibronic Dynamics of the Ultrafast all-trans to 13-cis Photoisomerization of Retinal in Channelrhodopsin-1. *Journal of the American Chemical Society* **138,** 1–8 (2016). doi: 10.1021/jacs.5b12251

Kovacs, G. N., Colletier, J.-p., Grünbein, M. L., Yang, Y., Stensitzki, T., Batyuk, A., Carbajo, S., Doak, R. B., **Ehrenberg, D.**, Foucar, L., Gasper, R., Gorel, A., Hilpert, M., Kloos, M., Koglin, J. E., Reinstein, J., Roome, C. M., Schlesinger, R., Seaberg, M., Shoeman, R. L., Stricker, M., Boutet, S., Haacke, S., Heberle, J., Heyne, K., Domratcheva, T., Barends, T. R. M. & Schlichting, I. Three-dimensional view of ultrafast dynamics in photoexcited bacteriorhodopsin. *Nature Communications* (2019). doi: 10.1038/s41467-019-10758-0

Ehrenberg, D., Varma, N., Deupi, X., Koyanagi, M., Terakita, A., Schertler, G. F., Heberle, J. & Lesca, E. The two-photon reversible reaction of the bistable jumping spider rhodopsin-1. *Biophysical journal* **116,** 1248–1258 (2019). doi: 10.1016/j.bpj.2019.02.025

Ehrenberg, D., Krause, N., Saita, M., Bamann, C., Kar, R. K., Schapiro, I., Heberle, J. & Schlesinger, R. Atomistic insight into the role of threonine 127 in the functional mechanism of channelrhodopsin-2. *Applied Sciences* **9,** 4905 (2019). doi: 10.3390/app9224905

Papers under revision:

Skopintsev, P., **Ehrenberg, D.**, Weinert, T., James, D., Kar, R., Johnson, P., Ozerov, D., Furrer, A., Martiel, I., Dworkowski, F., Nass, K., Knopp, G., Cirelli, C., Arrell, C., Gashi, D., Mous, S., Wranik, M., Gruhl, T., Kekilli, D., Bruenle, S., Deupi, X., Schertler, G., Benoit, R., Panneels, V., Nogly, P., Schapiro, I., Milne, C., Heberle, J. & Standfuss, J. Femtosecond to millisecond structural changes in a light-driven sodium pump. *Nature - under revision* (2020)

Manuscripts in preparation:

Ehrenberg, D. & Heberle, J. Voltage sensing by Raman Spectroscopy of Zeaxanthin. *Manuscript in preparation*

ABSTRACT

Light-based methodologies enjoy popularity due to their non-invasive nature. In particular in the field of optogenetics, where genetic targeting of neurons permits not only simultaneous imaging of a large number of cells but also optical control of neuronal activity. For this, ion channels or pumps are inserted into the membrane which are activated by light. A deep biophysical understanding of the optogenetic systems is key for their successful application.

In this thesis, I present a new member in the family of organic voltage sensors. I demonstrate that in a single lipid bilayer environment, the carotenoid Zeaxanthin has a linear and reversible spectral Raman response to an electric field applied across the membrane. The underlying mechanism is an increased photoisomerization rate resulting in a higher 13-*cis* population which is detected via a characteristic vibrational band at $1130\,\mathrm{cm}^{-1}$.

Channelrhodopsin-2 (ChR2) is a frequently used protein in optogenetics to silence neuronal activity. By variation of amino acid side chains, we found experimental evidence for ground-state heterogeneity in the hydrogen bond interactions of the retinal protonated Schiff base (PSB). We have identified with Raman spectroscopy two spectral components of the $C{=}N{-}H$ mode of the PSB at 1661 and $1665\,\mathrm{cm}^{-1}$, representing hydrogen bonds to different amino acid side chains. These two interactions of the PSB could be essential for a voltage-sensing mechanism in ChR2.

In a pioneering approach we combined time-resolved absorption spectroscopy with serial femtosecond X-ray crystallography to scrutinize mechanistic details of sodium pumping in *Krokinobacter eikastus* rhodopsin 2 (KR2). Using an infrared-emitting quantum cascade laser (QCL), we verified that crystalline KR2 exhibits reaction kinetics similar to those observed in its detergent solubilized form. Hereupon, we have identified a previously proposed transient sodium binding site during the O intermediate where the sodium is coordinated by the amino acid side chains of N112 and D251. The findings regarding the ion transport mechanism in KR2 will facilitate the design of protein variants for an optogenetic application.

Bistable G-protein coupled receptors (GPCRs) have two thermally stable conformations and are a promising class of rhodopsins which have the potential to serve as an optogenetic switch. We were able to conduct a first biophysical characterization of the invertebrate jumping spider rhodopsin-1 (JSR1). We propose a model of the two-photon reaction based on spectroscopic results. During these reactions, the Schiff base stays protonated implying that a deprotonation is not a prerequisite for the function of bistable GPCRs. A proposed mediating water molecule as part of the counterion complex in the inactive conformation is identified by Raman spectroscopy and later confirmed by an X-ray crystallographic structure.

In conclusion, this thesis provides insights into the mechanistic details of established and upcoming optogenetic tools. These results will help to adapt their biophysical properties better suiting the needs of application.

KURZFASSUNG

Lichtbasierende Methoden erfreuen sich aufgrund ihrer nicht-invasiven Eigenschaft großer Beliebtheit. Im Besonderen in der Optogenetik, wo Neuronen genetisch modifiziert werden um nicht nur die simultane Beobachtung einer großen Anzahl von Neuronen, sondern auch optische Kontrolle von neuronaler Aktivität zu ermöglichen. Hierzu werden Ionenkanäle oder -pumpen in die Membran gebracht, die durch Licht aktiviert werden können. Ein tiefes Verständnis von optogenetischen Systemen ist eine Schlüsselvoraussetzung für eine erfolgreiche Anwendung.

In dieser Arbeit präsentiere ich einen Neuzugang in die Familie der organischen Spannungssensoren. Ich demonstriere, dass das Karotenoid Zeaxanthin, eingebracht in eine einzelne Lipiddoppelschicht, eine lineare und reversible Reaktion zeigt, wenn ein elektrisches Feld über die Membran angelegt wird. Der zugrunde liegende Mechanismus ist eine größere Population an 13-*cis* Isomeren, hervorgerufen durch eine erhöhte Photoisomerationsrate. Dies führt zu einem Anwachsen einer charakteristischen Vibrationsbande bei 1130 $\mathrm{cm^{-1}}$.

Kanalrhodopsin-2 (ChR2) wird regelmäßig in der Optogentik genutzt um neuronale Aktivität zu verhindern. Durch Variation von Aminosäurenseitenketten liefern wir Beweise für eine Heterogenität in der Wasserstoffbrückeninteraktion der protonierten Schiffschen Base (PSB) im Grundzustand. Wir konnten mit Raman Spektroskopie zwei spektrale Komponenten in der PSB Vibrationsmode (C=N–H) bei 1661 und 1665 $\mathrm{cm^{-1}}$ identifizieren, die jeweils eine Wasserstoffbrücke zu einer anderen Aminosäurenseitenkette darstellen. Diese zwei Interaktionen könnten von Bedeutung für einen Spannungsmessungsmechanismus in ChR2 sein.

Um den Natriumpumpmechanismus von *Krokinobacter eikastus* rhodopsin 2 (KR2) zu untersuchen, haben wir in einer Pionierarbeit zeitaufgelöste Absorbtionspektroskopie mit Röntgenkristallographie kombiniert. Die Benutzung eines Quantumkaskadenlasers (QCL) ermöglichte es uns sicher zu stellen, dass kristallines KR2 vergleichbare Reaktionskinetiken aufweist als in Detergens gelöst. Wir konnten daraufhin eine im Vorfeld postulierte vorübergehende Natriumbindungsstelle während des O Intermediats zwischen den Seitenketten von N112 und D251 identifizieren. Die Ergebnisse über den Ionentransportmechanismus werden die Konzipierung von Proteinvarianten für eine optogenetische Anwendung erleichtern.

Bistabile G-Protein-gekoppelte Rezeptoren (GPCRs) haben zwei thermisch stabile Konformationen und sind eine vielversprechende Klasse von Rhodopsinen für einen optogentischen Schalter. Wir konnten eine erste biophysikalische Charakterisierung von jumping spider rhodopsin-1 (JSR1) durchführen. Wir schlagen, basierend auf spektroskopischen Ergebnissen, ein Model einer zwei-Photonen Reaktion vor. Während dieser Reaktionen bleibt die SB protoniert. Dies impliziert, dass eine Deprotonierung keine Voraussetzung für die Funktion von bistabilen GPCRs ist. Ein angenommenes Wassermolekül als Teil des Konterionennetzwerks konnte mit Raman Spektroskopie detektiert werden, was später durch eine Röntgenstruktur bestätigt wurde.

Zusammenfassend bietet diese Arbeit Einblicke in die Mechanismen von etablierten sowie neuen optogenetischen Werkzeugen. Die Resultate werden dazu beitragen, ihre biophysikalischen Eigenschaften an die Erfordernisse der Anwendung anzupassen.

CONTENTS

ACRONYMS

ATP	adenosine triphosphate
ATR	attenuated total reflection
bR	bacteriorhodopsin
bR$^{13\text{-}cis}$	bacteriorhodopsin with 13-*cis* retinal
bR$^{\mathrm{DA}}$	dark-adapted bacteriorhodopsin
bR$^{\mathrm{LA}}$	light-adapted bacteriorhodopsin
CaChR1	channelrhodopsin-1 from *Chlamydomonas augustae*
CCD	charge-coupled device
CI	configuration interaction
CrChR2	channelrhodopsin-2 from *Chlamydomonas reinhardtii*
DAS	decay associated spectra
DFT	density functional theory
DOPC	1,2-dioleoyl-sn-glycero-3-phosphocholine
DPMC	1,2-dimyristoyl-sn-glycero-3-phosphocholine
DPPC	1,2-dipalmitoyl-sn-glycero-3-phosphocholine
DPPTE	1,2-Dipalmitoyl-sn-Glycero-3-Phosphothioethanol
DPSS	diode pumped solid state
FEL	free electron laser
FTIR	Fourier transform infrared
GEVI	genetically encoded voltage indicator
GPCR	G-protein coupled receptor
HF	Hartree-Fock
HOMO	highest occupied molecular orbital
HOOP	hydrogen-out-of-plane
HPLC	high-performance liquid chromatography
hR	halorhodopsin
IR	infrared
ITO	indium-tin-oxide
JSiR1	jumping spider isorhodpsin-1
JSR1	jumping spider rhodopsin-1

KR2	*Krokinobacter eikastus* rhodopsin 2
LCAO	linear combination of atomic orbitals
LCP	lipidic cubic phase
LSP	localized surface plasmon
LUMO	lowest unoccupied molecular orbital
MAPE	mean absolute percentage error
MBN	4-Mercaptobenzonitrile
MCT	Mercury-Cadmium-Telluride
NMR	nuclear magnetic resonance
PES	potential energy surface
PM	purple membrane
POPC	1-palmitoyl-2-oleoyl-glycero-3-phosphocholine
PSB	protonated Schiff base
QCL	quantum cascade laser
QM/MM	hybrid quantum mechanics/molecular mechanics
REP	Raman excitation profile
SAM	self assembled monolayer
SERRS	surface-enhanced resonance Raman spectroscopy
SVD	singular value decomposition
TDA-DFT	time-dependent DFT with the Tamm-Dancoff approximation
tLB	tethered lipid bilayer

1 INTRODUCTION

Throughout nature, every cell uses the ability to accurately control and make use of an osmotic potential difference between the bulk and its interior. The cell's plasma membrane serves as a barrier which preserves the membrane potential by preventing the flow of ions. Transmembrane ion channels are used to temporarily allow ion flow along an electrochemical gradient while pumps transport an ion against the gradient. These processes are utilized for many important aspects in cell functioning, such as environmental sensing and energy conservation but also for neuron excitation. Observing changes in membrane potential of individual cells therefore provides information about how cells work, neuronal activity, or to characterize specific ion channels.

Using light as a read-out for membrane potentials has several benefits over conventional techniques. No physical contact is required to interact with a system, rendering light-based methods non-invasive. Another advantage is the achievable spatial resolution, permitting precise targeting of individual spots. These benefits, in combination with organic molecules, have promoted light-based methods in the field of neuroscience. Recent developments have demonstrated that neuronal activity can be monitored by detecting intensity fluctuations of organic reporter molecules embedded in the cell membrane[7]. Furthermore, neuronal activity can be controlled by introducing transmembrane light-activated ion pumps and channels into the neuron (optogenetics, fig. 1.1)[8].

Besides the mentioned light-based applications, the interaction of light with a system can deliver information about physical properties and structure on an atomistic scale. Throughout this work, spectroscopy is employed to study not just the underlying mechanisms behind established optogenetic tools but also of new and upcoming systems. The first theoretical chapter of this thesis will provide the fundamentals of the energy landscape of molecules, which is a prerequisite for understanding spectroscopic results. The following chapter will subsequently introduce the physical principles of three different spectroscopic techniques (UV/Vis, infrared and Raman spectroscopy) and highlights their distinct advantages. The chapter finishes with a brief description of a theoretical approach to calculate spectra of molecules and a small excursion into data analysis.

The results are divided into two main parts. One chapter is dedicated to optogenetic tools which can be used to control neuronal activity. Six different transmembrane proteins are investigated, scrutinizing mechanistic details on the atomistic level. The first results chapter introduces a new organic voltage sensor. The carotenoid Zeaxanthin shows a spectroscopic response to an external field which can be used to monitor action potentials or to study electrochemical gradients produced by transmembrane ion channels and pumps.

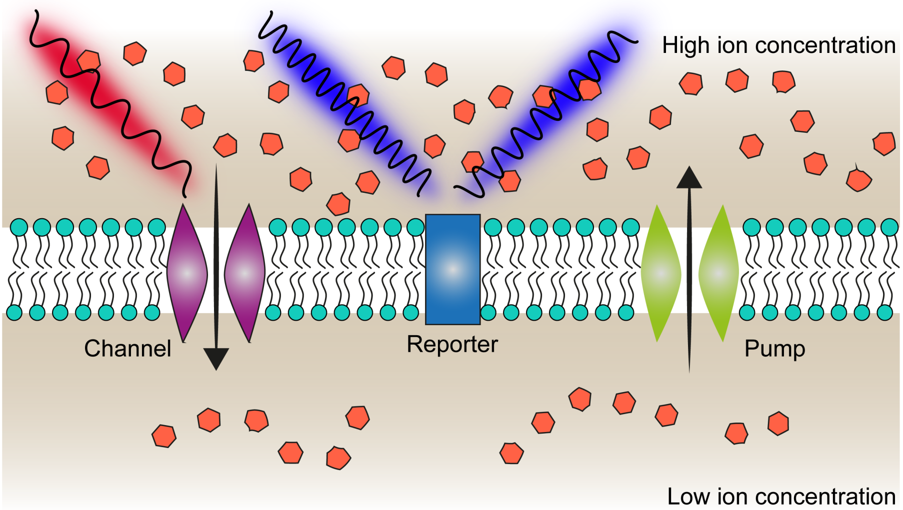

Figure 1.1: Illustration of a lipid bilayer with a light-activated transmembrane ion channel (left, purple) and a pump (right, green). The ion concentration difference preserved by the membrane creates an electrochemical gradient along which the ions can move if the channel is in an open conformation. In contrast, a pump transports ions against the gradient. A reporter molecule inside the membrane can interact with another light beam depending on the strength of the electrochemical gradient. In an ideal case, exciting and probing light are on opposing sides of the visible spectrum such that no optical cross talk arises.

1.1 Carotenoids

Carotenoids are organic pigments produced by many plants and algae that fulfill a set of functions including photosynthesis and photoprotection. The general structure of a C_{40}-carotenoid is a conjugated system of 9 to 11 double bonds alternating with single bonds along the polyene chain. This forms a delocalized π-electron system which lowers the overall energy and provide molecular stability. The carotenoid under investigation in this work is Zeaxanthin, an important xanthophyll (oxygen-containing carotenoid) for many plants, microorganisms and animals. It gives many vegetables like corn and paprika their distinct yellow color. In the leaves of plants, they play a crucial role in the xanthophyll cycle which protects the plant against light-induced oxidative stress. It can also be found in the macula lutea of retinae the human and some animals eyes. It protects the macula against photodamage by acting as a filter for high energy blue light. Zeaxanthin recently gained much attention due to the discovery of high-yield singlet fission which could increase the efficiency of organic molecular photovoltaics[9].

A general feature of carotenoids is an allowed electronic transition in the visible range of the electromagnetic spectrum (390 to 750 nm). Absorption of a photon leads to an excited state where the double bonds loose rigidity increasing the probability of isomerization. An isomer of a molecule has the exact same atoms but a different spatial arrangement. Among other interesting physical properties, the photoisomerization of carotenoids is utilized by nature in various ways. For example, animals, but also unicellular microorganisms, rely on a direct carotenoid derivative, retinal, which is the organic pigment involved in vision. Isomerization of retinal fuels the function of a protein called rhodopsin which subsequently triggers a downstream signaling cascade.

1.2 Light-activated transmembrane proteins

Proteins are biological macromolecules consisting of a sequence of proteinogenic amino acids (primary structure). The polypeptide chain folds into a three dimensional structure depending on the arrangement of the amino acids and the environment (secondary structure, fig. 1.2 **A**). The backbone of a protein is assembled by hydrogen bonds of amine ($-NH_2$) and carboxyl ($-COOH$) functional groups which every amino acid contains. The rest of an amino acid, often also referred to as R, is called the side chain which is specific to a certain amino acid and can be charged, polar, or hydrophobic. The side chains are not involved in forming the secondary structure but they play a crucial role in the function of the protein. Within organisms, proteins fulfill a large variety of functions such as catalyzing reactions, sensing of stimuli or transporting molecules. Hence, proteins are biological nanomachines with their function determined by their amino acid sequence.

This work takes a closer look at the families of microbial and invertebrate rhodopsins. Rhodopsins are transmembrane proteins composed of seven α-helices buried inside a biological membrane. Every cell has a protective barrier to be able to control biological processes and physical properties in its interior. This cell membrane is built up by a lipid bilayer where the lipid tails form a hydrophobic core. A typical membrane has a thickness of about 5 to 7 nm[10]. A cell interacts with its outside environment via these transmembrane proteins which can react to a variety of stimuli from the extracellular medium as well as from inside the cell.

In the case of Rhodopsins, the interaction with the environment is established by light. They harbor a chromophore retinal in the core of the protein which is covalently bound via a protonated Schiff base (PSB) to the peptide backbone. Retinal (fig. 1.2 **B**) is a form of vitamin A which animals consume by food or produce out of provitamin A carotenoids such as β-carotene or Zeaxanthin, while microorganisms have their own production pathway. Being a carotenoid derivative, retinal share many biophysical properties with these type of molecules. Retinal has a conjugated polyene chain with an extended π-electron system which can be excited by absorption of light in the visible spectrum. Photon absorption with subsequent isomerization of the retinal starts a cascade of events leading to protein function. To have a high yield of function per photon absorbed, the probability of retinal photoisomerization has to be increased. This can be achieved by electrostatic interaction but also steric effects of amino acid side chains can have an influence[11].

Microbial rhodopsins are classified into ion pumps, channels, and proton pumps (fig. 1.3). Pumps transport ions against an electrochemical gradient across the membrane, while channels open temporarily a pore where ions can freely move in- and outside of the cell. All of these functions are performed in a framework of cyclic reactions. After the photoisomerization, the protein adapts to the new retinal conformation leading to rearrangements in the secondary structure and eventually to functioning. This process is concluded by the reisomerization restoring the ground/resting state of the protein. Such a photocycle permits a re-execution of the function once the cyclic reaction is finished. In invertebrates, rhodopsins are exclusively used as light-sensors. They act as G-protein coupled receptors (GPCRs) which can bind a G-protein if activated, resulting in a downstream signaling cascade. Contrary to microbial rhodopsins, the reactions of invertebrate rhodopsins are not cyclic.

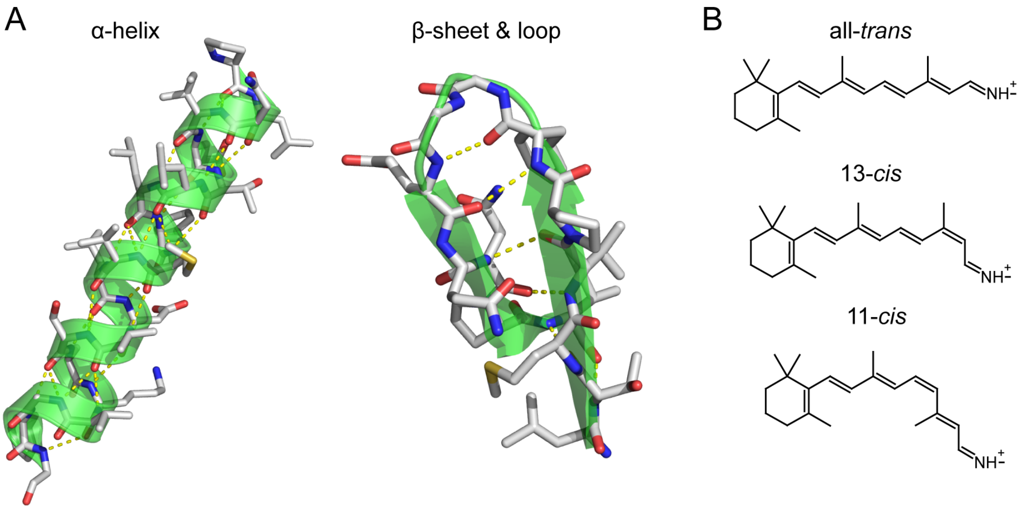

Figure 1.2: **A:** Illustrations of three different types of protein secondary structure sketched in green. Blue represents nitrogens, red oxygens and hydrogen bonds are indicated as yellow dashed lines. **B:** Three isomeric forms of retinal important for microbial and invertebrate rhodopsins.

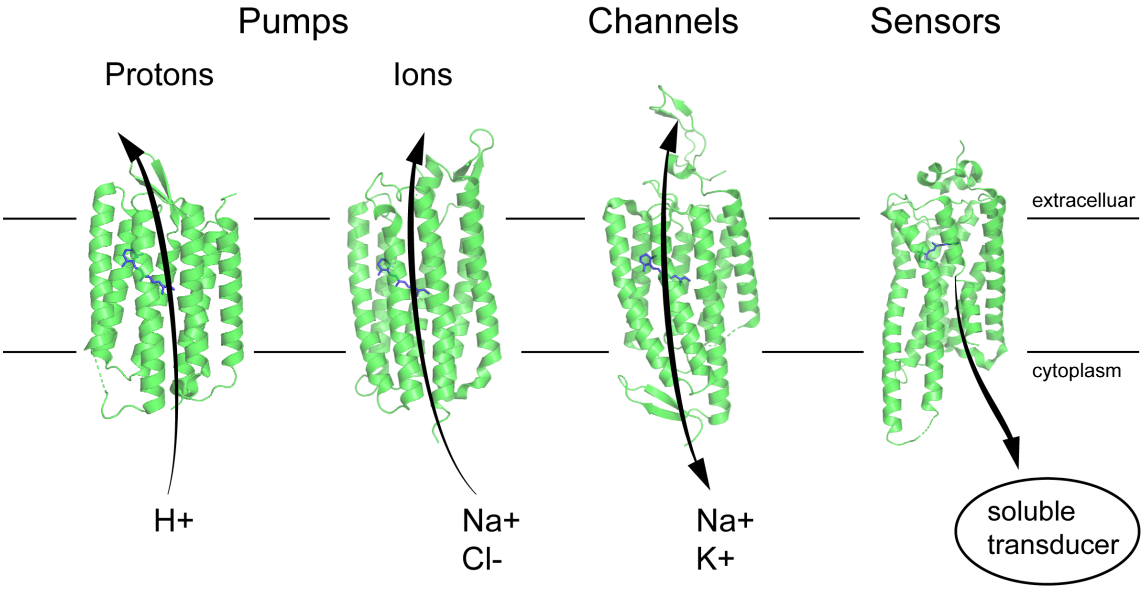

Figure 1.3: Microbial and invertebrate rhodopsins fulfill a varied set of functions: translocation of charge across the membrane against an electrochemical gradient (pumps), regulation of conductance (channels) or signal transduction (sensors). Proteins presented from left to right: bacteriorhodopsin (bR) (PDB: 3NS0), *Krokinobacter eikastus* rhodopsin 2 (KR2) (PDB: 6RF6), chimera of channelrhodopsin-1 & -2 (PDB: 3UG9), jumping spider rhodopsin-1 (JSR1) (PDB: 6I9K).

This means that there are two thermally stable protein conformations with different isomers of retinal, one is inactive, while the other is active to G-protein binding. Photon absorption therefore provokes a switch between these two protein conformations.

Since transmembrane proteins have the same dimensions as the cell membrane, optical microscopy is not able to resolve them. The diffraction limit is given by the Abbe resolution $\lambda/(2NA)$ with λ for the wavelength of light and NA is the numerical aperture of the objective. Even with state of the art objectives a resolution below 200 nm cannot be reached. Therefore, indirect techniques are mainly used to study molecular details of proteins in which the interaction of electromagnetic radiation with matter is exploited.

1.3 Voltage sensors

Precise measurements of membrane potentials remain a challenging task in molecular biophysics. Several techniques are used with their advantages and drawbacks. The mechanically invasive micro-electrodes permit direct monitoring of the membrane potential with a high temporal resolution but are limited to single cells. In the field of neuroscience, where observation of neuronal networks is crucial for understanding signal propagation or brain function, simultaneous monitoring of multiple individual cells is necessary. Multi-electrode arrays inserted in the brain provide spatial resolution with single-neuron precision without penetrating the cell[12]. Major drawbacks are heavy data processing, low spatial resolution and the lack of neuron-specificity. Exploiting the non-invasive nature of light in concert with suitable organic voltage-sensing (macro-)molecules addresses these points[13]. Ideal properties for an organic voltage sensors are linear voltage response, fast response kinetics, high brightness, as well as sensitivity (usually defined as signal change per 100 mV)[14]. Genetically encoded voltage indicators (GEVIs), which can target specific neurons, are successfully used to image neuronal signal propagation. They consist of a voltage-sensing domain that spans across the membrane and is connected to a fluorescent protein. Another class of GEVIs are nonfunctional mutants of ion channels or pumps. Prominent examples for both categories are ArcLight and QuasAr, respectively[15].

1.4 Optogenetics

The birth of optogenetics began with the discovery of the light-activated channelrhodopsin-2 (ChR2) by Nagel *et al.* in 2002[16]. Just three years later Boyden *et al.* succeeded to gain optical control of mammalian neurons by genetically introduce ChR2 into the cell membrane[17]. This pioneering work laid down the first stepping stone of optogenetics. Since then, it's a growing field with advances like the partial restoration of mice vision or ways to potentially treat Parkinson's disease[18,19]. But optogenetics is not just about controlling neurons, but also to optically monitor neuronal activity. Here, GEVIs are used which exhibit changes in fluorescence upon neuron excitation[14,15]. Studying neuronal networks can give insights into the sensing or behavioral processes of the brain. A recent approach to combine both methods, permitting simultaneous manipulating and recording of neuronal activity, will certainly revolutionize neuroscience, enabling new experiments[20]. For this all-optical approach, it is necessary that no optical crosstalk between the the two used system exists (fig. 1.1). Understanding the mechanism of optogenetic tools is a prerequisite to adapt their properties to the application needs. By variation of amino acid side chains it is possible to shift absorption maxima or to alter photocycle kinetics in order to adjust, for instance, lifetimes of the conductive conformation.

1.5 Scope of this thesis

The motivation of this thesis is to investigate established and new optogenetic tools. It is well-known that membrane-embedded carotenoids exhibit changes in their Raman spectrum if an electric field is applied across the lipid bilayer, but the underlying mechanism remained elusive[21]. This work demonstrates how the carotenoid Zeaxanthin can be used as an organic voltage sensor and also scrutinizes the origin of its spectral response.

Rhodopsins have found their way into optogenetics. A key for a successful optogenetic application is a deep biophysical understanding of protein function. Although many rhodopsins were intensively studied over the past years, such as bacteriorhodopsin (bR) and channelrhodopsin-2 (ChR2), many mechanistic details of protein function are still unknown. This thesis tackles certain mechanistic questions of five different microbial rhodopsins using spectroscopy. It also provides a first biophysical characterization of the invertebrate bistable jumping spider rhodopsin-1 (JSR1), which has the potential to serve as a model protein for bistable GPCRs. These can be used as an optogenetic switch to trigger a G-protein signaling cascade by light.

The recent development of free electron lasers (FELs) allows serial femtosecond X-ray crystallography on proteins to be performed. An aim of this work was to combine this technique with time-resolved absorption spectroscopy in order to track ion movement in rhodopsins. Both methods provide information on the atomistic level with their specific advantages and drawbacks. By using this powerful synergy of time-resolved techniques in collaboration with the group of Jörg Standfuß from the Paul Scherrer Institut (PSI), it was possible to shine light on the mechanism of sodium pumping in *Krokinobacter eikastus* rhodopsin 2 (KR2).

2 MOLECULAR ENERGY LANDSCAPE

The potential energy of a molecule is mostly a product of the Coulomb forces between the electrons and the nucleus which eventually lead to chemical bonding. In quantum mechanics, the energy of a system is defined by the Schrödinger equation. For a molecule and in particular for large macromolecules as proteins, approximations are introduced to solve the Schrödinger equation. The most fundamental one is the Born-Oppenheimer approximation which separates the wavefunction in a part for electrons and one for the nucleus. This permits to look at the electronic energy landscape and the vibrations of the nucleus separately. This chapter delivers the basic framework for the energy landscape of a molecule. The last section of this chapter briefly introduces the principle of spectroscopy where transitions between energetic states of a molecule are investigated.

2.1 Born-Oppenheimer approximation

One way to look at the Born-Oppenheimer approximation is that the total energy of a molecule is a sum of individual parts[22]

$$E_{total} = E_{trans} + E_{elec} + E_{vib} + \dots \quad . \tag{2.1}$$

Major contributions are translational energy of the whole molecule E_{trans}, energy coming from the motion of electrons E_{elec} and vibrational energy of the nucleus E_{vib}. Neglected are other types of energy, such as nuclear repulsion or energy due to spins. In terms of quantum mechanics, the energy of a system is defined by the Hamiltonian operator. For a molecule, the time-independent Schrödinger equation is

$$\hat{H}(\vec{r},\vec{R})\Psi(\vec{r},\vec{R}) = E_{total}(\vec{r},\vec{R})\Psi(\vec{r},\vec{R}) \quad , \tag{2.2}$$

where $\vec{r}$ and $\vec{R}$ denote the electron's and nucleus' coordinate, respectively, and $\Psi(\vec{r},\vec{R})$ describes the vibronic wavefunction of the complete molecule which depends on both coordinates. A approximation for eq. (2.2) is that the motions of electrons and nucleus are independent of each other due to the much lower mass of the electrons. With this, the vibronic wavefunction can be written as

$$\Psi(\vec{r},\vec{R}) = \chi_{nuc}(\vec{R})\Phi_{elec}(\vec{r};\vec{R}) \quad , \tag{2.3}$$

where $\chi_{nuc}(\vec{R})$ represents the wavefunction of the nucleus. The electronic wavefunction $\Phi_{elec}(\vec{r};\vec{R})$ now only depends parametric on $\vec{R}$ implying that for a description of the electrons the position of nucleus is assumed to be fix. Thus, in the Born-Oppenheimer approximation the molecular

Schrödinger equation can be separated in an electronic and a nuclei equation

$$\begin{aligned} \hat{H}_{elec}(\vec{r};\vec{R})\Phi_{elec}(\vec{r};\vec{R}) &= E_{elec}(\vec{R})\Phi_{elec}(\vec{r};\vec{R}) \\ \hat{H}_{nuc}(\vec{R})\chi_{nuc}(\vec{R}) &= E\chi_{nuc}(\vec{R}) \quad . \end{aligned} \tag{2.4}$$

The energy eigenvalues for the electronic part of the Hamiltonian $E_{elec}(\vec{R})$ depend on the nuclear coordinate $\vec{R}$. They form an effective potential energy surface on which the nucleus can move.

2.2 The electronic potential

To solve the electronic time-independent Schrödinger equation of eq. (2.4) for an one-electron atom, it is convenient to transform the Cartesian into three dimensional polar coordinates r, θ, ϕ. The solution for the wavefunction can then be written as a product of a radial $R(r)$ and a angular $Y(\theta, \phi)$ function[23]

$$\Phi_{nlm} = R_{nl}(r)Y_{lm}(\theta,\phi) \quad . \tag{2.5}$$

These solutions are called orbitals which are defined by three quantum numbers n, l, m. The principal quantum number n, which just appears in the radial function $R_{nl}(r)$, defines the average distance of the electron from the nucleus and can take integer values ($n = 1, 2, 3, \ldots$). Orbitals with same principal quantum number are referred to as shells. The shape of the orbital is defined by the angular quantum number l which can take integer values from 0 to $n-1$. A more common notation for the first three angular quantum numbers is s for $l = 1$, p for $l = 2$ and d for $l = 3$. These different subshells can have different orientations in space represented by the magnetic quantum number m with integer values from $-l$ to $+l$. The orbitals for the first two shells of the hydrogen atom are depicted in fig. 2.1.

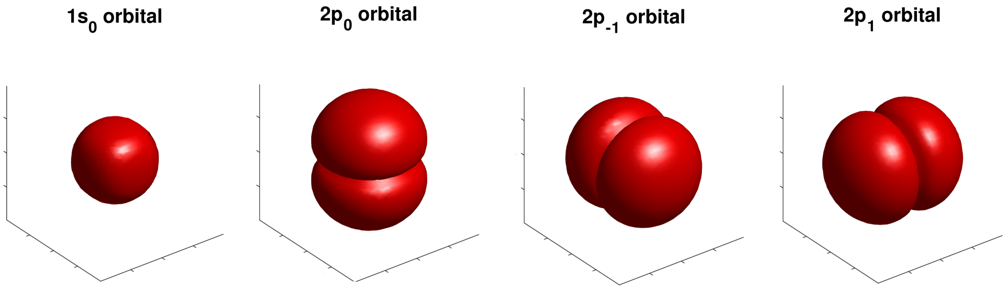

Figure 2.1: Electron density for hydrogen molecular orbitals of the first two shells plotted as isosurfaces. The magnetic quantum number is given as subscripts.

Restricted to an one-electron atom system, the energy eigenvalues E do obviously not depend on the nucleus coordinate $\vec{R}$ and are therefore just defined by the principal quantum number n. Here, a larger n means a larger atomic energy. It has to be noted that the energy does not depend on the other quantum numbers leading to a energetic degeneracy of the individual subshells.

2.2.1 Molecular orbitals

Introducing another atom and a covalent bond between the atoms (H_2^+) makes the energy eigenvalues dependent on the nucleus coordinate $\vec{R}$ and the corresponding molecular wavefunction gets more complicated to calculate. Within the molecular orbital theory, one technique to calculate molecular orbitals is a linear combination of atomic orbitals (LCAO). Here, the molecular orbital is represented by a linear combination of atomic wavefunctions for each individual atom[24]

$$\Phi = \sum_i c_i \phi_i \tag{2.6}$$

For the H_2^+ molecule, the Schrödinger equation has then two solutions

$$\begin{aligned} \Phi_+ &= -c[\phi_{1s}^A + \phi_{1s}^B] \\ \Phi_- &= -c[\phi_{1s}^A - \phi_{1s}^B] \quad , \end{aligned} \tag{2.7}$$

with ϕ_{1s}^A and ϕ_{1s}^B describing the 1s orbital of hydrogen atom A and B, respectively. The sum of the two atomic orbitals Φ_+ forms a bonding molecular orbital due to the constructive inference between the the two hydrogen atoms as illustrated in fig. 2.2 **A**. Due to constructive overlap, the electron is shared between the two atoms which is a energetically a favorable state with a low energy eigenvalue. In contrast, the Φ_- wavefunction is an anti-bonding orbital with a nonconstructive overlap along the molecular bond coordinate. The spatial probability $||\Phi_-||^2$ for the electron is then to be either at atom A or at atom B with a zero probability for the space between the two atoms. A molecular orbital consisting of a combination of 1s atomic orbitals is always symmetric to the internuclear axis and is denoted as σ. Contrary, a combination of p orbitals results in a π-orbital which is asymmetric to a rotation around the bond. Anti-bonding orbitals are marked with a star (*).

Molecular orbitals can be described by a primary quantum number n, the angular momentum quantum number Λ, the reflection symmetry ($+/-$), a spin quantum number S and the parity of the wavefunction (g/u)

$$n^{2S+1}\Lambda_{g/u}^{+/-} \quad . \tag{2.8}$$

According to the diatomic case, the angular momentum is described by capital Greek letters (Σ, Π, ...) for polyatomic centrosymmetric while capital arabic letters (A, B, ...) are used for non-linear molecules. The symmetric properties of a molecular orbital is of great importance for electronic transitions and will be further discussed in section 3.1.

A special case of π-bonds is found for polyenes, in particular important for carotenoids investigated in this work. For a conjugated polyene chain, where single and double bonds between the carbon atoms alternate, the individual atomic p orbitals overlap and form a system of π-bonds. For the

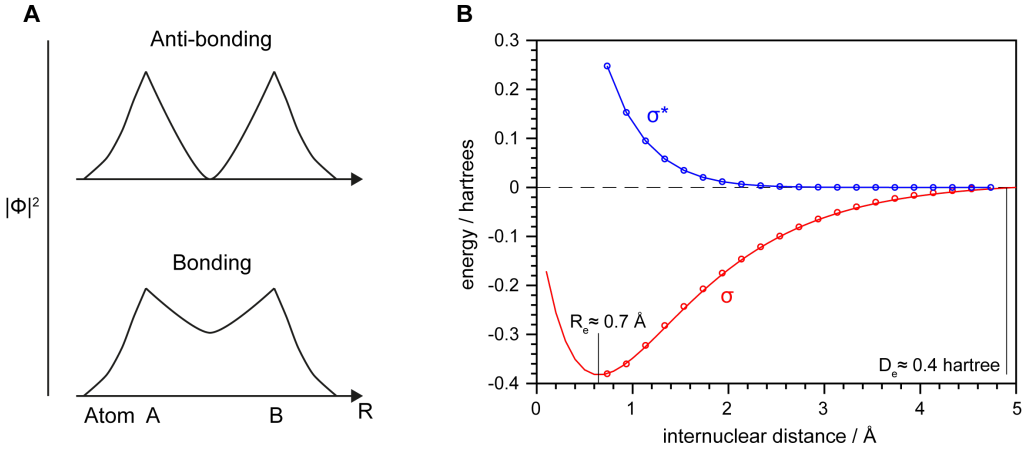

Figure 2.2: **A:** Illustration of the linear combination of two 1s atomic orbitals. Plotted is the electron probability density $|\Phi|^2$. **B:** Potential energy surface (PES) for the bonding and anti-bonding σ orbitals of H_2^+. Energies were calculated for specific internuclear distances with Gaussian09 (dots). The blue line is a spline connecting the datapoints while the red is a fit using a Morse potential (eq. (2.9)). The dissociation energy is denoted as D_e

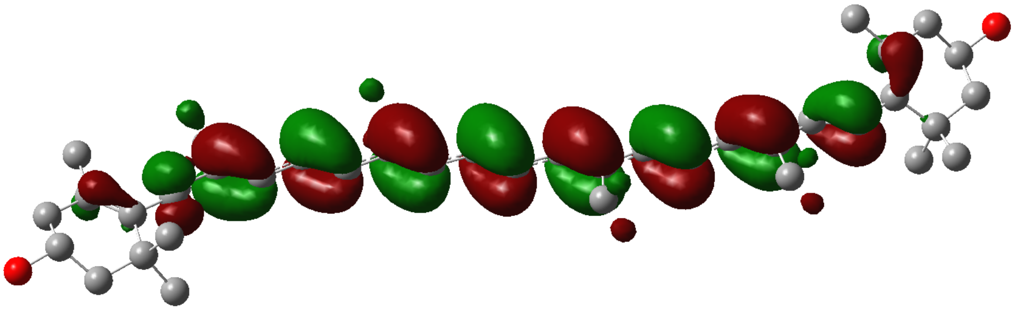

Figure 2.3: π-electron system of the HOMO state in the carotenoid Zeaxanthin. Here, the electronic orbitals are mostly out of phase (color code).Calculation was done with Gaussian09.

energetically lowest lying bonding state, all orbitals are in phase resulting in a delocalization of the electrons over the whole polyene chain. Higher energy states involve some out-of-phase orbitals while still remaining a bonding state. This upshift in energy narrows the energy gap to an anti-bonding orbital which is a lowest unoccupied molecular orbital (LUMO) for carotenoids (fig. 2.3). Upon electronic excitation, an electron is transitioned from a highest occupied molecular orbital (HOMO) to a LUMO. Due to the decreased energy difference for a delocalized π-electron system, this transition is for carotenoids in the range of the visible spectrum.

With molecular orbitals at hand, it is possible to calculate the energy eigenvalues which depend on the internuclear distance. Figure 2.2 **B** shows the potential energy surface (PES) for the σ and σ^* orbitals of a H_2^+ molecule. The energies were obtained at specific internuclear distances with the Gaussian09 software. It becomes clear that the bonding orbital has a energetic minimum which represents the bond length between the two hydrogen atoms. Electrons in the anti-bonding orbitals do not contribute to any bonding and are therefore higher in energy. A good approximation for a bonding orbital is the Morse potential

$$V(R) = D_e(1 - e^{-a(R-R_e)})^2 \tag{2.9}$$

where R_e is the equilibrium bond distance and a controls the width of the potential (red line in fig. 2.2). D_e denotes the dissociation energy which is needed to break up the bond.

2.3 Vibrational energies

Let's return to the time independent Schrödinger equations in the Born-Oppenheimer approximation of eq. (2.4). The nucleus equation for a one dimensional case is

$$\hat{H}_{nuc}(R)\chi_{nuc}(R) = -\frac{h^2}{8\pi^2\mu}\frac{d^2\chi_{nuc}(R)}{dR^2} + V(R)\chi_{nuc}(R) = E\chi_{nuc}(R) \quad . \tag{2.10}$$

To to get a better understanding of the nucleus energy eigenvalues, the potential energy can be assumed to solely represent the bonding interaction. If the Morse potential is approximated by a harmonic potential, the molecular bond can be thought of as spring connecting the two atoms. Inserting Hooke's law for $V(R) = {}^1\!/{}_2 KR^2$ leads to

$$\frac{d^2\chi}{dR^2} + \frac{8\pi^2\mu}{h^2}(E - \frac{1}{2}KR^2)\chi = 0 \quad , \tag{2.11}$$

where μ is the reduced mass, R the displacement from an equilibrium position and K is a constant representing the strength of the bond. The energy eigenvalues of eq. (2.11) are

$$E_n = h\nu(n + \frac{1}{2}) \quad . \tag{2.12}$$

The quantized eigenvalues show that the molecule can just vibrate at a certain frequencies of[25]

$$\nu = \frac{1}{2\pi}\sqrt{\frac{K}{\mu}} \quad . \tag{2.13}$$

The quantum number n can take integer values starting from 0 leading to equally spaced energies. The frequency of the vibration is dependent on the bond strength K and the mass of the atoms μ. If, for example, an atom is exchanged with an atom of higher mass while the bond is not altered, the frequency would downshift. Contrariwise, if the atomic masses are known, statements about the bond strength can be made. Since the binding energy is higher for a double bond than for a single bond and so on, the following approximation can be made

$$\nu_{\mathrm{C\equiv C}} > \nu_{\mathrm{C=C}} > \nu_{\mathrm{C-C}} \quad . \tag{2.14}$$

Although a harmonic potential is an accurate model around the energy minimum of this system, the potential energy surface (PES) defined by the electronic Schrödinger equation can be more accurately approximated by the anharmonic Morse potential given in eq. (2.9) (see section 2.2.1). This leads to corrected energy eigenvalues of

$$E_n = h\nu(n + \frac{1}{2}) - h\eta\nu(n + \frac{1}{2})^2 \quad , \tag{2.15}$$

with η as a measure for the degree of anharmonicity. In this approximation the energy levels are not equidistant anymore with a decreasing gap for higher eigenvalues.

2.3.1 Normal modes

Let's consider a more general case of a polyatomic molecule. In that case, all atoms together have $3N$ degrees of freedom (for each atom three Cartesian coordinates). The potential energy is then given by the generalization of Hooke's law in the quadratic form

$$V(q) = \frac{1}{2} \sum_{j=1}^{3N} \sum_{i=1}^{3N} f_{jk} q_j q_k \quad . \tag{2.16}$$

Bonds are represented by the force constant f_{jk} and Cartesian displacement coordinates by q_j. Transformation to mass-weighted Cartesian coordinates leads to an elimination of cross terms in eq. (2.16) leaving just $3N$ equations. A general solution of Newton's equation of motion then becomes

$$q_i = A_i \cos\left(\sqrt{\lambda_i} t + \phi_i\right), \tag{2.17}$$

with ϕ_i as the phase and A_i as the amplitude of displacement in direction of a certain Cartesian axis. The solution of this system of $3N$ equations has N solutions where all atoms vibrate with the same frequency λ[26]. As all degrees of freedom have now been considered, 6 (5) of these frequencies represent translational/rotational motion of the whole non-linear (linear) molecule and are therefore zero which leaves then $3N - 6$ ($3N - 5$) normal modes. Though using mass-weighted Cartesian coordinates is intuitive and descriptive, it has the disadvantage that the information of one normal mode is spread across $3N$ equations. For an easier description of vibrational transitions in quantum mechanics, the mass-weighted Cartesian coordinates are transformed into a more compact representation by

$$Q_k = \sum_{i=1}^{3N} l_{ik} q_i \quad , \tag{2.18}$$

with individual transformation coefficients l_{ik} for each normal mode k. Using these normal coordinates yields solutions in a similar form as for the mass-weighted Cartesian coordinates

$$Q_k = A_k \cdot \cos\left(\sqrt{\lambda_k} t + \phi_k\right) \quad , \tag{2.19}$$

but now A_k and ϕ_k are arbitrary constants[27].

Since a molecule of N atoms has $N - 1$ bonds, there are $N - 1$ stretching (changes in bond length) and $2N - 5$ deformational (changes in bond angle) modes. A H_2O water molecule has therefore 3 vibrational modes, a symmetric and asymmetric stretch and a bending vibration. Considering largely localized vibrations in more complex (macro-)molecules expands the picture of vibrational motions. Figure 2.4 depicts these motions, where the stretch, bending and rocking vibrations take place in the plane of the system while the other deformational modes are out-of-plane.

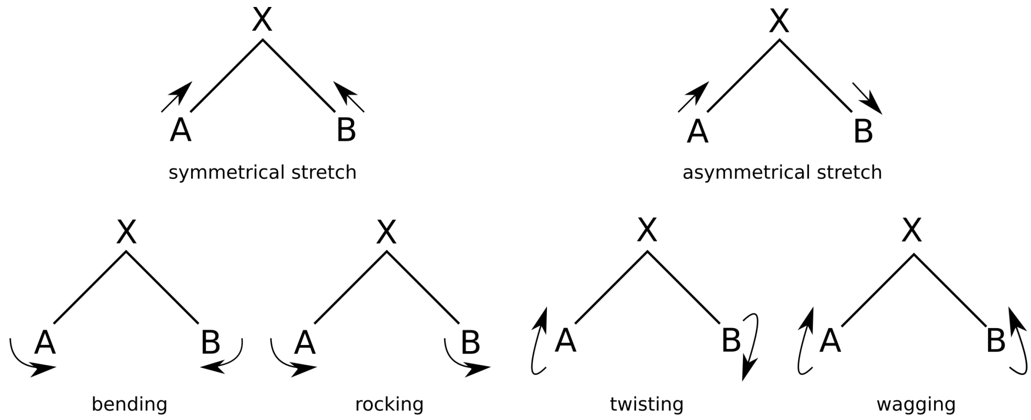

Figure 2.4: Vibrational modes of a triatomic system where atom X is connected to a rigid environment.

2.4 Transition probabilities

Interrogation of the molecular energy landscape allows to gather a lot of information about the sample of interest including spectral identification of compounds, electrostatic interactions of molecules, structural information and chemical changes such as protonation events. One way to determine electronic and vibrational excited states energy levels is to exploit the interaction of molecules with electromagnetic radiation. If the energy of a photon matches an energy difference between two electronic or vibrational states, the molecule has a certain probability to absorb the energy of the photon promoting the molecule to a higher energy level. In quantum mechanics, the probability for such a transition from state i (initial) to f (final) due to photon absorption is defined by

$$P_{fi} = \langle \Phi_f | \hat{\mu} | \Phi_i \rangle \quad , \tag{2.20}$$

with $\hat{\mu}$ as the transition dipole moment operator[28]. A probability of zero is referred to as a forbidden transition while a nonzero probability is called allowed. In a spectroscopic experiment, the rate of photon absorption at a certain frequency is detected. This measured intensity of bands in a spectrum depends quadratically on the dipole moment operator

$$I_{fi} \propto |P_{fi}|^2 \quad . \tag{2.21}$$

3 EXPERIMENTAL METHODS

Spectroscopy is a versatile technique in which the energy landscape of a molecule can be interrogated by the interaction with electromagnetic radiation. In a spectroscopic experiment, the radiation intensity is measured as a function of wavelength/frequency. To study electronic transitions, absorption spectroscopy in the visible to ultraviolet spectral region (250 to 700 nm) is used. For vibrational transitions, two different methods are employed in this work, infrared absorption and Raman scattering spectroscopy. Due to the lower energy difference between vibrational energetic levels compared to electronic transitions, the radiation used for vibrational absorption spectroscopy needs to be of higher wavelengths found in the infrared spectral region. In Raman spectroscopy, essentially the same information is obtained as with infrared absorption but the underlying physical principle is different leading to a quantum mechanical effect called resonance enhancement. With this, certain vibrational modes can be spectrally enhanced if they are couple to an electronic transition.

A theoretical approach to compute the energy landscape of a molecule is density functional theory (DFT). Using this method permits to calculate a spectrum of a molecule at a relatively low computational cost. Comparison with experimental data can give interesting structural details of the molecule. The last section will cover two data analysis techniques frequently used in this work, singular value decomposition (SVD) and global fitting.

3.1 UV/Vis spectroscopy

Many atoms and molecules undergo an electronic transition if a photon of the ultraviolet–visible (UV/Vis) part of the electromagnetic spectrum is absorbed. Since UV/Vis spectroscopy deals with electronic transitions, the nucleus can be assumed to be fix in the Born-Oppenheimer approximation (section 2.1). The electronic transition dipole moment is a sum over all n electrons and N nuclei of the molecule[29]

$$\hat{\mu} = -e\sum_n \hat{r}_n + e\sum_N Z_N \hat{R}_N \quad , \tag{3.1}$$

Inserting in eq. (2.20) gives for an transition from an initial electronic state i to an excited state f

$$\begin{aligned} P_{fi} &= \int \Phi^*_{elec,f}\chi^*_{vib,f}\left(-e\sum_n \hat{r}_n + e\sum_N Z_N \hat{R}_N\right)\Phi_{elec,i}\chi_{vib,i}d\tau \\ &= -e\sum_n \int \Phi^*_{elec,f}\hat{r}_n\Phi_{elec,i}d\tau \int \chi^*_{vib,f}\chi_{vib,i}d\tau \\ &+ e\sum_N Z_N \int \Phi^*_{elec,f}\Phi_{elec,i}d\tau \int \chi^*_{vib,f}\hat{R}_N\chi_{vib,i}d\tau \quad , \end{aligned} \tag{3.2}$$

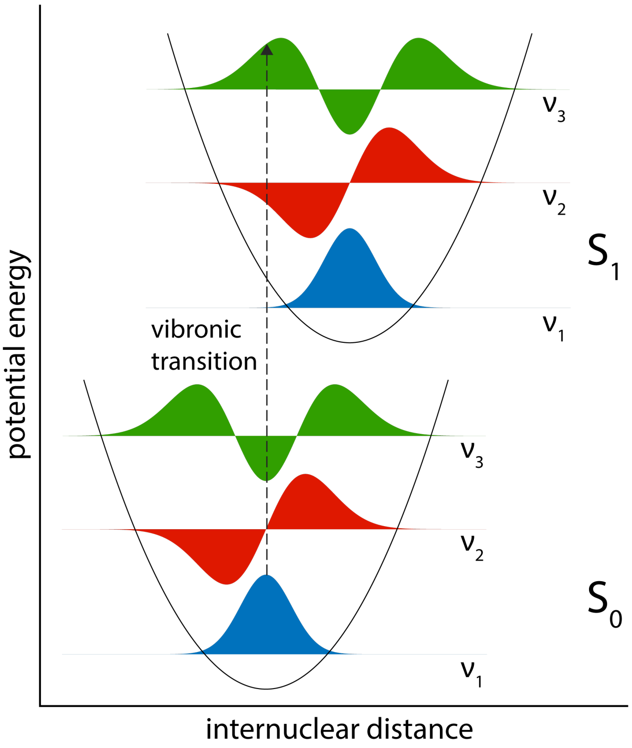

Figure 3.1: Interpretation of the Franck-Condon principle. The electronic states S_x are described by the potential energy surface (PES) approximated by an harmonic potential in which the nucleus can move. Vibrational levels are quantized (ν_x) with probability densities defined by the corresponding wavefunctions (colored curves). An electronic excitation usually elevates one electron to an anti-bonding orbital resulting in a bond weakening and hence an increase in internuclear distance. The Franck-Condon factor states that electronic transitions are more probable when the probability densities for the nucleus in the ground an excited state have a strong overlap. Here, the transition $\nu_1(S_0) \rightarrow \nu_3(S_1)$ has the strongest overlap. In the Born-Oppenheimer approximation, the electrons move way faster than the nucleus. This includes that an electronic transition happens so fast such that the nucleus is not able to adapt to the new electronic configuration represented by the vertical arrow.

with the elementary charge e and Z_N for the charges of the nucleus. The integral in the second summand over the electronic part of the wavefunction for two different states is zero due to orthogonality. This does not hold for the integral over the vibrational term because the two wavefunctions are solutions for different potential energy surface (PES) of the initial and final electronic state, respectively. Hence,

$$\begin{aligned} P_{fi} &= \overbrace{-e\sum_n \int \Phi^*_{elec,f}\hat{r}\Phi_{elec,i}d\tau}^{\hat{\mu}_{elec,fi}} \overbrace{\int \chi^*_{vib,f}\chi_{vib,i}d\tau}^{S(vib_f,vib_i)} \\ &= \hat{\mu}_{elec,fi}S(vib_f,vib_i) \quad . \end{aligned} \tag{3.3}$$

The electric dipole transition moment $\hat{\mu}_{elec,fi}$ arises due to a redistribution of electrons provoked by the electromagnetic wave. The Franck-Condon factor $S(vib_f, vib_i)$ is a measure for the overlap of the vibrational wavefunctions of the initial and final electronic state. A higher overlap translates therefore into a higher transition probability. For a displaced excited electronic state, the electronic transition is therefore additionally accompanied by a change of the vibrational state. Figure 3.1 illustrates the principle of vibronic transitions.

In addition to the Franck-Condon factors, electronic transitions are also governed by selection rules (for a description of molecular orbitals see eq. (2.8))[29]

1. $\Delta\Lambda = 0, \pm 1 \quad ,$
2. $\Delta S = 0 \quad ,$
3. the parity has to change .

3.1.1 Instrumentation

In a typical UV/Vis absorption experiment, the sample is put between a light source of intensity I_0. After the light passes the sample it will have a decreased intensity I_1 due to absorption of photons. The capability for photon absorption of a specific molecule depends on one the hand on the quantum-mechanical properties discussed in the previous chapter but on the other hand also on macroscopic attributes like sample concentration c and length of the light path l through the sample. The absorption A of the sample is given by the Beer–Lambert law[30]

$$A(\lambda) = \log_{10}\left(\frac{I_0\lambda)}{I_1(\lambda)}\right) = \epsilon(\lambda)cl \quad , \tag{3.4}$$

with $\epsilon(\lambda)$ as the molar extinction coefficient at a given wavelength λ which is an intrinsic property of the sample. Steady-state absorption experiments were conducted on a UV-2450 spectrometer from Shimadzu.

For time-resolved measurements a commercially available flash photolysis setup from Applied Photophysics (LKS80) was used and is depicted in fig. 3.2. The idea is to first measure the absorption of an unperturbed sample $A_0(t)$ and then subsequently changes in absorption over time $A_1(t)$ after the sample was excited by a short laser flash. By subtraction of $\Delta A(t) = A_0(t) - A_1(t)$ even small signal changes will be highlighted in a difference dataset. Negative absorption changes are a result of vanishing absorption due to the transformation of the initial state to a newly formed species which in turn will give rise to positive signals.

The inducing laser flash is provided by a solid state neodymium-doped yttrium aluminum garnet (Nd:YAG) laser in pulsed mode (10 ns) emitting at the third harmonic of 355 nm. The laser output is coupled to an optical parametric oscillator (OPO) permits to tune the wavelength suitable for the experiment. A xenon arc lamp serves as a white probing light source which passes a monochromator to select a certain wavelength. A photomultiplier detects the light after passing the sample. Using this setup, it is necessary to scan through the wavelengths to obtain spectral information. For measurements in the ns to µs range, the xenon lamp is put into pulsed mode to enhance photon flux while for measurements up to seconds cw-operation is used. To construct a dataset over the whole time range, the slow time trace is appropriately scaled and merged with faster time trace. This setup achieves a sufficient signal-to-noise ratio for single-shot experiments (no averaging).

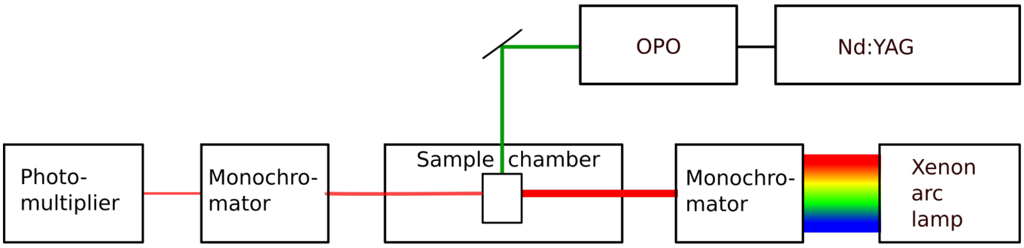

Figure 3.2: Schematic of the used setup for time-resolved absorption experiments in the visible.

3.2 Infrared spectroscopy

While electronic transitions are in the energy range of visible or UV radiation, vibrational modes of a molecule can be excited by infrared light. The investigation of vibrations can give insights into the (hydrogen) bond strength, chemical structure, electrostatic environment and it even permits the tracking of protonation events. Infrared spectroscopy is widely used in biophysics, in particular for studying the folding or the reaction dynamics of proteins. This section will provide the theoretical basics and introduce the two techniques used in this work, Fourier transform infrared (FTIR) and transient absorption spectroscopy using infrared emitting quantum cascade lasers (QCLs).

3.2.1 Theoretical Background

As a vibrational transition will be induced by the absorption of a photon, the process is controlled by the transition dipole moment operator (eq. (3.1))[27]

$$\hat{\mu} = e \sum_{N} Z_N \hat{R}_N \quad . \tag{3.5}$$

The electrons are here omitted since their motions are neglected in the Born-Oppenheimer approximation. The probability for a transition from an initial vibrational level i to a final state f is given by

$$P_{fi} = \langle \chi_f | \hat{\mu} | \chi_i \rangle \quad , \tag{3.6}$$

where χ denotes the nuclear wavefunction. A Taylor expansion of the dipole operator in respect to normal coordinates for a non-linear molecule yields

$$\hat{\mu} = \mu_0 + \sum_{k=1}^{3N-6} \underbrace{\left(\frac{\delta \mu}{\delta Q_k} \right)_0}_{\mu_k} \hat{Q}_k + \dots \quad . \tag{3.7}$$

Neglecting higher order terms and insertion into eq. (3.6) results in

$$P_{fi} = \mu_0 \langle \chi_f \chi_i \rangle + \sum_{k=1}^{3N-6} \mu_k \langle \chi_f | \hat{Q}_k | \chi_i \rangle \quad . \tag{3.8}$$

It has to be noted that the factors μ_0 and μ_k have lost their operator status due to the evaluation at 0 in the Taylor expansion and can therefore be taken out of the integrals. The first term of eq. (3.8) is zero because of the orthogonality of vibrational wavefunctions. The second term is not zero if two conditions are fulfilled (selection rules)

1. $\mu_k = \left(\frac{\delta\mu}{\delta Q_k}\right)_0$ is not zero. This implies that the dipole moment changes due to vibrational displacement of the nucleus,
2. the integral has to be non-zero. For harmonic potentials this is the case if the vibrational quantum number changes by one unit ($\Delta\nu = \pm 1$)[31].

Vibrational transitions with $\Delta\nu = \pm 1$ are called fundamentals while higher order transitions are referred to as overtones. Overtone transitions become potentially allowed due to the anharmonicity of the potential energy surface (PES) (section 2.3)[32].

3.2.2 FTIR spectroscopy

Conventional infrared spectrometer used dispersive elements like prisms or gratings to create a monochromatic probing beam out of a polychromatic infrared light source. These spectrometers have certain limitations such as low scan speed and poor wavelength accuracy. A modern approach is to use a Michelson interferometer consisting of a beamsplitter, a fixed and a movable mirror. Here, the light will create an inference pattern on the detector, depending on the frequency ν and the position of a movable mirror δ (fig. 3.3). In case of a perfect beamsplitter (reflectance and transmittance both equal to 0.5), the intensity after the the interference of the two beams at a given frequency ν_0 is[28]

$$I(\delta) = 0.5 I(\nu_0)\cos(2\pi\nu_0\delta) \quad , \tag{3.9}$$

with $I(\nu_0)$ denoting the intensity output of a monochromatic light source. Considering $B(\nu)$ for the detected light emitted from a polychromatic light source, the integral over all the frequencies has to be taken

$$I(\delta) = 0.5\int_{-\infty}^{+\infty} B(\nu)\cos(2\pi\nu\delta)d\nu = 0.5\int_{-\infty}^{+\infty} B(\nu)e^{2\pi i\nu\delta}d\nu \quad , \tag{3.10}$$

The resulting intensity pattern is measured with a Mercury-Cadmium-Telluride (MCT) detector at given mirror positions (interferogram). A complex Fourier transformation (FT) of eq. (3.10) over the mirror position δ then yields the desired spectral information[33]

$$B(\nu) = \int_{-\infty}^{+\infty} I(\delta)e^{-2\pi i\nu\delta}d\delta = \int_{-\infty}^{+\infty} I(\delta)\cos(2\pi\nu\delta)d\delta \quad . \tag{3.11}$$

The integral is from minus infinity to infinity but in practice, the optical path difference is confined by the maximal mirror displacement Δ. Taking this into account, the interferogram can be multiplied by function $A(\delta)$ a which is zero for $-\infty < \delta < -\Delta$ and $+\Delta < \delta < \infty$

$$B(\nu) = \int_{-\infty}^{-\infty} A(\delta)I(\delta)\cos(2\pi\nu\delta)d\delta \quad . \tag{3.12}$$

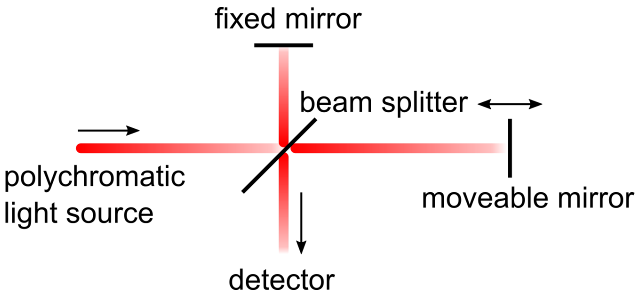

Figure 3.3: Illustration of a Michelson interferometer. A light beam from a polychromatic light source is splitted and hits a fixed and a movable mirror. Depending on the frequency and the mirror position, the light beam will interfere on the way to the detector.

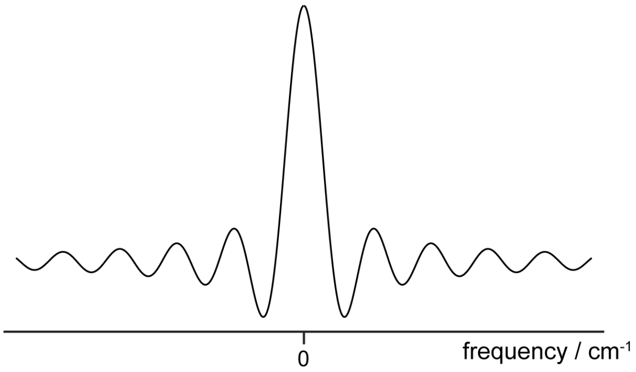

Figure 3.4: Fourier transformation (FT) of a boxcar function.

This function introduces certain properties for the spectral absorption bands. Figure 3.4 shows the FT for a boxcar function which is 1 for $-\Delta < \delta < +\Delta$. The center peak defines the spectral resolution of the final spectrum. Because it will also introduce the ripples besides of that peak, empirical apodization functions for $A(\delta)$ can be used to reduce the amount of ripples. Each apodization function has their own characteristics and it is possible to significantly reduce the amount of ripples while maintaining a $1/\Delta$ spectral resolution. The range of resolved frequencies is defined by the step-size of the movable mirror x (Nyquist criterion)

$$\nu_{max} = \frac{1}{2x} \quad . \tag{3.13}$$

Hence, it is of great importance to precisely determine the mirror position during the measurement. This is done by detecting an interference pattern provided by an additional Helium-neon laser emitting at 633 nm. To avoid artifacts later in the spectrum, ν_{max} should cover all the frequencies which are registered at the detector.

Two different modes of operation exist for time-resolved measurements after an exciting laser flash (see section 3.1). In rapid scan, the movable mirror is quickly displaced, i.e. whole interferograms are taken at a high repetition rate. The time resolution in a rapid-scan experiment is limited by the speed of the movable mirror. For the Vertex 80v from Bruker, which is used in this work, a time resolution of 10 ms can be achieved. To cover the time range down to ns, the interferogram is constructed out of time-resolved measurements at fixed mirror positions (step-scan mode). This means that a kinetic trace is measured at each mirror position resulting in long measuring times because the number of desired spectral averages is multiplied by the number of data points. For a good step-scan experiments it is necessary to ensure a high mirror position and sample stability over the course of the experiment. The time resolution is limited by the response time of the detector.

3.2.3 QCL-based transient absorption spectroscopy

The polychromatic light source used in Fourier transform infrared (FTIR) spectroscopy is an advantage if a wide frequency range has to be measured in favor of low intensity outputs at a given frequency. Quantum cascade lasers (QCLs) are tunable infrared lasers which deliver high intensities but just in a limited spectral range. The high photon flux is beneficial in experiments were besides the system of interest other components of the sample strongly absorb. Is is also suitable for samples which experience a pronounced photodegradation and thus the number of averages play an important role. In external cavity QCLs, the broadband output of a QCL-chip is directed to an external grating. By tilting of that grating, specific frequencies can be selected[34]. In this work, mostly the MIRcat-QT from Daylight solution is used in the wavenumber range of 1500 to 1700 $\mathrm{cm^{-1}}$.

The design of an experimental setup for transient absorption spectroscopy is basically the same as discussed for the visible range in section 3.1. The depicted scheme in fig. 3.5 was realized by Schultz *et al.*[35]. Briefly, the single frequency output of the QCL is directed through an adjustable iris which controls the attenuation of the intensity. The laser beam is then directed through the sample before it is finally detected by MCT detector. As it is the case for the step-scan FTIR operation, the time resolution is limited by the rise time of the detector. Excitation of the sample was usually achieved by a Minilite pulsed Nd:YAG laser from Photonic Solution emitting at 532 nm. The photovoltage at the MCT is digitized by two oscilloscopes with different sampling rates taking account for the fast time regime from ns to µs/ms and the slow regime up to seconds, respectively.

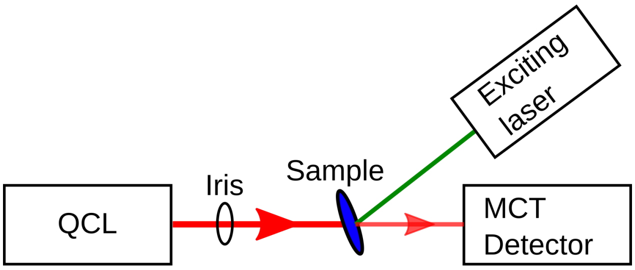

Figure 3.5: Scheme of a home-built QCL setup for transient absorption spectroscopy.

3.3 Raman spectroscopy

In UV/Vis as well as in infrared spectroscopy, the physical principle of photon absorption is exploited. If the energy of the photon matches an electronic or vibrational transition, the molecule is excited to an higher energy state. Another approach to study the vibrational states of a molecule with light is by Raman Scattering where a photon is inelastically scattered at a molecule. The scattered photon can have a lower (Stokes) or a higher energy (anti-Stokes) than the initial one and exactly this energy difference contains information about the vibrational state. If the photon gets elastically scattered (Rayleigh), it will have the same energy as before the scattering process and thus no information about the molecular vibrational levels is obtained.

Unfortunately, Raman scattering is a very improbable event. While just one out of about 10^{-4} to 10^{-3} photons is Rayleigh scattered, the probability for Raman scattering is even 3 to 5 orders of magnitude less[28]. By choosing an initial photon energy matching a vibronic transition (resonance), the Raman scattering probability can be significantly enhanced. This section will first provide a classical description of the Raman scattering process which delivers a basic concept. It is followed by a quantum mechanical treatment which is necessary to describe the effect of resonance enhancement.

3.3.1 Classical picture

An linearly polarized electromagnetic wave can be expressed as

$$E = E_0 \cos(2\pi\nu_0 t) \quad , \tag{3.14}$$

where E_0 denotes the amplitude and ν_0 is the frequency of the electromagnetic wave. If the electric field interacts with a molecule, it will induce an electric dipole μ due to distortion of the molecular electron cloud. As long as the electric field of the radiation is not too strong, the induced dipole moment is proportional to the electric field[31]

$$\mu = \alpha(q)E = \alpha(q)E_0 \cos 2\pi\nu_0 t \quad . \tag{3.15}$$

The polarizability factor $\alpha(q)$ describes the ability of the electron distribution to respond to the electromagnetic wave which depends on the position of the nucleus q. Considering that the electromagnetic wave interacts with a vibrating molecule with a normal mode frequency ν_k, the displacement is defined by the normal coordinate Q_k[25]

$$q = Q_k \cos 2\pi\nu_k t \quad . \tag{3.16}$$

For small amplitudes of vibration, the polarizability $\alpha(q)$ can be approximated as

$$\alpha(q) = \alpha_0 + \left(\frac{\partial\alpha}{\partial Q_k}\right)_0 Q_k + \ldots \quad . \tag{3.17}$$

Neglecting higher order terms and combining eqs. (3.15) and (3.17) with applying trigonometrical relations results in

$$\mu = \underbrace{\alpha_0 E_0 \cos(2\pi\nu_0 t)}_{Rayleigh} + \frac{1}{2}\left(\frac{\partial\alpha}{\partial Q_k}\right)_0 Q_k E_0 \left[\underbrace{\cos(2\pi(\nu_0+\nu_k t))}_{Anti-Stokes} + \underbrace{\cos(2\pi(\nu_0-\nu_k t))}_{Stokes}\right] \quad . \tag{3.18}$$

This equation essentially describes the Raman scattering process as photons emitted by oscillating induced dipoles. The first term denotes Rayleigh scattering, while the second and third term represent Anti-Stokes and Stokes scattering, respectively, where the energy of the emitted photon is changed

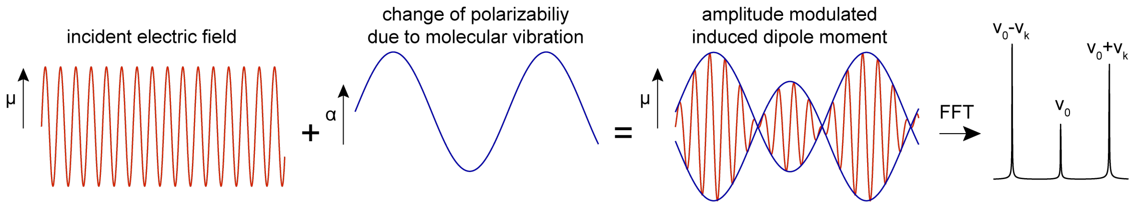

Figure 3.6: Scheme of Raman scattering. If the polarizability of the molecule changes during a vibration, the electromagnetic radiation emitted by the oscillating dipole gets amplitude modulated. Decomposition of the resulting wave reveals three components with constant amplitude at frequencies of ν_0 (Rayleigh), $\nu_0 - \nu_k$ (Stokes) and $\nu_0 + \nu_k$ (anti-Stokes).

according to the vibrational mode of the molecule. Equation (3.18) also states a selection rule for Raman activity. If $(\partial\alpha/\partial q)_0$ is zero, no Raman scattering occurs. In other words, a vibration is Raman active if the displacement of the nuclei during the vibration provokes a change in the polarizability of the electron cloud.

Figure 3.6 illustrates the Raman mechanism in a classical picture. The incoming electromagnetic wave with frequency ν_0 induces an oscillating dipole in the molecule with an amplitude depending on the polarizability α. If the polarizability changes during a molecular vibration, the induced dipole gets amplitude modulated. A decomposition of the resulting wave reveals three components with constant amplitude at the frequencies of ν_0 (Rayleigh), $\nu_0 - \nu_k$ (Stokes) and $\nu_0 + \nu_k$ (anti-Stokes).

3.3.2 The resonance effect

To explain certain aspects of Raman scattering, in particular the resonance effect, classical physics reaches its limits. As discussed in section 3.3.1, the classical principle of Raman scattering is radiation emitted by induced dipoles. Hereby, the polarizability α is a crucial factor defining the intensity I_R of Raman scattering

$$I_R \propto \nu_0^4 I_0 N \left(\frac{d\alpha}{dQ}\right)^2 \quad , \tag{3.19}$$

with N for the number of molecules, I_0 and ν_0 denote the intensity and frequency of the exciting light[36]. It is obvious that the intrinsic parameter of polarizability defines the scattering intensity of a molecule. The process of Raman scattering involves quantum mechanically two photons (absorbed & emitted) which requires second order perturbation theory. A simplified Kramer Heisenberg Dirac (KHD) equation describes the polarizability operator $\hat{\alpha}$ for a vibrational transition from i to f in the electronic ground state G

$$(\alpha_{\rho\sigma}) = \frac{1}{\hbar}\sum_{S,s}\left(\frac{\langle G,f|\hat{\mu}_\rho|S,s\rangle\,\langle S,s|\hat{\mu}_\sigma|G,i\rangle}{\nu_{is} - \nu_0 - i\Gamma_S}\right) \quad , \tag{3.20}$$

where $\hat{\mu}_\sigma$ and $\hat{\mu}_\rho$ denote the electric dipole moment of the incident and scattered photon. The correction term Γ_s represents the lifetime of the excited state which is usually small. Considering the nominator of eq. (3.20), it basically describes an absorption of a photon which lifts the molecule to an excited vibronic state S, s with a subsequent photon emission leading to a relaxation to the vibrational state f (fig. 3.7). The summation of all vibronic states S, s creates a so-called virtual state which is

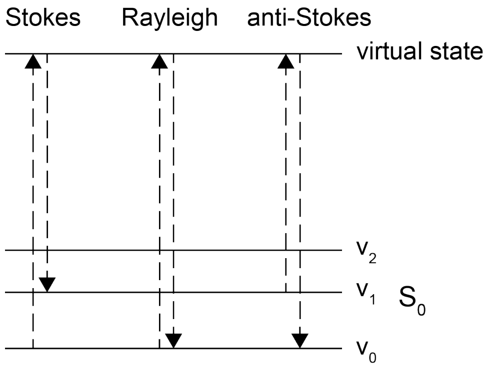

Figure 3.7: Quantum mechanical scheme of the Raman effect as a two-photon process.

not a solution of the molecules Schrödinger's equation (see chapter 2). It rather can be thought of a vibronic state of the perturbed molecule after photon absorption without a defined energy. If the energy of the incident photon ν_0 is far away from a vibronic transition, all states contribute nearly equally to the summation. But as soon as ν_0 matches a real vibronic state, this transition will dominate the summation and resonance enhancement occurs (denominator enhancement).

The transition probabilities in the nominator are the same as in eq. (3.2) for vibronic transitions. Considering resonance enhancement, the summation over the electronic states can be omitted. Denoting the electronic transition from the ground state G to the electronic state S as M_{GS} leads to

$$(\alpha_{\rho\sigma}) = \frac{1}{\hbar}\sum_{s}\left(\frac{\langle f|s\rangle\,\langle s|i\rangle\, M_{GS,\rho}M_{GS,\sigma}}{\nu_{is}-\nu_0-i\Gamma_S}\right) \quad . \tag{3.21}$$

With a Taylor expansion of M_{GS} in respect to normal coordinates Q_k, eq. (3.21) can be simplified to

$$\begin{aligned}(\alpha_{\rho\sigma}) &= \overbrace{M^0_{GS,\rho}M^0_{GS,\sigma}\frac{1}{\hbar}\sum_{s\neq i,f}\frac{\langle f|s\rangle\,\langle s|i\rangle}{\nu_{is}-\nu_0-i\Gamma_s}}^{\text{A-term}}\\ &+ \underbrace{\frac{1}{\hbar}\sum_{s\neq i,f}\frac{\langle f|\hat{Q}_k|s\rangle\,\langle s|i\rangle\,(\frac{\delta M_{GS,\rho}}{\delta Q_k})_0 M_{GS,\sigma}+\langle f|s\rangle\,\langle s|\hat{Q}_k|i\rangle\,(\frac{\delta M_{GS,\sigma}}{\delta Q_k})_0 M_{GS,\rho}}{\nu_{is}-\nu_0-i\Gamma_s}}_{\text{B-term}}\end{aligned} \tag{3.22}$$

The two terms represent two different scattering mechanisms. In the A-term, the nominator consists of the electronic transition factors M_{GS} and the vibrational Frank-Condon factors. Hence, the same statements as in section 3.1 apply, in particular that the excited electronic state has to be displaced in respect to the ground state. An example is the $\pi \rightarrow \pi^*$ transitions in carotenoids. The population of the anti bonding orbital after photoexcitation leads to a decrease in bond order from 2 to 1 of the polyene chain. The C=C bonds have now more single bond character and therefore an increased bond length. In this case, vibrations associated with this change will gain strong enhancement from the A-term. Contrary, the C−H bond is unaffected by the $\pi \rightarrow \pi^*$ transition and will not experience any enhancement from the A-term.

The scattering resulting from the B term is called Herzberg-Teller Coupling. Here, the nominator contains besides Frank-Condon factors also Q-dependent vibrational overlap integrals. This allows enhancement for non-shifted electronic states. As in section 3.2, the Q-dependent transitions require a change of the vibrational quantum number by one in an harmonic approximation. This holds not true for the A-term where no vibrational selection rules can be derived.

Since only vibrations coupled to an electronic transition will be enhanced by the resonance effect, it is a perfect tool to simplify a Raman spectrum. This advantage can for example be applied to chromophore containing proteins where resonance enhancement leads to an selective increase of Raman modes of the chromophore while bands originating from the apo-protein remain in the background. By choosing a probing wavelength in the vicinity of an real electronic transition, other relaxation processes, such as fluorescence, take place and a baseline correction becomes necessary.

3.3.3 Surface enhancement

Another mechanism to increase the probability of Raman scattering is surface enhancement. An electromagnetic wave interacting with a metal surface can induce a charge separation which propagates along the surface (surface plasmons). The induced electric dipole in the metal oscillates with a plasmon frequency ν_{pl} and will therefore emit electromagnetic radiation which additionally excites a molecule close to the metal surface. Matching the incoming photon's energy with the plasmon frequency of the metal surface gives strongest enhancement (resonance). If the metal surface is not big enough for surface plasmon propagation, the charge separation leads to a localized surface plasmon (LSP), which produces greatly enhanced electric fields near the surface. Placing a molecule near to metal nanoparticles is the principle of surface-enhanced Raman spectroscopy (SERS).

If an electromagnetic wave has a larger wavelength as a metal colloid, the quasistatic approximation can be applied (the electromagnetic radiation is considered constant). Considering a metal sphere with radius a, the total electric field can be express as[27,37,38]

$$E_{total}(\nu_0) = E_0(\nu_0) + E_{ind}(\nu_0) = E_0(\nu_0) + E_0\cos(\theta) + g\left(\frac{a^3}{r^3}\right)E_0\cos(\theta) \quad , \tag{3.23}$$

with E_0 for the amplitude of the incoming electric field, E_{ind} for the induced field by the metal nanoparticle, θ is the angle relative to the electric field and r denotes the distance from the metal surface. The induced electric field is strongest for 0° and 180°, where a vibration points along the polarization direction. It becomes obvious that larger metal spheres leads to stronger electric field enhancements. Another crucial factor for surface enhancement is the factor g which is connected to the polarizability of the metal sphere α

$$\alpha = 4\pi\epsilon_0 \underbrace{\frac{\epsilon(\nu_0) - \epsilon_M}{\epsilon(\nu_0) + 2\epsilon_M}}_{g} \quad , \tag{3.24}$$

with ϵ_M denoting the dielectric constant of the surrounding medium. The polarizability is maximized if the dielectric function of the metal equals $\epsilon(\nu_0) = -2\epsilon_M$ (Fröhlich condition). Considering a metal sphere of around 50 to 60 nm in air, the LSP resonance is at 530 nm for gold and at 435 nm for silver. Other factors influencing the dielectric function are the shape and the size of the metal nanoparticles[39].

According to eq. (3.19), the Raman intensity is proportional to the incoming electric field E_0

$$I_R \propto \left| \left(\frac{d\alpha}{dQ} \right) E_0 \right|^2 \quad . \tag{3.25}$$

An enhancement factor for surface-enhanced Raman (SER) can be defined as

$$\mathrm{EF} = \frac{|E_{ind}|^2}{|E_0|^2} \quad . \tag{3.26}$$

Considering that the molecule near the metal surface itself also emits an electromagnetic field due to normal Raman scattering but with shifted frequency (E'_{ind}). With an approximation of $E_{ind} \approx \sqrt{2} g E_0$ this leads to an enhancement factor of

$$\mathrm{EF} = \frac{|E_{ind}|^2 |E'_{ind}|^2}{|E_0|^4} = 4g^2 g'^2 \quad . \tag{3.27}$$

For a small Raman frequency shift ($g \approx g'$) the EF scales with g^4 which is origin of the E_0^4 enhancement often found in literature (relating to the proportionality of E_{ind} and E_0)[40].

Inserting for ϵ a dielectric function of a Drude metal results in[41]

$$\alpha(\nu_0) = \frac{(\epsilon_b \nu_0^2 - \nu_p) + i\nu_0 \gamma \epsilon_b}{[(\epsilon_b + 3)\nu_0^2 - \nu_p^2] + i\nu_0 \gamma (\epsilon_b + 3)} \quad . \tag{3.28}$$

Hence, the polarizability depends on the incident frequency, a contribution of interband transitions represented by ϵ_b, the metal's plasmon resonance frequency ν_p and a electronic scattering rate γ. Equation (3.28) has a maximum at $\nu_R = \frac{\nu_p}{\sqrt{\epsilon_b + 3}}$ with a width of $\gamma(\epsilon_b)$. Hence, if the contribution of interband transitions is large, the enhancement will be decreased. For a Raman excitation in the visible range, gold has relatively high ϵ_b while silver will give rise to a stronger enhancement.

In addition to the electromagnetic enhancement, there is also a chemical contribution to surface enhancement. It is a result if the molecule forms a chemical bond to the metal surface which permits charge transfer. This interaction with the metal ions increases the polarizability and consequently the scattered Raman intensity. Both forms of enhancement, electromagnetic and chemical, are short-range effects where the induced electric field decays with r^{-3}. Since the surface enhancement for Raman spectroscopy scales with E_0^4, the distance dependence is even increased to r^{-12} [40].

A recent paper by Mueller *et al.* proposes a quantum mechanical treatment of surface enhancement as a higher order Raman process[42]. The idea is that the incoming photon of energy ϵ_0 excites a LSP with energy ϵ_L. Via near-field coupling, a molecule gets excited from a ground state to a virtual state i of energy ϵ_i. Upon relaxation to the final vibrational state f with energy ϵ_f, the LSP is excited again by $\epsilon_i - \epsilon_f = \epsilon_S$. Finally, the LSP emits the Raman shifted photon of energy ϵ_S. Figure 3.8 schematically

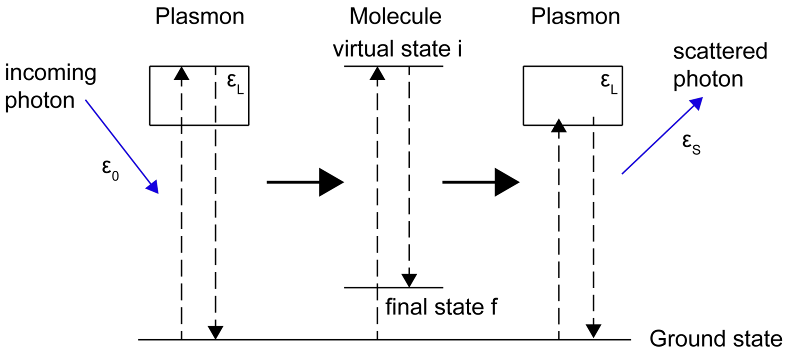

Figure 3.8: Illustration of SER as a higher order Raman process. Adopted from Mueller *et al.*[42].

depicts these processes. In the framework of 4th order perturbation theory, the SER enhancement factor depends on the LSP resonance and can be expressed as

$$\mathrm{EF}(\epsilon_L) = \left| \frac{M_1 M_2}{(\epsilon_0 - \epsilon_f - \epsilon_L - i\Gamma)(\epsilon_0 - \epsilon_L - i\Gamma)} + \frac{M_1}{\epsilon_0 - \epsilon_L - i\Gamma} + \frac{M_2}{\epsilon_0 - \epsilon_f - \epsilon_L - i\Gamma} \right|^2 , \tag{3.29}$$

with M_1 and M_2 as coupling and Γ as damping factors. There are two resonance cases for eq. (3.29). One if the incoming photon energy ϵ_0 matches a LSP mode ϵ_L (incoming) and another one when the Raman scattered photon's energy $\epsilon_S = \epsilon_0 - \epsilon_f$ matches a LSP mode (outgoing). It becomes also obvious that the vibrational energy of the final state ϵ_f influences the EF giving rise to potentially different intensities of a vibrational mode in normal Raman and SER experiments. The authors highlight an interesting point where the proposed treatment leads to larger EFs compared to the electromagnetic theory. With this, the chemical enhancement becomes less important and the surface-enhancement due to LSP resonances dominates.

3.3.4 Setup

Since Raman spectroscopy is not relying on photon absorption, the experimental requirements are different to absorption spectroscopy. Light scattering is a process where an atom or molecule interacts with an electromagnetic wave resulting in beam deflection and a potential change of frequency. In contrast to absorption spectroscopy, the information contained in a Raman scattered photon does not depend on the frequency of the probing light. This permits to use one monochromatic light source like a laser without the need of tuning or scanning through different frequencies. However, since the energy difference gives the vibrational information, a frequency stabilized laser with a narrow bandwidth is a prerequisite for a Raman experiment. The Raman setup used in this work is supplied by three diode pumped solid state (DPSS) lasers emitting at 457, 532 and 647 nm.

Raman light scattering is isotropic and the light will therefore be scattered in all spatial directions. Therefore, it is not required to conduct a Raman experiment in a transmission configuration where the light is collected after it passes the sample (see sections 3.1 and 3.2). Most common Raman setups utilize a 90° configuration, where the scattered light is detected perpendicular to the probing light beam, or a 360° setup as depicted in fig. 3.9. The essential optical element in a 360° configuration is a

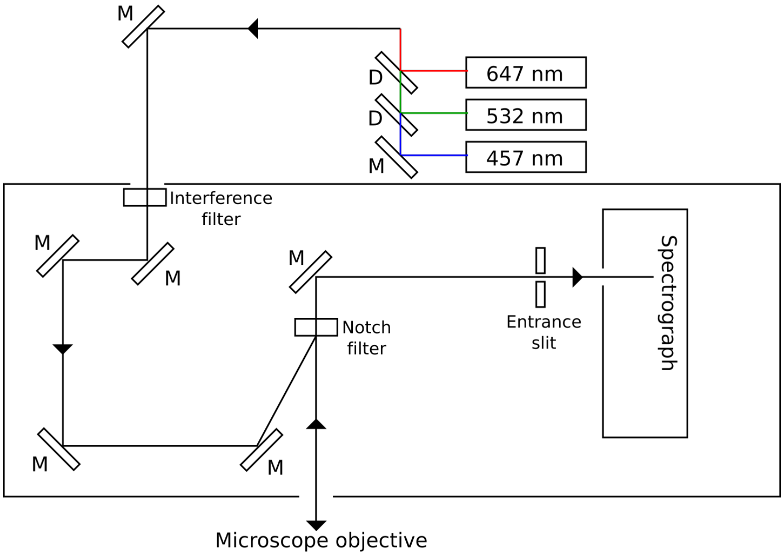

Figure 3.9: Scheme of the Raman setup with three DPSS lasers emitting at 457, 532 and 647 nm. These can be coupled to the measuring light path via dichroic mirrors (D). A set of mirrors (M) inside the spectrometer is needed to perfectly align the light beam onto the Notch filter. The frequency shifted light due to the Raman process is dispersed by a grating inside the spectrograph and detected by a CCD camera.

notch filter, which reflects light of a certain frequency while other frequencies are transmitted. After the probing light is reflected onto the sample through a microscope objective, the backscattered light, which is now frequency shifted by the Raman process, can pass the notch filter and is directed to a spectrograph. A grating disperses the Raman shifted light which is then detected by a charge-coupled device (CCD) camera with 1024 pixels. This allows the measurement for one complete spectrum at once without the need for a scanning mechanism. Typically, CCD integration times between 1 and 3 s are chosen.

For time-resolved measurements, the CCD is used with a permanently open shutter. With this, acquisition plus read-out time for one spectrum is cut down to 20-25 ms. A Raspberry Leonardo is used to orchestrate the timings of the CCD and the master device (a potentiostat or laser) which starts the experiment. Data collection is achieved with self-written software in LABVIEW. To take account for the fast read-out times, the recorded data is first collected in the RAM and just written to the hard disk after finishing the experiment.

3.4 Density functional theory

To calculate the vibrational modes of a molecule, its Schrödinger equation has to be solved. As pointed out in chapter 2, molecular vibrations are determined by the potential defined by the electrons. For a many-electron system, the electronic part of the molecular Schrödinger equation can be written as

$$\hat{H}\Psi = \left(\hat{T} + \hat{V}\right)\Psi = \left(\hat{T} + \hat{V}_{eN}(\vec{r}_i) + \hat{V}_{ee}(\vec{r}_i, \vec{r}_j)\right)\Psi \quad , \tag{3.30}$$

where $\hat{T}$ denotes the translational energy, $\hat{V}_{eN}$ the Coulomb interaction between nucleus and electrons and $\hat{V}_{ee}$ represents the electron-electron interaction. The many-electron wavefunction Ψ of N electrons depends on $3N$ coordinates which can not be dealt separately because $\hat{V}_{ee}(\vec{r}_i, \vec{r}_j)$ connects two electrons. In a Hartree-Fock (HF) calculation, Ψ is approximated by a linear combination of atomic orbitals (LCAO) which leads to an effective Hamiltonian $\hat{h}_{HF}$ for each electron's wavefunction Φ_j[43]

$$\hat{h}_{HF,j}\Phi_j = \Big(\hat{T} + \hat{V}_{eN}(\vec{r}) + \underbrace{\sum_{i \neq j}^{N} \frac{\Phi_i^* \Phi_i}{r_{ij}} d\tau}_{\hat{V}_{Coulomb}} + \underbrace{\sum_{i \neq j}^{N} \frac{\Phi_i^* \Phi_j}{r_{ij}} d\tau}_{\hat{V}_{Exchange}}\Big)\Phi_j = \epsilon_j \Phi_j \quad . \tag{3.31}$$

The one electron wavefunctions are provided by a so-called basis set. Within HF theory, the electron-electron interaction is reduced to an electron interacting with an average electron cloud potential defined by $\hat{V}_{Coulomb}$ (mean-field approximation). The total energy of the system is then

$$E_{total} = \sum_i \epsilon_i \geqq E_{ground} \quad , \tag{3.32}$$

which is always greater than the true ground state energy (variational principle). With this in mind, the energy is minimized in a HF calculation by adjusting the LCAO. Additionally, the resulting wavefunctions have to be self-consistent, meaning that the constructed Hamiltonian should have the same wavefunctions as eigenfunctions. Although an exchange operator $\hat{V}_{Exchange}$ is included in HF theory, it lacks an energy contribution called correlation E_{corr}

$$E_{corr} = E_{HF} - E_{ground} \quad . \tag{3.33}$$

There are several post-HF methods taking account for the missing E_{corr} but they add extra computational time to the already expensive HF calculation. One widely used method is configuration interaction (CI) where the HF wavefunction is extended by exciting electrons into unoccupied orbitals[44]

$$\Psi_{CI} = a_0 \Psi_{HF} + \sum_{i=1} a_i \Phi_i \quad . \tag{3.34}$$

The advantage of promoting electrons is that it makes it easier for the electrons to avoid each other. The computational extra cost strongly depends on the number of electrons and the size of the basis set. Therefore, the extension of eq. (3.34) have to be truncated to reduce the computational time. Examples are to only consider singly excited states or to allow also multiply promoted electrons but only in an confined (active) space.

Another approach for solving the many-electron Schrödinger equation is used in density functional theory (DFT) which provides better computational efficiency[45]. Within DFT, the Hohenberg-Kohn theorems basically state that the total energy of a system is uniquely describes by the electron density $\rho(\vec{r})$ and that the variational principle of eq. (3.32) still holds. The electron density is defined as

$$\rho(\vec{r}) = \sum_{k=1}^{occ} n_k \left|\Phi_k(\vec{r})\right|^2 \quad . \tag{3.35}$$

The effective Hamiltonian is then defined by the Kohn-Sham equations

$$\hat{h}_{KS} = \hat{T} + \hat{V}_{eN}(\vec{r}) + \int \frac{\rho(\vec{r}')}{|\vec{r} - \vec{r}'|} d\vec{r}' + \frac{\delta E_{xc}(\rho(\vec{r}))}{\delta \rho(\vec{r})} \quad , \tag{3.36}$$

with E_{xc} as exchange–correlation energy functional. In principle, DFT is an exact theory if the real E_{xc} is known but in practice it remains unknown and has to be approximated. Obviously, this functional is crucial to obtain accurate molecular ground state energies and has to be chosen with care. The algorithm to solve the N Schrödinger equations is essentially the same as in HF calculations, where the obtained Kohn-Sham wavefunctions Φ^{KS} have to self-consistently reproduce the electron density which previously defined the effective Hamiltonian. The big advantage over HF theory is the inclusion of the correlation energy of eq. (3.33) which consequently yields more accurate results. Once the electronic energy landscape is obtained, its straight forward to calculate the vibrational frequencies via eq. (2.13) with the spring constant K in the harmonic approximation

$$K = \frac{\delta^2 E}{\delta^2 r} \quad . \tag{3.37}$$

It is possible in the CI framework to calculate electronic excitation energies. To obtain accurate results, it is mandatory to include multi electron configurations which quickly gets computational expensive. In the case of DFT, such an ansatz is not feasible due to the physical meaningless Kohn-Sham orbitals. Considering that an electronic excitation occurs in interaction with an external electronic field, such as light, which can be included in a time-dependent Schrödinger equation. Fortunately, pendants to the Hohenberg-Kohn theorems and Kohn-Sham equations exist for the time-dependent case. Of course, the inclusion of time increases CPU time but solving the full time-dependent equations is not need to calculate excitation energies. For this, it is sufficient to assume that the electric field only gives rise to a small perturbation $\delta v(\vec{r}, t)$ of the system. The electron density reacts to this perturbation which can be written as a functional Taylor series

$$\rho(\vec{r}, t) - \rho_0(\vec{r}) = \rho_1(\vec{r}, t) + \rho_2(\vec{r}, t) + \dots \quad . \tag{3.38}$$

Truncating after the first term on the right hand side yield the approximation[46]

$$\delta \rho = \chi \delta v \quad , \tag{3.39}$$

where χ is the linear response function. With time-dependent DFT it is possible to obtain χ which permits the calculation of the excitation energies and also oscillator strengths (proportional to intensity).

3.5 Data treatment

To extract useful information and to increase the signal-to-noise ratio of time-resolved spectral datasets, two techniques were mainly employed in this work. This section gives a small overview of the mathematics behind singular value decomposition (SVD) which can significantly reduce the noise in a dataset as well as identify important spectral components. Global fitting is performed to determine reaction time constants and to extract spectra of participating species. Both techniques were implemented in MATLAB.

3.5.1 Singular value decomposition

Among many other techniques, singular value decomposition (SVD) is probably the most important matrix factorization applied to extract information out of a large high-dimensional dataset. It is for example widely used in machine learning but it can also be used to compress digital pictures. In this thesis, it is mainly performed to increase the signal-to-noise ratio of time-resolved spectral data. Basis of SVD is the claim that every matrix is diagonal if proper basis vectors are provided. To understand the underlying mathematics, a bit of linear algebra is necessary.

An eigenvector ν to a matrix $\boldsymbol{A}$ is defined as

$$\boldsymbol{A}\nu = \lambda\nu \quad , \tag{3.40}$$

with the eigenvalue λ. Hence, if the matrix $\boldsymbol{A}$ is acting on the vector ν, it just changes the scale of ν but not its orientation. If a square $n \times n$ matrix with n distinct eigenvectors is assumed, it can be represented as

$$\boldsymbol{A}\left[\nu_1 \dots \nu_n\right] = \left[\lambda_1\nu_1 \dots \lambda_n\nu_n\right] = \underbrace{\left[\nu_1 \dots \nu_n\right]}_{\boldsymbol{V}} \underbrace{\begin{bmatrix} \lambda 1 & \dots & 0 \\ \vdots & \ddots & \vdots \\ 0 & \dots & \lambda_n \end{bmatrix}}_{\boldsymbol{\Sigma}} \Rightarrow \boldsymbol{AV} = \boldsymbol{V\Sigma} \quad . \tag{3.41}$$

Here, $\boldsymbol{V}$ is a matrix of eigenvectors ν_n and $\boldsymbol{\Sigma}$ a diagonal matrix with the corresponding eigenvalues λ_n. Equation (3.41) can be rewritten to

$$\boldsymbol{A} = \boldsymbol{V\Sigma V}^{-1} = \sum_{i=1}^{n} \lambda_i (\nu)_{ith\ column} (\nu^{-1})_{ith\ row} \quad . \tag{3.42}$$

This equation only holds if the eigenvectors ν_i are linear independent rendering $\boldsymbol{V}$ invertible. If the eigenvectors are normalized to 1, the corresponding eigenvalues λ_i can be thought of as a significance of the eigenvector in representing the original matrix $\boldsymbol{A}$. Sorting the eigenvalues from high to low values and truncating the sum of eq. (3.42) at a certain position k will omit eigenvectors with less significance in the reconstruction of $\boldsymbol{A}$. This can be utilized to strain off noise in an experimental dataset.

Until now a squared matrix $\boldsymbol{A}$ was assumed but SVD states that every $n \times m$ matrix can be diagonalized such that

$$\boldsymbol{A} = \boldsymbol{USV}^T \quad , \tag{3.43}$$

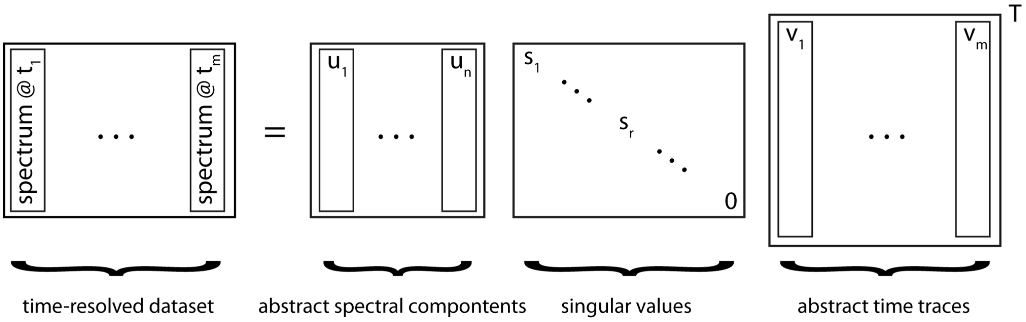

Figure 3.10: Concept of SVD for a time-resolved spectral dataset.

with $\boldsymbol{U}$ and $\boldsymbol{V}$ being orthogonal ($\boldsymbol{X}^T\boldsymbol{X} = \boldsymbol{X}\boldsymbol{X}^T = \boldsymbol{I}$) and $\boldsymbol{S}$ diagonal. To better understand the meaning of the matrices describing $\boldsymbol{A}$, eq. (3.43) can be converted to

$$\begin{aligned} \boldsymbol{A}^T &= (\boldsymbol{U}\boldsymbol{S}\boldsymbol{V}^T)^T = \boldsymbol{V}\boldsymbol{S}\boldsymbol{U}^T \\ \boldsymbol{A}^T\boldsymbol{A} &= \boldsymbol{V}\boldsymbol{S}\boldsymbol{U}^T(\boldsymbol{U}\boldsymbol{S}\boldsymbol{V}^T) = \boldsymbol{V}\boldsymbol{S}^2\boldsymbol{V}^T \\ \boldsymbol{A}^T\boldsymbol{A}\boldsymbol{V} &= \boldsymbol{V}\boldsymbol{S}^2 \\ \boldsymbol{A}^T\boldsymbol{A}v_i &= \lambda_i^2 v_i \quad \text{(eigenvalue decomposition).} \end{aligned} \tag{3.44}$$

This demonstrates that $\boldsymbol{V}$ contains the eigenvectors of $\boldsymbol{A}^T\boldsymbol{A}$ and the diagonal entries of $\boldsymbol{S}$ are the square roots of the corresponding eigenvalues. Equation (3.44) can be repeated for $\boldsymbol{U}$ revealing that it contains the eigenvectors of $\boldsymbol{A}\boldsymbol{A}^T$ with the same eigenvalue matrix $\boldsymbol{S}$. With this the matrix $\boldsymbol{A}$ can be expressed as

$$\boldsymbol{A} = \sum_{i=1}^{n} \lambda_i (u)_{ith\ column} (v^T)_{ith\ row} \quad , \tag{3.45}$$

but now this equation is valid for every $n \times m$ matrix.

Performing a SVD analysis on time-resolved spectral data can help to extract important spectral features and to reduce noise. Figure 3.10 illustrates what this means in terms of the matrices $\boldsymbol{U}$, $\boldsymbol{S}$, $\boldsymbol{V}$. The matrix $\boldsymbol{U}$ contains abstract spectral components sorted by the significance represented by the singular values of $\boldsymbol{S}$. It becomes clear by eq. (3.45) that terms with a low singular value can be omitted due to their low contribution to the original dataset. Hence, the signal-to-noise ratio can be increased by choosing an appropriate cut-off value without loosing significant spectral information. Time information is stored in the $\boldsymbol{V}$ matrix which can be subjected to a global fitting procedure.

3.5.2 Global fitting

An advantage of SVD is that it is not model biased and can therefore be applied to every dataset without prior knowledge about the underlying processes. In contrast, global fitting requires a model as fitting instruction. With this, models can be tested and parameters determined. Sticking to time-resolved spectral data, a model contains how spectral components evolve over time. A mathematical expression for a reaction $\mathrm{A} \xrightarrow{k_1} \mathrm{B} \xrightarrow{k_2} \mathrm{C}$ consisting of three species with exponential decay constants k_1

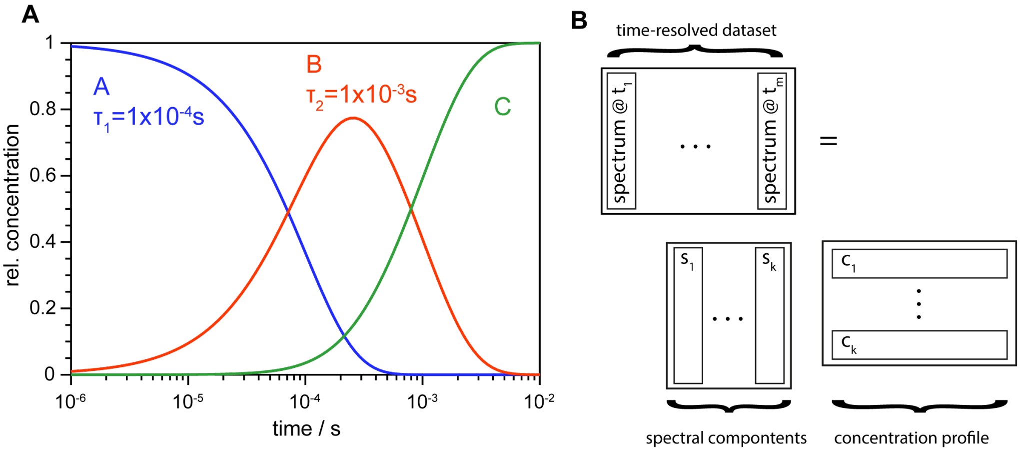

Figure 3.11: A: Concentration profile for a A $\xrightarrow{k_1}$ B $\xrightarrow{k_2}$ C reaction with indicated time constants ($\tau = {}^1/_k$). **B:** Concept of global fitting.

and k_2 is

$$\begin{aligned}[]
[\mathrm{A}] &= [\mathrm{A}]_0 e^{-k_1 t} \\
[\mathrm{B}] &= [\mathrm{A}]_0 \frac{k_1}{k_2 - k_1}\left(e^{-k_1 t} - e^{-k_2 t}\right) \\
[\mathrm{C}] &= [\mathrm{A}]_0 - [\mathrm{A}] - [\mathrm{B}] \quad .
\end{aligned} \tag{3.46}$$

Here, the resulting system of ordinary differential equations (ODEs) is already solved and the concentration of species C is determined by the mass balance principle. Figure 3.11 **A** exemplary shows such a concentration profile matrix $\boldsymbol{C}$ for eq. (3.46) with $\tau_1 = {}^1/_{k_1} = 1 \times 10^{-4}$ s and $\tau_2 = 1 \times 10^{-3}$ s. If the assumed reaction scheme is correct, it is in principle possible to express the experimental dataset $\boldsymbol{A}$ as

$$\boldsymbol{A} = \boldsymbol{S}\boldsymbol{P} \quad , \tag{3.47}$$

where $\boldsymbol{P}$ contains the concentration profile and $\boldsymbol{S}$ the corresponding spectral features (fig. 3.11 **B**). Once a concentration profile is calculated, the spectral components, also called decay associated spectra (DAS), can be determined by solving the system of linear equations given by eq. (3.47). The residuals of that solution are dependent on the chosen time constants. With this, eq. (3.47) is subjected to a fitting procedure which minimizes the residuals by adjusting the time constants.

With global fitting it is possible to determine the rate constants of the participating species as well as to extract their spectral features (DAS) once an appropriate reaction scheme is known. A prior SVD analysis can help to identify the number of species throughout the reaction. Global fitting can also be applied to the abstract time traces which reduces the dimension of the global fitting procedure if the dataset is very large. In this work, global fitting was performed on the raw data with a model of sequentially occurring species.

4

ZEAXANTHIN AS A MEMBRANE VOLTAGE SENSOR

A manuscript covering the results of this chapter is in preparation:

Ehrenberg, D. & Heberle, J. Voltage sensing by Raman Spectroscopy of Zeaxanthin. *Manuscript in preparation*

Currently, most of the employed single molecule organic voltage dyes are based on fluorescence where the emission intensity depends on the strength of the electric field across the membrane. The underlying physical mechanism is the Stark effect which shifts the energy levels of a molecule due to an external electric field (electrochromism)[47]. The read-out via fluorescence does yield a high sensitivity but it lacks structural information about the reporter molecule and therefore also selectivity. Raman spectroscopy provide chemical specificity about molecular structure, in particular when the resonance effect is employed, at the cost of sensitivity[48]. Good candidates for resonance Raman voltage probes are carotenoids. They consists of 40 carbon atoms and are found in many plants and diverse animal species where they fulfill a set functions including light absorption with subsequent energy transfer to photosynthetic complexes, photoprotection or protection against reactive oxygen species[49]. The conjugated polyene chain with its extended π-electron system has an allowed optical electronic transition from the ground state S_0 to an excited state S_2 in the visible spectral region rendering carotenoids highly suitable for resonance Raman spectroscopy.

It was discovered already in the 1970s that the Raman spectrum of a membrane embedded carotenoid in frog sciatic nerve cells changes during action potential propagation[21]. It is well known that carotenoids exhibit an electrochromic shift if the external electric field vector points along the polyene chain[50]. Using an empirical correlation between the visible absorption and the frequency of the intense C=C vibration (ν_1), it is in principle possible to monitor the Stark shift via Raman spectroscopy[51]. But it seems that the shift in visible absorption is too small to be exploited for voltage sensing and was experimentally never observed in that context[52]. However, an intensity ratio difference between the ν_1 and the ν_2 (C−C−H vibrations) band was observed upon nerve excitation[21]. Later this was explained by different Raman excitation profiles (REPs) for both vibrations resulting in different enhancement factors if the visible absorption shifts due to the Stark effect[53,54]. This is most pronounced if the slope of the REPs for ν_1 and ν_2 have opposite signs.

In this section, the carotenoid Zeaxanthin is presented as a new candidate in the field of organic voltage indicators. Zeaxanthin was chosen because of commercially availability, a predominant perpendicular alignment of the polyene chain across the membrane and promising REPs[55]. If excited with 457 nm the REP of ν_1 and ν_2 are suggested to have opposing slopes for a blue as well as a red electrochromic shift. Surface-enhanced resonance Raman spectroscopy (SERRS) was conducted to characterize Zeaxanthin embedded in a single lipid bilayer while be able to accurately control the membrane potential. The experimental findings are supported by calculations using density functional theory (DFT).

4.1 Preliminary Work

The concept of this study is to embed the carotenoid Zeaxanthin in a lipid bilayer and probe its response to an electric field via SERRS. To accurately characterize the carotenoid and to quantify the voltage contrast, it is obligatory to design an experiment where measurements can be done in a single bilayer environment. This was achieved by vesicle fusion on a SERRS-active substrate installed in a suitable electrochemical cell. While creating single bilayers on top of a surface can be achieved with vesicle fusion, the combination of surface and resonance enhancement delivers the spectral sensitivity to probe even low concentrations of Zeaxanthin (fig. 4.1 illustrates the experimental concept).

SERRS-active substrates were produced by vacuum evaporation of silver, generating particle islands with suitable plasmon resonances. A stable single lipid bilayer requires a strong interaction of the lipids with the surface. Tethered lipid bilayer (tLB) were created by using the lipid 1,2-Dipalmitoyl-sn-Glycero-3-Phosphothioethanol (DPPTE), which has a terminal thiol group (see fig. 4.4 for a chemical structure). The S−H group forms a covalent bond with the silver surface, providing stability of the lipid bilayer as well as facilitate vesicle fusion. A prepared sample was then investigated in a home-built electrochemical cell which will be described in the next section.

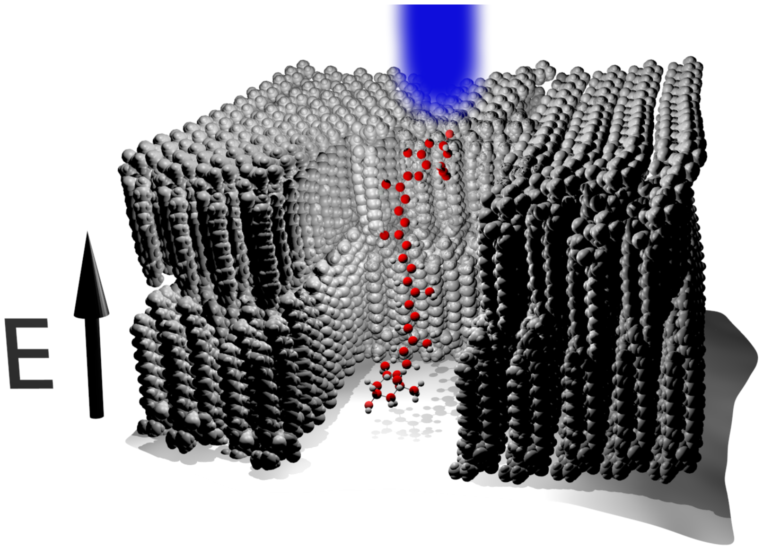

Figure 4.1: Experimental concept of Zeaxanthin as a voltage sensor. A tLB containing Zeaxanthin (colored in red) is casted on a SERRS active silver substrate. The combination of surface and resonance enhancement provides single bilayer sensitivity. Raman spectra are measured while an external electric field is applied across the membrane.

4.1.1 Electrochemical cell

To perform spectro-electrochemistry (spectroscopy with simultaneous electrochemical control) a home-build electrochemical cell was designed (fig. 4.2). Such a cell permits a well defined positioning of three electrodes in a confined environment. As raw material, Polytetrafluoroethylene (PTFE) was chosen due to its chemical stability and electrical non-conductivity. An electrode arrangement where all three electrode are in close vicinity to each other guarantees a small Ohmic drop and a low solution resistance. Reference was a Ag/AgCl electrode, the counter electrode was made of platinum and as working electrode served a glass slide coated with indium-tin-oxide (ITO). This way, the working electrode is conductive while transparent for visible light radiation. The glass slide is placed on top of an O-ring and subsequently fixed by the the top cap. Four screws ensure an even force distribution and the sealing of the electrochemical chamber. Two fill holes enable filling the chamber with 640 µl electrolyte without dismantling the cell. The substrate gets excited by the laser beam from the top. In this configuration, the light does not need to travel through the electrolyte and thus minimizes scattering, although water is a weak Raman scatterer. Due to the travel distance through the substrate and the limited space provided by the top cap, oculars not higher than 20x can be used (for a scheme of the Raman setup see fig. 3.9).

4-Mercaptobenzonitrile (MBN) is an excellent molecule to test the electrochemical SERS setup. The thiol group of MBN can bind to the silver surface with an orientation along the surface normal (in direction with the electric field) and its C≡N bond exhibits a pronounced vibrational Stark shift[56,57]. ITO substrates with silver islands (for details see section 4.2) were bathed in ethanol containing 1 mM MBN generating a self assembled monolayer (SAM). After 1 h, the substrate was thoroughly rinsed with water and subsequently mounted on top of the electrochemical cell. Electrolyte solution was 10 mM HEPES and 150 mM NaCl dissolved in water. Raman excitation was at 457 nm and spectra

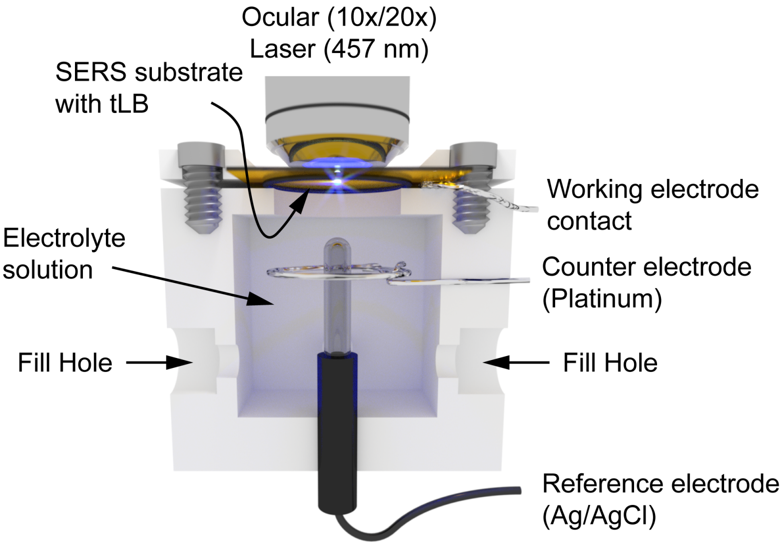

Figure 4.2: Sketch of the home-build electrochemical cell. Dimensions are 32 mm(L)x32 mm(W)x20 mm(H) with an electrolyte chamber holding 640 µl. Electrode arrangement ensures a low Ohmic drop and solution resistance. Illumination of the substrate from the top minimizes any scattering of the electrolyte solution.

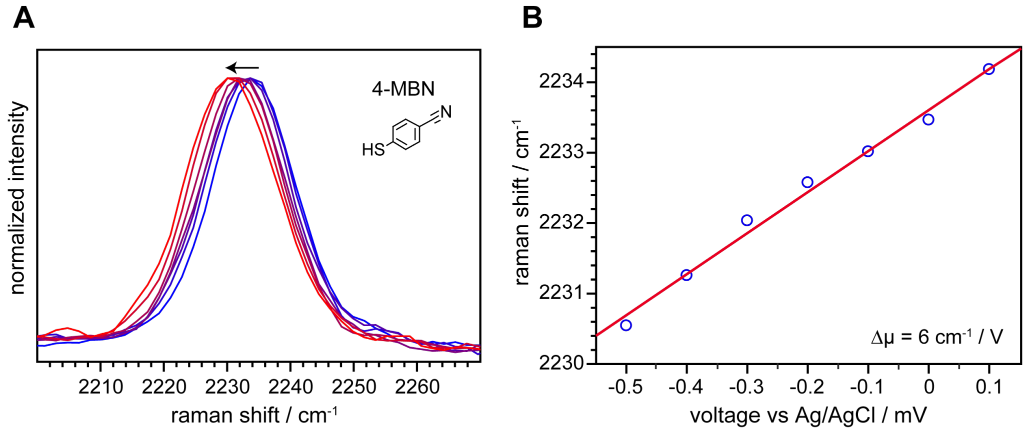

Figure 4.3: Determination of the Stark tuning rate of 4-Mercaptobenzonitrile (MBN). **A:** Band shift of the C≡N vibration due to applied voltages in the range of 0.1 to −0.5 V in 0.1 V steps (vs Ag/AgCl). The arrow indicates the scan direction from higher to lower voltages (blue to red). **B:** A linear fit of peak positions over applied voltage yields a Stark tuning rate of 6 $\text{cm}^{-1}\,\text{V}^{-1}$. Band positions were determined by fitting with Gaussian profiles.

were recorded in a voltage range from 0.1 to −0.5 V vs in 0.1 V steps (vs Ag/AgCl). Figure 4.3 clearly shows the vibrational Stark shift of the C≡N mode. To estimate the Stark tuning rate $\Delta\mu$, each band was fitted with a Gaussian profile to accurately determine peak positions. A linear fit of the peak positions over the applied voltage yields a tuning rate of 6 $\text{cm}^{-1}\,\text{V}^{-1}$ in line with published values[57]. This demonstrates the proper functionality of the established spectro-electrochemistry SERRS setup.

4.1.2 Raman characterization of DPPTE

Throughout this section, DPPTE is used to create a tLB on a SERS-active silver substrate. Spectral characterization of DPPTE in solution and bound to the surface is obligatory to exclude contributions of the lipid in the spectra of the membrane-embedded Zeaxanthin. Therefore, spectra were recorded of lipids solubilized in chloroform and of surface-bound DPPTE as described in section 4.1.1. As in the case of MBN, the thiol group located at the hydrophilic head of the lipid will form a covalent bond with the silver surface creating a SAM.

Solubilized DPPTE exhibit the usual band pattern for lipids (fig. 4.4 red spectrum) with vibrations originating from the methyl groups of the tail (1302 cm^{-1}: CH_2 twisting, 1439 cm^{-1}: CH_2 bending, 2854/2893 cm^{-1}: CH_2 stretching, 2960 cm^{-1}: CH_3 stretching of the tail end) and from the head group (2930 cm^{-1}: CH_2 stretching)[58–60]. It was demonstrated that a frequency of 1078 cm^{-1} in combination with missing *trans* bands at 1160 and 1130 cm^{-1} indicates a gauche defected, highly distorted lipid tail[61]. It seems that the lipid can not take *trans* configurations of the tails without being in a membrane like environment. The C=O vibration of the ester group is found at 1737 cm^{-1} and the S−H stretch is at 2580 cm^{-1}.

Binding of DPPTE to the silver surface breaks the S−H bond resulting in the loss of the band at 2580 cm^{-1} in the SERS spectrum (blue spectrum). Overall, the spectral signatures are almost completely different compared to the solubilized spectrum. All of the vibrational bands originating from the lipid tails have drastically decreased in intensity. Besides of the surface selection rule

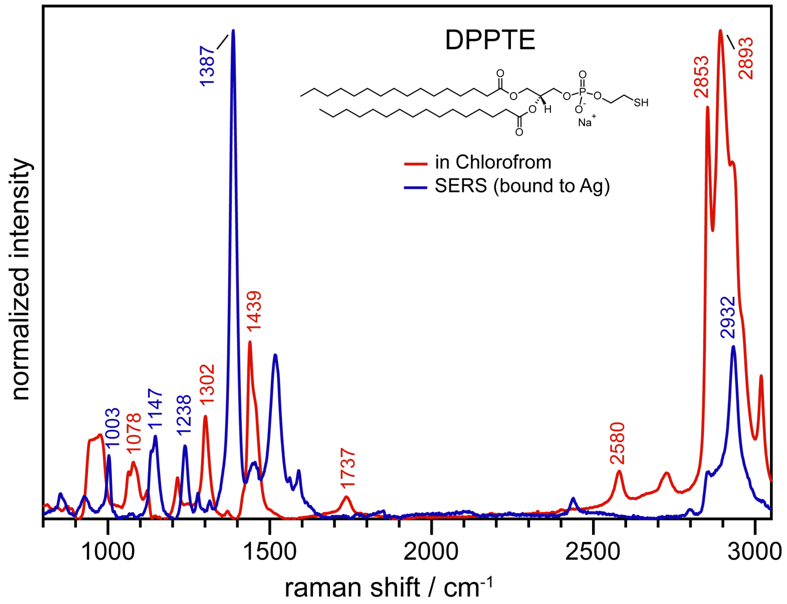

Figure 4.4: Raman spectra of DPPTE. Red spectrum denotes to lipids solubilized in chloroform (normal Raman) while surface bound DPPTE is shown in blue (SERS). The active substrate were silver islands produced by vacuum evaporation. Raman excitation wavelength was at 532 nm. Both spectra are normalized to their maximum.

for SERS, which selectively enhances vibrations along the surface normal, this is explained by the exponentially decaying penetration depth of the surface-enhanced radiation[62]. Accordingly, bands of the lipid head should dominate the SERS spectrum. Indeed, the CH_2 vibration of the head group is still present in the SERS spectrum at 2932 cm^{-1} and vibrational modes of the phosphate group can be found at 1003, 1147 and 1238 wavenumbers[58,60,63]. For the analysis of the new emerged bands upon lipid binding, interactions between the head group and the silver surface have to be considered. The C=O band at 1737 cm^{-1} has vanished pointing to a deprotonation of the carboxyl group. This is solidified by the peak at 1387 cm^{-1} which is a characteristic frequency of COO^- interacting with the silver surface[58,59,64,65].

4.2 Experimental Details

This section will briefly discuss the experimental specifics for the SERS measurements on membrane-embedded Zeaxanthin. The approach is to cast a lipid bilayer containing Zeaxanthin on a SERS-active ITO substrate via vesicle fusion. Subsequently, the sample is installed into the electrochemical cell and excited from the top with a laser emitting at 457 nm.

Vesicle preparation In chloroform solubilized lipids were mixed with 5 mol% Zeaxanthin or β-carotene and dried in a rotary evaporator at 80 mbar for at least 1 h. The dried film was resuspended in buffer solution containing 10 mM HEPES and 150 mM NaCl and throughly vortexed resulting in multilamellar vesicles. The vesicle solution was then centrifuged at 1000 x g and the supernatant was harvested removing potential aggregates. Applying a freeze and thaw method with a subsequent

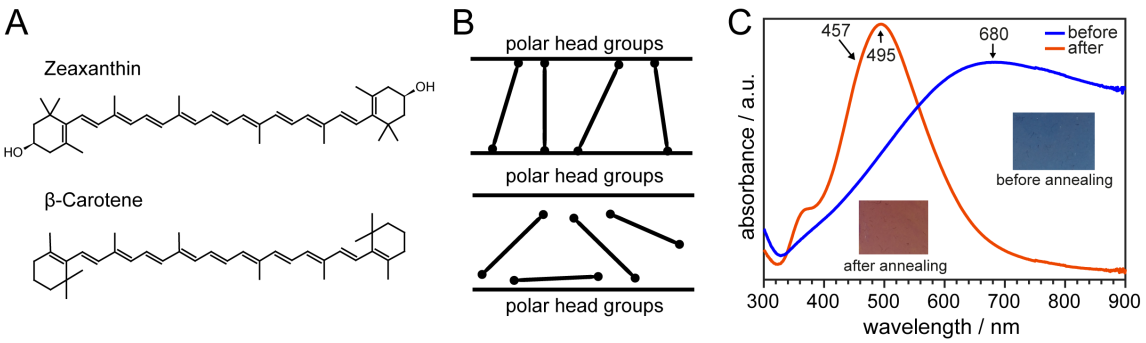

Figure 4.5: A: Chemical structures of the carotenoids used in this section, Zeaxanthin and *β*-carotene. **B:** Expected orientation in the lipid bilayer for Zeaxanthin (top) and *β*-carotene (bottom). **C:** UV/Vis absorption spectra of silver islands deposited on top of ITO substrate via vacuum evaporation. Annelation shifts the plasmon resonance from the red part of the visible spectrum to the blue with a peak at 495 nm.

extrusion through a 100 nm pore produced unilamelar vesicles[66]. Another centrifuge run at 10000 x g finally ensured an aggregate free vesicle solution. In this section, following lipids were employed on its own or as a mixture of two different lipids:

1. 1,2-Dipalmitoyl-sn-Glycero-3-Phosphothioethanol (DPPTE)
2. 1,2-dimyristoyl-sn-glycero-3-phosphocholine (DPMC)
3. 1,2-dipalmitoyl-sn-glycero-3-phosphocholine (DPPC)
4. 1,2-dioleoyl-sn-glycero-3-phosphocholine (DOPC)
5. 1-palmitoyl-2-oleoyl-glycero-3-phosphocholine (POPC)

If not other stated, a standard lipid mixture of 25 % DPPTE and 75 % DPMC was used. The amount of DPPTE ensures the tethering of the lipid bilayer while it is expected that Zeaxanthin is highly oriented in DPMC membrane with an angle of 25° to the membrane normal[67].

The two investigated carotenoids Zeaxanthin and *β*-carotene are both C_{40} molecules but they differ at the terminal groups (fig. 4.5 **A**). Zeaxanthin possesses hydroxyl groups at the ionone rings rendering it polar and hydrophilic at these positions. Embedded in a lipid membrane these groups are anchored in the lipid polar head groups leading to well defined orientation in the bilayer. Contrary, *β*-carotene does not have any polar groups and may therefore be more randomly oriented in the lipid bilayer (fig. 4.5 **A**)[68–71].

Surface-enhanced Raman spectroscopy Substrates for SERS measurements were produced via vacuum evaporation of silver onto a glass substrate coated with indium-tin-oxide (ITO). The coating renders the glass surface to be electric conductive while preserving the transparency for visible radiation. Silver was transferred to an evaporation chamber and evaporated from a tungsten boat with a rate of 0.2 $\text{Å}\,s^{-1}$ at a base pressure of 1×10^{-6} mbar. The glass slide was rotated during the evaporation process until 65 Å of silver was deposited. The produced silver islands were predominantly absorbing in the red resulting in a purple color. This plasmon resonance is not ideal since Zeaxanthin absorbs around 450 nm and the Raman laser emits at 457 nm. Annelation of the substrate at 200 °C for 1 min changed the color to orange shifting the plasmon resonance to the blue with a peak at 495 nm (fig. 4.5 **C**).

DPPTE with its thiol group is capable of covalently bind to the silver surface of the glass slides. Bathing of the substrates in vesicle solution for at least 1 h leads to vesicle fusion onto the surface generating a tethered lipid bilayer (tLB). After chemisorption of the lipid vesicles, the substrate was thoroughly washed with buffer (10 mM HEPES and 150 mM NaCl) to remove exceeding vesicles which are not bound to the silver islands. Everything, from producing the SERS active substrates to casting of tLB was done under anaerobic conditions to avoid oxidation of the silver islands.

Preliminary cyclic voltammetry measurements demonstrated a stable potential regime for the tLB between the open-circuit potential of ca. 0 and −0.5 V vs Ag/AgCl where just capacitive currents were recorded (data not shown). At lower voltages hydrogen evolution started. If the applied potential was changed, spectra acquisition was delayed by a short equilibration time. During spectral acquisition, the sample was moved with a home-built xy-stage minimizing photodamage. All Raman spectra are baseline corrected using a polynomial and normalized to the ν_2 band at around 1158 cm^{-1}.

4.3 Results

4.3.1 E-dependent SERRS on Zeaxanthin

To study the effect on an external electric field applied on a membrane-embedded Zeaxanthin, it is beneficial to establish a single membrane environment. Vesicle fusion on top of an electrical conductive substrate in concert with SERS provides this environment as well as the sensitivity to measure a tethered lipid bilayer (tLB). Furthermore, by choosing a Raman excitation wavelength close to the visible absorption of Zeaxanthin will specifically enhance signals of the carotenoid over other spectral influences (resonance effect). Surface-enhanced resonance Raman (SERR) spectra of a tLB containing Zeaxanthin indeed just show vibrational modes of the carotenoid while lipid bands are absent (fig. 4.6 at 0 V and section 4.1.2). Most prominent bands are the C=C (ν_1) stretching vibration at 1526 cm^{-1} and the C−C stretch coupled to CH_2 bending mode at 1158 cm^{-1} (ν_2) in the fingerprint region (1100 to 1400 cm^{-1}). The coupling of the fingerprint vibrations render these modes to be highly sensitive to the isomeric state of the carotenoid. The spectrum of Zeaxanthin experiences distinct changes if an electric field is created across the tLB. While most of the bands does not show any frequency shifts or intensity changes, a new shoulder at 1130 cm^{-1} emerges (fig. 4.6 **A**). Additionally, the C=C mode displays a broadening. Tracking both vibrations over the applied voltage from 0 to −0.5 V (vs Ag/AgCl) and vice versa revealed that these bands react to the external electric field in a linear fashion (fig. 4.6 **B**). Furthermore, this process is highly reversible and the intensity alteration does not depend on the scanning direction. To highlight spectral changes occurring due to the electric field, difference spectra were constructed with the spectrum at the resting potential of 0 V as basis (fig. 4.6 **C**). Clearly, the shoulder at 1130 cm^{-1} is evolving with higher absolute voltages and the broadening of the ν_1 band is asymmetric with a stronger increase on the lower frequency side. But the difference spectra also unveil another emerging band at 1242 cm^{-1}. The intensity increase of this mode and the higher frequency side of ν_1 both also show the same reversible voltage dependent behavior (fig. 4.6 **D**).

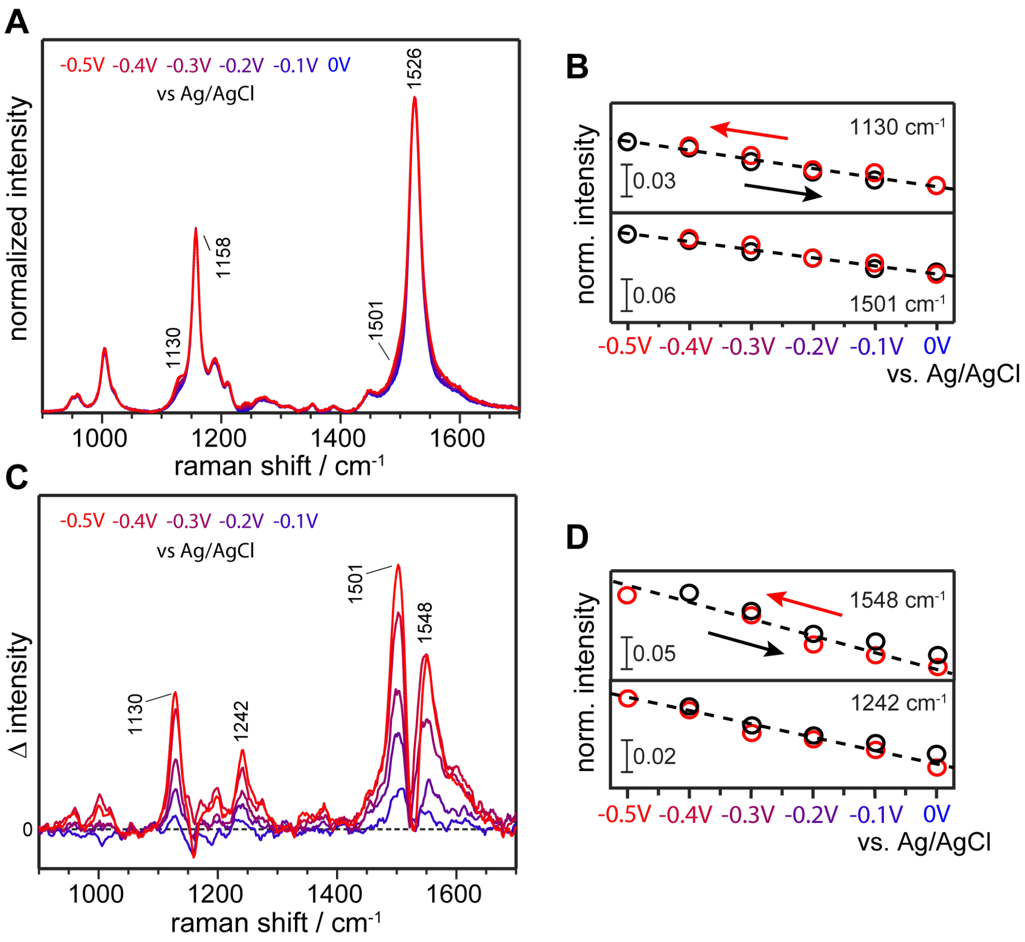

Figure 4.6: Electric field dependent SERRS spectra of Zeaxanthin embedded into a tLB composed of 25 % DPPTE and 75 % DPMC. 150 mM served as electrolyte. **A:** Absolute spectra at 0 to −0.5 V vs AgAgCl in 0.1 V steps (from blue to red). **B:** Intensity changes of an emerging band at 1130 cm^{-1} and of the lower frequency line broadening of the C=C mode represented by 1501 cm^{-1}. Arrows indicate the scanning direction. **C:** Difference spectra constructed with the spectrum at 0 V as basis. **D:** Intensity alterations of an emerging band at 1242 cm^{-1} and of the higher frequency band broadening of the C=C mode represented by 1548 cm^{-1}.

Former experiments on chromatophores and frog sciatic nerves containing a C_{40}-carotenoid reported a decrease of the intensity ratio between the two major bands at 1526 (ν_1) and 1158 cm^{-1} (ν_2) upon changing the membrane potential[21,53,54]. Later, Johnson *et al.* monitored with β-carotene a proton gradient established by bacteriorhodopsin (bR) and essentially also detected the intensity fluctuations of ν_1 and ν_2. However, in the electric field dependent SERRS experiment with Zeaxanthin presented in fig. 4.6, the intensity ratio between ν_1 and ν_2 stays constant. In the light of this, the same experiment was repeated but Zeaxanthin was exchanged with β-carotene (fig. 4.7 **A**). Here, the intensity ratio of ν_1 and ν_2 does fluctuate but not in a linear fashion as it should be if it were a response to the applied electric field. Interestingly, the emerging band at 1130 cm^{-1} and the line broadening of the C=C mode in the case of Zeaxanthin was not observed (fig. 4.7 **B**). The major structural difference between Zeaxanthin and β-carotene is the missing hydroxyl group at the ionone ring in the latter. This functional group renders the rings of Zeaxanthin more hydrophilic resulting in an alignment preferentially along the membrane normal with the hydrophilic rings anchored in the polar head groups of the lipids[67]. Contrary, β-carotene lacks the hydrophilic groups and is thus more randomly

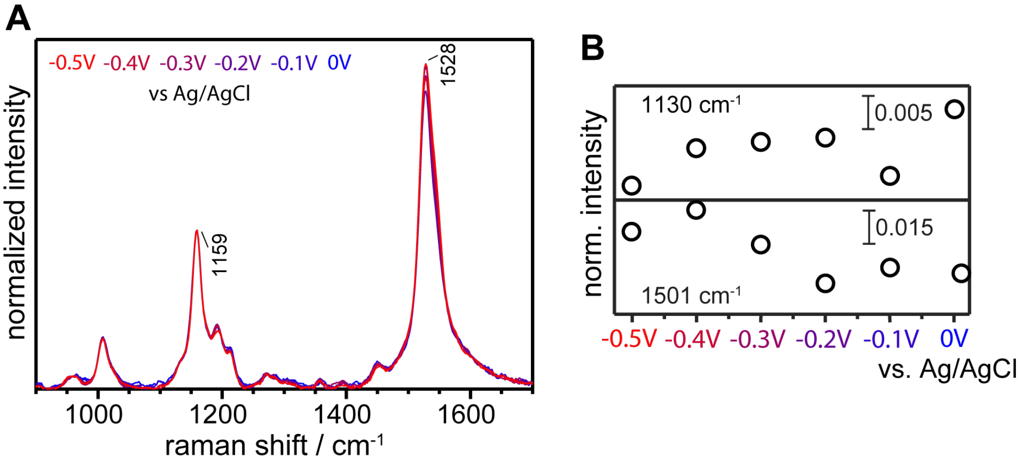

Figure 4.7: Electric field dependent SERRS spectra of β-carotene embedded into a tLB composed of 25 % DPPTE and 75 % DPMC. 150 mM served as electrolyte. **A:** Absolute spectra at 0 to −0.5 V vs AgAgCl in 0.1 V steps (from blue to red). **B:** Intensity alterations at the same frequencies where Zeaxanthin shows pronounced linear changes due to the external electric field (fig. 4.6 **B**).

oriented inside the hydrophobic core of the membrane, (fig. 4.5 **A**)[68–71]. It can be suggested that the more loose alignment of β-carotene suppresses a defined spectroscopic response. According to the surface selection rule for SERS, the alignment could also lead to the intensity fluctuation of the C=C band if alternating orientations were sampled. In contrast, due to the more defined orientation of Zeaxanthin close to the membrane normal, the electric field can act along the polyene chain of the carotenoid which seems to be important for the voltage response.

Among the important properties for an voltage sensor are reversibility, linearity as well as fast response kinetics. Time-resolved SERRS experiments were essentially performed on the same setup as for the steady-state recordings except from keeping the shutter of the detector open during the measurement. With a self-written software it was possible to get a minimum integration and read-out time for the light detecting charge-coupled device (CCD) of 25 ms. Figure 4.8 **A** shows the kinetics for bands with the most pronounced intensity fluctuations at 1130 and 1501 cm^{-1} (170 accumulations). The intensity changes were converted to contrast ($\Delta I/I$) for comparison with other organic voltage sensors. Over the course of the measurement the potential was switched between 0 and −0.4 V three times for 300 ms before the potential of −0.4 V was held for 1 s (dashed gray trace). Both bands follow these voltage jumps in a reversible manner. A histogram of the individual data points during 0 (blue) or −0.4 V (red) illustrates how the contrast increases upon applying an electric field across the membrane. The contrast increase is about 10 to 20 % and comparable to other non-invasive voltage indicators[72]. The voltage response of Zeaxanthin is completely reversible without desensitization and is even stable if the potential holding duration is prolonged to 1 s. To increase signal-to-noise ratio three consecutive potential jumps were averaged (fig. 4.8 **B**). Unfortunately, the time-resolution of 25 ms is not sufficient to resolve the rise kinetics in detail. On the other hand, this implies reaction kinetics faster than the time-resolution of the experiment.

Subjecting the time-resolved SERRS dataset to a singular value decomposition (SVD) analysis increases the signal-to-noise ratio and renders the spectral changes more apparent. Figure 4.9 **A** shows the temporal evolution of the third SVD component if three different spectral windows are used for the

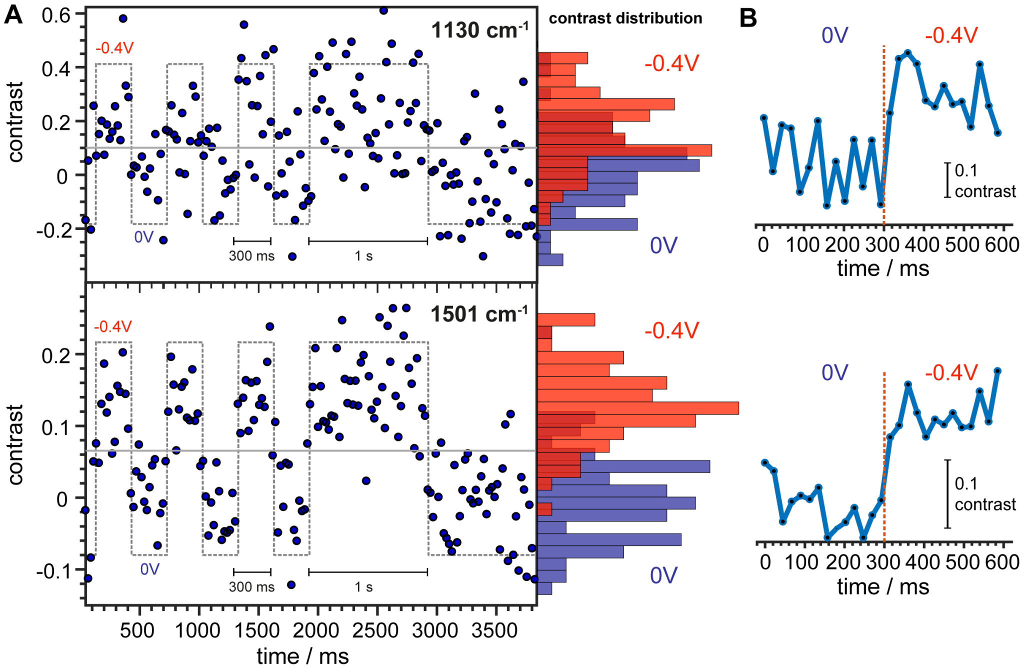

Figure 4.8: Time-resolved SERRS measurement on membrane embedded Zeaxanthin with a time resolution of 25 ms (170 accumulations). **A:** Contrast changes at 1130 and 1501 cm^{-1} upon applying a scheme of potential jumps from 0 to -0.4 V (dashed grey line). An histogram of the contrast distribution highlights the contrast change due to the electric field. **B:** Average of three consecutive potential jumps for increasing the signal-to-noise ratio.

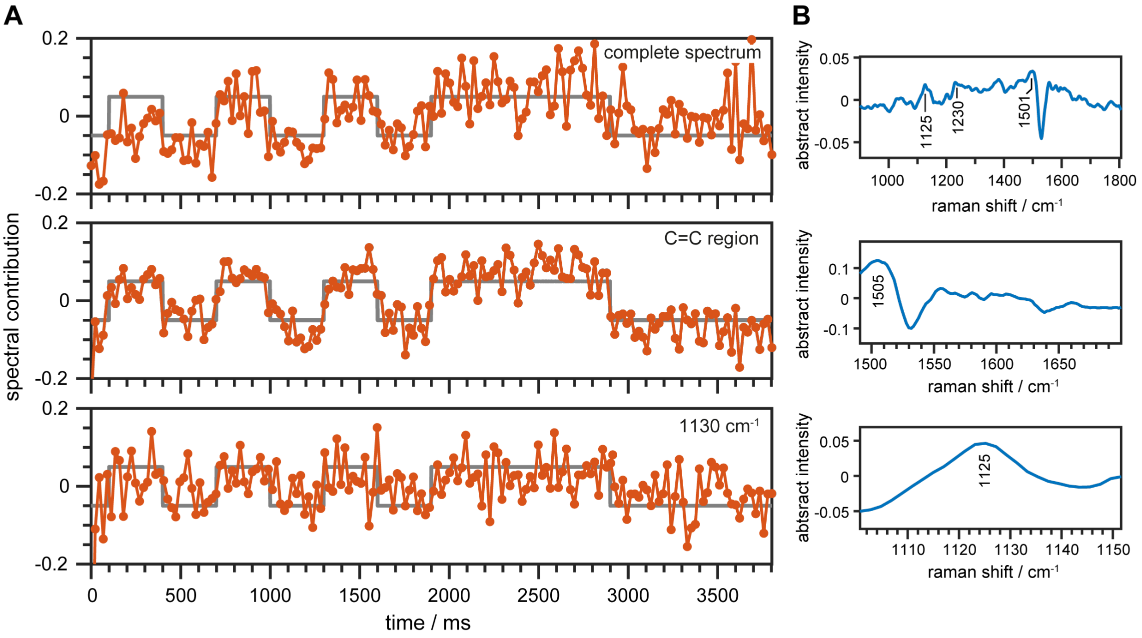

Figure 4.9: SVD analysis of the time-resolved SERRS dataset. **A:** Temporal evolution of the third singular value decomposition (SVD) component if the complete spectrum, just the C=C region or the 1130 cm^{-1} band was subjected to the analysis. Grey lines represent the potential jumps. **B:** Corresponding SVD components.

analysis (taking the 3rd column of the ***V*** matrix; for a detailed description see section 3.5.1). Taking the complete spectrum clearly shows that the spectral contribution of the SVD component follows the potential jumps. The corresponding abstract spectrum shown fig. 4.9 **B** exhibits the typical spectral features with slightly shifted wavenumbers for the C−C region. Limiting the spectral window to the 1130 $\mathrm{cm^{-1}}$ band accentuates the intensity changes as already seen in the raw dataset of fig. 4.8 but again with a low signal-to-noise ratio. In contrast, an analysis of the C=C region clearly demonstrates the fast response kinetics of the spectral changes due to the potential jumps.

4.3.2 Aggregation

The observed spectral changes are most likely not a consequence of the electrochromic shift which would lead to intensity fluctuations of the ν_1 and ν_2 bands and/or a frequency shift of the ν_1 mode. Wang *et al.* have shown that Zeaxanthin exhibits an additional peak in the fingerprint region at 1130 $\mathrm{cm^{-1}}$ if it aggregates inside a lipid bilayer[73]. There are two different types of carotenoid aggregation. In the H-aggregate, the π-electron systems are stacked on top of each other which leads to blue shift in visible absorption while losing the S_2 vibronic fine structure. Aggregates, where the carotenoids molecules are arranged besides each other, are called J-type. The visible absorption is then red shifted while preserving the vibronic fine structure[74]. Hence, aggregation also has an influence on the C=C stretching vibration. Carotenoid molecules form aggregates upon hydration of a polar solvent or due to the properties of the hydrophobic core of a lipid membrane, in particular the phase of the bilayer[75–77].

To create different types of Zeaxanthin aggregates, the lipid composition was changed to 75 % POPC ($T_m = -2\,°\mathrm{C}$) or DPPC ($T_m = 41\,°\mathrm{C}$) each with 25 % DPPTE ($T_m = 41\,°\mathrm{C}$) or mixing DOPC ($T_m = -17\,°\mathrm{C}$) with DPPTE in a 1:1 ratio[78]. Although it was demonstrated that an membrane-embedded carotenoid has just little effect on the phase transition temperature T_m, a mixture of two kinds of lipids strongly alters the phase probabilities[79,80]. Zeaxanthin tends to aggregate if the bilayer is in the gel phase while it is preferentially in its monomeric form in the fluid phase. Therefore, the monomeric Zeaxanthin is expected in the POPC vesicles due to the low phase transition temperature of the lipids. A UV/Vis spectrum of these vesicles indeed exhibit the typical band pattern of non-aggregated Zeaxanthin with two prominent peaks at 454 and 481 nm (fig. 4.10 **A** black spectrum)[74]. DPPC on the other hand has a high phase transition temperature resulting in a gel phase at room temperature. The UV/Vis spectrum of the DPPC vesicles clearly exhibit peak shifts and an emerged band at 513 nm (red spectrum). This peak pattern resembles the so-called J1-aggregate investigated by Wang *et al.*[81]. The blue spectrum of the DOPC/DPPTE mixture in a 1:1 ratio shows a similar but shifted absorption profile as the J1-aggregate with just small shoulder at 513 nm. Because of the similarity to J1 this aggregate is termed as J2. Albeit of the low T_m of DOPC, the fact that Zeaxanthin is not in its monomeric form suggests that the phase transition temperature of the lipid mixture is above room temperature.

Resonance Raman spectra of the different vesicles at room temperature look essential the same (fig. 4.10 **B**). In particular, no additional band around 1130 $\mathrm{cm^{-1}}$ can be observed excluding aggregation as an explanation for this band in the electric field dependent measurements. However, the C=C stretching vibration experiences a downshift and an intensity decrease upon aggregation. In the

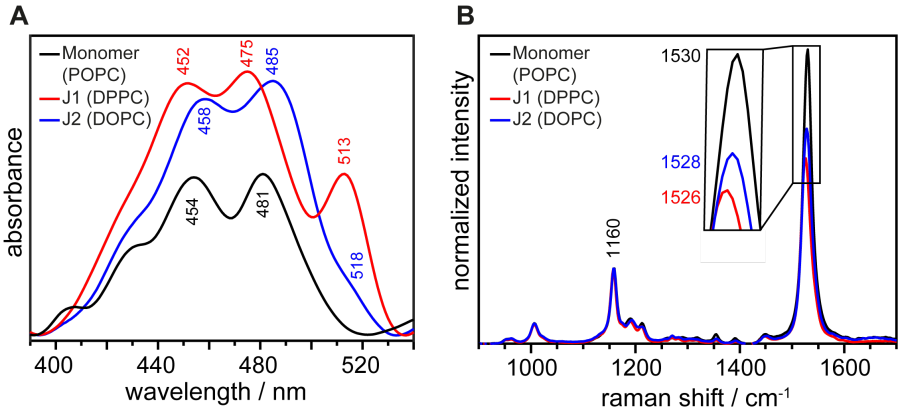

Figure 4.10: Spectroscopy on Zeaxanthin containing vesicles with different lipid compositions. 75 % POPC ($T_m = -2$ °C) with 25 % DPPTE ($T_m = 41$ °C) in black, 75 % DPPC ($T_m = 41$ °C) with 25 % DPPTE in red and DOPC ($T_m = -17$ °C) with DPPTE in a 1:1 ratio. All measurements of the vesicle solutions were performed at room temperature. UV/Vis spectroscopy clearly shows the aggregation of Zeaxanthin (**A**) and resonance Raman spectroscopy gives structural information (**B**).

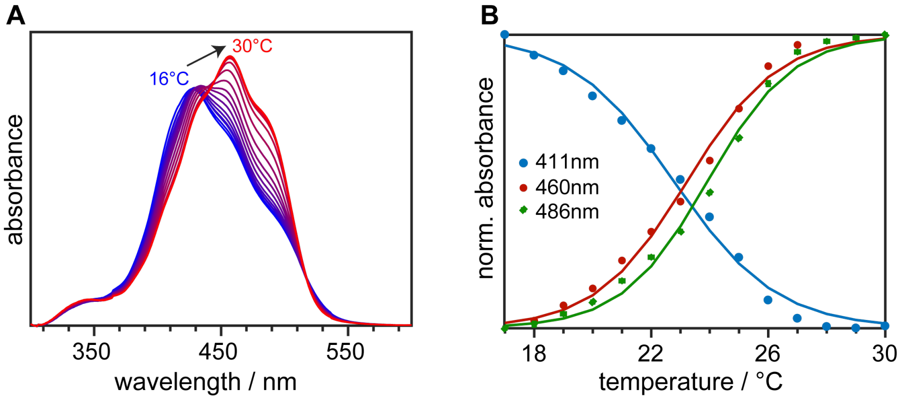

Figure 4.11: Temperature dependent UV/Vis spectroscopy vesicles containing Zeaxanthin in a temperature range from 16 to 30 °C. Lipid mixture was 75 % DPMC and 25 % DPPTE. **A:** Baseline corrected absolute spectra. Temperature increases from blue to red. **B:** Intensity changes at three different wavelengths. Sigmoidal fits yielded a phase transition temperature of $T_m = 23.3 \pm 0.4$ °C.

J1-aggregate, this band shifts from the monomeric position at 1530 to 1526 cm^{-1}. An intermediate position is taken by the J2-aggregate with a frequency of 1528 cm^{-1}. Since the ethylenic mode stretches over the whole polyene chain, it is sensitive to changes of the π-electron system. A downshift in frequency could therefore translate to an expansion or to a flattening of the conjugated system[81,82].

Temperature-dependent spectroscopy was performed on the vesicles used for the SERRS measurements (compromised of 75 % DPMC ($T_m = 24$ °C) and 25 % DPPTE) to further scrutinize possible aggregation (fig. 4.11). It was already illustrated in the late 1970s how the phase transition of a bilayer can be monitored via spectral changes of Zeaxanthin due to aggregation[83]. The UV/Vis spectrum of the vesicles at 16 °C clearly exhibit a blue shifted absorption maximum characteristic for an H-aggregate of Zeaxanthin[81]. Upon heating the solution to 30 °C, the spectrum transforms to a more monomeric spectral profile (fig. 4.11 **A** blue to red). This transformation apparently is a sigmoidal process indicative for a phase transition with a $T_m = 23.3 \pm 0.4$ °C (fig. 4.11 **B**).

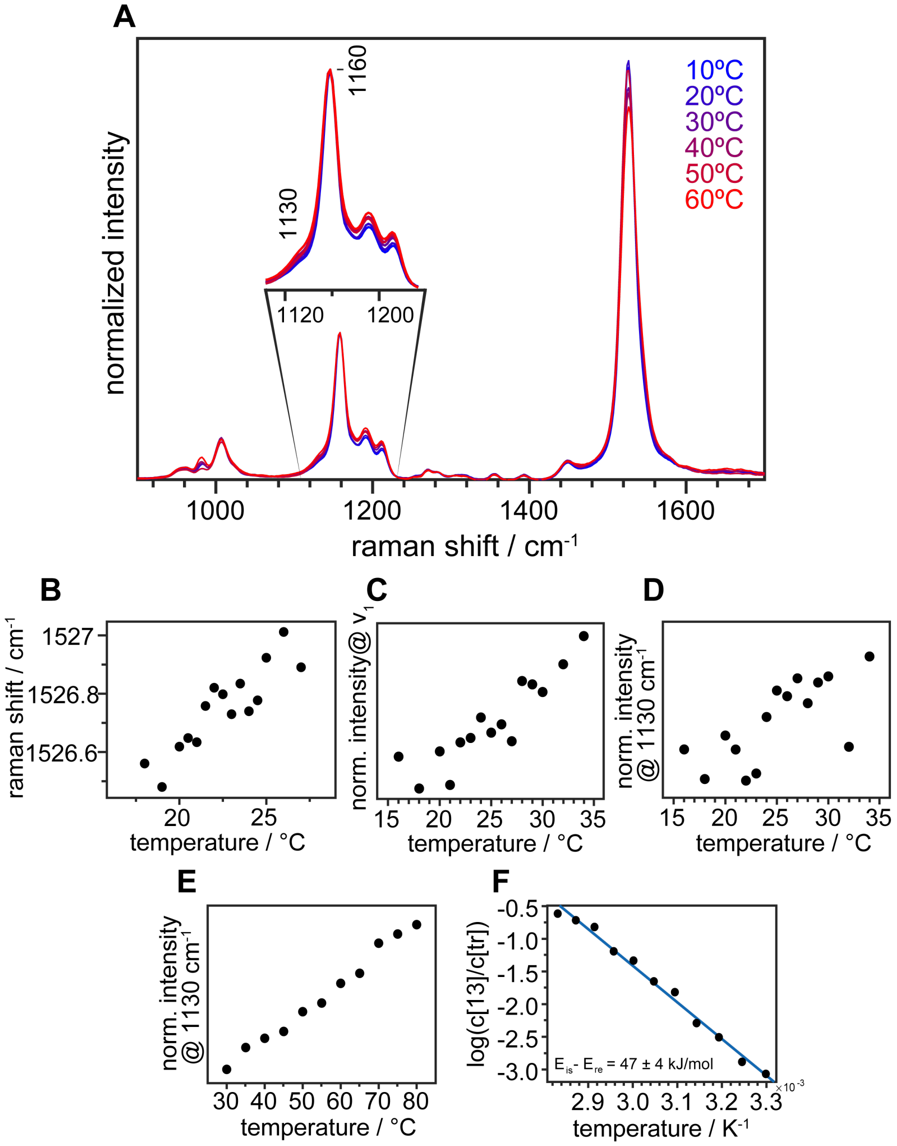

Figure 4.12: Temperature dependent Resonance Raman spectroscopy on vesicles containing Zeaxanthin in a temperature range from 10 to 80 °C. Lipid mixture was 75 % DPMC with 25 % DPPTE. **A:** Absolute spectra. Temperature increases from blue to red. The C=C stretching vibration experiences a frequency upshift and intensity increase (**B+C**) in the region around the phase transition temperature of the lipid bilayer. Intensity changes were also observed at 1130 cm^{-1} even with elevated temperatures (**D+E**). Interpreting the intensity gain as a rising *cis* population revealed an Arrhenius like behavior (**F**).

Vibrationally, this phase transition could probably be traced by tracking changes of the C=C stretching band[84]. Resonance Raman spectra of vesicles were recorded in a temperature range between 10 and 80 °C (fig. 4.12 **A** blue to red). Analysis of the ν_1 vibration revealed a frequency upshift as well as an intensity increase in the region of the phase transition temperature (fig. 4.12 **B** and **C**). But these changes are not sigmoidal excluding them as a response to different phases of the lipid bilayer. The upshift of this mode is also not a result of an increased temperature elongating the polyene chain which would actually result in a frequency downshift[85]. Interestingly, the intensity also increases at 1130 cm^{-1} with rising temperature and it keeps increasing if the sample is heated up to 80 °C (fig. 4.12 **D** and **E**). A mechanism becoming more likely with increasing temperature is a thermal isomerization of Zeaxanthin[86,87]. Such a process should obey the Arrhenius equation if the intensity increase at 1130 cm^{-1} is interpreted as a rising *cis* population. Plotting the logarithm of the intensity ratio increase over the inverse temperature clearly shows a linear behavior (fig. 4.12 **F**). A linear fit of the data yields an energy difference between isomerization and reisomerization of $E_{is} - E_{ri} = 47 \pm 4\,\mathrm{kJ\,mol}^{-1}$ which is close to the reported value of $53 \pm 3\,\mathrm{kJ\,mol}^{-1}$.[88]

4.3.3 Raman spectra calculation of isomers

Frequency calculation using DFT can shed light onto characteristic spectral features of Zeaxanthin isomers. Structures of all-*trans*, 9-, 11-, 13- and 15-*cis* Zeaxanthin were optimized using the B3LYP functional with a 6-311+G(d,p) basis set in vacuum. Obtained geometries were then used for a normal mode and Raman intensities calculation with the same combination of functional and basis set which was demonstrated to give results in agreement with experimental data[89]. A frequency-scaling factor of 0.975 was applied reproducing to good accuracy the absolute experimental values. Raman spectra were modeled using Gaussian functions with a fixed bandwidth. Calculations were done with the Gaussian09 package[90].

A comparison of an SERRS spectrum at 0 V with a calculated spectrum obtained using DFT for the all-*trans* configuration of Zeaxanthin shows a high similarity with the two major ν_1 and ν_2 bands at 1526 and 1160 cm^{-1} supporting the choice of functional and basis set. The isomeric state sensitive fingerprint region is resembled in good accordance except from the shoulder at 1130 cm^{-1} in the experimental spectrum. This pinpoints to a spectral contribution of a different Zeaxanthin isomer.

To elucidate the origin of the band at 1130 cm^{-1} and thus a possible thermal- and photoisomerization, Raman spectra of different isomers of Zeaxanthin were calculated (fig. 4.14). Spectra of the 9- and 11-*cis* isomer exhibit just slight differences compared to the all-*trans* form (fig. 4.14 **A**). The C=C stretch frequencies at 1526 cm^{-1} are essentially similar but in the fingerprint region a band at 1190 cm^{-1} gains intensity in both isomers. Characteristic bands for the 9- and 11-*cis* configuration are at 1128 and 1268 cm^{-1}, respectively, but rather weak in intensity.

Calculated spectra for the 13- and 15-*cis* isomers show distinct differences in the fingerprint as well as in the ethylenic stretch region (fig. 4.14 **B**). In the latter, the 13-*cis* form has Raman intensity for two vibrations at 1526 and 1540 cm^{-1}. For the 15-*cis* configuration, the main C=C stretching band is upshifted to 1535 cm^{-1}. The band at 1195 cm^{-1} also increases in intensity in both isomers suggesting that this band is in general peculiar to isomerization. Excellent maker bands for the 13- and 15-*cis* forms with significant intensity are at 1130 and 1246 cm^{-1}, respectively, which are absent in the all-*trans* spectrum. The characteristic bands of these two isomers in the fingerprint as well as in the C=C stretching region originate mainly from vibrational modes close to the *cis* bond. Similar bands were calculated and observed for the same isomers of β-carotene[91,92]. Importantly, the marker bands in the fingerprint region are at the same positions as the features observed in the voltage dependent SERRS experiment.

To accurately compare the distinct calculated spectral differences between the 13- and 15-*cis* isomers to the all-*tans* form with the experimentally obtained data, difference spectra were constructed (fig. 4.15). The corresponding experimental data is the –0.5 minus 0 V difference spectrum. The fingerprint

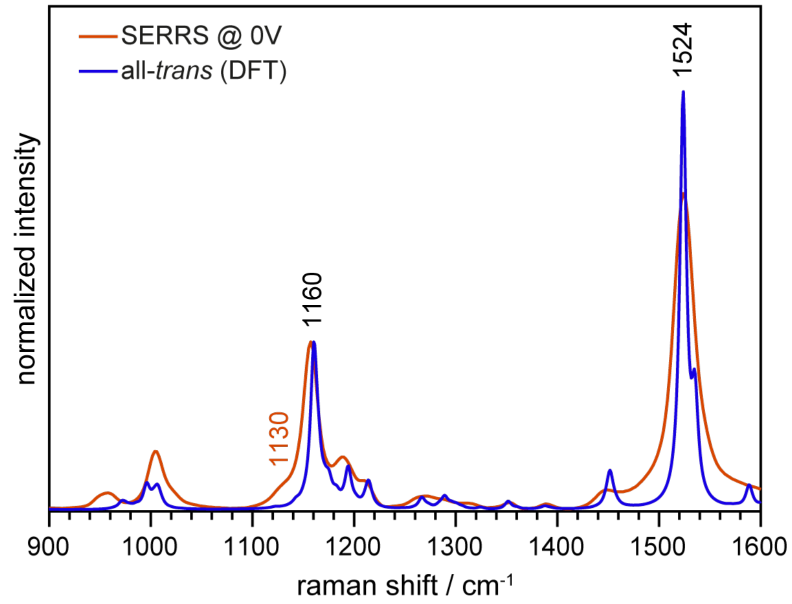

Figure 4.13: Comparison of experimental and calculated Raman spectra of Zeaxanthin. SERRS spectrum at 0 V is colored in red and the blue spectrum was obtain with DFT Raman frequency calculation of the all-*trans* form (B3LYP/6-311+G(d,p) level of theory).

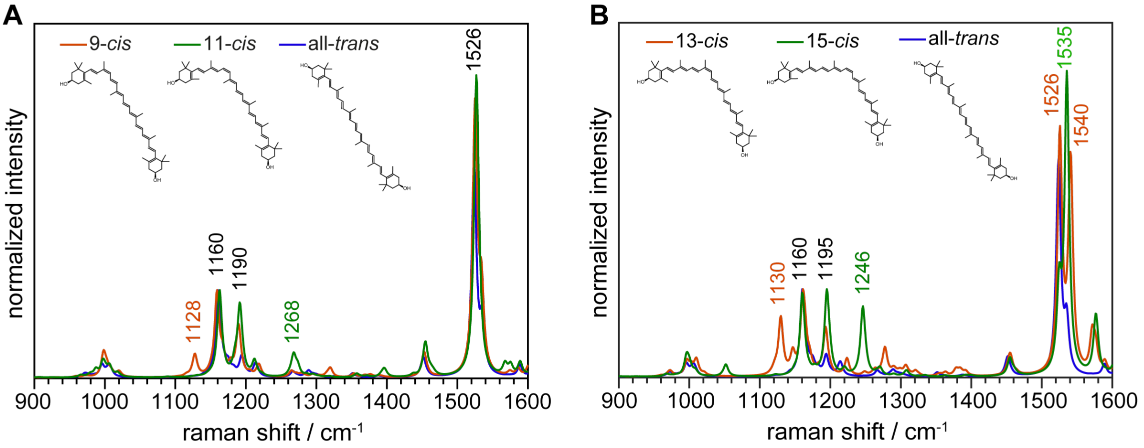

Figure 4.14: Calculated Raman spectra of different Zeaxanthin configurations at the B3LYP/6-311+G(d,p) level of theory. Distinct bands are indicated and colors represent features characteristic to the specific isomer.

region, which is sensitive to the isomeric state of the carotenoid, is resembled in very good accordance to the experimental data. In particular the marker bands for the two isomers at 1130 and 1246 cm^{-1} correspond well to the observed electric field dependent bands. The C=C stretch region is just partly reproduced. This could be due to construction of the calculated spectra with Gaussian functions at a fixed bandwidth, neglecting any potential line broadening. However, the characteristic high frequency ν_1 modes of the isomers may account for the observed asymmetric broadening of the band in the experimental data. These findings suggest that the applied electric field in our experiment enhances the probability of Zeaxanthin to isomerize due to photon absorption and that predominantly 13-*cis*

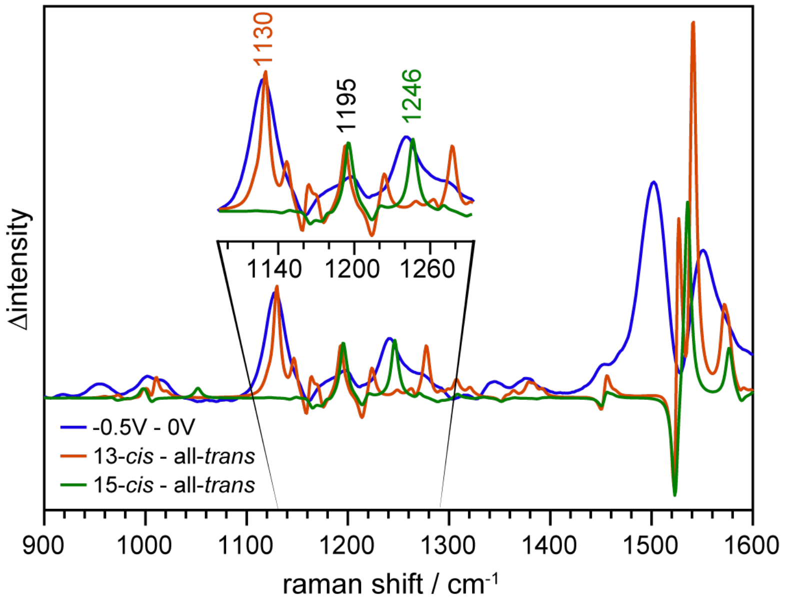

Figure 4.15: Comparison of difference spectra constructed with experimental and calculated data. Distinct spectral features are indicated and colors represent marker bands characteristic to the specific isomer.

isomers are formed besides a small population of 15-*cis*. Experiments on Zeaxanthin solubilized in either n-hexane or a mixture of MTBE:methanol (5:95, v/v) exhibited the same tendency of produced isomers as in our study for both cases, thermal- and photoisomerization[86,88].

4.3.4 Excited states calculation

Upon photon absorption, carotenoids are excited from S_0 ($1^1A_g^-$) into the optically allowed bright state S_2 ($^1B_u^+$) with subsequent conversion to the lower energy S_1 state ($2^1A_g^-$). A direct optical transition from S_0 to S_1 is symmetry forbidden (dark state; see section 3.1). The photoisomerization pathway continues with a internal conversion from S_1 to triplet states with an eventual isomerization during the decay of the triplet state T_1[86,93]. The yield for such an intersystem crossing is usually low for carotenoids (in the order of 1×10^{-3}). According to the energy gap law, the yield depends on the energy difference between the singlet and triplet state. Hence, it can be increased if the S_1 and the triplet state approach each other in energy.

To calculate the electronic transition energies, time-dependent DFT with the Tamm-Dancoff approximation (TDA-DFT) on the already optimized geometries were performed using the 6-311+G(d,p) basis set with different functionals. It was demonstrated that TDA-DFT in combination with (meta-)GGA functionals yields a correct ordering of states (dark and bright state) and reasonable excitations energies despite of the double excitation character of S_1[94–96]. Using BLYP, VSXC, M06L, HCTH or TPSS returned a correct ordering of an lower energy dark state and an elevated bright S_2 state (table 4.1). Unfortunately, these functionals tend to overestimate the delocalization of the π-electron system resulting in too low excitation energies for S_2. The range-separated hybrid CAM-B3LYP improves the bond length alternation and yields an energy of 2.77 eV (448 nm) for S_2 with an HOMO-to-LUMO

Table 4.1: Calculated TDA-DFT excitation energies for all-*trans* Zeaxanthin using the 6-311+G(d,p) basis set with different functionals. For each state the energy E, contribution of the HOMO-to-LUMO transition to that state (H → L) and the oscillator strength are given.

	S_1			**S_2**		
Functional	E [eV]	H → L [%]	f	E [eV]	H → L [%]	f
TPSS	2.13	0	0.08	2.22	77	4.32
BLYP	2.05	0	0.06	2.16	74	4.13
M06L	2.22	3	0.14	2.29	80	4.45
VSXL	2.17	2	0.11	2.26	74	4.30
HCTH	2.07	0	0.07	2.17	80	4.08
CAM-B3LYP	-	-	-	2.77	90	4.67
	T_1			**T_2**		
TPSS	1.13	98	0	1.80	0	0
BLYP	1.12	98	0	1.78	0	0
M06L	1.17	98	0	1.86	0	0
VSXL	1.18	98	0	1.87	0	0
HCTH	1.11	98	0	1.77	0	0

contribution of 90 % in good accordance to experimental data[97,98]. The dark S_1 state is mainly composed of a HOMO-1-to-LUMO and a HOMO-to-LUMO+1 transition. The states found with VSXC and M06L do additionally carry a HOMO-to-LUMO contribution and are hence elevated in energy and excluded from further analysis. Obtained excitation energies for the S_1 state are in the range of 2.05 eV for BLYP to 2.13 eV for TPSS. These values are slightly higher than the experimental values of around 1.75 eV[99]

The influence of an external electric field on the energy landscape of Zeaxanthin was investigated by including a field with the strength of 1.5 MV cm^{-1} (0.6 V across a membrane of 4 nm thickness) during TDA-DFT. Geometries were pre-optimized within the electric field before performing TDA-DFT. Applying the field along the polyene chain shifts all states to lower energies. The bright S_2 state is lowered by 0.028 eV corresponding to a 5 nm redshift which is an expected value[50]. This shift in visible absorption is too small to detect in resonance Raman spectroscopy explaining why a frequency shift of the C=C band was never observed. The S_1 and T_2 states also experience a downshift in energy but to a different extend (table 4.2). While the energy of the triplet state T_2 is just slightly reduced by about 0.025 eV, the dark S_1 state is strongly downshifted by 0.056 eV for BLYP and up to 0.060 eV for TPSS. This difference in energy downshifts brings these two states closer in energy, which translates in an increased intersystem crossing rate. Changing the orientation of the electric field vector to point perpendicular to the polyene chain decreases significantly the experienced downshifts. This supports the observation that an orientation of the field along the polyene chain is crucial for voltage sensing with Zeaxanthin.

Table 4.2: Shifts in energy of the S_1 and T_2 state if an electric field of with 1.5 MV cm^{-1} (0.6 V across a membrane of 4 nm thickness) is applied along the polyene chain (↑) or perpendicular (→).

	S_1 [eV]		T_2 [eV]	
Functional	↑	→	↑	→
TPSS	0.060	0.015	0.025	0.015
BLYP	0.056	0.014	0.025	0.014
HCTH	0.058	0.015	0.025	0.014

4.4 Conclusions & Outlook

This section has illustrated how Zeaxanthin can be used to sense changes in membrane potential. Incorporating Zeaxanthin in a lipid bilayer leads to an orientation of the polyene chain close to the membrane normal due to its hydrophilic terminal groups. Such an alignment is a prerequisite for voltage sensing as it has been shown experimentally with β-carotene which do not exhibit any spectral voltage response. Applying an electric field across a Zeaxanthin containing tLB provoked distinct changes in the recorded SERRS spectra. In particular, two bands in the fingerprint region emerged at 1130 and 1242 cm^{-1} and the ν_1 mode experienced an asymmetric line broadening. These spectral features are reversible, stable and have reaction kinetics beyond the time resolution of 25 ms provided by the detector. Experimental setups with better time resolution are necessary to completely resolve the dynamics of the spectral changes. To directly correlate these spectral features to the electric field strength, more detailed investigations of the membrane surface are needed. This includes determination of the tLB quality by impedance spectroscopy but also the incorporation of Stark label containing polypeptides into the membrane. Hereby the electric field strength can be estimated by measuring the nitrile C≡N stretch frequency[100].

Aggregation of Zeaxanthin due to a different ionic environment around the membrane was precluded as an underlying mechanism for the voltage response. Resonance Raman spectra of different Zeaxanthin aggregates do not exhibit the changes observed as in the voltage dependent SERRS measurements. But temperature dependent Raman spectra revealed an 1130 cm^{-1} band which increased in an Arrhenius behavior suggesting thermal isomerization. To further elucidate this possibility, Raman spectra of different isomers of Zeaxanthin were calculated using DFT. It turned out that the bands at 1130 and 1242 cm^{-1} are characteristic for an 13- and 15-*cis* isomer, respectively. Constructed difference spectra of theoretical and experimental data showed a high similarity which strongly points to an enriched population of these isomers if an electric field is applied under resonance conditions.

A crucial step in photoisomerization is an intersystem crossing from the optically forbidden dark S_1 state to T_2. An increased rate of isomerization translates therefore into an increased intersystem system crossing probability between these two states. Indeed, transition energy calculations using TDA-DFT in absence and in presence of an external electric field revealed Stark shifts for all states but with different magnitudes. The energy downshift of the dark S_1 state is significantly more pronounced than for T_2 which decreases the energy gap between these states making intersystem crossing more probable (fig. 4.16). Switching the orientation of the electric field vector from a parallel to a perpendicular arrangement to the polyene chain mostly diminishes the energy shifts. Although

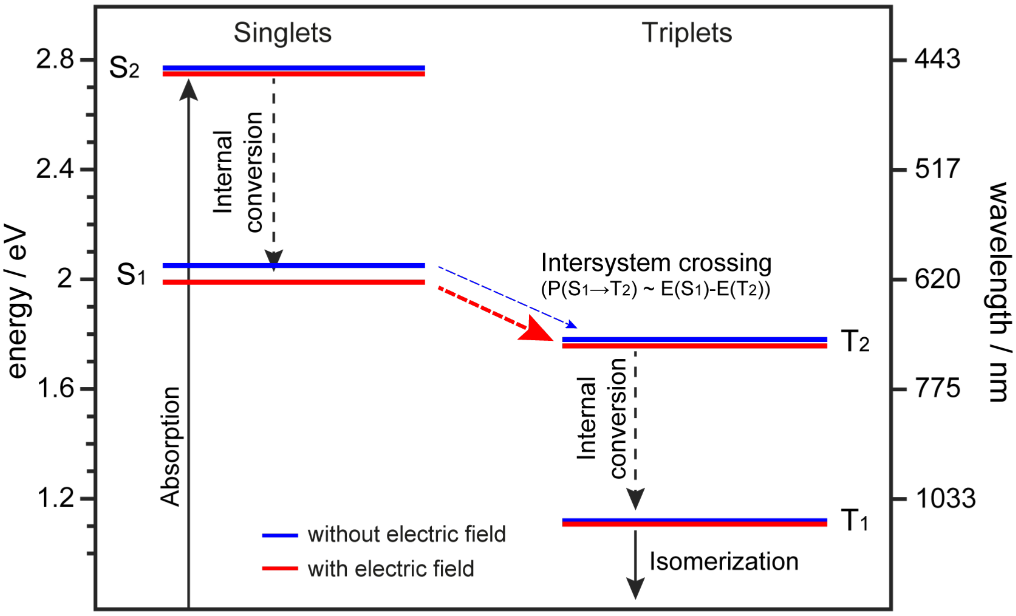

Figure 4.16: Jablonski energy diagram for all-*trans* Zeaxanthin computed with TDA-DFT using the 6-311+G(d,p) basis set. The optically allowed bright S_2 was calculated with the CAM-B3LYP functional while for all other exciting states BLYP was used. Blue bars represent exciting energies without applying an electric field while for the red bars a field was included which points along the polyene chain with a strength of $1.5\,\mathrm{MV\,cm^{-1}}$

the dark S1 state could be obtained via TDA-DFT, this method does not properly take account for the double excitation character of this state. For an accurate description of S_1, a more sophisticated multi-reference method like CASSCF is mandatory[99]. It was proposed that intersystem crossing from an singlet state lying in energy between S_2 and S_1 can also be an efficient process[101]. Recently it was discovered that singlet fission in a Zeaxanthin J1-aggregate significantly increases the triplet state population in a photostationary mixture[9]. Further analysis of the isomerization pathway for Zeaxanthin should consider these options.

Exploiting the increased isomerization probability due to an external electric field is a promising new approach for organic voltage sensors. The currently low contrast change of about 10 to 20 % can be significantly improved by using sensitivity-enhanced techniques like coherent anti-Stokes Raman spectroscopy (CARS). But also a synthetic tuning of the carotenoid for a lower energy gap between S_1 and T_2 or its aggregates for a higher yield of singlet fission could improve the voltage contrast.

5 MICROBIAL AND INVERTEBRATE RHODOPSINS

Rhodopsins are frequently used in optogenetics to manipulate neuronal activity. These transmembrane proteins harbor the carotenoid derivative retinal chromophore which isomerizes upon photon absorption. This initiates a cascade of structural rearrangements of the backbone eventually leading to protein function. To have a high yield of functioning per photon absorption, the retinal environment in the binding pocket is tuned by electrostatic and steric interaction such that the quantum yield for photoisomerization of retinal is increased by up to a factor of 4 compared to free retinal[102].

During this section about microbial and invertebrate rhodopsins, certain aspects of the photocycle for six different proteins will be investigated ranging from the interaction of retinal with its microenvironment in the resting state to an intense description of reaction kinetics. UV/Vis spectroscopy sheds light on the changes of retinal visible absorption to identify intermediate states of the photocycle. To get information about the structural changes of the retinal, resonance Raman spectroscopy is a suitable technique while infrared spectroscopy can give insights about mechanistic details of the whole protein on an atomistic level.

First, the light/dark adaption of the proton pump bR is covered. During dark adaption, a fraction of retinal isomerizes from an all-*trans* to a 13-*cis* configuration without absorbing a photon. However, upon illumination this process is reversed resulting in 100 % all-*trans* isomers. Interaction of the protonated Schiff base (PSB) of retinal with neighboring amino acid side chains is discussed for the ion channel ChR2. Light is shed on the changes in retinal structure during the conversion from the ground state to the first photoproduct in channelrhodopsin-1 (ChR1). How the photoisomerization of the retinal leads to structural rearrangements of the protein backbone important for functioning is followed for the case of the chloride pump halorhodopsin (hR). To study the reaction kinetics and mechanistic details in protein function of the sodium pump *Krokinobacter eikastus* rhodopsin 2 (KR2), vibrational spectroscopy was combined with time-resolved X-ray crystallography. Finally, a first biophysical characterization of the bistable rhodopsin jumping spider rhodopsin-1 (JSR1) is presented.

5.1 The light/dark adaptation of Bacteriorhodopsin

This project was motivated by a collaboration with Gabriela Nass Kovacs from the MPI Heidelberg and is partly published in:

Kovacs, G. N., Colletier, J.-p., Grünbein, M. L., Yang, Y., Stensitzki, T., Batyuk, A., Carbajo, S., Doak, R. B., **Ehrenberg, D.**, Foucar, L., Gasper, R., Gorel, A., Hilpert, M., Kloos, M., Koglin, J. E., Reinstein, J., Roome, C. M., Schlesinger, R., Seaberg, M., Shoeman, R. L., Stricker, M., Boutet, S., Haacke, S., Heberle, J., Heyne, K., Domratcheva, T., Barends, T. R. M. & Schlichting, I. Three-dimensional view of ultrafast dynamics in photoexcited bacteriorhodopsin. *Nature Communications* (2019). doi: 10.1038/s41467-019-10758-0

I contributed to the conceptualization of the experiment.

One of the best studied microbial rhodopsin is bacteriorhodopsin (bR). It was indirectly discovered in 1967 by Stoeckenius & Rowen in a work where the authors found that the membrane of *Halobacterium salinarum* was colored purple by an unknown membrane bound substance[103]. This halophilic bacterium thrives in high salt conditions which it requires for growth and structure preservation. If the salt concentration is too low, the membrane dissociates into fragments of which some will have a distinct purple color. Further studies on the purple membrane fragments soon revealed that the substance is an opsin-like protein which binds a retinal chromophore[104]. This was an onset for several spectroscopic studies, mainly UV/Vis and resonance Raman but later also Fourier transform infrared (FTIR) spectroscopy[105,106].

Bacteriorhodopsin in the ground state has a maximum in visible absorption at 568 nm which in turn gives rise to the purple color of the membrane. The absorption of a photon leads to an isomerization of the bound retinal cofactor from an all-*trans* to a 13-*cis* configuration, starting a sequence of structural rearrangements which eventually lead to proton transfer from the cytoplasmic side of the membrane to the extracellular medium. Hence, the absorbed energy is used to pump a proton against the electrochemical gradient across the membrane. Back flow of this proton is subsequently used by a synthase to produce adenosine triphosphate (ATP), the chemical energy storage of bacteria. The conversion of light into chemical energy is a form of photosynthesis albeit being a much simpler system and with less efficiency compared to the photosystem I and II found in plants[107].

The molecular details of this process were intensively studied and the crystal structure was solved several times. The photocylce of bR consists of five intermediate states, each characterized by their absorption maximum in the visible (fig. 5.1 **A**). A largely blueshifted M intermediate features a proton transfer from the protonated Schiff base (PSB) to D85 which triggers the release of another proton to the extracellular side. The reprotonation of the retinal Schiff base is from D96 with a subsequent uptake of a proton from the cytoplasm (fig. 5.1 **B**). Reisomerization of retinal to all-*trans* restores the initial ground state. Interestingly, bR exhibits two different forms of a resting state. Under light exposure, the ground state of bR consist of solely all-*trans* configured retinal but without any illumination a fraction of the retinal molecules thermally isomerize to 13-*cis* leading to a blueshift of

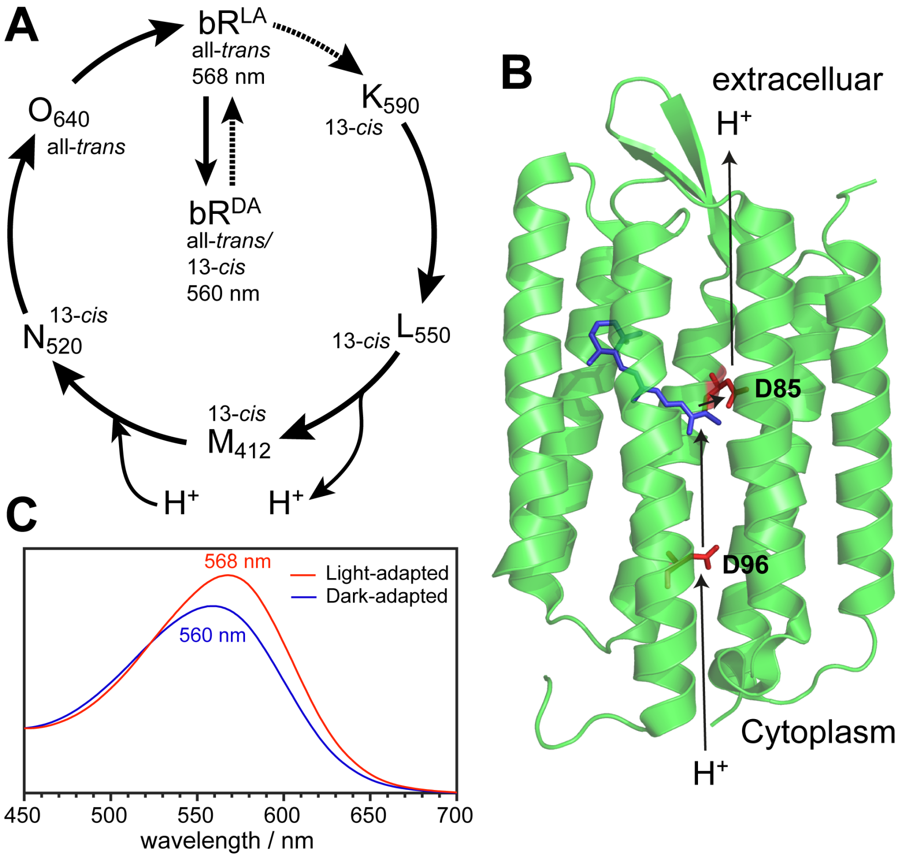

Figure 5.1: A: Photocycle of bR. Dashed arrows indicate light-induced processes while solid arrows represent thermally driven transitions. The different intermediate states are characterized by their absorption maximum in the visible (given as subscripts). An isomerization of the retinal from all-*trans* to 13-*cis* starts the photocycle until it gets reisomerized to all-*trans* during N state decay. In complete darkness, bR converts to its dark-adapted form which consists of all-*trans* as well as 13-*cis* configured retinal. **B:** Crystal structure of bR at 1.8 Å resolution (PDB: 3NS0)[108]. The retinal is colored in blue while important key residues for its function as a proton pump are colored in red. These are D85 as the primary acceptor of the Schiff base proton in the formation of the M intermediate and D96 as the amino acid which donates the proton back to the Schiff base during M state decay. **C:** UV/Vis absorption spectra of light- and dark-adapted purple membrane.

the visible absorption maximum to 560 nm (fig. 5.1 **C**). Photon absorption of this 13-*cis* form leads to an isomerization to all-*trans* but without proton pumping activity presumably due to lack of a pK_a difference between the PSB and D85[109].

Although many experiment were done on bR under different conditions, little was known about the conditions needed for light/dark adaptation of bR in the crystalline phase. For solving X-ray crystal structures, it is important to estimate the different states which the protein adopts during data collection. Exact knowledge of illumination times to fully light adapt microcrystals and the time constant of their dark adaptation were addressed in collaboration Gabriela Nass Kovacs from the MPI Heidelberg and are the topic of this section.

5.1.1 Light adaptation

Dark-adapted bacteriorhodopsin (bR^{DA}) consists of all-*trans* as well as of 40 to 60 % 13-*cis* configured retinal[110,111]. Upon light exposure, the fraction of 13-*cis* retinal molecules isomerizes to all-*trans* so that light-adapted bacteriorhodopsin (bR^{LA}) has a homogeneous isomeric composition. Resonance Raman spectroscopy is in principle an ideal tool to monitor changes in retinal configuration due to the selectivity of resonance enhancement but the probing light will inevitably interfere with bR^{DA} converting it to its light-adapted form. Using infrared radiation avoids the undesirable absorption of probing photons by the retinal chromophore. Thus, recording an infrared vibrational spectrum of bR^{DA} becomes feasible as long as the sample is kept in the dark over the course of the measurement.

Purple membrane (PM) fragments were dried on top of an attenuated total reflection (ATR) cell and subsequently rehydrated via the vapor phase while keeping the sample in the dark for at least 1 h before a spectrum of bR^{DA} was recorded. Light adaptation was achieved by illumination with a white LED lamp at 650 mW for more than 1 min which was switched off during data recording. Figure 5.2 shows the light-dark difference spectrum of the PM film with negative signals corresponding to bacteriorhodopsin with 13-*cis* retinal ($bR^{13\text{-}cis}$) while positive bands are due to light adaptation. The changes in vibrational modes are mainly confined to three spectral windows. The fingerprint region, which is sensitive to the isomeric state of the retinal due to a coupling of $C-C$ stretches with $C-C-H$ bends, has a pronounced negative/positive feature at 1180(-)/1201(+)cm^{-1}. These are marker bands for a 13-*cis* and an all-*trans* configuration, respectively, and therefore illustrate the transition from dark to light-adapted bR[110,112]. The peaks at 1342(-) and 1242(+)cm^{-1} originate from a coupled mode of $N-H$ and $C_{15}-H$ in-plane bending vibrations of the retinal skeleton[113]. Amide I modes originating from the protein backbone appear around 1660 cm^{-1}. In the case of light adaptation of bR, amide I modes are absent arguing for an isomerization of retinal without large backbone rearrangements. Without spectral contributions of amide I modes, the band at 1641 cm^{-1} can unambiguously be assigned to the $C=N-H$ stretching mode of the PSB in bR^{LA}. The corresponding vibration of the 13-*cis* dark-adapted retinal can not be explicitly assigned. Resonance Raman experiments on bR^{DA} identified the PSB vibration at 1634 cm^{-1} arguing for a weaker hydrogen bond of the Schiff base proton to its counterion in the dark-adapted 13-*cis* state[110]. The most pronounced feature at 1537(-)/1528(+)cm^{-1} are due to changes in the $C=C$ stretch frequency. This vibrational mode is associated to the π-electron system of the retinal rendering it to a sensor for the electronic transition in the visible[114]. A frequency upshift to 1537 cm^{-1} translates to a blueshift for $bR^{13\text{-}cis}$ in accordance to literature (fig. 5.1).

For successfully conduct X-ray crystallography on microcrystals, the light conditions needed to fully light adapt bR microcrystals are of importance. Efremov *et al.* showed that the spectral features in the infrared of a single (macro-)crystal upon light adaptation are the same as for PM solution[115]. Experiments were done as before except from exchanging the PM fragments with microcrystals in lipidic cubic phase (LCP). The changes in the $C=C$ stretch frequency served as an indicator for light adaptation. Two different light sources were used, one diode pumped solid state (DPSS) laser emitting at 532 nm with 50 mW and a white light LED connected to an optical fiber with a power of 650 mW. Both light spots were adjusted in such a way that they covered the complete sample surface. Light intensities were chosen in order to mimic the experimental conditions at a X-ray beamline.

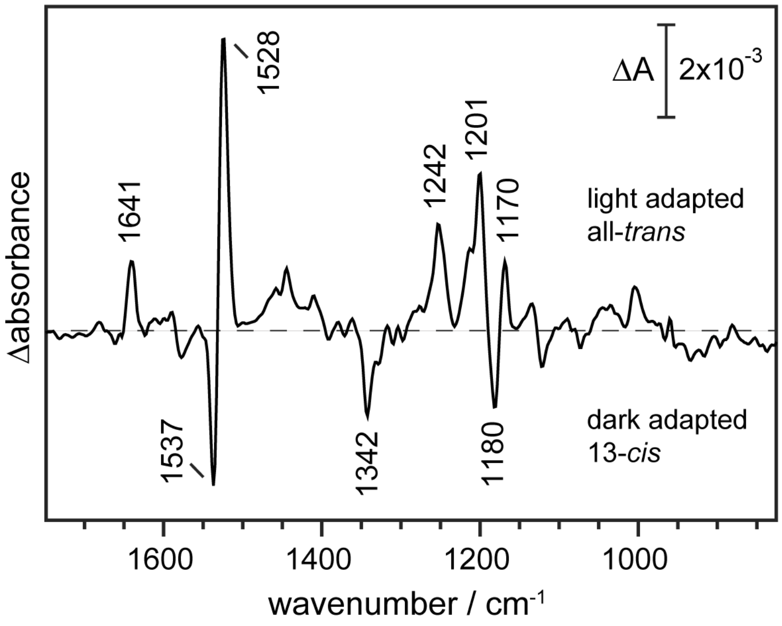

Figure 5.2: Light adaptation FTIR difference spectrum of rehydrated purple membrane patches in ATR configuration. Positive bands correspond to the light-adapted pure all-*trans* form while negative signals originate from the 13-*cis* contribution in the dark-adapted state. Illumination was done with a white light LED at 650 mW for 1 min and switched off during data recording.

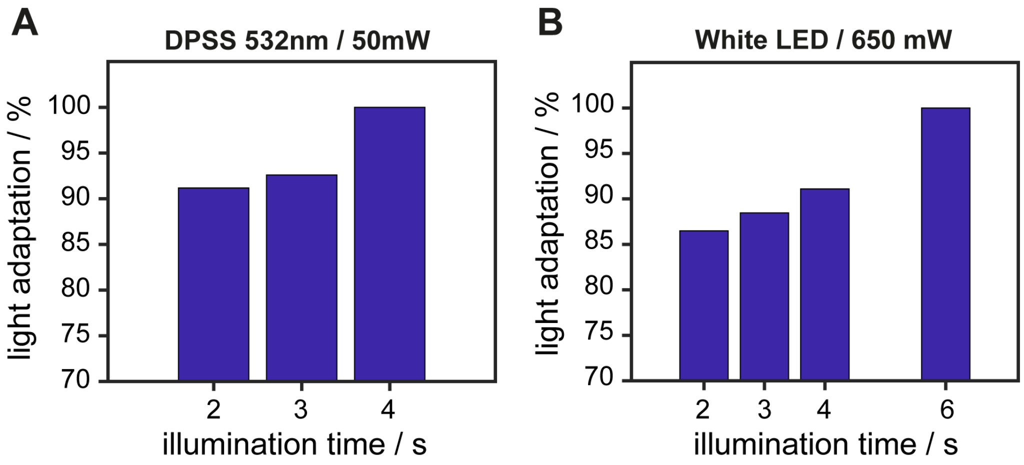

Figure 5.3: Illumination duration needed to convert bR microcrystals to the fully light-adapted state for two different light sources. Light adaptation was tracked via the C=C difference signal (see fig. 5.2). **A:** DPSS laser with an emission wavelength of 532 nm at 50 mW. **B:** White light LED lamp transmitted through an optical fiber with a power of 650 mW. Both light spots were covering the whole sample area.

Illumination with the LED for 1 min served as a 100 % light-adapted reference point because no further spectral changes could be observed for even longer exposure times (data not shown). It can be seen from fig. 5.3 that it just takes a couple of seconds for both light sources to fully convert the microcrystals into the light-adapted state. Light adaption is slightly faster achieved by illumination with the DPSS laser compared to the white light LED presumably due to its monochromatic emission at 532 nm which is close to the absorption maximum of the 13-*cis* fraction from bR^{DA} (459 to 555 nm)[110,116].

5.1.2 Dark adaptation

If light-adapted bR is not exposed to light, it converts to its dark-adapted from. This includes a thermal isomerization of the retinal from an all-*trans* to a 13-*cis* configuration. In section 5.1.1 the light adaptation was tracked via the changes in the C=C stretch frequency. Consequently, the transition from light to dark-adapted bR can be monitored in the same way. But since thermal isomerization is a rather slow process, the dark adaptation has a time constant of minutes[117]. Over the course of such a long experiment the baseline in an FTIR experiment can start to fluctuate. Another way to monitor dark adaptation is by detecting changes in visible absorption due to the blueshift of bR^{DA}. Using a UV/Vis spectrometer with microcrystals brings the drawback of scattering of the probing light at the crystals but also the benefit of a stable baseline. A solution of microcrystals in LCP was squeezed between two windows and subsequently sealed using vacuum grease. Prior to the measurement, microcrystals were light-adapted by illumination with a white light LED at 650 mW for at least 1 min (see fig. 5.3). During the experiment, which spanned 85 min, the sample was kept in the dark and every 2 min a spectrum was taken to minimize a possible light adaption caused by the probing light (fig. 5.4 **A**). Due to dark adaptation, the absorption maximum shifts to the blue while also loosing intensity indicating a lower extinction coefficient of 13-*cis* configured retinal (fig. 5.1 **C**)[118]. To obtain a time constant, the transition has to be fitted with an exponential function at a certain wavelength. The difference spectrum of the very first (bR^{LA}) minus the last (bR^{DA}) recording (fig. 5.4 **B**) revealed that the highest intensity changes are at 600 nm. Figure 5.4 **C** shows the normalized intensities at this wavelength assuming the first spectrum to be a fully light-adapted state. The decay is clearly monoexponential with a time constant of 24 min (red). Performing the same experiment with a rehydrated PM film yielded at time constant of 28 min (gray). It can be suggested that a different hydration of bR proteins in a PM film and the microcrystals influences the decay rate or that the more static protein environment in the microcrystals facilitates the thermal isomerization of the retinal.

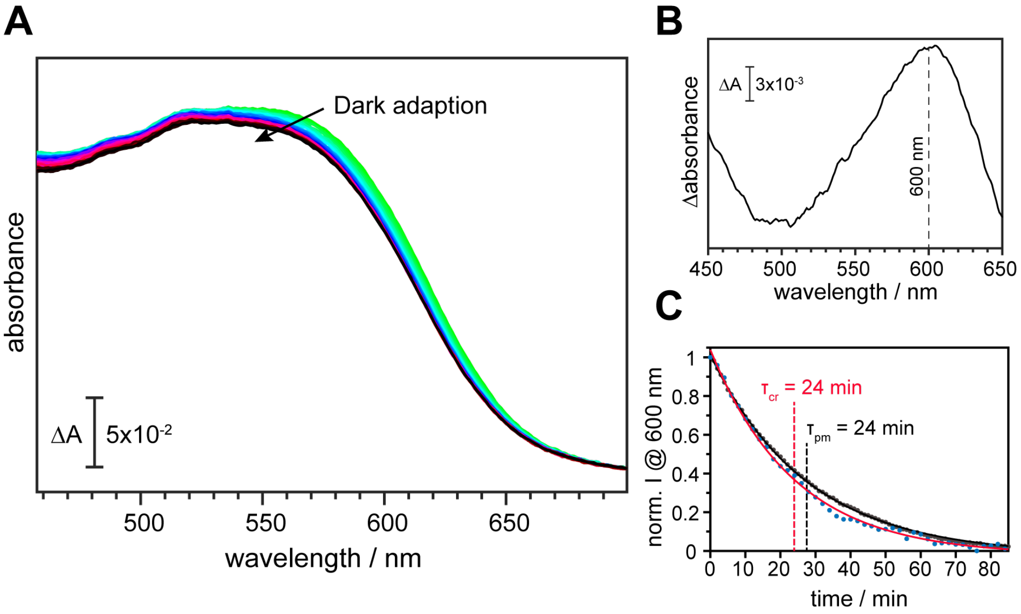

Figure 5.4: UV/Vis spectra of light-adapted bR microcrystals converting from light to its dark-adapted form. The crystals were illuminated with a white light LED at 650 mW for at least 1 min prior to the experiment and subsequently kept during the measurement in the dark. Time between two consecutive spectra is 2 min. **A:** Absolute spectra from green (light-adapted) to black (dark-adapted). **B:** Difference spectra between light and dark-adapted bR crystals (the very first minus last spectrum of A). The most pronounced change is at 600 nm. **C:** Normalized intensity decrease at 600 nm over the course of the experiment assuming that the first spectrum represents a fully light-adapted state. Experiment on microcrystals is depicted as blue dots with a exponential fit in red while PM patches is colored in gray. Time constants are indicated.

5.1.3 Conclusion

The light/dark adaptation of bR involves an interconversion of retinal configuration between all-*trans* and 13-*cis* forms and can be monitored in various ways. The isomerization of the 13th carbon atom around its double bond leads to a change of the C=C stretch frequency as well as to a shift of the visible absorption maximum. In this section, infrared and UV/Vis spectroscopy was used to scrutinize the light and dark adaptation of bR microcrystals, respectively. While light adaptation is a very fast process with just a couple of seconds to complete (fig. 5.3), the thermally driven dark adaptation has a time constant of 24 min (fig. 5.4).

These findings were helpful for the collaborators from the MPI Heidelberg for X-ray measurements on microcrystals using a free electron laser (FEL). Prior to the injection of the microcrystals into the X-ray beam, they stay for a certain amount of time in the dark. This means that as soon as the X-ray beam hits a microcrystal, a certain fraction of the retinal chromophores already isomerized to 13-*cis*. To calculate the amount of dark-adapted bR, the obtained time constant was of particular importance[2].

5.2 Retinal structure of the ground and first photoproduct state in ChRs

Channelrhodopsins (ChRs) are light-gated ion channels that have a sensor related function in flagellate green algae. Sitting in the eyespot of these organisms, they are part of the molecular machinery responsible for phototactic movement. Phototaxis describes the movement of organisms in response to light optimizing their environmental conditions such as photosynthetic growth[119]. Upon absorption of a photon, the retinal chromophore of ChRs isomerizes leading to an open protein conformation which permits the flow of ions along an electrochemical gradient across the membrane. Depolarization of the membrane triggers an yet unknown signaling cascade to the flagella base which is finally translated into phototactic movement[120]. Before the discovery of ChRs, many other ion channels were known with different trigger mechanism like voltage- or pressure-gated channels. But the unique feature of ChRs is the activation by photon absorption. Genetically encoded, they can be used to induce action potentials of neurons when illuminated by light of the corresponding wavelength. This possibility set the foundation of a new emerging field in neuroscience called optogenetics[8].

In the last years various ChRs of different algae were discovered but the first two ChRs were found in the model organism *Chlamydomonas reinhardtii* (Cr). They were divided in ChR1 and ChR2 based on differences in structure, activation mechanism and biophysical properties. What they do have in common, despite their name and function, is a substantial reduction in photocurrent under sustained illumination. This phenomenon of desensitization can be explained by a heterogeneous isomeric composition of the retinal cofactor[121–123]. ChRs would then possess two different closed conformations which lead to different conductive open states when activated. The closed states have an all-*trans* or 13-*cis* configured retinal, respectively, but how these states are connected to each other is still under discussion (fig. 5.5). In one model, the second closed state is a late intermediate of the all-*trans* photocycle with a long decay constant of seconds. Under sustained illumination, this state gets photoactivated and forms another open configuration (model **A**). Contrary it is also proposed that both closed states coexist if the protein is in the dark. Upon photoexciation, both states start a photocycle leading to two open conformations (model **B**). Both models have in common that a heterogeneous composition of closed and open states is formed under continuous illumination referred to as light adaption. Accordingly, the dark-adapted state describes the composition of states in the dark. This is not be confused with the dark adaptation of bacteriorhodopsin (bR) where the retinal slowly thermally isomerizes from an active all-*trans* to an inactive 13-*cis* configuration as described in section 5.1. In the case of ChRs, both retinal configurations have channel activity and the interconversion takes place in the timescale of seconds[121].

Although channelrhodopsin-2 from *Chlamydomonas reinhardtii* (CrChR2) is widely used in neuroscience and for prospective medical applications like restoring vision or hearing[120], the mechanistic details of ChRs are not yet completely understood. Exact knowledge about the activation mechanism can help to improve certain biophysical aspects by variation of amino acid side chains. This could include to decrease the degree of desensitization or to shift the absorption maximum more to the red

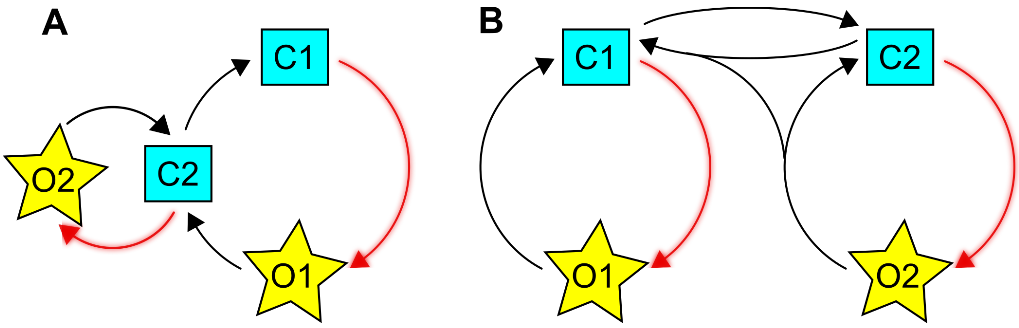

Figure 5.5: Two photocycle models explaining the desensitization of ChRs. Closed states are denoted as turquoise squares while open conformations are represented as yellow stars. Light-induced transitions are colored in red.

which increases the penetration depth through tissue of the exciting light. In this section, CrChR2 and channelrhodopsin-1 from *Chlamydomonas augustae* (CaChR1) are investigated by resonance Raman spectroscopy to gather insights about the retinal environment and its primary photochemistry.

5.2.1 On the Schiff base counterion(s) in CrChR2

This project is published in:

Ehrenberg, D., Krause, N., Saita, M., Bamann, C., Kar, R. K., Schapiro, I., Heberle, J. & Schlesinger, R. Atomistic insight into the role of threonine 127 in the functional mechanism of channelrhodopsin-2. *Applied Sciences* **9**, 4905 (2019). doi: 10.3390/app9224905

I recorded the Raman spectra of the variants and contributed to data analysis as well as interpretation.

While the isomeric light/dark adaptation is well understood for bacteriorhodopsin (bR) (see section 5.1), it is still actively discussed for channelrhodopsin-2 from *Chlamydomonas reinhardtii* (CrChR2)[124]. From first Raman and high-performance liquid chromatography (HPLC) experiments it was concluded that CrChR2 has predominantly all-*trans* but also 13-*cis* configured retinal in a 70:30 ratio for the dark-adapted state[125]. Upon light adaption this ratio just slightly increases in favor of 13-*cis* retinal. Later, a combined Raman and nuclear magnetic resonance (NMR) spectroscopy study found two dark states, one quickly formed after illumination is switched off which is referred to as apparent dark-adapted state (DA_{app}) and one after hours in the dark named the initial dark-adapted sate (IDA)[122]. These two states differ in the isomeric composition such that the IDA state consists solely of all-*trans* isomers. Additionally, electrophysiology measurements required a model where two conductive open states coexist[126] (fig. 5.5). Recent works tried to unify different photocycle models but came to slightly different conclusions[127,128].

Besides the heterogeneity of the isomeric configuration of the retinal, hybrid quantum mechanics/molecular mechanics (QM/MM) simulations revealed a flexible structure around the protonated Schiff base (PSB) permitting three different hydrogen bond interactions[129]. The most occupied scenario is a hydrogen bond between the proton of the Schiff base and the side chain of E123 which has an upward orientation towards the PSB (fig. 5.6 **A**). In this orientation, the hydrogen bond is presumably strong due to a small distance to the PSB of 2.6 Å. The authors additionally found a stable rotamer of E123 with a downward orientation pointing away from the PSB. Due to this flip into a remote position, the positive charge at the PSB is mostly stabilized by the ionized D253 which serves later as the proton acceptor of the Schiff base proton in the P_2^{390} state[130]. A third scenario is a hydrogen bond network involving the PSB, a water molecule, E123 and D253.

In bR it was found by Fourier transform infrared (FTIR) spectroscopy that a threonine (T89) has an influence on the primary proton transfer step from the PSB to D85[132]. X-ray crystallographic structures then clarified that T89 is not directly interacting with the PSB itself but rather forms an hydrogen bond with D85[133]. A threonine at that position is conserved in many channelrhodopsins and the corresponding residue in CrChR2 is T127. It is located in vicinity to the PSB but is too far away for a direct hydrogen bond interaction. As in bR, this residue forms a hydrogen bond to E123 which is the homologous residue to D85 (fig. 5.6). Thus, T127 is a good candidate for mutations in order to scrutinize the hydrogen bond interactions of the PSB in CrChR2.

Resonance Raman spectroscopy is a suitable technique to address the hydrogen bond network of the PSB. To avoid any photoexcitation and thus accumulation of any intermediate states of CrChR2, Raman spectra were recorded under cryogenic conditions at 80 K with an excitation wavelength of

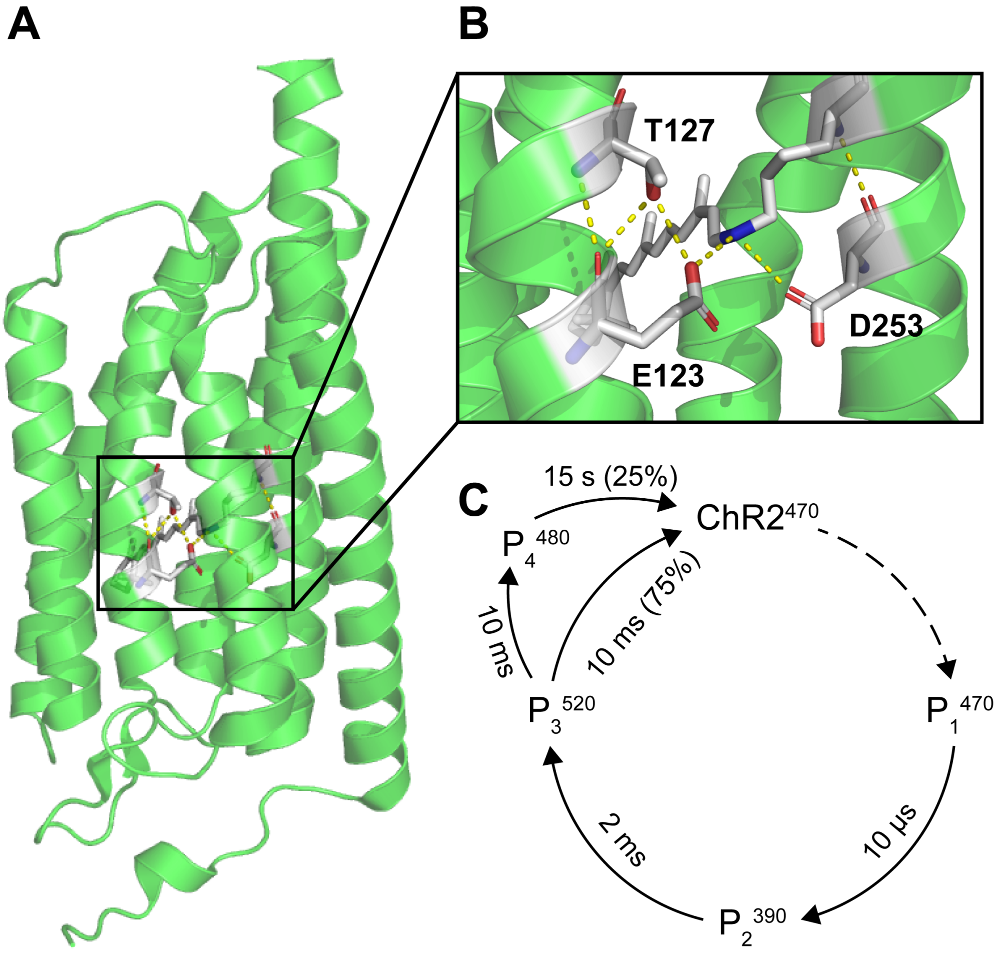

Figure 5.6: A+B: Crystal structure of CrChR2 with an upward E123 orientation (PDB: 6EID)[131]. Inset shows the retinal Shiff base region with amino acids as labeled. Hydrogen bonds are indicated by dashed yellow lines. **C:** Photocycle of CrChR2 under single-turnover conditions according Saita *et al.*[127]. Visible absorption maxima are indicated as superscripts. Decay of the P_3^{520} state has a probability of 25 % to occur via a P_4^{480} state which potentially desensitizes CrChR2 under sustained illumination.

457 nm matching the ground state visible absorption maximum of 470 nm. A spectral contribution of the first photoproduct P_1^{500} can be neglected due to the shifted excitation wavelength and usually low concentrations under these conditions (see section 5.2.1). Although the Schiff base vibration of wild-type CrChR2 was so far treated as a single vibration[125], it should actually be a convolution of two bands according to the two E123 rotamer model[129]. A detailed analysis of the asymmetric band shape of the ground state C=N−H vibration indeed revealed two spectral Gaussian components at 1661 and 1665 cm^{-1} (fig. 5.7 black spectrum). The latter can be tentatively assigned to the PSB$\cdots$E123 motif, because of the short distance between E123 and the PSB. Consequently, the former vibration can be attributed to the PSB$\cdots$D253 (and/or to the motif involving a water molecule) interaction. This assignment is solidified by a E123D mutation whose Raman spectrum looks essentially identical to wild-type except that the Schiff base vibration can be fitted sufficiently well with just one Gaussian centered at 1660 cm^{-1} (green spectrum). The shorter side chain of an aspartic compared to a glutamatic acid prevents a hydrogen bond interaction between the residue at position 123 and the PSB. This imitates the downward rotamer scenario of E123 and thus the PSB$\cdots$D253 motif is favored.

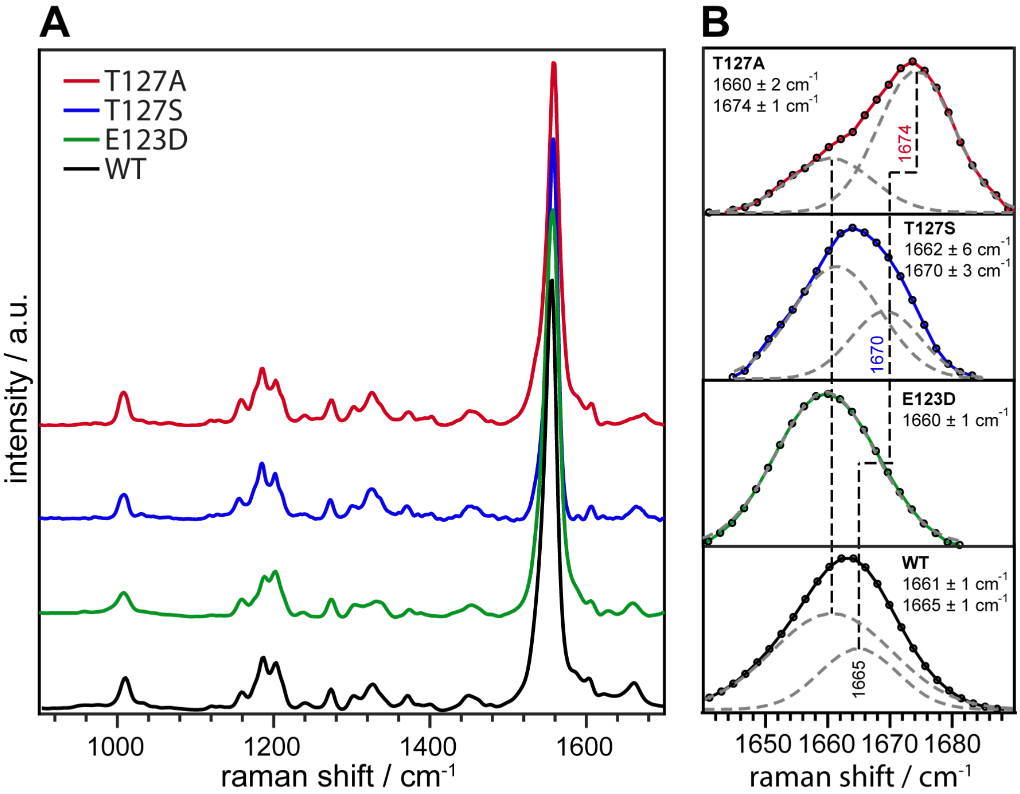

Figure 5.7: A: Resonance Raman spectra of the resting (dark-adapted) state in wild-type as well as in three mutants of CrChR2 at 80 K with 457 nm excitation. **B:** Enlarged presentation of the PSB vibration. Dots represent measured datapoints while dashed grey lines indicate band fitting using a Gaussian shape profile. Band positions with corresponding errors resulting from the fit are given.

According to the crystal structure, T127 presumably forms a hydrogen bond with E123 (fig. 5.6). A mutation of T127 should therefore influence the hydrogen bond between the PSB and E123 providing a possibility to indirectly probe this interaction. The C=N−H vibrational band of a T127S mutant needed again two Gaussians for a sufficiently good fit (blue spectrum). While the lower band position stays constant compared to wild-type, the higher frequency mode shifts upwards from 1665 to 1670 $\mathrm{cm^{-1}}$. A mutation to a serine retains the hydroxyl group of threonine and preserves the hydrogen bond to E123. In fact, due to the conservative mutation to a serine, the hydrogen bond between E123 and the PSB gets slightly stronger while the PSB$\cdots$D253 motif is not affected.

In contrast, a mutation of T127 to an alanine breaks the hydrogen bond interaction to E123 because of the missing hydroxyl group. The PSB band of the T127A mutant is clearly asymmetric in shape which required two Gaussians for a satisfying fit (red spectrum). The lower frequency peak is again unaffected indicating that the PSB$\cdots$D253 interaction is comparable as in wild-type. But the band assigned to the PSB$\cdots$E123 motif is significantly upshifted by 9 $\mathrm{cm^{-1}}$ to 1674 $\mathrm{cm^{-1}}$. Such a PSB frequency is the highest so far observed for any rhodopsin. Exchange of the Schiff base proton to a deuterium can definitely identify this high frequency mode as a C=N−H vibration. The higher mass of deuterium decouples the N−X bend from the C=N stretch which results in a downshift in frequency of the PSB mode to a pure C=N stretch vibration[134]. Thus, the isotope shift in D_2O is directly correlated to the hydrogen bond strength of the Schiff base proton. For the T127A mutant,

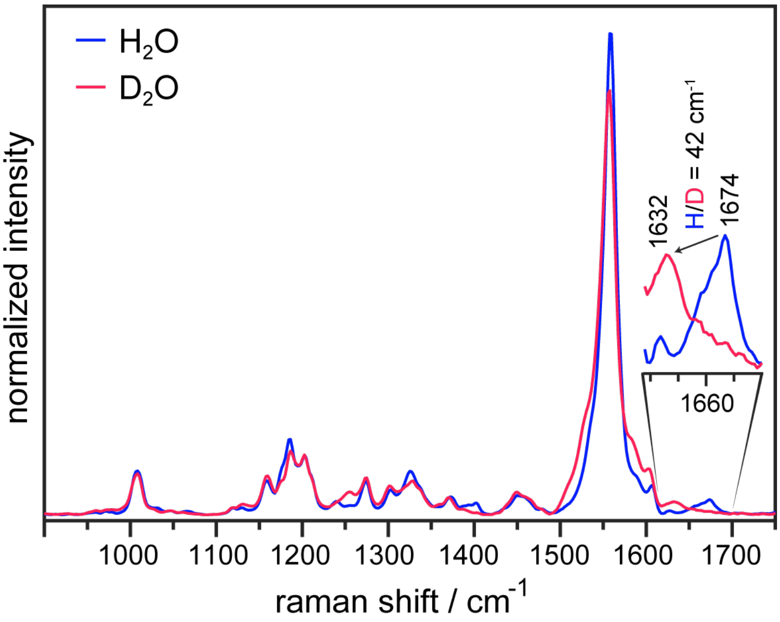

Figure 5.8: Resonance Raman spectra of the T127A mutant of CrChR2 at 80 K with 457 nm excitation. Prior to cooling, the dried protein film was rehydrated either with H_2O (blue spectrum) or D_2O (red spectrum) via the vapor phase. Spectra are normalized to the all-*trans* retinal band at 1201 cm^{-1}. Inset highlights the isotope shift of the retinal Schiff base vibration upon H/D exchange.

this band downshifts by 42 cm^{-1} indicating a extremely strong hydrogen bond interaction. The decoupling of the C=N−H mode transforms the asymmetric PSB band to a symmetric shape since it is now a C=N stretch uninfluenced by hydrogen bonds (fig. 5.8). As the interaction between T127 and E123 is removed in this mutant, the carboxylic side chain of E123 is able to form a stronger hydrogen bond to the N−H of the PSB.

Conclusion

Detailed analysis of the asymmetric band shape of the PSB vibration (coupled mode of the C=N stretching and the N-H bending vibration) of wild-type CrChR2 with resonance Raman spectroscopy revealed the presence of two overlapping bands. This heterogeneity can be well explained by a molecular model brought up by the Elstner and Hegemann groups[129]. They propose two rotamers of E123 in the ground state, one upward orientation forming a strong hydrogen bond with the Schiff base while the other one pointing downwards away from the PSB. In this scenario, the counterion D253 adopts the stabilization of the Schiff base proton. A mutation of E123 to an aspartic acid leads to a symmetrical shaped PSB vibrational band missing the high frequency component. Further mutations of T127, which forms a hydrogen bond to E123, keeps the lower frequency component unaffected. Hence, the lower frequency mode at 1661 cm^{-1} in the wild-type can be assigned to the PSB$\cdots$D253 motif. On the other hand, the higher frequency mode experiences an upshift upon T127 mutation and is missing in the E123D mutant. On this basis, the higher frequency component at 1665 cm^{-1} is correlated to the PSB$\cdots$E123 scenario. In fact, E123 forms the strongest hydrogen bond to a PSB so far observed upon mutation of T127 to an alanine with an isotope shift of 42 cm^{-1}. This is in particular remarkable because the increase in hydrogen bond interaction is not accompanied by a shift in visible absorption[4]. It seems that the different electrostatics at the PSB are compensated at another part of the retinal, possibly at the ionone ring[135,136].

This study lend support to the proposed model of two rotamers of E123 in CrChR2 giving rise to different hydrogen bond motifs of the PSB. It was observed that the photocycle kinetics of CrChR2 is decelerated at depolarized membrane potentials[137]. This voltage sensitivity was abolished upon an E123T substitution. The different hydrogen bond motifs of E123 could be therefore essential for a voltage-sensing mechanism in CrChR2.

5.2.2 Primary photochemistry of CaChR1

This project was motivated by Vera Muders from the FU Berlin and Christoph Schnedermann from the University of Cambridge and is published in:

Schnedermann, C., Muders, V., **Ehrenberg, D.**, Schlesinger, R., Kukura, P. & Heberle, J. Vibronic Dynamics of the Ultrafast all-trans to 13-cis Photoisomerization of Retinal in Channelrhodopsin-1. *Journal of the American Chemical Society* **138,** 1–8 (2016). doi: 10.1021/jacs.5b12251

I recorded the Raman spectrum of P_1^{580} *and contributed to writing the manuscript.*

From the two first discovered channelrhodopsins of *Chlamydomonas reinhardtii*, ChR2 was more intensively studied because its biophysical properties better suit the needs of optogenetic applications. Although ChR1 has faster (de-)activation kinetics and a redshifted visible absorption maximum which allows a deeper penetration of the activation light into tissue, its major drawbacks are a low conductance at pH 7 and a rapid decrease in current amplitude (desensitization or inactivation) severely hampers its use as an optogenetic tool[138,139]. In addition, ChR1 is difficult to overexpress limiting the production of purified protein for biophysical studies. However, understanding the molecular details of ChR1 is of interest because it can give insights in how to improve existing cation channels for optogenetics.

Channelrhodopsin-1 from *Chlamydomonas augustae* (CaChR1) can be heterologously expressed in large quantities in the yeast *Pichia pastoris* permitting comprehensive biophysical analysis. Interestingly, CaChR1 also suffers from low photocurrents and slow (de-)activation kinetics as channelrhodopsin-1 from *Chlamydomonas reinhardtii* (CrChR1) but its level of desensitization is drastically decreased[139]. The ground state P_0^{518} of CaChR1 absorbs green light at 518 nm while under continuous illumination a blue shifted P_2^{380} state accumulates[140]. The characteristic blue shift in visible absorption is a result of a deprotonated Schiff base (SB), which is protonated in P_0^{518}, as revealed by resonance Raman spectroscopy[140]. A combination of time-resolved visible absorption spectroscopy and electrophysiology connected the rise and decay of the P_2^{380} intermediate with light induced passive photocurrents on a millisecond timescale[141]. Closure of the channel leads to a long lived state referred to as P_4^{520}. Skipping the number 3 in the nomenclature of states indicates that a late red shifted intermediate - as observed in channelrhodopsin-2 from *Chlamydomonas reinhardtii* (CrChR2) - is missing in CaChR1. Moreover, the P_4^{520} intermediate has the same absorption maximum as the ground state and is therefore spectrally silent in a UV/Vis difference experiment and was just observed by Fourier transform infrared (FTIR) spectroscopy[142]. It is distinguished from P_0^{518} by ongoing conformational changes of the protein backbone as well as by a 13-*cis* configured retinal. Photoexcitation of the ground state, which is mainly composed of all-*trans* retinal, results in an isomerization to 13-*cis* and a first red shifted P_1^{590} photoproduct. Reisomerization back to all-*trans* does not take place until the decay of the P_4^{520} state[140,142,143]. Spectroscopy on intermediates as the P_2^{380} and P_4^{520} state is facilitated by their accumulation under continuous illumination or by a long lifetime, respectively. In contrast, trapping the short living P_1^{580} requires cryogenic temperatures and in the case of Raman spectroscopy also a sophisticated way of eliminating spectral signatures originating from the ground state.

The isomeric composition of the retinal chromophore in the ground state of CaChR1 is still a matter of debate. Ogren *et al.* postulate that the ground state consists of almost pure all-*trans* configured retinal based on resonance Raman and FTIR measurements which would favor the one photocycle model of fig. 5.5 **A**[144]. Contrary, a work published by Muders *et al.* conclude a heterogeneous ground state population comprised of 30 % 13-*cis* and 70 % all-*trans* retinal using also resonance Raman but corroborated by high-performance liquid chromatography (HPLC) analysis[140]. Despite this controversy, both studies agree that CaChR1 does not exhibit any light/dark adaptation as bacteriorhodopsin (bR). In a resonance Raman spectrum, ground state 13-*cis* configured retinal can be distinguished from all-*trans* by its characteristic vibration around 1180 $\mathrm{cm^{-1}}$ in the fingerprint region. Additionally, the 13-*cis* isomer shifts the visible absorption maximum slightly to the blue giving rise to a higher frequency of the C=C stretching vibration compared to all-*trans*[110,145]. Conclusively, vibrational analysis of the ground state $P_0{}^{518}$ and the first excited state $P_1{}^{580}$ with a focus on the fingerprint and the ethylenic stretch mode region can further help to clarify the isomeric composition of CaChR1.

A ground state spectrum of CaChR1 was recorded at 80 K with a probing laser wavelength of 647 nm. Cryogenic temperatures in combination with a pre-resonant excitation ensure to completely avoiding spectral features of later occurring intermediate states. The spectrum obtained under these conditions (fig. 5.9 blue spectrum) is in agreement with already published data[140,146]. In the fingerprint region, two bands at 1164 and 1203 $\mathrm{cm^{-1}}$ are characteristic for an all-*trans* configuration[145]. The C=C stretch mode at 1536 $\mathrm{cm^{-1}}$ is slightly upshifted compared to published spectra recorded at room temperature[140,146]. With decreasing temperature, the polyene chain shortens leading to a expected shift of 3 to 4 $\mathrm{cm^{-1}}$. In a typical resonance Raman spectrum of retinal containing proteins, the highest frequency mode can be attributed to a C=N−H coupled vibration of the protonated Schiff base (PSB). This mode at 1650 $\mathrm{cm^{-1}}$ is also slightly upshifted which can not be explained by a shortening of the π-electrode system. For retinal containing rhodopsins it is well established that the conjugated polyene chain can give rise to up to four distinct C=C vibrational modes[110,145]. Curve fitting of the ethylenic stretch band revealed three components at 1527, 1537 and 1550 $\mathrm{cm^{-1}}$. Previous studies on bR and CrChR2 also identified three bands in this region where the lower and higher frequency modes were attributed to a 13-*cis* isomer while the remaining band was assigned an all-*trans* configured retinal[110,147]. Based on this, it was concluded that the higher frequency mode in CaChR1 at 1550 $\mathrm{cm^{-1}}$ is also a result of a present 13-*cis* species although the frequency difference of 13 $\mathrm{cm^{-1}}$ to its all-*trans* counterpart is twice as large as it is the case in bR and CrChR2.

Illumination of the sample at 80 K with a second laser emitting at 514 nm, simultaneously to the 647 nm probing laser, starts the initial photoreaction, namely the *trans* to *cis* isomerization while the thermal transitions are not taking place. This leads to an accumulation of the first $P_1{}^{580}$ intermediate state and the emergence of additional bands in the Raman spectrum (fig. 5.9 red spectrum). The emerging band at 1196 $\mathrm{cm^{-1}}$ is indicative of a 13-*cis* photoproduct while the intensity gain at the lower frequency side of the C=C band translates into a redshift in the visible[148]. To extract the $P_1{}^{580}$ intermediate spectrum out of the photostationary mixture (red spectrum), the contributions from the ground state $P_0{}^{518}$ have to be carefully subtracted (blue spectrum). For this, a subtraction method based on asymmetric least squares was employed[149]. The optimization function of the problem is

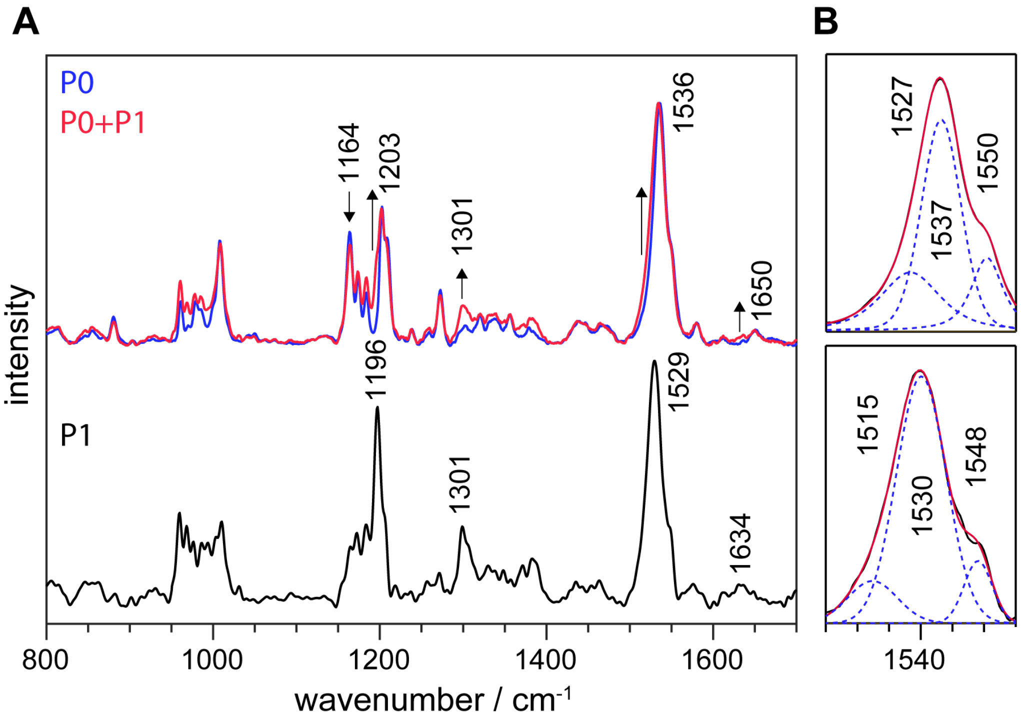

Figure 5.9: Comparison of Raman spectra of CaChR1 at 80 K. **A:** Resonance Raman spectra of the ground state under pre-resonant condition (top blue) and the photostationary mixture with additional illumination with 514 nm (P_0^{518} + P_1^{580}, top red). Spectral changes are indicated with arrows. The bottom black resonance Raman spectrum represents the P_1^{580} intermediate obtained with a subtraction procedure was based on asymmetric least squares (see text). **B:** Deconvolution of the main C=C stretch band for the ground state P_0^{518} (top) and the P_1^{580} state (bottom).

$$L = (P_0P_1 - \boldsymbol{k} \cdot P_0)^T \cdot \boldsymbol{W} + \lambda_1 \cdot ||\boldsymbol{Dk}||^2 + \lambda_2 \cdot ||\boldsymbol{D}(P_0P_1 - \boldsymbol{k} \cdot P_0)||^2 \qquad (5.1)$$

where P_0P_1 denotes the photostationary spectrum, P_0 the ground state spectrum, $\boldsymbol{k}$ is a vector composed of scaling factors for each data point and $\boldsymbol{D}$ is a difference matrix. A weighting matrix $\boldsymbol{W}$ is computed in each iteration step containing high weighting values as a punishment if a datapoint corresponds to a negative intensity value. A smooth scaling vector profile is ensured by $||Dk||$. λ_1 and λ_1 are smoothing parameters and were set to 10^5 and 10^7, respectively. An appropriate initial scaling vector $\boldsymbol{k}$ has to be chosen prior to the optimization process. Taking the ratio of the bands at 1196 to 1201 cm^{-1} yields a 30 % spectral contribution of the P_1^{580} intermediate. The initial scaling factor was therefore set to 0.8 for each data point to approach the optimization from just positive intensities values.

The P_1^{580} spectrum obtained with this method is shown in fig. 5.9 in black. The characteristic 13-*cis* peak of a first photoproduct at 1196 cm^{-1} is well pronounced while the all-*trans* counterpart at 1203 cm^{-1} is absent. The C=C stretch band is downshifted by 7 cm^{-1} and matches the redshifted absorption of 580 nm. Deconvolution of this band yields three peaks at 1515, 1530 and 1548 cm^{-1}. While the two lower lying bands are clearly downshifted compared to the ground state P_0^{518}, the position of the higher frequency mode is just slightly affected. This suggests that this vibration is due

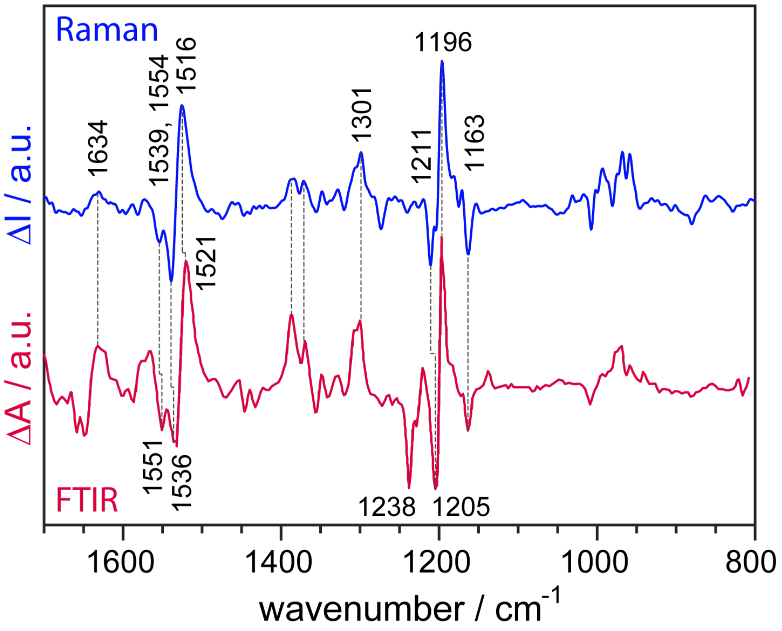

Figure 5.10: Comparison of the difference spectra obtained by resonance Raman (blue) and FTIR spectroscopy (red) on CaChR1 at 80 K. Raman spectra were subtracted to match the difference intensities of the FTIR spectrum. Negative peaks are due to ground state vibrations while positive bands are attributed to the formation of P_1^{580}. Similar band positions are indicated by dashed lines. The FTIR difference spectrum was reproduced with permission from the American Chemical Society[150].

to a more localized C=C mode which is not influenced by isomerization. The C=N−H frequency of the PSB downshifts to 1634 cm^{-1} representative for a weaker hydrogen bond to the counterion in the P_1^{580} intermediate.

Comparison of the observed Raman spectra with a FTIR difference spectrum of the P_1^{580} intermediate at 80 K published by Ogren *et al.* may validate the experimental Raman protocol[150]. For this, the ground state Raman spectrum was subtracted from P_1^{580} in a way to match the difference intensities of the FTIR data. Negative bands therefore correspond to ground state vibrations while positive signals indicate vibrational changes due to P_1^{580} formation. Overall, both datasets agree well, confirming the subtraction procedure and that the same P_1^{580} intermediate has been trapped at 80 K. The fingerprint region exhibits a similar band pattern as bR illustrating the isomerization from all-*trans* to 13-*cis*[109]. The PSB was already assigned at 1634 cm^{-1} using isotope labeling and is confirmed by the Raman measurement[150]. In the C=C stretch region, bands appear at similar frequencies. Clearly, the feature at 1539(-)/1516(+)cm^{-1} is due to the changes of the main ethylenic mode and reflects the redshift of the photoproduct. The higher frequency mode at 1554 cm^{-1} is present in both spectra. It was demonstrated by FTIR spectroscopy that this band is unaffected by exchanging the retinal with its A_2 analog (one more double bond in the ionone ring). It also does not experience any shift upon isotope labeling of the carbons around the isomerization bond but it disappears upon H/D exchange. Hence it was assigned as an amide II vibration of the peptide NH groups[150]. This assignment is contradicted by the appearance in the resonance Raman data. Here, it is not expected to detect vibrations of the apoprotein due to the resonance enhancement which selectively enhances vibrational modes of the retinal. Furthermore, the amide II mode involves mainly N−H bendings and C−N stretches of the polyene chain which just experience a small change in polarizability and have thus just little Raman activity. Even if it were an amide II mode, one would also expect to see an amide I vibrational mode, which should be even more pronounced[151]. Altogether, it seems likely that the vibrational band around 1550 cm^{-1} is a localized C=C stretch mode of the retinal.

Conclusion

Cryogenic temperatures permit to trap the first photoproduct of microbial rhodopsins. Here, a pure resonance Raman spectrum of $\text{P}_1{}^{580}$ was obtained with a suitable illumination protocol and a subsequent subtraction method based on a asymmetric least squares regression. It exhibits a fingerprint band pattern indicative for a 13-*cis* configured retinal with a slightly weaker hydrogen bond of the PSB to its counterion represented by a downshift from 1650 to 1634 cm^{-1} in $\text{P}_1{}^{580}$. Further analysis of the C=C stretch vibration revealed a higher frequency mode at 1548 cm^{-1} which is just slightly downshifts from 1550 cm^{-1} in the ground state. This vibration was previously assigned to be a characteristic 13-*cis* band which seems unlikely due to its insensitivity upon photoisomerization[140]. A previous FTIR study concluded that a negative peak at 1551 cm^{-1} originates from an amide II vibration[150]. A constructed resonance Raman difference spectrum reproduced a similar band pattern in the amide II & C=C region as in the infrared data. This excludes a protein backbone vibration as origin of the 1551 cm^{-1} peak based on the retinal selectivity of the resonance effect. It seems that the vibration around 1550 cm^{-1} is a more localized C=C stretch mode of the retinal and is not characteristic for a 13-*cis* isomer. Thus, the amount of retinal heterogeneity remains elusive and further experiments are needed to clarify this issue.

5.3 Retinal isomerization triggers changes in the secondary structure of HR

This project was motivated by a collaboration with Gabriela Nass Kovacs from the MPI Heidelberg

Soon after the discovery of bacteriorhodopsin (bR), evidence became available that the *Halobacterium salinarum* possesses two other rhodopsins. One of the two is an inward directed chloride pump named halorhodopsin (hR)[152]. Halobacteria thrive in environments with high salt concentration as for example the Dead Sea. For these archaeons it is essential for survival to maintain osmotic balance, in particular during cell growth. This duty is hold by several active transporters which transfer chloride across the membrane into the cell preventing water efflux. One of these transporters is hR which consumes light energy to pump chloride ions against a negative inner electrical potential. Several halorhodopsins have been found in halobacteria which differ in amino acid sequence and in activation dynamics[153]. This section is about hR from *Halobacterium salinarum*.

As for other microbial rhodopsins, photon absorption of the retinal leads to a transition to the first excited electronic state. During relaxation back to the electronic ground state, the retinal can isomerize from a previous all-*trans* to a 13-*cis* configuration. This triggers a series of events leading to a release with an subsequent uptake of a chloride ion. An ion release prior to an uptake requires that the excess chloride ion is already bound at the extracellular side of the protein in the ground state of hR. It was shown that the absorption maximum of hR experiences spectral shifts upon exchanging chloride with other halides[154–156]. This change in electronic properties of the retinal infers a halide binding site in the vicinity of the protonated Schiff base (PSB). Upcoming X-ray crystallographic structures indeed showed an halide binding site embedded in an extensive counterion complex involving several amino acid side chains and water molecules (fig. 5.11 **A**)[157–159].

During ion pumping, hR undergoes structural changes leading to a series of photointermediates which are most commonly characterized by their absorption maximum in the visible. In case of hR, this approach is in fact used but strongly overlapping absorption profiles make a spectral disentanglement of photoproducts a tedious task. This eventually led to different values for the absorption maxima throughout literature. In this section, a combined analysis and nomenclature for the hR photoreaction introduced by Varo *et al.* and later revised by Hutson *et al.* will be used[160,161]:

$$\mathrm{hR} \rightarrow \mathrm{hK} \rightarrow \mathrm{hL}_1 \rightarrow \mathrm{hL}_2\ (\leftrightarrow \mathrm{hN}) \rightarrow \mathrm{hR} \quad .$$

Photoisomerization of all-*trans* to 13-*cis* results in the hK intermediate. In contrast to bR, where this primary photoproduct has a redshifted absorption maximum, hK has a similar absorption profile as the ground state. This means that in a visible absorption difference experiment hK will be spectrally silent because the absorption of ground state bleach and formation of the intermediate state cancel. The first photointermediate is followed by a blueshifted hL state. Kinetic modeling of UV/Vis data required a subset of hL_1 and hL_2 states to achieve a sophisticated fit. A late hN state with the same absorption maximum as the ground state, which is largely in equilibrium with hL_2, was proposed but never confirmed by transient infrared spectroscopy. It has to be highlighted that there is no far

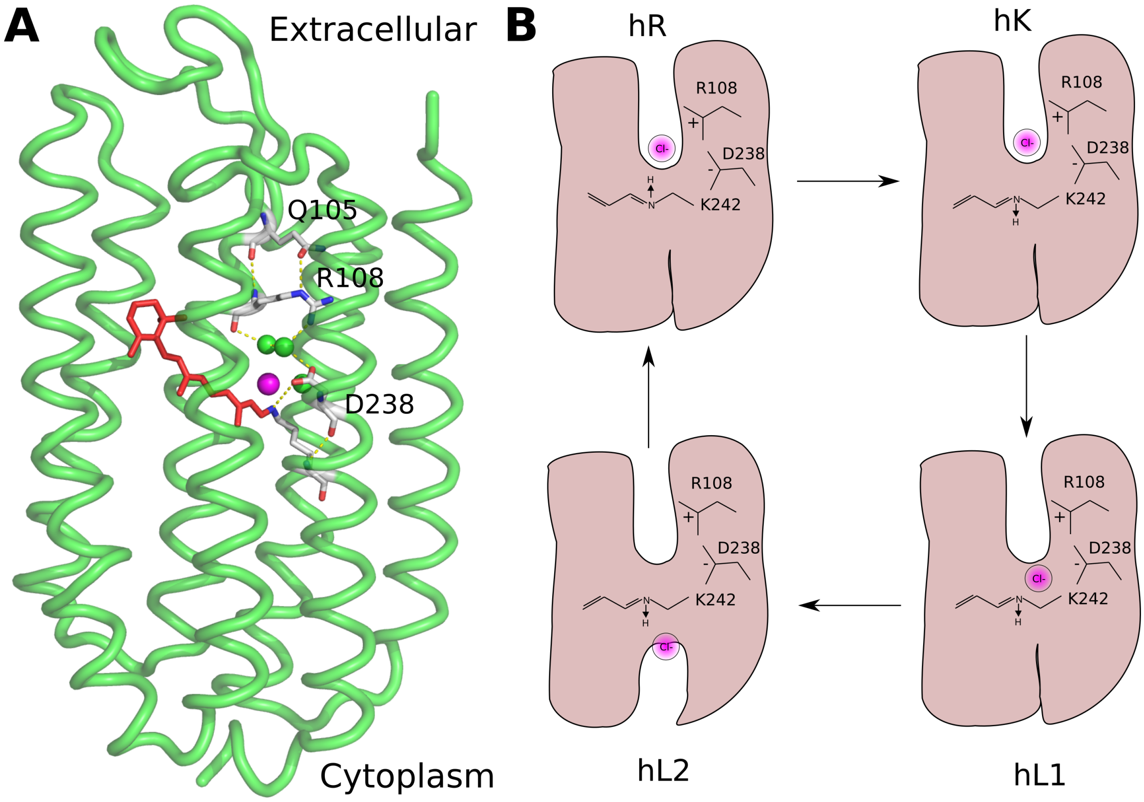

Figure 5.11: A: Crystal structure of the hR ground state (PDB: 1E12)[157]. Retinal is colored in red, water molecules in green and the chloride ion in magenta. Important amino acid residues are labeled and hydrogen bonds are indicated with dashed yellow lines. **B:** Mechanistic model of the photoreaction adopted from Essen[162]. Chloride ion is colored in magenta and important charged amino acid side chains are labeled. The arrow at the PSB indicates the direction of the dipole moment. The accessibility switch for the chloride ion is supposed to take place during the transition between the two substates hL_1 and hL_2.

blue shifted intermediate in the photoreaction of hR indicating that the Schiff base stays protonated throughout the photocycle. Since the chloride ion is negatively charged, a deprotonation of the Schiff base would establish electrostatic repulsion and thus elevate the energy needed for the chloride ion to overcome the retinal binding pocket.

A mechanistic overview of the proposed hR photocycle is depicted in fig. 5.11 **B**. The retinal has an all-*trans* configuration in the ground state and the chloride ion is bound on the extracellular side in the vicinity of the PSB. It is held in place by a complex counterion system involving two charged amino acids, R108 and D238, amongst others. After absorption of a photon, the retinal isomerizes to 13-*cis* inverting the dipole moment vector of the PSB. The negatively charged chloride ion gets pulled towards the retinal in the hL_1 state before it gets dragged over to the cytoplasmic side of the retinal by the flipped dipole moment of the PSB in hL_2[158,163]. Simultaneously, the transition to hL_2 is supposed to switch the accessibility of the chloride ion to the cytoplasm as it was similarly proposed for the proton between the two M-intermediate substates in bR[160,164]. Recovery of the hR ground state is then accompanied by ion release into the cytoplasm, ion uptake from the extracellular medium and the reisomerization of the retinal to all-*trans*[165].

Several infrared studies were focusing on the special role of the two hL substates including steady state light induced difference spectroscopy at cryogenic temperatures and time-resolved methods[158,161,166]. Interestingly, all of the published spectra are different. They have in common that the transition between the two substates is accompanied by changes mostly in the amide I region indicating structural rearrangements of the protein backbone. These changes could reflect the accessibility switch of the chloride ion. The discrepancy between the spectra are most likely due to different measurement conditions, mainly salt concentration and hydration level[167,168]. The latter is extremely important because it can alter the photoreaction dynamics significantly. The drawback of having a well hydrated protein film is the strong infrared absorption of water in the amide I region. Too few photons in this spectral window lead to a drastic decrease of the signal-to-noise ratio which also could account for the inconsistency among the published spectra. The high intensity output of infrared radiation provided by quantum cascade lasers (QCLs) permits to maintain a good signal-to-noise ratio of protein films in the amide I region despite of high hydration levels. It additionally allows to perform transient difference spectroscopy on protein crystals where the switch will also be analyzed.

5.3.1 Isomeric composition in the ground state

The primary photochemical event in hR is retinal isomerization from all-*trans* to 13-*cis*. However, the isomeric composition of the ground state is not homogeneous and hR exhibits a light/dark adaption as it is the case for bR. In the dark, all-*trans* and 13-*cis* retinal are equally present which changes under continuous illumination. Unlike bR, the light-adapted state of hR, which absorbs at 580 nm, still has a remainder of about 20 % 13-*cis* configured retinal. This mixture relaxes back to the dark-adapted state with a long time constant of 165 min determined by Fourier transform Raman spectroscopy[169]. The 13-*cis* form has a blueshifted absorption maximum at around 550 nm and also undergoes a photoreaction but without ion pumping activity[160]. This photocycle misses a L-like state and forms instead a long-lasting slightly redshifted intermediate. Thus, in a time-resolved transient absorption experiment it is important to keep the all-*trans* population on a constant high level which in turn minimizes contamination from the *cis* form.

Resonance Raman spectroscopy is an ideal technique to study the isomeric state of retinal due to its chromophore selectivity. The Raman ground state spectrum of hR membrane patches shown in fig. 5.12 was obtained with a probing laser emitting at 532 nm. Concentrated protein solution containing 2 M NaCl at pH 7 was pre-illuminated with white light for light adaptation and subsequently put in a rotational cuvette. Fast spinning of the cuvette in combination with a photocycle duration on the millisecond timescale ensures that no photoproducts will interact with the probing beam. As a matter of fact, the spectrum obtained under these conditions is in accordance with already published data[170–172]. The C=C stretch mode has a linear relationship with the visible absorption maximum and a wavenumber of 1520 cm^{-1} accordingly matches the ground state absorption of hR. A relatively low frequency of 1633 cm^{-1} for the PSB vibration indicates a weak hydrogen bond to the counterion complex. The fingerprint region, which is sensitive to the isomeric configuration of the retinal, displays two pronounced peaks at 1169 and 1202 cm^{-1} with a small shoulder at 1182 cm^{-1}. It was shown that the two bands are characteristic for an all-*trans* configuration while the latter

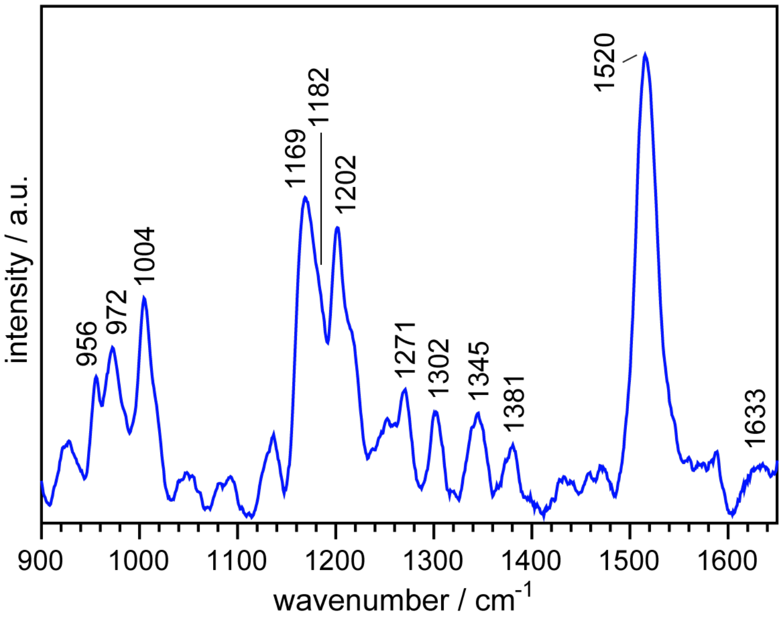

Figure 5.12: Resonance Raman spectrum of ground state hR obtained at 532 nm using a rotational cuvette. The protein was embedded in membrane patches solubilized in 2 M NaCl at pH 7. Sample was pre-illuminated prior to the measurement enriching the all-*trans* population.

vibrational mode is indicative for a relaxed 13-*cis* retinal[110,169]. Due to the distinct blueshift in the visible of the 13-*cis* form, its presence can also be detected via the ethylenic stretch mode at around 1534 $\mathrm{cm^{-1}}$. Such a band is just very poorly pronounced if at all present. It can be concluded that the 13-*cis* population is minor under the applied experimental conditions. The rotation of the cuvette and the 532 nm Raman excitation in fact mimic a flash induced time-resolved experiment and thus a 13-*cis* spectral contamination can be neglected if a similar excitation laser wavelength is used.

5.3.2 Monitoring the switch with infrared spectroscopy

It is proposed that the accessibility switch for the chloride ion takes place during the transition from hL_1 to hL_2. This assumption is mainly based on crystal structures of hR from *Halobacterium salinarum* and *Natromonas pharaonis* where the ion just slightly moves in the hL_1 but crosses the retinal in hL_2/hN in concert with formation of a water channel on the cytoplasmic side of the protein[158,163]. Additionally, visible and Fourier transform infrared (FTIR) spectroscopy found that the two distinct hL intermediates share the same retinal structure but differ in their amide I modes[158,161,165,166]. In other words, the differences between these two states are focused on changes of the protein backbone. Electrophysiological measurements showed that the charge is released after the formation of hL_2[173,174]. All these observations lead to the conclusion that the accessibility of the chloride ion switches during the transition between the two hL substates.

Amide I modes have a frequency around 1660 $\mathrm{cm^{-1}}$ where also water strongly absorbs. In the case of hR, it is important to have a high hydration level in order to maintain its function. This makes an infrared experiment in this region a difficult task. The high intensity output of QCLs permits a time-resolved measurement from nanoseconds to seconds even with high hydration levels at good

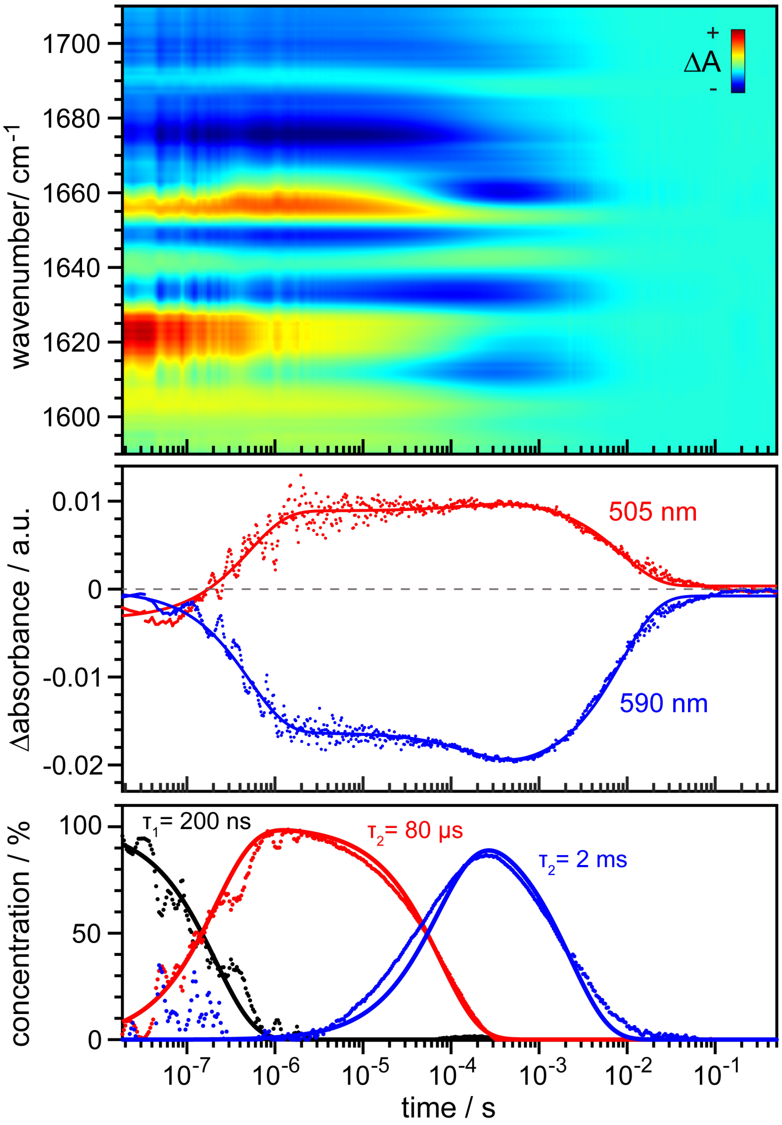

Figure 5.13: Time-resolved absorption spectroscopy on pelleted hR membrane patches. The protein was solubilized in a buffer containing detergent and 2 M NaCl at pH 7. Excitation was with 532 nm with a repetition rate of 2 Hz. **Top panel:** Contour plot of the difference absorption signal in the amide I region. Step size is 1 cm^{-1}. **Middle panel:** Time traces of two characteristic wavelengths. Dots represent raw data and the line is a result of a global fit. Ground state bleach is represented by the negative signal at 590 nm while L state formation can be monitored at 505 nm. **Bottom panel:** Concentration profile of a global fit on the infrared data consisting of three sequential intermediate states. Corresponding time constants are labeled.

signal-to-noise ratios. Membrane patches containing hR were pelleted in solution containing 2 M NaCl at pH 7. After removing the supernatant, hR was sandwiched between two BaF_2 windows and sealed with vacuum grease. This procedure ensured to maintain a sufficient amount of water in the sample. Figure 5.13 shows data recorded in the amide I region (top panel) as well as two characteristic time traces in the visible (middle panel). Formation of the hL intermediates can be monitored via the positive absorption change at 505 nm which is mirrored by the ground state bleach at 590 nm. A predecessor of hL is spectroscopically not directly observable in both traces. The fact that the ground state bleaching signal starts to increase accordingly to the rise of hL suggests that the

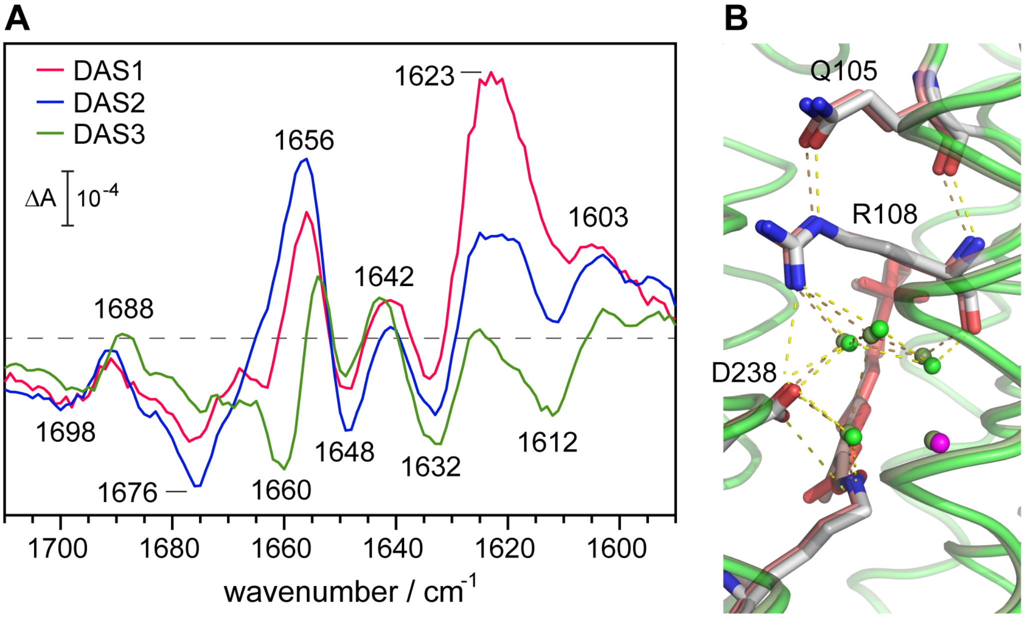

Figure 5.14: A: Decay associated spectra (DAS) associated to the concentration profile of fig. 5.13 bottom panel. Major peak positions are indicated. **B:** Crystal structures of hR ground state (darker colors) and the hL$_1$ intermediate (lighter colors) (PDB: 2JAF and 2JAG)[158]. Waters are in green while the chloride ion is colored in magenta. Hydrogen bonds are indicated by dashed yellow lines.

first photoproduct after isomerization hK has a similar absorption profile as the ground state which cancels in a difference experiment. The ground state bleaching signal clearly carries a biexponential behavior while the time trace at 505 nm still shows the presence of hL. This speaks in favor of two hL substates before hR relaxes back to the ground state. A concluding potential hN state is not detectable with the setup used. It may be that this state is spectrally silent or that hN is in equilibrium with hL$_2$[160].

Infrared data recorded in the amide I region clarifies the existence of two hL substates (fig. 5.13 top panel). Negative absorption changes are colored in blue and are associated with ground state bleaching while positive changes in red are due to emerged intermediate states. During the lifetime of the absorbance change at 505 nm, the infrared spectral signatures changes significantly. Meaning that there are two states with similar retinal structure but different arrangement of the protein backbone. This solidifies the phrasing of these states as hL$_1$ and hL$_2$. Before hL formation, there is another state detectable in the infrared data representing the hK intermediate which is spectrally silent in the difference visible absorption measurement. The decay of hL$_2$ concludes the dataset with a zero line excluding a strictly consecutive hN state with is spectrally silent in the visible. Yet, a possible hL$_2$/hN equilibrium can not be ruled out.

A global fit analysis of the infrared data revealed three distinct spectral components with time constants of τ_1=200 ns, τ_2=80 µs and τ_3=2 ms (fig. 5.13 bottom panel). These values are in accordance with the ones determined with UV/Vis flash photolysis measurements by Varo *et al.* for hK, hL$_1$ and ground state recovery[160]. A work by Dioumaev & Braiman used FTIR spectroscopy from nano- to milliseconds to kinetically resolve the intermediates of hR[175]. They as well obtain similar time constants but ascribed the second decay process to a late bathoproduct termed hK$_L$ (late hK). This assignment was based on a similar spectral profile between the first and second global fit component, in particular for retinal bands. Although the presented data in fig. 5.13 lacks the retinal region, the UV/Vis time trace at 505 nm clearly rises with the second infrared spectral component excluding a hK_L at this stage. Thus, the observed spectra transitions are

$$hR \rightarrow hK \rightarrow hL_1 \rightarrow hL_2 \rightarrow hR \quad .$$

Decay associated spectra (DAS) are presented in fig. 5.14 **A**. These spectra correspond to the decay processes determined by the global fit of fig. 5.13 (bottom panel). The first spectrum, colored in red, resembles a published spectrum of hK obtained at 81 K[176]. In section 5.3.1, the PSB vibration was identified at 1633 cm^{-1}. After photoisomerization, this band shifts to 1621 cm^{-1} as it was observed with Raman spectroscopy for *Natromonas pharaonis*[177,178]. Bands with similar frequencies can be observed in DAS1 can thus be assigned to PSB vibrations of the ground and hK state, respectively. A low PSB frequency hints to weaker hydrogen bond to the counterion complex directly after photoisomerization. Changes in amide I modes around 1660 cm^{-1} reflect structural rearrangements of the protein backbone which are already present in the first photointermediate hK. The negative band at 1698 cm^{-1} was previously assigned to an asymmetric arginine vibration based on its shift in D_2O[179]. Such a high frequency points to an arginine which is buried inside the protein such as R108. This band presumably shifts to 1691 cm^{-1} in hK indicating a change in the hydrogen bonding network of the counterion complex. Later studies questioned this assignment because no deuterium shift was observed for these bands[165,166].

The second DAS looks essentially identical as the first one except from a absorbance decrease at 1623 cm^{-1} and an increase at 1656 cm^{-1} (blue spectrum). The Schiff base vibration in the hL intermediate was found to be at 1642 wavenumbers[172]. Thus, the decrease at 1623 cm^{-1} may be caused by a shift of the PSB band revealing another vibration with similar frequency. This could also explain the unusual high absorbance of this band in hK compared to the amide I modes. Possible candidates for 1623 cm^{-1} vibration in hL_1 are a symmetric arginine vibration or a NH_2 vibration from a glutamine[180]. Q105 is positioned in hydrogen bonding distance to R108 one helix turn up which could indirectly sense the electrostatic changes of the counterion complex. A X-ray structure of hL_1 indeed resolved distinct changes in this region predominantly involving water molecules, R108 and Q105 (fig. 5.14 **B**). A small positive feature at 1642 cm^{-1} could be due to the PSB vibration in hL but this band is just weakly pronounced. Amide I modes just slightly change in shape and the high frequency arginine feature at 1691 cm^{-1} stays constant. Besides a possibly different PSB interaction, no other significant spectral changes occur during the transition from hK to hL_1.

Transition from the second to the third DAS is accompanied by distinct spectral changes (green spectrum). The band at 1623 cm^{-1} vanishes while a new negative peak at 1612 cm^{-1} emerged. It is supposed that the chloride ion moves during the transition from hL_1 to hL_2 from the extracellular to cytoplasmic binding site[158,162,163]. Loss of the negative charge is presumably sensed by the hydrogen bonding network involving R108 and Q105 resulting in the spectral changes below 1625 cm^{-1}. However, the highest frequency feature just downshifts by 2 cm^{-1} to 1688 cm^{-1}. If this is an arginine vibration, it is rather insensitive to its electrostatic environment. The spectral signature in the amide I region changes significantly with a shift from 1656 to 1654 cm^{-1} and a new pronounced negative band at 1660 cm^{-1} appears. This frequency is indicative for an α-helix which undergoes structural

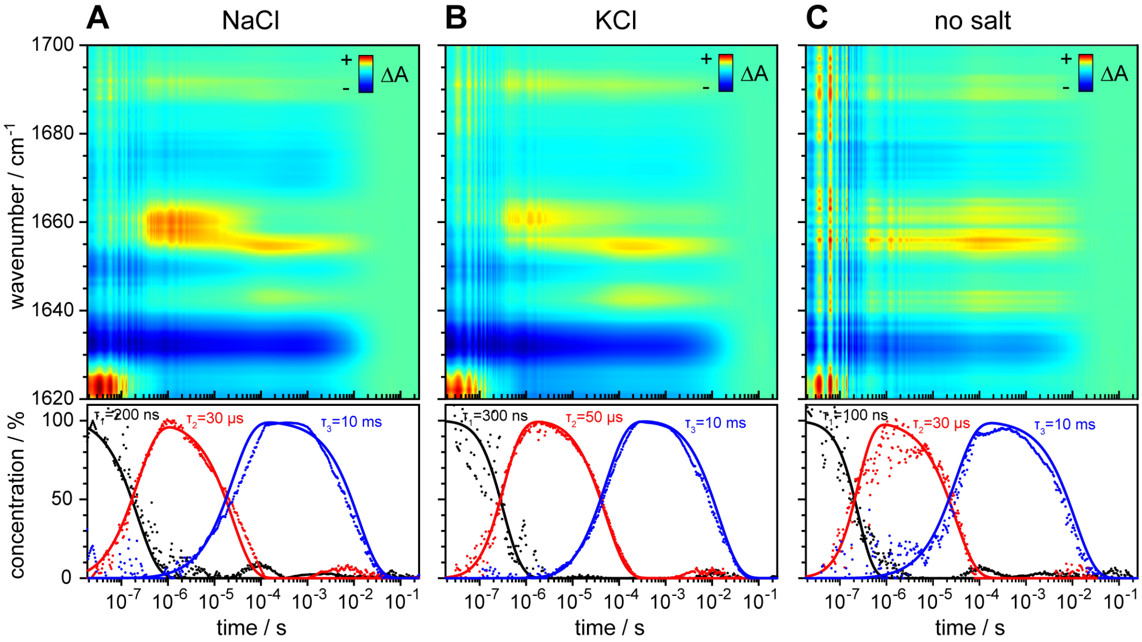

Figure 5.15: Time-resolved infrared spectroscopy (top panel) on hR microcrystals in lipidic cubic phase (LCP) grown under different salt conditions. Excitation was at 532 nm with a repetition rate of 2 Hz. Singular value decomposition (SVD) was applied to enhance signal-to-noise ratio. Step size is 1 cm^{-1}. **A:** 150 mM NaCl. **B:** 150 mM KCl. **C:** no salt in the grow medium. Bottom panel displays the concentration profile of a global fit consisting of a model with three sequential decay processes. Corresponding time constants are labeled.

rearrangements[180]. Kouyama *et al.* found for hR crystals from *Natromonas pharaonis* that chloride ion movement takes place concurrent to deformation of helix F. This leads to a creation of a water wire connecting the retinal binding pocket to the cytoplasm. Therefore, the spectral changes of the amide I region upon hL_2 formation most likely indicate the accessibility switch of the chloride ion to the cytoplasmic medium.

It is interesting to investigate if the same structural rearrangements of the protein backbone also develop when hR is packed in a crystal lattice. To answer this question, the same infrared (IR) experiment as for the pelleted membrane fragments was performed but with microcrystals grown by Gabriela Nass Kovacs from the MPI Heidelberg. The crystals have to remain in the growth medium to maintain the LCP and thus the integrity of the crystal lattice. Here, the QCL approach comes in handy providing a higher density of photons compared to a conventional FTIR setup. Figure 5.15 **A** shows the data obtained with a crystal growth medium containing 150 mM NaCl. A global fit analysis of the infrared data revealed three states where the last process rises faster and decays slower than for solubilized protein. In principle, the lower amount of chloride ions in the growth medium could influence the substrate uptake rate leading a slower decay of the last intermediate[181]. Although the contour plot of the infrared data looks similar to the membrane fragments, the negative band at 1660 cm^{-1} on the later timescale is missing suggesting a missing accessibility switch of the chloride ion. If the protein crystals are functional in terms of pumping activity, the photocycle should be influenced by different salt conditions. Exchanging NaCl with KCl does not result in any spectral nor kinetic changes which could proof that the crystals do pump chloride or are non-functional. The latter seems to be true because even without any salt in the growth medium there is no alteration

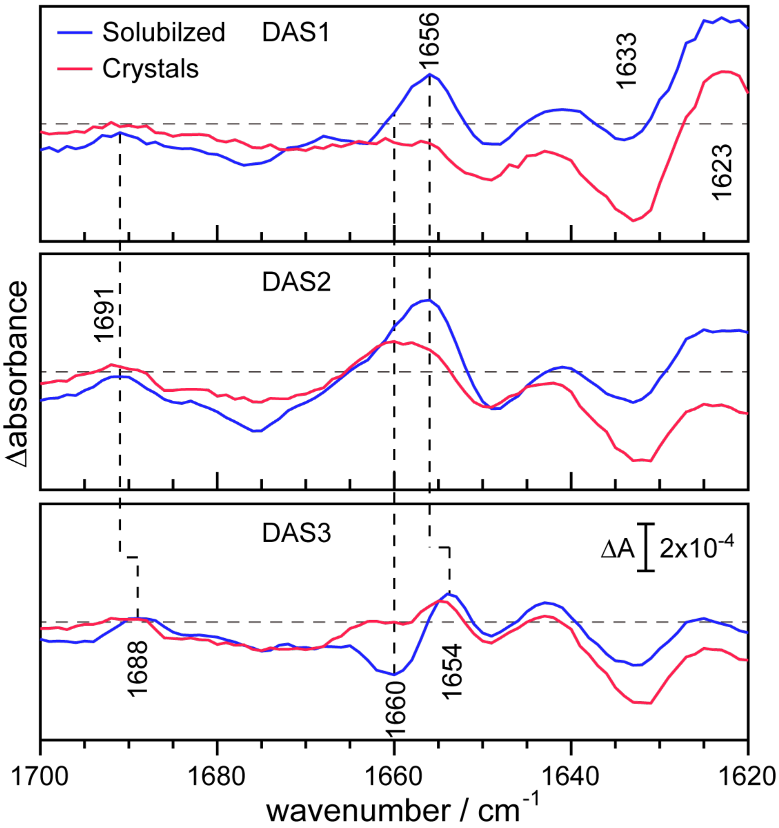

Figure 5.16: DAS for pelleted hR membrane fragments (blue line) and for the microcrystals grown in NaCl (red line). Spectra are not scaled.

of the photocycle (fig. 5.15 **B+C**). This observation in concert with the missing band at 1660 cm^{-1} strongly argue for a missing accessibility switch and consequently for non-functioning hR in the crystal lattice.

Comparison of DAS for pelleted hR membrane fragments and for the microcrystals grown in NaCl permits detailed analysis about possible missing mechanistic processes. (fig. 5.16). The first DAS of the crystals exhibit the PSB shift from 1633 to 1623 cm^{-1}, albeit differences in absorbance, pointing to a similar retinal environment in hK. The higher frequency feature presumably due to R108 is less pronounced if at all present. Significant differences arise in the amide I region where the positive band at 1656 cm^{-1} observed for pelleted membrane fragments is missing indicating that the mediation of photoisomerization to early changes of the protein backbone is hampered. Despite of this missing structural step, the second spectra (hL_1) looks essentially as the one for solubilized hR with an emerged broad feature at 1660 cm^{-1} but still lacking absorbance at 1656 cm^{-1}. Missing structural rearrangements prolong to the last spectrum, corresponding to hL_2, where the negative feature at 1660 cm^{-1} is clearly absent. Concurrently, the higher frequency feature at 1691 cm^{-1} has vanished. Overall, these results argue for a too rigid protein environment in the crystal lattice of hR which prevents structural rearrangement needed for a proper functioning of the protein. This is in line with the salt independence of the infrared data in fig. 5.15.

5.3.3 Conclusion

This section has demonstrated that an isomerization of the retinal can trigger rearrangements of the protein backbone eventually leading to its function. The high intensity output of QCLs permitted to record transients in the amide I region despite of high hydration levels needed for proper chloride pumping in hR. In concert with time-resolved UV/Vis spectroscopy, hK, hL_1 and hL_2 states were identified. Spectral analysis of amide I modes showed that the accessibility switch of the chloride ion is accompanied by a α-helical deformation in agreement with crystallography data[158,163]. In particular, a negative band at $1660\,\mathrm{cm}^{-1}$ in hL_2 is characteristic for this process (fig. 5.14). Performing the same experiment on hR microcrystals grown in 150 mM NaCl revealed significant differences in the amide I region compared to pelleted membrane fragments. It seems that the rigid crystal lattice prevents structural movements concluding in a missing $1660\,\mathrm{cm}^{-1}$ band in the hL_2 intermediate. Without a switch of chloride ion accessibility to the cytoplasmic medium, ion pumping is prohibited. This observation is solidified by the similarity of the infrared datasets with and without salt in the growth medium (fig. 5.15).

5.4 Combining serial X-ray crystallography & time-resolved spectroscopy on KR2

This project was motivated by Petr Skopintsev from the Paul-Scherer Institute in Switzerland and is currently under revision:

Skopintsev, P., **Ehrenberg, D.**, Weinert, T., James, D., Kar, R., Johnson, P., Ozerov, D., Furrer, A., Martiel, I., Dworkowski, F., Nass, K., Knopp, G., Cirelli, C., Arrell, C., Gashi, D., Mous, S., Wranik, M., Gruhl, T., Kekilli, D., Bruenle, S., Deupi, X., Schertler, G., Benoit, R., Panneels, V., Nogly, P., Schapiro, I., Milne, C., Heberle, J. & Standfuss, J. Femtosecond to millisecond structural changes in a light-driven sodium pump. *Nature - under revision* (2020)

I helped to secure a constant supply of sample during the beamtime. I did the time-resolved spectroscopic experiments and contributed to interpretation and writing the manuscript.

It was long believed that light-activated ion transporting rhodopsins can be classified into three functional groups: proton pumps, chloride pumps and ion channels. While channels transport ions along an electrochemical gradient, a pumping mechanism requires an accessibility switch for the ion which prevents its backflow. In proton pumps, as for example in bacteriorhodopsin (bR), the proton of the Schiff base itself takes part in the pumping process (see section 5.1). For other ion pumps however, the substrate has to overcome the positive charge of the protonated Schiff base (PSB) which is energetically feasible if the ion is negatively charged. In that case, the negatively charged substrate can contribute to the counterion complex which stabilizes the PSB. Photoisomerization eventually flips the dipole moment of the N–H bond which drags the substrate across the retinal as shown for halorhodopsin (hR) (see section 5.3). But if the substrate carries a positive charge, it will experience electrostatic repulsion from the PSB which in turn makes an ion transfer unfavorable. Therefore, it was no surprise to the rhodopsin community that no non-proton cation pumps were found.

In 2013 Inoue *et al.* discovered the first light-driven Na^+ pump in a marine bacterium called *Krokinobacter eikastus*[183]. This addition to the family of functional rhodopsin groups triggered high interest in the actual transport mechanism. KR2 is nowadays probably the most intensively studied rhodopsin. From an electrostatic point of view, the positively charged Na^+ ion cannot serve as a counterion and is consequently not bound in direct vicinity to the PSB in the ground state of KR2. This was concluded from UV/Vis spectroscopy where the visible absorption maximum does not shift in the presence or absence of sodium. However, Fourier transform infrared (FTIR) difference spectra of a sodium to potassium exchange indicated structural rearrangements of the protein backbone as well as changes in retinal vibrational bands[183]. Based on crystal structures and electrophysiology measurements, an intracellular ion uptake cavity was proposed which extends up to Q123[184,185].

As the substrate is not acting as a counterion, a negatively charged amino acid side chain has to take this role. By several variations of amino acid side chains, UV/Vis spectroscopy and electrophysiology identified the aspartate D116 as the counterion to the PSB[183]. Just recently, a new study found that

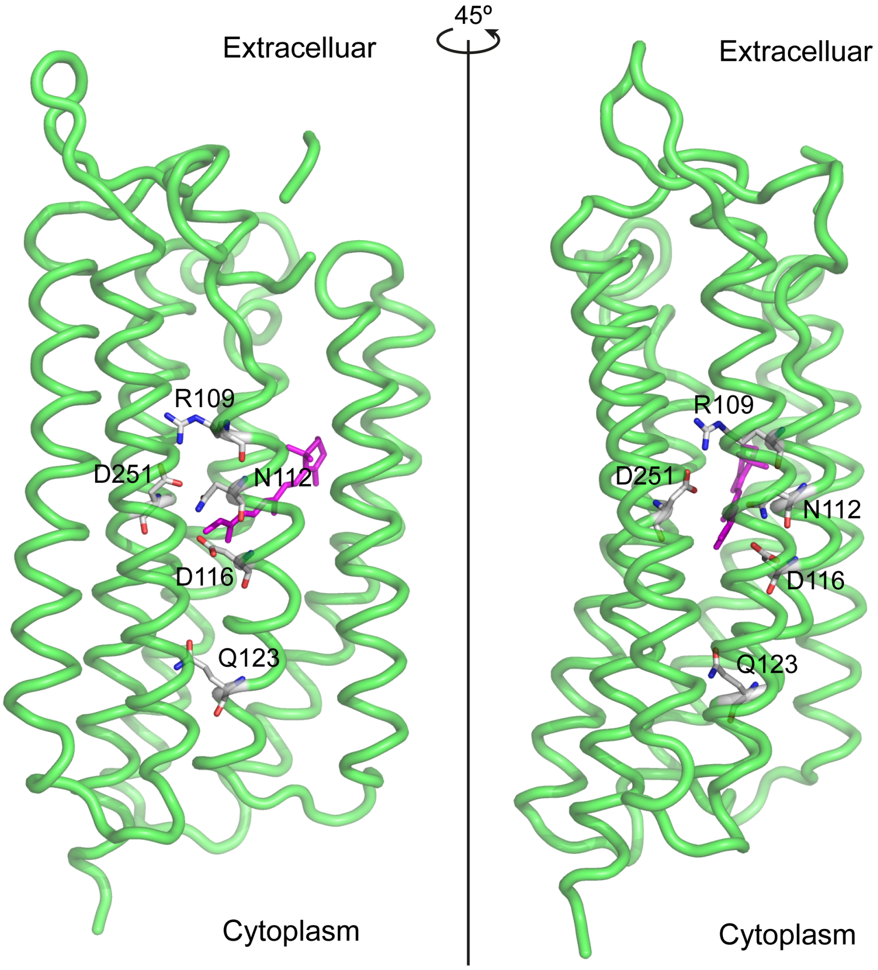

Figure 5.17: Crystal structure of the outward directed sodium pump *Krokinobacter eikastus* rhodopsin 2 (KR2) (PDB: 6RF6)[182]. The retinal is colored in magenta and important amino acid residues are indicated. D116 acts as the counterion and proton acceptor of the PSB but also R109 is assumed to be part of a more expanded counterion complex. Q123 is thought to play a role in initial sodium ion binding while the ion is supposed to be coordinated by N112 and D251 in the O intermediate.

also R109 influences the electronic excitation of the retinal in the ground state along with an alteration of photocycle kinetics[186]. It seems that the stabilization of the PSB is managed by a more complex system of amino acid side chains (fig. 5.17).

In order to pump the positively charged Na^+ ions, the Schiff base has to deprotonate at a certain point during the pumping mechanism to diminish the electronic repulsion. Indeed, a blue shifted M intermediate was found in the photocycle indicating a deprotonated Schiff base. D116 was proposed as the acceptor of the Schiff base proton due to the lack of M state formation upon its variation to an asparagine[183]. A first model, where the protonated D116 flips away from the Schiff base to free up space for the sodium ion, was later questioned by new crystallography data taken from crystals under different conditions[182,184,185].

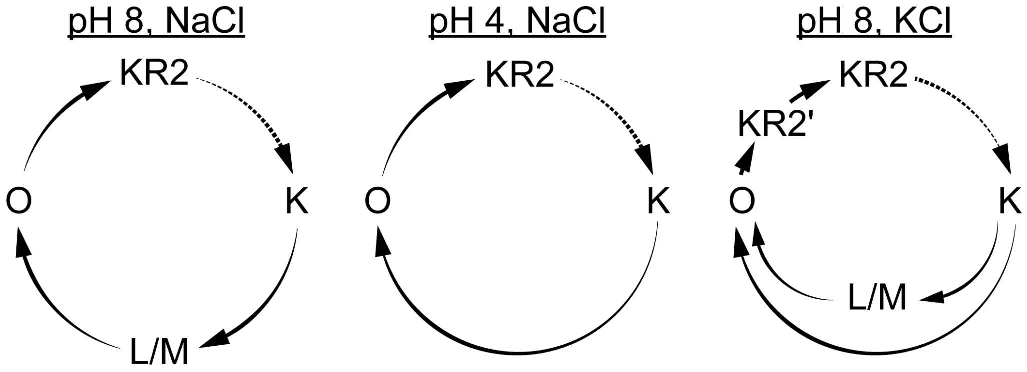

Figure 5.18: Photocycles of KR2 under different conditions adapted from[183,192]. At pH 8, KR2 pumps sodium if ions are present. Under acidic pH the acceptor of the Schiff base proton gets protonated inhibiting sodium pumping activity. If no sodium ions are present at neutral pH, two competing processes arise of which the one with an L/M equilibrium is assumed to take account for proton pumping.

KR2 shows no light/dark adaptation and has a 100 % all-*trans* configured retinal in the ground state[187]. Upon photoisomerization, the pumping process takes place via a K, L, M and O intermediate. In contrast to bR, the intermediates L and M are strongly in equilibrium with each other (fig. 5.18). This means that these two states cannot be clearly distinguished in a time resolved experiment (denoted as L/M for an equilibrium between L and M)[183,188]. Deprotonation of the Schiff base occurs during M state formation permitting the sodium ion to pass the electrostatic barrier. Subsequently, a sodium ion is taken up from the cytoplasm during decay of the M state (i.e. O state formation) while the ion on the extracellular side is released during O state decay[189]. FTIR and resonance Raman spectra of the O intermediate show distinct marker bands of a 13-*cis* configuration of the retinal leaving the transition from O to the ground state as the reisomerization step back to all-*trans*[190,191].

Changing the pH or the sodium concentration strongly influences the function and photocycle kinetics of KR2. Under acidic conditions the counterion D116 gets protonated resulting in a redshift of the visible absorption maximum[184]. With a protonated proton acceptor the Schiff base cannot deprotonate inhibiting the formation of the M intermediate (fig. 5.18). Sodium pump activity is abolished under these conditions due to the persisting electrostatic repulsion between the PSB and the positively charged sodium ion. The photocycle under these conditions exhibits therefore just a prolonged K and a weakly pronounced O like state which decays slightly faster as under neutral pH. If KR2 pumps protons instead of sodium ions under acidic pH is still a matter of debate[182]. Exchanging sodium to potassium results in a constant photocurrent which is not dependent on the potassium concentration indicating that potassium ions do not contribute to the photocurrent but rather protons[183]. The photocycle of KR2 in KCl is poorly understood and it seems that two competing processes are taking place[183,192]. One process includes a M intermediate implying a deprotonated Schiff base. It is reasonable that this deprotonation step is necessary for proton pumping because of the same electrostatic repulsion as it is the case for the positively charged Na^+ ions. Same holds true for bR where the M state is a crucial step for proton pumping. The other reaction is similar to the photocycle under acidic conditions where a deprotonation of the Schiff base is omitted. Interestingly, the relaxation back to the ground state of both reactions precedes a state sharing the same absorption profile in the visible as the ground state with a slightly smaller extinction coefficient. This KR2' (KR2 prime) state subsequently decays in seconds to the ground state taking considerably longer than the sodium photocycle[183,192].

Under physiological conditions KR2 forms pentamers in lipids[193]. It was demonstrated that pentameric KR2 shows sodium pump activity. If KR2 also pumps sodium ions as a monomer is not yet clear. Kovalev *et al.* raised this question by solving the crystal structure under different pH values and found that two conformations of the Schiff base cavity exist, a compact and an expanded form. These two conformations mostly differ in the region between N112 and D251 which is proposed as the transient sodium ion binding site after passing the retinal Schiff base[182,184,194]. They speculate that monomers always take a compact cavity conformation which would prohibit sodium pumping. Crystals grown under acidic pH yields monomers of KR2 and therefore will be non functional even if soaked to physiological pH. This conclusion is solely based on the ground state crystal structures missing electrophysiology measurements and in particular experiments on the structural dynamics of monomeric KR2. Additionally, the putative sodium binding site between N112 and D251 has still to be explicitly identified.

5.4.1 Structural dynamics of monomeric KR2

Infrared spectroscopy is a useful technique to trace structural changes after photoexciation. Conducting a conventional FTIR experiment on proteins in the crystalline phase is a challenging task as mentioned in section 5.3. A QCL with a high intensity output is a suitable probing light source for spectroscopy on protein crystals, in particular for microcrystals which are used for time-resolved X-ray experiments using a free electron laser (FEL). To be able to draw conclusions about structural rearrangements and functionality of KR2 microcrystals, a dataset of detergent solubilized protein under sodium pumping conditions is needed for comparison. An initial salt concentration of 7.5 mM NaCl before drying the KR2 solution was chosen because drying will increase the concentration by 20 to 30 fold[195]. Transient absorption changes in the infrared were recorded in a wavenumber range from 1510 up to 1690 cm^{-1} covering the C=C stretch of the retinal and the amide I region. Thus, the infrared spectral window yields information about changes of the protein backbone as well as indirectly about shifts of the visible absorption maximum via the interconnection of C=C stretching vibration to the extended π-electron system. However, a corresponding dataset of transient changes in visible absorption on the same sample was additionally recorded allowing a direct correlation of emerging intermediate states with structural changes of the protein detected with infrared spectroscopy.

Figure 5.19 shows the datasets of absorption changes in the infrared and in the visible spectral region (top and middle panel, respectively) as contour plots spanning the same time frame. Negative absorption changes are colored in blue and are associated with ground state bleaching (signals vanishing due to the transition from the ground state to photoproducts) while positive changes in red are due to emerged intermediate states. The UV/Vis data (middle panel) exhibit an early red shifted intermediate with a rise time beyond the time resolution of nanoseconds. This early intermediate is indicative of a K state with an 13-*cis* isomerized retinal which persists long with a time constant of about 10 µs. The decay of the first photoproduct is followed by a rise of a blue shifted intermediate representing a species with a deprotonated Schiff base. For bR this M intermediate is

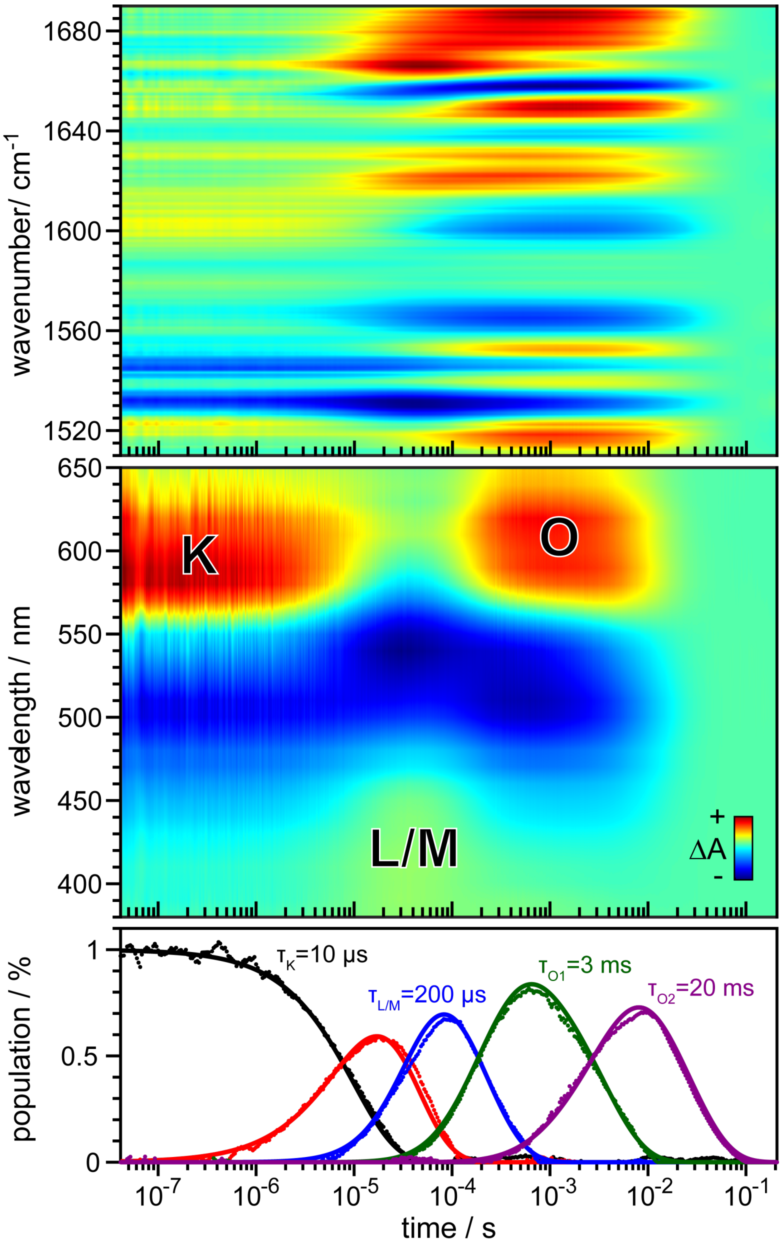

Figure 5.19: Time-resolved absorption changes in the infrared (top panel) and in the visible region (middle panel) of detergent solubilized KR2 sandwiched between BaF_2 windows. Spectral sampling of the quantum cascade laser (QCL) was 1 cm^{-1}. Excitation was achieved by a laser emitting at 532 nm with a repetition rate of 2 Hz. Salt concentration before drying was 7.5 mM NaCl and the film was rehydrated using a 40 % glycerol to water (v/v) mixture. The UV/Vis data exhibit intermediate states as indicated. The bottom panel displays a fitted concentration profile based on the infrared data using a sequential unidirectional model consisting of five states. The two exponentials for the L/M intermediate take account for the equilibrium between the two. In the case of the O state, the two exponentials denote two subspecies referred to as O_1 and O_2.

clearly pronounced in a time-resolved experiment while for KR2 the positive signal is weak. Possible explanations are that the M intermediate in KR2 has a low extinction coefficient or that M is in strong equilibrium with a preceding L intermediate which absorbs close to the ground state. Reconstructed absolute absorption spectra indeed show a contribution of a L state to the corresponding L/M equilibrium spectrum[183]. Such an equilibrium with L could also be true for the K state explaining its late decay in microseconds but was not yet identified by UV/Vis spectroscopy. Here, the K state absorption also does not carry any L-like character. In contrast to the previously occurring L/M equilibrium, the red shifted O state is clearly pronounced and exhibits single species character. Ground state recovery takes place during O state decay concluding the dataset with zero difference absorption.

The infrared absorption difference data in the top panel of fig. 5.19 exhibit a similar kinetic profile as in the visible. The correlation of these two datasets clearly demonstrates that strong changes in the amide I region from 1640 to 1670 cm^{-1} start to arise with the formation of the L/M equilibrium. During the transition to the O state, the amide I signature changes which then decays concurrent with the O intermediate. A global fit with a model of five unidirectional sequential intermediate states is in agreement with the UV/Vis data (fig. 5.19, bottom panel). The first state corresponds to the K state while the following two states reflects the L/M equilibrium. The last two states appear along the O state and are consequently framed as O_1 and O_2. These two subspecies do not necessarily reflect distinct different intermediate species and it may well be that the O intermediate just does not decay in a monoexponential manner (stretched exponential).

The retinal absorption of visible radiation depends on the amount of electron delocalization (π-electron system) along the polyene chain. Same holds true for the coupled C=C vibrations which permits a direct comparison of the infrared with the UV/Vis data. Figure 5.20 **A** top panel shows identified ethylenic stretch bands based on visible kinetics (bottom panel). The ground state bleaching signal is at 1531 cm^{-1} matches the visible absorption at λ_{max} = 525 nm[196]. An early positive signal at 1520 cm^{-1} decays with the same time constant as the trace at 620 nm in the visible. The shift to a lower frequency translates into a redshift in the visible corresponding to the K state. In a stimulated Raman spectroscopy experiment an K/L (K in equilibrium with L) state was found on a nanosecond timescale with characteristic C=C stretching vibrations at 1519 and 1547 cm^{-1}[188]. While the K state frequency is in accordance, an L associated band could not be identified. Therefore a pure K state is considered.

The ground state bleach follows a similar kinetic course with a pronounced negative feature around 30 µs in both datasets. This minimum correlates with the positive signal at 420 nm corresponding to the L/M equilibrium. The ground state bleach signal in the infrared at 1531 cm^{-1} also exhibit this negative feature at the same time but a kinetically corresponding positive signal could not be identified. This may be explained by the equilibrium between L and M but also by the intrinsic lower dipole moment of retinal with a deprotonated Schiff base[197]. Since the O intermediate is also redshifted compared to the ground state absorption, its C=C stretch frequency should be similar as for the K state. Already present in the time trace at 1520 cm^{-1} but more pronounced at 1516 cm^{-1}, the positive signal decays in correspondence with the later positive signal at 620 nm in the visible.

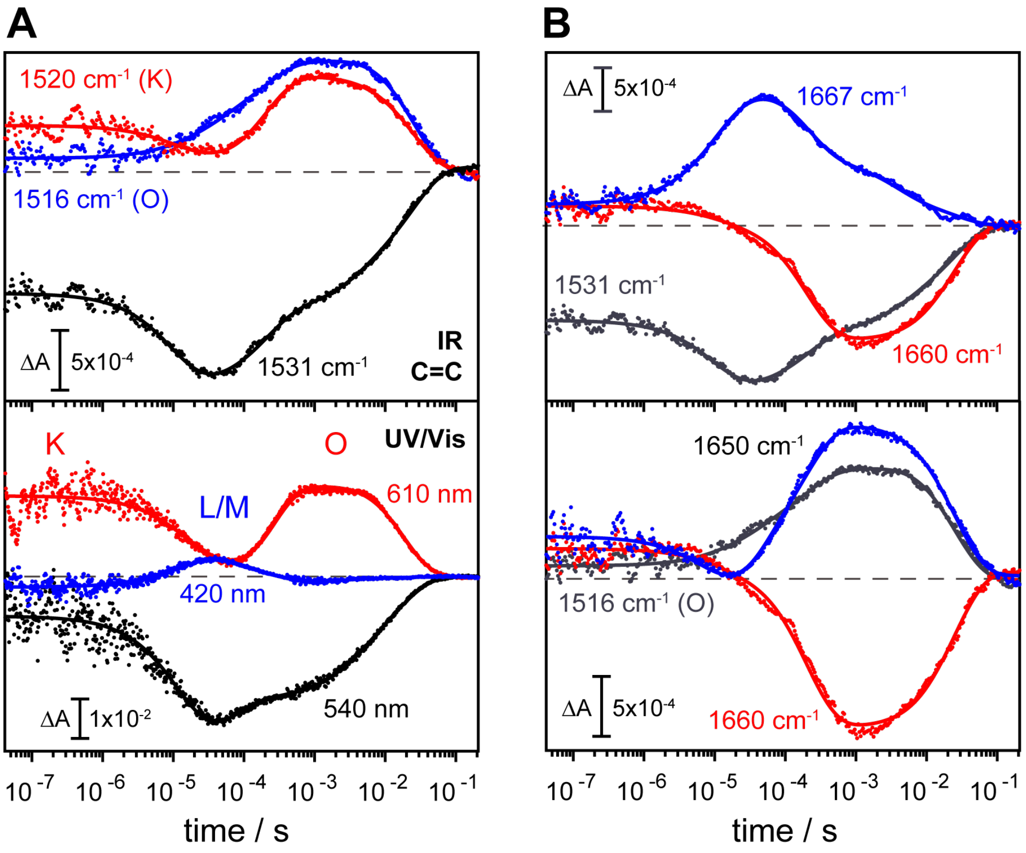

Figure 5.20: Transient absorption changes of detergent solubilized KR2 of characteristic bands (slices of fig. 5.19). Raw data is represented by dots while the line is a result of a global fit analysis. **A:** Comparison of C=C stretch vibrations (top panel) with signatures in the visible (bottom panel). Intermediate states are indicated. **B:** Changes of the amide I vibrations corresponding either to the L/M equilibrium tracked via the ground state bleach signal at 1531 cm^{-1} (top panel) or to the O intermediate represented by the C=C stretch trace at 1516 cm^{-1} (bottom panel). Marker bands for the intermediate states are colored in grey.

Summarized, the C=C stretch frequencies of the K and O states could be identified at 1520 and 1516 cm^{-1}, respectively. Although such an assignment is missing for the L/M equilibrium, this state can be traced via the negative feature in the time trace of the ground state bleach at 1531 cm^{-1}.

With these spectroscopic markers at hand it is possible to assign the amide I changes to either the L/M or to the O state (fig. 5.20 **B**). Taking the marker feature for the L/M equilibrium in the ground state bleach signal at 1531 cm^{-1}, the pronounced positive signal at 1667 cm^{-1} can be assigned to this transition (top panel). A kinetically corresponding negative signal is not apparent because the negative amide I band at 1660 cm^{-1} shows a different progression more similar to the evolution of the O state traced via the 1516 cm^{-1} band (bottom panel). Another band with the same kinetic profile as the O state can be found at 1650 cm^{-1} experiencing a positive change in absorption. These assignments suggest that the amide I vibration at 1660 cm^{-1} of the ground state first shifts to higher wavenumbers in the L/M equilibrium before shifting to a lower frequency in the O intermediate. A frequency of 1660 cm^{-1} is characteristic for an α-helical component whose hydrogen bond network first weakens (upshift in frequency) with subsequent reorganization and stabilization of the hydrogen bonds reflected by the downshift to 1650 cm^{-1}[192,198].

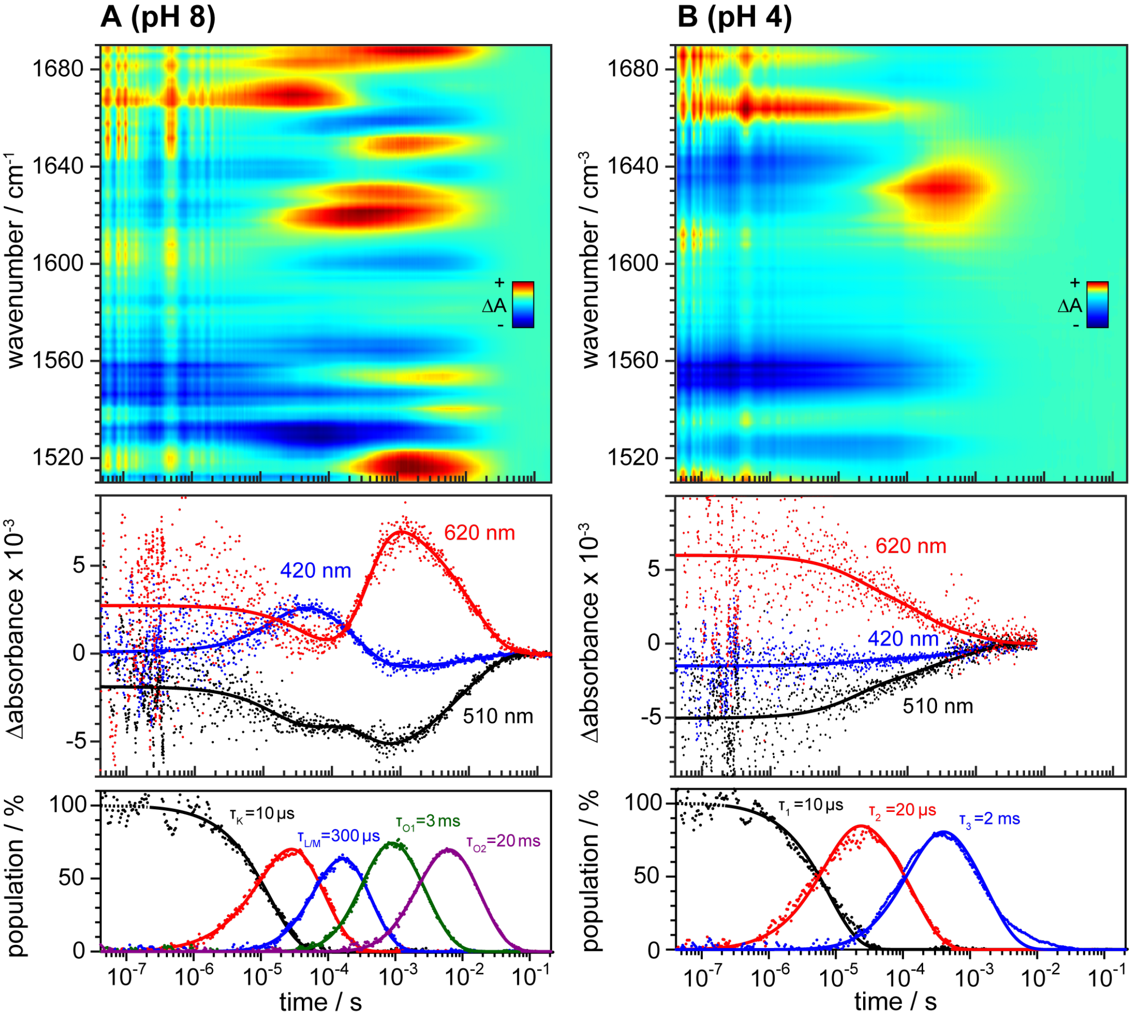

Figure 5.21: Time resolved absorption spectroscopy on KR2 microcrystals grown at pH 4 (**A**) and soaked to pH 8 (**B**) with 150 mM NaCl. Changes in the infrared are detected with a QCL as probing light source with a spectral sampling of 2 cm^{-1} (top panel). An excitation laser emitting at 532 nm at 2 Hz was used. Presented data were treated by singular value decomposition (SVD) to increase signal-to-noise ratio. Corresponding transient absorption changes in the visible are represented by three characteristic wavelengths at 420, 510 and 620 nm associated with the L/M equilibrium, the ground state bleach and the redshifted intermediates, respectively. Raw data is represented by dots while the line is a result of a global fit analysis. Repetition rate was 2 Hz for pH 8 and 20 Hz for pH 4. The high noise in particular at beginning of the data recording is due to light scattering on the microcrystals. Bottom panel displays a fitted concentration profile based on the infrared data using a sequential unidirectional model. At the start of the recording there is a laser scattering artifact which was identified as a distinct state in the global fit analysis. For a better representation, this artifact state was summed up with the subsequent K intermediate represented as dotted lines.

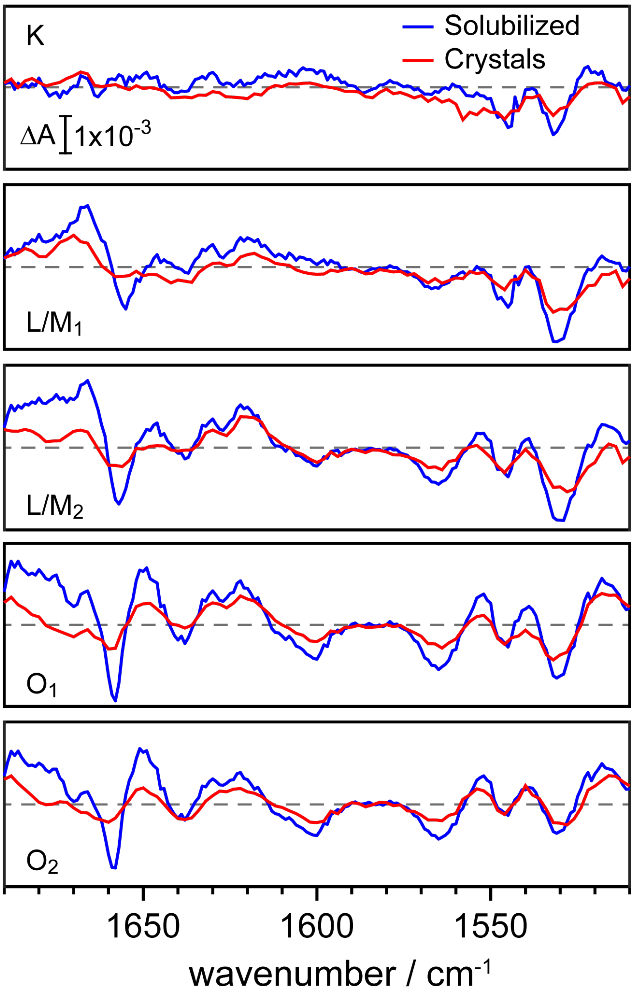

Figure 5.22: Decay associated spectra (DAS) of detergent solubilized KR2 (blue) and microcrystals grown at pH 4 with soaking to pH 8 (red). The spectra correspond to the fit of the infrared data shown in the bottom panels of fig. 5.19 and fig. 5.21. For solubilized KR2, the spectral sampling of the QCL was 1 cm^{-1} and the DAS were obtained from raw data. For measurements on the crystals a spectral sampling of 2 cm^{-1} was chosen and the DAS were constructed out of SVD treated data for noise reduction. Spectra are not scaled.

Data recorded on KR2 microcrystals grown at pH 4 and soaked to pH 8 with 150 mM NaCl look essentially the same as for detergent solubilized (fig. 5.21 **A**). Representative time traces in the visible region at 420, 510 and 620 nm show the evolution of intermediates during the photocycle (middle & bottom panel). A long lasting K state is formed beyond the time resolution of the measurement. This state decays into a blue shifted L/M equilibrium on the microsecond timescale with subsequent formation of a red shifted O intermediate. Ground state recovery is completed with a time constant of 100 ms. Global fit analysis yields the same time constants for the intermediates as for detergent solubilized KR2 except from a slightly slower L/M decay. Apart from the same kinetic behavior of the crystals compared to the detergent solubilized protein, the spectra associated with the fitted concentration profile (DAS) resemble each other as shown in fig. 5.22. The same spectral intermediates are formed and band positions and intensities mostly match excluding the amide I region between 1640 and 1680 cm^{-1}. Although the spectral features are similar, intensities of these bands are less in the case of microcrystals. This points to a more rigid protein environment in the crystalline

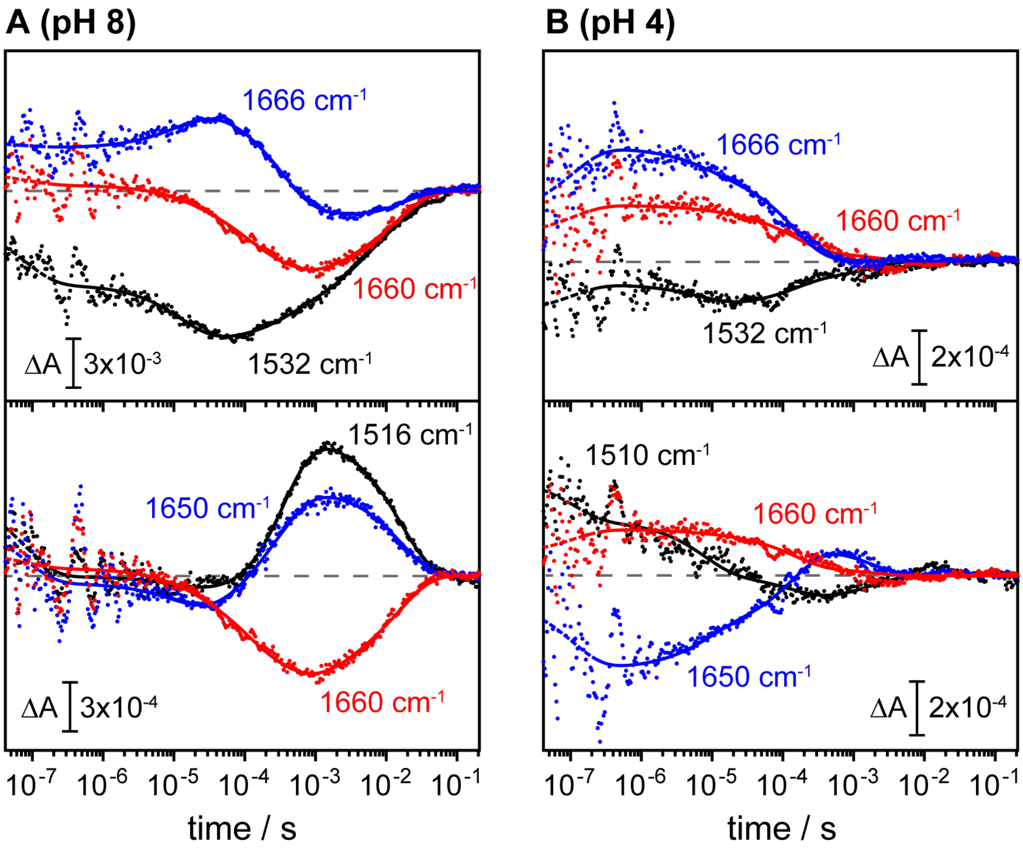

Figure 5.23: Spectral evolution of previously assigned marker bands (see fig. 5.20) for the L/M equilibrium and the O intermediate for KR2 microcrystals at pH 8 (**A**) and pH 4 (**B**). Raw data is represented by dots while the line is a result of the global fit analysis. A dashed line indicate the duration of the laser artifact (see fig. 5.21).

phase impairing structural rearrangements of the protein backbone. Another explanation could be differences in water content or lipidization[115]. However, it seems that these constraints do not alter photocycle kinetics suggesting a functional KR2 in the crystal lattice.

In contrast, KR2 microcrystals at pH 4 without the soaking procedure undertake a completely different reaction pathway (fig. 5.21 **B**). Looking at the changes in the visible region, a first red shifted K state is formed (middle panel). The decay of this first photoproduct does not result in a blue shifted L/M state as at pH 8 but rather in another red shifted intermediate with decreased extinction coefficient as indicated by the intensity decrease at 620 nm. This second red shifted O like intermediate decays bi-exponentially back to the ground state with a time constant of 2 ms (bottom panel). At pH 4, it is assumed that the counterion is protonated preventing deprotonation of the Shiff base and therefore formation of a blue shifted M intermediate is inhibited[184]. The spectral signatures at pH 8 and pH 4 for the K intermediate are similar except of a downshift of the C=C stretch vibration at pH 4. The exact position is not resolved due to the limitation of 1510 $\mathrm{cm^{-1}}$ as lower wavenumber bound of the QCL. This indicates that the photoisomerization is not significantly affected by the low pH. Formation of the O like intermediates at pH 4 is accompanied by the disappearance of most of the bands in the infrared. There are no changes in the amide I region involved in this transition and there is also no C=C stretch band associated. But a pronounced positive absorption change at 1632 $\mathrm{cm^{-1}}$ accompanies the rise and decay of the O intermediates (fig. 5.21 **B**).

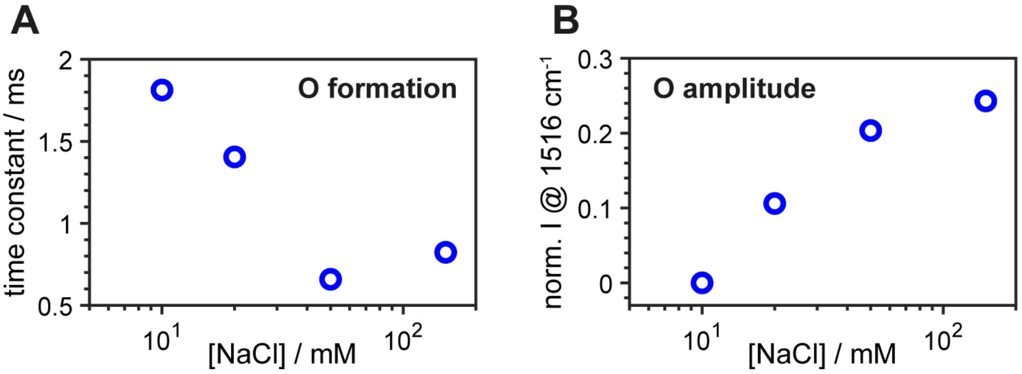

Figure 5.24: Dependence of the O intermediate on the sodium concentration monitored via the absorption changes at 1516 cm^{-1}. **A:** Obtained time constant for a fit of the time trace with 3 connected exponentials where the second exponential corresponds to O state formation. **B:** Amount of O state formation estimated by normalizing the amplitude to the ground state bleach signal.

The kinetic evolution of the infrared marker bands with their correlated amide I changes for the L/M equilibrium and the O intermediate determined for solubilized protein in fig. 5.20 is similar in the case of crystals soaked to pH 8 (fig. 5.23 **A**). Only the time trace at 1666 cm^{-1} experiences a different evolution during the O state. At pH 4, all of these bands exhibit a different kinetic behavior with no apparent correlation to O state formation. It can be concluded from these two datasets that the crystals react to pH alterations as solubilized KR2 (fig. 5.18). More importantly, the soaking of the crystals to pH 8 resulted in the same spectroscopic dynamics as for rehydrated protein film.

It is assumed that sodium uptake and release take place concurrent to the rise and decay of the O intermediate, respectively[199]. If this also holds for monomeric crystalline KR2, the kinetics of the O state should depend on the sodium concentration[189]. Figure 5.24 shows O state characteristics of microcrystals soaked to pH 8 at different sodium concentrations. It has to be noted that the soaking time was kept minimal to speed up the experiment. The evolution of the O intermediate can be monitored via the infrared band at 1516 cm^{-1} (see fig. 5.20). The time trace was fitted with three connected exponentials taking account for ground state depletion, O state formation and decay (fig. 5.24 **A**). Clearly, the M state decay/O state formation is accelerated with higher sodium concentrations as reported by Kato *et al.* for KR2 reconstituted into lipids[189]. The amount of O state formation can be estimated by normalizing its peak height at 1516 cm^{-1} to the ground state bleach signal (fig. 5.24 **B**). At 1 mM no positive signal was observed indicating that no O intermediate is formed. But with increasing sodium concentration, positive signals arise showing that not just the decay of M is dependent on the salt concentration but also the amount of O states being formed. These findings strongly argue for a sodium ion uptake during O state formation in the microcrystals grown at pH 4 and soaked to pH 8. It seems that the monomeric compact conformation found by Kovalev *et al.* is either not the conformation of the crystals under investigation or that the compact conformation is also capable of transiently binding a sodium ion in the O intermediate.

5.4.2 Identifying the transient sodium binding site

In contrast to chloride ion pumps as hR, the sodium pump KR2 does not bind a sodium ion close to the retinal Schiff base in the resting state[183]. A pumping mechanism in microbial rhodopsins usually is composed of an initial photon absorption leading to an isomerization of the retinal. Subsequently, ion translocation occurs followed by a reaction step where the accessibility of the ion is switched preventing ion backflow (IST model[200]). To recover the initial state these steps have to be reversed but in which order all these steps occur depends on the function of the protein. This means for KR2, that there has to be at least a transient sodium ion binding site while the switch take place[199]. Because of the acceleration of O state formation upon increasing sodium ion concentration, the ion is supposed to be transiently bound in the O intermediate after passing the retinal Schiff base (fig. 5.24). It was proposed by Gushchin *et al.* on the basis of resting state crystal structures that D251 is part of the sodium coordination while a flip of N112 leads to an expansion of the Schiff base cavity[201]. To clearly locate the transient binding site, the O state has to be trapped. Alternatively, time resolved X-ray crystallography can provide structural information over time and in principle resolve the ion translocation. Despite of the fact that the latter experiment is very challenging, the electron density of a water molecule and a sodium ion is essentially the same. Hence, it is hard to distinguish these two in an electron density map. Infrared spectroscopy is a very sensitive technique on an atomistic level and can help to pinpoint where the sodium ion is bound during the O intermediate in KR2.

Petr Skopintsev from the Paul Scherrer Institut in Switzerland succeeded to conduct such a time resolved X-ray experiment at the SwissFEL in Villingen. A crystal structure at 1 ms, corresponding to an early O intermediate (see fig. 5.21), shows an appearance of electron density fitting to a water molecule or sodium ion between N112 and D251 (fig. 5.25). The coordination of this electron density

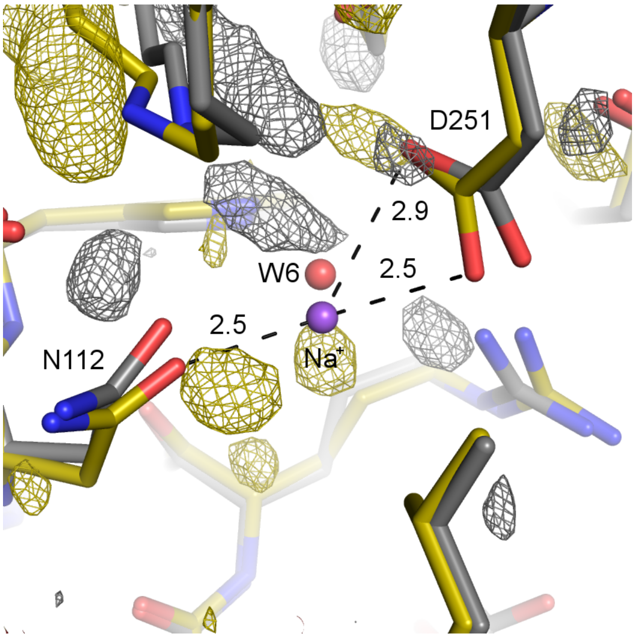

Figure 5.25: Crystal structure of the transient sodium binding site in the O state at 1 ms colored in olive. Ground state structure is colored in grey and the sodium ion is violet. Distances are indicated in angstroms. Data was recorded together with the group of Jörg Standfuß at the SwissFEL.

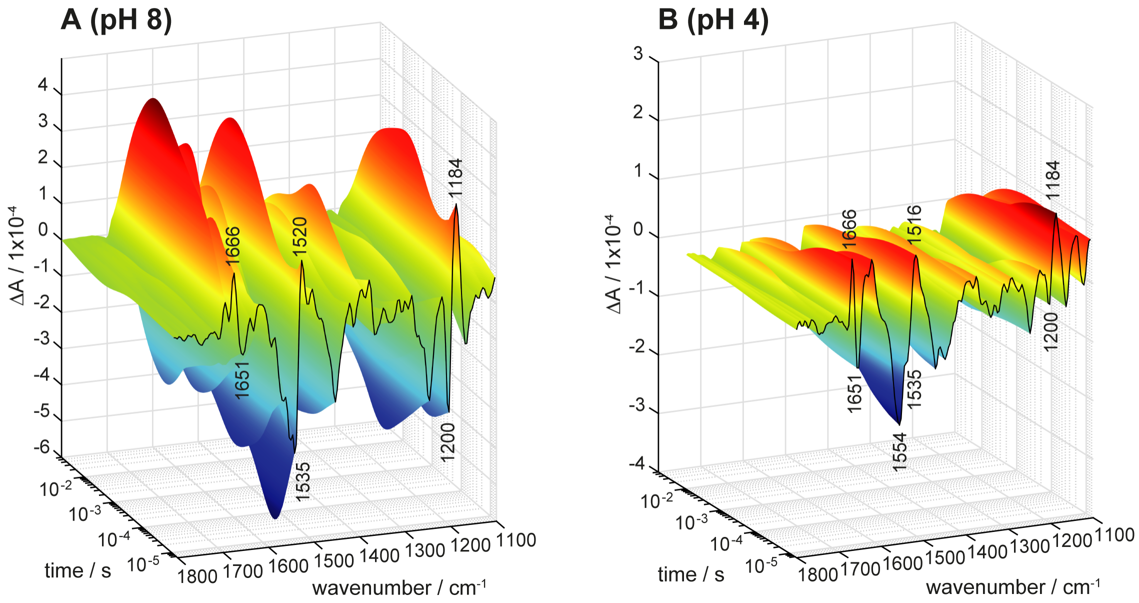

Figure 5.26: 3D representations of FTIR step scan data recorded of detergent solubilized KR2 at pH 8 (**A**; repetition rate 2 Hz) and at pH 4 (**B**; repetition rate 3 Hz). Excitation was achieved by a laser emitting at 532 nm. Salt concentration before drying was 7.5 mM NaCl and the film was rehydrated using a 40 % glycerol/water (w/w) mixture. The first spectrum at 6.25 µs is highlighted as a black line in each plot.

and the orientation of the two amino acid side chains are indicative for a sodium ion. Analysis of the vibrational modes of these two amino acid side chain can help to solidify this transient sodium binding site during the O intermediate. Reported vibrations of an asparagine are around 1678 cm^{-1} but can go up to 1704 cm^{-1} in a protein environment[180]. For deprotonated aspartic acid side chains, the asymmetric COO^- vibrational mode is around 1576 cm^{-1} while the symmetric is at 1402 cm^{-1}. These vibrations are highly sensitive to ion interaction and undergo pronounced shifts up to 60 wavenumbers[202]. Unfortunately, the symmetric mode lies outside of the QCL infrared window of 1510 to 1690 cm^{-1}. Therefore another technique is necessary to fully analyze the vibrational modes belonging to the sodium binding site in the O state.

FTIR spectroscopy offers besides a broad spectral window two time-resolved modes, step scan and rapid scan. The former offers a time range of (nanoseconds/)microseconds up to milliseconds while the latter has a time resolution of milliseconds. Hence, for studying O state kinetics, step scan is the suitable mode of operation. Figure 5.26 shows two 3D plots of FTIR step scan data recorded on detergent solubilized KR2 films at pH 8 and pH 4. Sample preparation was the same as for the QCL measurements. The fist spectrum at 6.25 µs is highlighted as black line in each dataset. At pH 8, this spectrum corresponds to the decay of the K intermediate with its C=C stretch vibration at 1520 cm^{-1} and small amide I changes. The fingerprint region of the retinal shows a negative band at 1200 cm^{-1} attributed to an all-*trans* C–C–H coupled vibration and a positive peak at 1184 cm^{-1} which is indicative of an isomerization to 13-*cis*. The spectrum of the K intermediate at pH 4 is similar to pH 8 except from the ground state bleaching signal. The intensity at 1535 cm^{-1} is decreased while the shoulder at higher frequencies is more pronounced due to a red shifted absorption maximum at pH 4 which shifts the C=C stretch vibration of the ground state to lower frequencies. The similarity between the two K spectra demonstrates that the first photoreaction is not dependent on the pH in

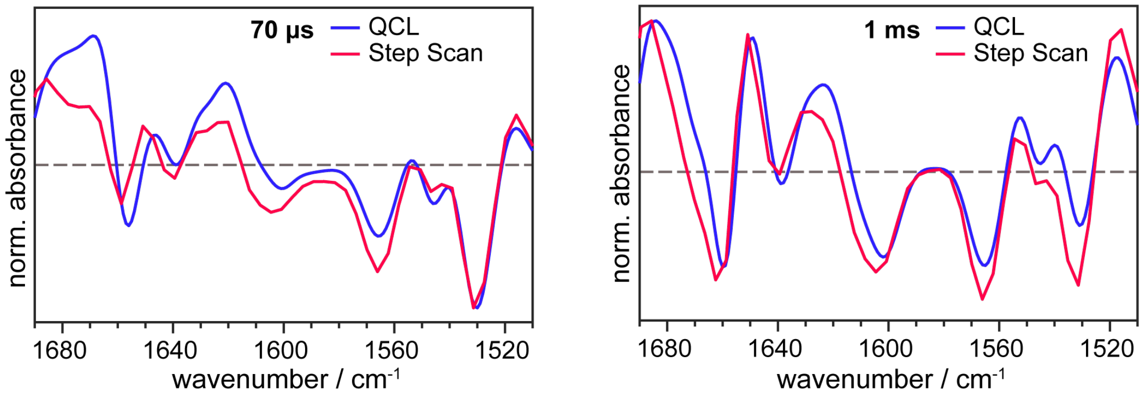

Figure 5.27: Superposition of normalized spectra at 70 µs and 1 ms at pH 8 corresponding to the L/M equilibrium and the O intermediate, respectively. Blue spectra are obtained with FTIR in step scan mode while red spectra are recorded using a QCL. Repetition rate of the 532 nm emitting laser was 2 Hz in both cases. The QCL spectra were smoothed to match the 8 cm^{-1} spectral resolution of step scan experiment using a FFT algorithm[203].

agreement to the QCL data of KR2 crystals. But the ongoing reaction pathway is different at pH 4 such that the K state decays into an O like intermediate still possessing weak intensity at the C=C stretch frequency at 1516 cm^{-1}. This suggests that K and O have a similar redshifted absorption maximum in the visible. The rise of the O state is not accompanied by pronounced changes in the amide I region contrasted by the O state at pH 8. Here, the late intermediate exhibits the strongest intensity changes over the whole spectral window. Before further analyzing the FTIR data, is has to be ensured that the same reaction is detected as in the QCL measurement. A superposition of normalized spectra at 70 µs and 1 ms, corresponding to the L/M equilibrium and the O intermediate, respectively, yields high resemblance in particular for the 1 ms spectra (fig. 5.27). Minor differences at 70 µs could be due to slightly different measurement conditions.

The crystal structure taken at 1 ms corresponds to the O_1 state as depicted in fig. 5.21. According to a global fit of the FTIR step scan data of fig. 5.26 this state has a maximum population at 3 ms. A comparison of O state spectra under sodium pumping conditions with O like intermediates formed under sodium pumping inhibiting conditions may help to identify spectral features exclusively associated with the transient sodium binding site (see fig. 5.18). In the case of KCl, the photocycle is substantially prolonged which makes step scan a tedious task. Therefore, rapid scan was chosen to record time-resolved data. All spectra presented in fig. 5.28 correspond to O(-like) states in the photocycles under the given conditions and time points. The spectra are normalized to the ground state bleach signal of the C=C stretch vibration at around 1535 cm^{-1}. This peak shifts to lower wavenumbers matching the redshift of O intermediates. The fingerprint region exhibits the usual 1201(-)/1180(+)cm^{-1} feature indicating that the isomeric state of the retinal is still 13-*cis* in these O states. Although the sodium ion does not bind in the vicinity of the PSB, the characteristic all-*trans* C–C–H mode of the retinal in the ground state is shifted to lower frequencies in case of potassium. Same holds for the positive 13-*cis* signal but not as pronounced. It seems that binding of an ion to an uptake cavity at hydrophobic/hydrophilic protein boundary has long range effects reaching the retinal binding pocket[183,184]. Band pattern in the amide I region are different for each spectrum probably representing the different functions under the measurement conditions. Lowest intensities

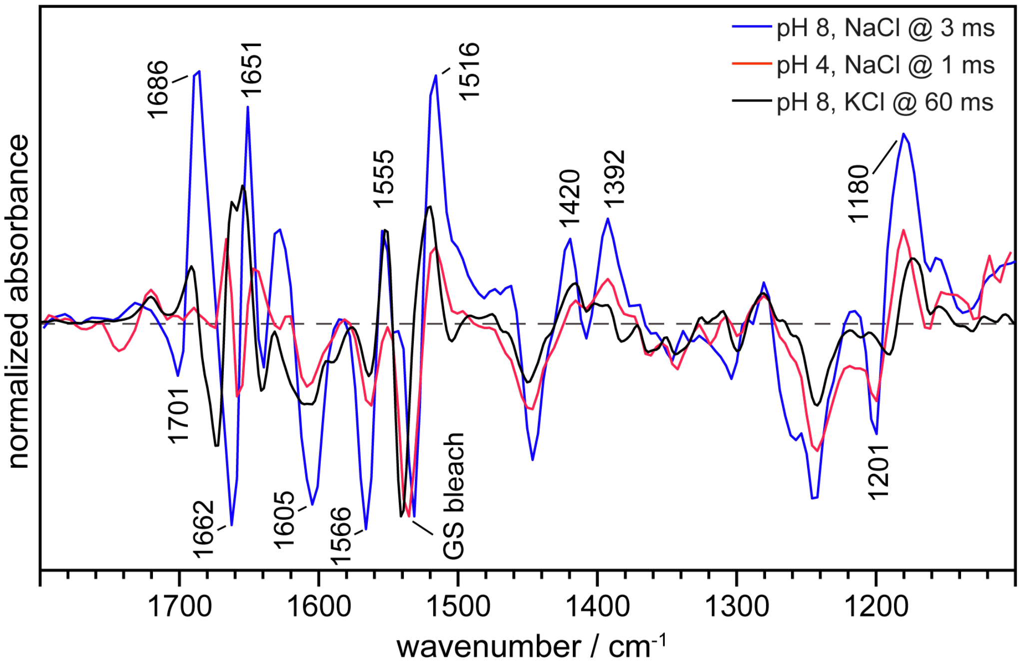

Figure 5.28: Comparison of the O like states of detergent solubilized KR2 at different sample conditions. Spectra in blue and red correspond to pH 8 and pH 4 from the data shown in fig. 5.26. Additionally, the spectrum in black denotes to KR2 at pH 8 with the same amount of salt but sodium was exchanged to potassium. Under this condition sodium pumping is abolished and proton pumping is favored[183]. The long photocycle in KCl required to use rapid scan instead of step scan producing a first spectrum at 9 ms. Repetition rate of 0.016 Hz was chosen to ensure ground state recovery before each laser flash.

are observed at pH 4 due to a potential loss of function. Unfortunately, no intermediate related signal kinetics could be detected in the carboxylic region above 1700 cm^{-1}. At least at pH 8, one protonation event from the PSB to D116 needs to occur but the signal could be obscured in an L/M equilibrium.

Regarding the sodium binding site at pH 8 shown in fig. 5.25 with the participating amino acid side chain N112, there is a pronounced positive band in the region around the literature value of 1678 cm^{-1} for the C=O vibration of an asparagine at 1686 cm^{-1}. This vibration vanishes under non sodium pumping conditions promoting this band to a sodium coordinating asparagine vibration in the O intermediate. A similar band was also observed for another sodium pump from *Gillisia limnaea*[195]. The corresponding mode in the ground state could be at 1701 or 1662 cm^{-1} while the latter is already in the range indicative of amide I vibrations. Candidates for the asymmetric COO$^-$ mode of D251 are 1605(-), 1566(-) and 1555(+)cm^{-1}. Both negative bands experience a decrease in intensity under non sodium pumping conditions. At pH 4 the positive peak at 1555 cm^{-1} disappeared while it has the same intensity at pH 8 in either NaCl or KCl. Two bands at 1420(+) and 1392(+)cm^{-1} have frequencies matching the literature values for a COO$^-$ symmetric vibrations. Both bands decrease in intensity if no sodium is pumped and the peak at 1420 cm^{-1} additionally downshifts to 1416 cm^{-1}. Negative signals associated with ground state vibrations of the symmetric mode can not be observed. The time traces of the mentioned frequencies further clarify if they are characteristic features of the O intermediate at pH 8 (fig. 5.29 **A**). The kinetic of the 1686 cm^{-1} band resembles the characteristic O state C=C stretch vibration at 1516 cm^{-1} (top panel). Looking at the possible COO$^-$ asymmetric bands it is apparent that the positive peak at 1555 and the negative one at 1605 cm^{-1} follow O state

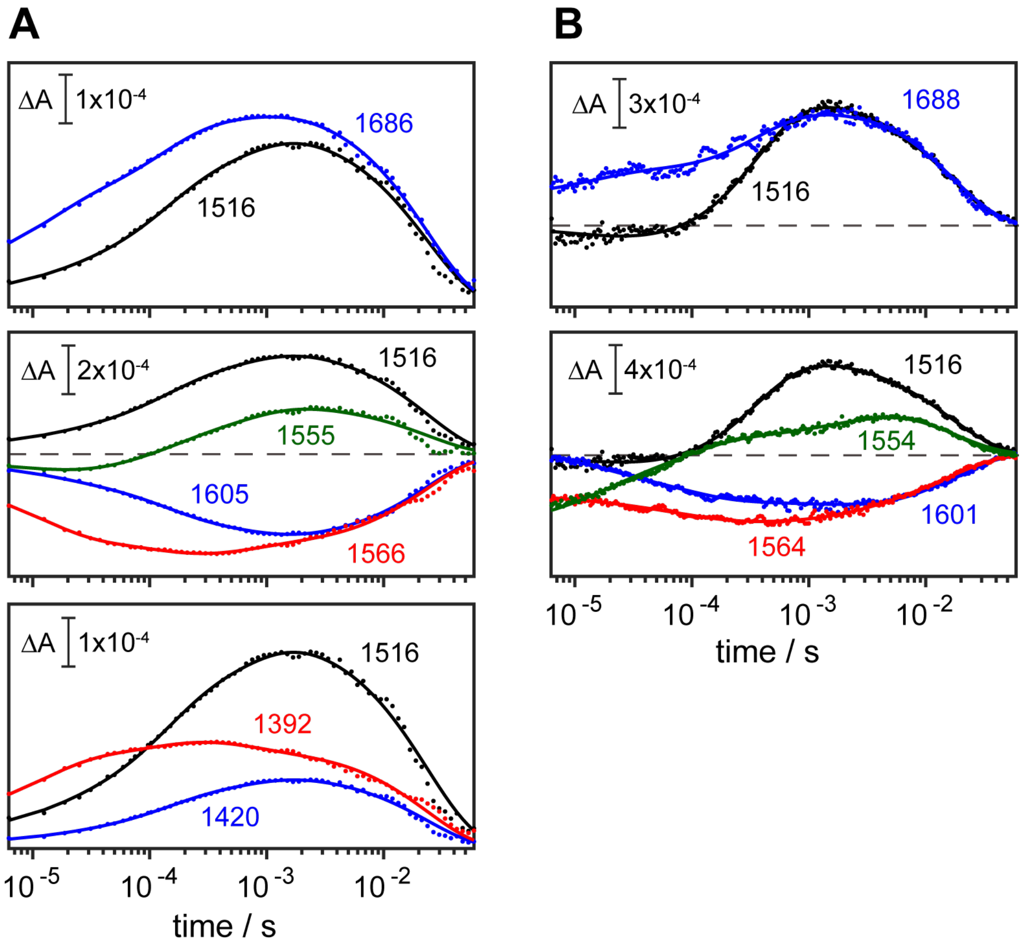

Figure 5.29: Kinetic comparison of potential vibrational bands involved in transient sodium binding in the O intermediate. The C=C stretch frequency at 1516 cm^{-1} serves as marker band for O state formation and decay. **A:** FTIR step scan data on detergent solubilized KR2 at pH 8. Dots represent SVD treated data. **B:** Transient absorption spectroscopy using QCLs on KR2 microcrystals at pH 8. Here dots represent the raw data.

kinetics (middle panel). The rise of the negative band at 1566 cm^{-1} starts earlier and is most likely not associated with O state formation. The band at 1392 cm^{-1} also do not follow the kinetic of 1516 cm^{-1} in contrast to the time trace of the 1420 cm^{-1} vibration (bottom panel). The additional observed downshift of this band under non sodium pumping conditions further points to a sodium dependent COO^{-} symmetric vibration in the O intermediate. Chen *et al.* did a FTIR step scan experiment on KR2 under H/D exchange[198]. Any vibrations which involve a hydrogen experience a frequency shift upon exchange to deuterium. The C=O vibrational mode of an asparagine is coupled to the NH$_2$ group which also shifts this band in D$_2$O. Indeed, the band at 1686 cm^{-1} as well as the negative peak at 1701 cm^{-1} shift while the other negative peak at 1662 cm^{-1} stays constant. This qualifies the latter band to be an amide I mode which is a combination of mostly C=O stretching vibrations. In contrast to the asparagine mode, the vibrational modes of COO^{-} do not involve any hydrogen. Upon H/D exchange, all the mentioned frequencies do not shift in KR2. This also rules out the possibility that the bands at 1605(-), 1566(-) and 1555(+)cm^{-1} are of amide II origin, because this mode involves the NH of the protein backbone. Summarized, the N112 C=O mode downshifts in the O intermediate from 1701 to 1686 $\mathrm{cm^{-1}}$. The ground state asymmetric and symmetric $\mathrm{COO^-}$ stretch vibrations of D251 could not be clearly identified but they may be at 1555 and 1420 $\mathrm{cm^{-1}}$, respectively, in the O state.

A comparison with the crystal kinetics in fig. 5.29 **A+B** shows essentially the same kinetic behavior as in the FTIR step scan experiment. It is therefore reasonable to assume that all conclusions drawn from the detergent solubilized experiments of KR2 can also be applied to microcrystals.

5.4.3 Conclusion

Transient absorption spectroscopy in the infrared and visible region has shown that KR2 microcrystals grown at pH 4 with subsequent soaking to pH 8 behave spectroscopically similar to rehydrated dried films of detergent solubilized KR2. Although amide I intensities differ, the photocycle kinetics are identical which was not observed for bR crystals[115]. It was supposed that monomeric KR2 is not capable of sodium pumping due to a compacted Schiff base cavity[182]. Missing transient sodium binding would then hamper O state formation which is not observed in the presented data on monomeric detergent solubilized and crystalline KR2. Further analysis of the influence of sodium ion concentration on O state formation in microcrystals revealed that higher sodium concentration accelerates M state decay/O state formation as reported for pentameric KR2 reconstituted into lipids[189]. These findings strongly indicate that the O state with a transiently bound sodium is formed in monomeric microcrystals.

Although a water molecule and a sodium ion have the same electron density, serial femtosecond X-ray crystallography on the KR2 microcrystals found a potential sodium binding site consisting of N112 and D251 at 1 ms. But further proof is needed and can be provided by the vibrational modes of the participating amino acid side chains. FTIR step scan measurements on detergent solubilized KR2 show that a positive band at 1686 $\mathrm{cm^{-1}}$ in the O state is only observed under sodium pumping conditions. The absence of this band in KCl and at pH 4 argues for sodium dependent arginine band. The kinetics of this band additionally fit with O state formation. A shift from 1701 $\mathrm{cm^{-1}}$ to 1686 $\mathrm{cm^{-1}}$ is consistent with sodium coordinating side chain of N112 in the O intermediate[195].

For analyzing the coordination of a carboxylate side chain, the asymmetric and the symmetric vibrational mode have to be considered. There is a rule of thumb about the coordination type and the frequency difference between both vibrations[204]

$$\Delta\nu_{a-s}(\text{unidendate}) > \Delta\nu_{a-s}(\text{ionic;bridging}) > \Delta\nu_{a-s}(\text{bidendate}) \tag{5.2}$$

with $\Delta\nu_{a-s}$(ionic) being around 165 $\mathrm{cm^{-1}}$. Figure 5.30 illustrates the different coordination modes. Two negative bands, representing ground state vibrations, appear in the range of an asymmetric $\mathrm{COO^-}$ vibration in the FTIR difference spectrum of the O intermediate at 1566 and 1605 $\mathrm{cm^{-1}}$. Both peaks experience an intensity decrease and also slight frequency shifts under non sodium pumping conditions. Kinetically, the latter band is correlated with O state formation but its frequency is rather high for an hydrogen bonded (ionic) carboxylate. Such a high frequency is indicative for a (pseudo-)bridging coordination character[204]. A frequency of 1566 $\mathrm{cm^{-1}}$ on the other hand favors the ionic character in the ground state of KR2[205]. The time trace of this band starts to rise before O state

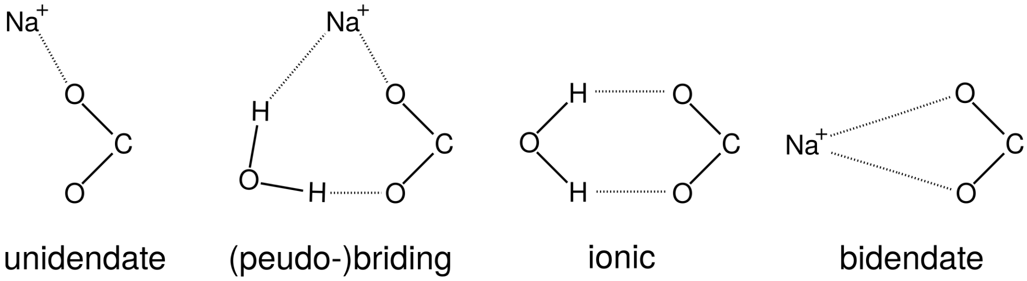

Figure 5.30: Coordination structures of a COO^- side chain.

formation arguing for disturbance of hydrogen bonds of D251 at earlier stages of the photocycle or that this band originates from another negatively charged aspartate. Unfortunately, a corresponding symmetric vibrational mode could not be identified prohibiting a detailed analysis of the coordination mode in the ground state.

Upon O state formation three possible carboxylate bands appear at 1555, 1420 and 1392 cm^{-1}. A downshift of the asymmetric mode to 1555 cm^{-1} indicate a bidendate sodium coordination[204,206]. At pH 4, this band vanishes but it is present at pH 8 in KCl. This suggests that this frequency is not just characteristic for the bidendate mode of sodium coordination. Indeed, a theoretical study on sodium coordinating carboxylates found identical frequencies for the asymmetric mode for bidendate sodium coordination and its hydrogen bonded form[205]. Following eq. (5.2) the two scenarios should differ in their symmetric vibrational frequency. This vibration was identified at 1420 cm^{-1} because it is kinetically related to O state formation. This yields a frequency difference of $\Delta\nu_{a-s} = 135\,\text{cm}^{-1}$ favoring that the sodium is coordinated by D251 in bidendate mode. A perfect bidendate coordination usually have an even smaller $\Delta\nu_{a-s}$, so as a value of 135 cm^{-1} could reflect the not identical distance of both oxygens to the sodium ion of 2.5 and 3.1 Å, respectively (see fig. 5.25)[207,208]. This rounds up the picture of the sodium binding site in the O intermediate of KR2 and confirms the findings of the crystal structure at 1 ms.

This section demonstrated that the combination of serial femtosecond X-ray crystallography with time-resolved absorption spectroscopy is a powerful tool for studying protein dynamics and can give detailed insights in structural changes. Both techniques have atomistic resolution but also their strengths and weaknesses. The spatial information provided by crystallography permits identification of key residues involved in protein function and their movements. Infrared spectroscopy is very sensitive to changes in bond strength caused by hydrogen bonds or metal ion coordination. Additionally, it can resolve protonation dynamics which is not possible with crystallography. Certainly, further studies on photo-activated proteins will make use of these strengths.

5.5 Exploring the bistability of JSR

This project was in done in collaboration with Niranjan Varma and Elena Lesca from the Paul-Scherer Institute in Switzerland and published in:

Ehrenberg, D., Varma, N., Deupi, X., Koyanagi, M., Terakita, A., Schertler, G. F., Heberle, J. & Lesca, E. The two-photon reversible reaction of the bistable jumping spider rhodopsin-1. *Biophysical journal* **116,** 1248–1258 (2019). doi: 10.1016/j.bpj.2019.02.025

I performed the spectroscopic experiments, photostationary state simulations and global fit analysis. I contributed to data analysis, interpretation and writing the manuscript.

Microbial rhodopsins share an isomerization of the all-*trans* retinal to a 13-*cis* configuration with a cyclic reaction path concluded by the reisomerization back to *trans* as a common activation mechanism. During the photocycle, the retinal stays in 13-*cis* but its electrostatic environment changes, resulting in intermediate states with different absorption maxima in the visible[209]. While lower organisms use these type of rhodopsins for light energy conversion and signaling, animals rely on a subset of light-sensitive G-protein coupled receptors (GPCRs). Animal opsins are mainly involved in vision and circadian clock entrainment[210]. Despite sharing very low sequence similarity to microbial rhodopsins, GPCRs also consists of seven transmembrane α-helices with covalently bound retinal chromophore in the core of the protein. Structural rearrangements are initiated by retinal photoisomerization eventually lead to an active conformation which permits G-protein binding with subsequent onset of downstream signaling cascades[211].

Animal rhodopsins can be classified as monostable or bistable depending on the thermal stability of the active conformation. In monostable opsins, the active state is not thermally stable. Its decay is accompanied by hydrolysis of the Schiff base and subsequent loss of the retinal. Therefore, another retinal molecule has to bind to the protein for dark state recovery. In contrast, the active conformation in bistable opsins is thermally stable and the retinal resides in the binding pocket throughout the entire photoreaction. Dark state recovery achieved by absorption of a second photon leading to a re-isomerization to 11-*cis*[212]. Hence, bistable opsins have two thermally stable protein conformations and exhibit both, forward and backward photoreactions: i.e. retinal isomerizes back and forth between 11-*cis* in the resting and all-*trans* in the active state (fig. 5.31). This ability is advantageous over monostable rhodopsins which rapidly lose the capability to respond to subsequent light pulses due to loss of retinal[213].

To date, biophysical studies on bistable opsins are scarce and narrowed to predominately two opsins, octopus and squid rhodopsin. Previous spectroscopic studies on these rhodopsins revealed three common intermediates in the forward reaction to an active a(cid)-Meta state:

$$\text{Rho} \rightarrow \text{Batho} \rightarrow \text{Lumi} \rightarrow \text{Meso} \rightarrow \text{a(cid)-Meta} \quad .$$

For octopus rhodopsins, an additional spectrally silent intermediate was proposed between Meso and a-Meta referred to as transient-Meta (t-Meta)[214–216]. During the activation process the SB stays protonated, also in the active a-Meta conformation. Thus, a deprotonation of the Schiff base seems not

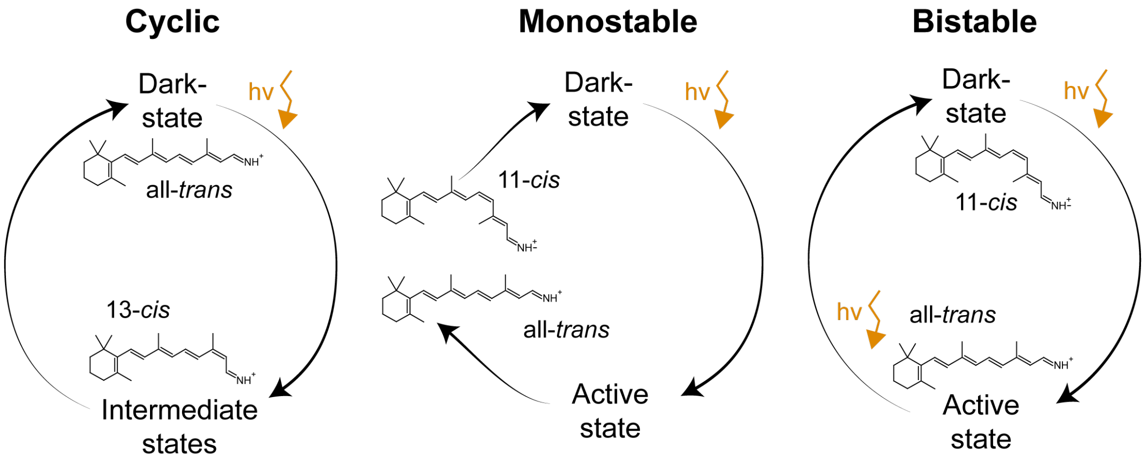

Figure 5.31: Schematic illustration of cyclic, mono- and bistable reaction pathways. Photon absorption is indicated with a yellow arrow. Cyclic reactions in microbial rhodopsins starts with photoisomerization of the retinal from all-*trans* to 13-*cis* followed by structural changes leading to protein function. These steps are finally reversed before returning back to the ground state. In monostable opsins, the dark state accommodate a 11-*cis* retinal which isomerizes to all-*trans*. Subsequent structural rearrangements eventually form an active state. This active conformation is not thermally stable and its decay is accompanied by loss of the retinal. Therefore another 11-*cis* is needed for dark state recovery. In contrast, the active state in bistable opsins is thermally stable. The protein will remain in its active conformation until another photon absorption will lead to the reisomerization and dark state recovery.

to be necessary for protein function. Information about the reverse reaction is very limited because accumulation of the active species is often hampered by similar absorption profiles of the ground and active states. In octopus rhodopsin, the photorecovery has been proposed to be considerably slower than the forward reaction consisting of only two detectable intermediates (a-Meta → I_1 → I_2 → Rho)[217]. In the case of squid rhodopsin, a de- and reprotonation of the retinal Schiff Base during the recovery of the ground state has been suggested[218,219].

The main reason for the confined amount of biophysical studies on bistable opsins is the absence of a model system – as bovine rhodopsin for monostable opsins – that can be recombinantly expressed and purified to yield large quantities of functional protein[220,221]. Squid and octopus rhodopsin were sourced from native retinae precluding large scale production and molecular engineering[222]. In 2012, Nagata *et al.* found a rhodopsin in the eye of the jumping spider *Hasarius adansoni* which they could express in HEK293S cells[223]. Jumping spider rhodopsin-1 (JSR1) has the potential to serve as a model system for the study of novel light-controlled molecular switches in optogenetic applications. This section sheds light on the mechanistic basis of bistability in light-sensitive GPCRs by a biophysical characterization of JSR1.

5.5.1 Obtaining a pure dataset for photoactivation

Photoactivation of opsins proceeds through a series of intermediate states which can be traced by changes in visible absorption of the retinal chromophore (see sections 5.3 and 5.4)[224]. Detection of these states in a difference experiment requires that the absorption of the formed state does not have a similar absorption profile as the initial (dark) state. If they do, they cancel each other and

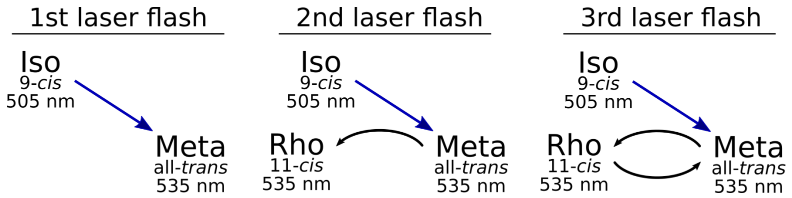

Figure 5.32: Illustration how the contribution of the equilibrium reaction (Rho ↔ a-Meta) increases of the course of a flash photolysis experiment. The first laser flash will invoke the reaction of interest from Iso to a-Meta (denoted in blue). A second flash additionally introduces a reaction of a-Meta to Rho. The third flash will finally complete the equilibrium reaction whose contribution will then increase with each flash while the initial isorhodopsin state depletes.

the intermediate is spectrally silent. Although the inactive dark and the active a-Meta state differ in extinction coefficient in JSR1, both states have the same absorption maximum[223]. This means, that the conversion from an inactive to an active conformation can not be traced in a difference experiment. Incorporation of 9-*cis* retinal results in a blueshift of about 30 nm from 536 to 503 nm permitting observation of the active state formation[3]. The protein with 9-*cis* isomer will be referred to as jumping spider isorhodpsin-1 (JSiR1).

For achieving unperturbed signals for the reaction of interest, homogeneity of the initial dark state is necessary. This is usually not a problem for cyclic reactions because the initial state will be restored after each exciting laser flash. For monostable opsins, excitation leads to a reduction of photoactivatable sample reducing in fact the signal intensity but the homogeneity is preserved. In the case of bistable opsins, each laser flash will drive the system in a stationary equilibrium of inactive and active states eliminating the homogeneity of the sample. In a stationary mixture, both states will absorb photons which will eventually start both reactions, the forward and reverse pathway (Rho ↔ a-Meta, equilibrium reaction). Restoration of a homogeneous initial state before each laser flash would in principle solve this issue but is not feasible by illumination for JSR1 due to the similar absorption profile of inactive and active conformations. Starting the experiment from a homogeneous JSiR1 (9-*cis* retinal) will result in a even more complex situation of three simultaneous reactions as illustrated in fig. 5.32. Excitation of JSiR1 leads to the formation of the active state as it was demonstrated for bovine rhodopsin[225]. A succeeding laser flash will then not just start the reaction Iso → a-Meta but also the reaction of a-Meta to Rho. A third flash consequently starts additionally the reaction of Rho to a-Meta leading of an interconversion of both (equilibrium reaction). The quantum yield of a reaction from a-Meta or Rho to Iso is usually low and can be neglected[226,227].

Hence, each laser flash will decrease the signal of interest of photoactivation from Iso to a-Meta while increasing spectral contribution of the equilibrium reaction. In lieu of this, a single-shot experiment was performed in the range from 400 to 620 nm in 20 nm steps (omitting 460 nm due to scattering by the photolyzing laser). This measurement was done in both wavelength directions, i.e. from 400 to 620 nm and vice versa (fig. 5.36). A fresh sample was used for each scanning direction in order to start the measurement with an homogeneous sample. The contour plot for the 620 to 400 nm scan begins with a negative signal around 540 nm representing ground state depletion. The dataset concludes with a pronounced positive absorption change indicating formation of the active a-Meta species. In fact, this state seems to be thermally stable as otherwise ground state recovery would result in zero absorption change as for cyclic reactions (sections 5.3 and 5.4). Contrary, formation of a-Meta can not be observed in the 400 to 620 nm scan. This suggests that by reaching higher wavelengths,

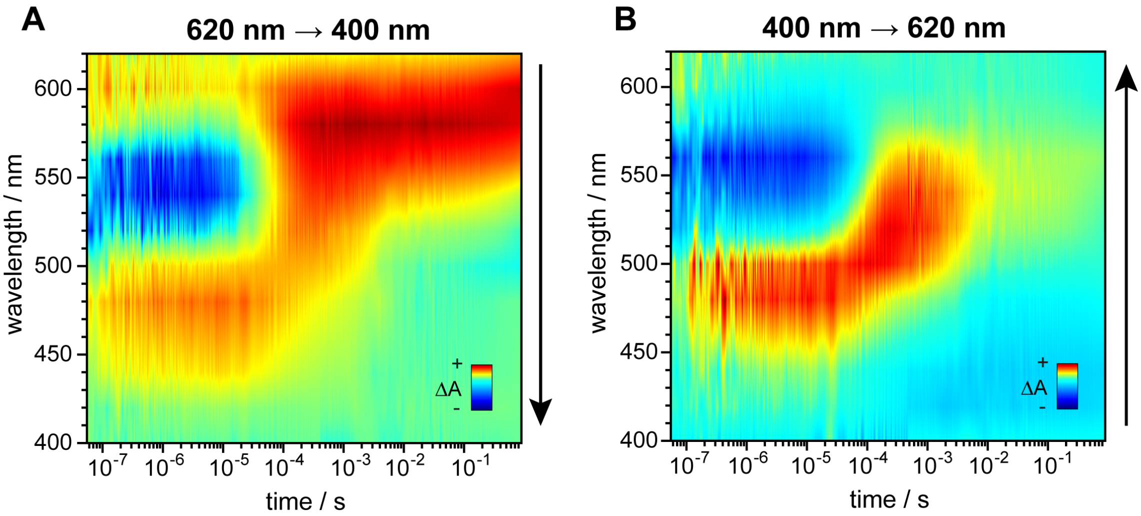

Figure 5.33: Time-resolved UV/Vis experiments at 20 °C on JSR1 reconstituted with 9-*cis* retinal (JSiR1, isorhodopsin) and solubilized in 0.195 mM DDM, 140 mM NaCl at pH 6.5. Excitation was at 465 nm with an energy density of 3 to 4 $\mathrm{mJ\,cm^{-2}}$ at the sample. Single-shot absorption changes were recorded in a range from 400 to 620 nm in 20 nm steps in both scan directions, i.e. from 620 to 400 nm (**A**) and vice versa (**B**). Arrows indicate direction of wavelength scan. Recording at 460 nm was omitted due to scattering by the exciting laser. Each wavelength scan was started with a fresh homogeneous sample of isorhodopsin.

isorhodopsin has already depleted by a significant amount and the equilibrium reaction dominates the measured signal. An interconversion of a-Meta and Rho does not result in any absorption change due to the similar absorption profile explaining the concluding zero line (fig. 5.36 **B**). Indeed, UV/Vis spectra recorded prior the experiment and after 11 laser flashes needed for one wavelength scan demonstrate the depletion of isorhodopsin by a redshift of the absorption maximum (fig. 5.34 **A**). Comparison to a fully converted sample obtained by illumination for 5 min yields an isorhodopsin depletion of approximately 40 % after one wavelength scan. This translates to a 8 % conversion yield of Iso per laser flash (fig. 5.34 **B**).

To obtain a pure dataset comprised of solely Iso to a-Meta reactions, contributions of the equilibrium reaction have to be subtracted (data shown in fig. 5.36 **B**). As an estimation, an exponential increase of the Rho/a-Meta equilibrium up to 60 % after 11 laser flashes is assumed (fig. 5.34 **B**). Since isorhodopsin population has already substantially depleted while advancing the wavelength scan, merging of the two datasets is controlled by weighting factors which potentially increases the signal-to-noise ratio. A simplified version of the equation used to calculate a pure Iso → a-Meta dataset is

$$\begin{aligned} d_{iso\to a-Meta} = & \frac{1}{1-e_{620\to400}} w \cdot d_{620\to400} - e_{620\to400} \cdot d_{equilibrium} \\ & + \frac{1}{1-e_{400\to620}} (1-w) \cdot d_{400\to620} - e_{400\to620} \cdot d_{equilibrium} \quad , \end{aligned} \tag{5.3}$$

where d_x denote the particular dataset, e_x controls the contribution of the equilibrium reaction and w is a weighting factor for the 620 to 400 nm dataset. The first factor in eq. (5.3) corrects for the decreased signal intensity of the Iso → a-Meta reaction due to isorhodopsin depletion. The weighting factor w

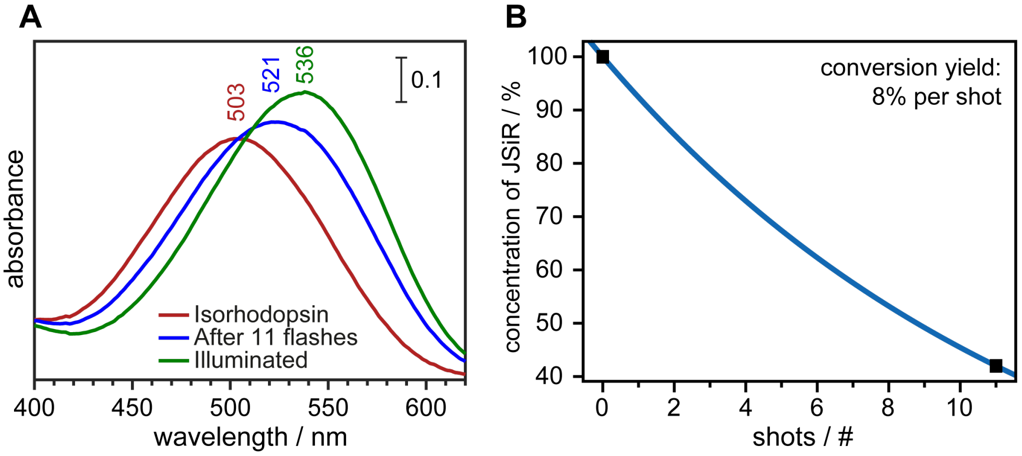

Figure 5.34: **A:** UV/Vis spectra of JSiR1 prior time-resolved measurement (red), after 11 laser flashes needed for one wavelength scan (blue) and after illumination by a 473 nm laser at 30 mW for 5 min consisting just of a-Meta and Rho states (green). After 11 flashes, isorhodopsin has depleted to approximately 40 %. **B:** Assuming an exponential decrease of isorhodopsin yields a conversion yield of 8 % per laser flash for the Iso → a-Meta reaction.

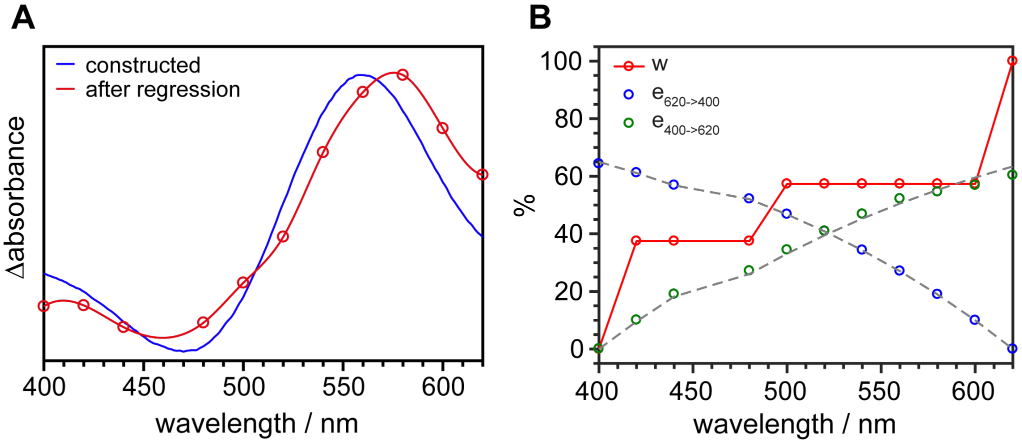

Figure 5.35: **A:** Comparison of a constructed a-Meta-minus-Iso difference spectrum constructed with steady state UV/Vis spectra and the resulting spectrum obtained after a nonlinear least squares regression of eq. (5.3). Dots represent measured datapoints while the line is a result of a spline function. **B:** Factors of eq. (5.3) after the optimization process.

accounts for the fact that for each wavelength scan the first recording is actually a pure Iso to a-Meta reaction. This equation was subjected to a nonlinear least squares regression in MATLAB expecting the dataset to finish with a difference spectrum of Meta-minus-Iso constructed with steady state spectra of both species (fig. 5.35 **A**). Additionally, the exponential increase of the equilibrium reaction was constrained to be between 6 to 10 %. The resulting difference spectrum of an optimization by eq. (5.3) has slightly shifted absorption peaks possibly due to sample heterogeneity introduced by the pulsed laser excitation compared to continuous illumination (fig. 5.35 **A**). Analysis of the factors of eq. (5.3) demonstrates the exponential increase of the equilibrium reaction as well as the equally contributing datasets in the middle of the wavelength scan (fig. 5.35 **B**).

5.5.2 Dynamics of photoactivation

The dataset obtained after the nonlinear least squares regression elucidated in the previous section (section 5.5.1) represents exclusively the photoactivation of JSiR1 to a-Meta (fig. 5.36 **A**). According to other mono- and bistable opsins, it is assumed that excitation of the isorhodopsin containing 9-*cis* retinal will lead to the same active a-Meta conformation as for photoactivation of the inactive Rho state with 11-*cis* retinal[225,226]. Representative time traces at 480, 520 and 580 nm show the bleach of the initial isorhodopsin and evolution of distinct intermediate states (fig. 5.36 **A** upper panel). At later stages, a positive absorption signal maintains at 580 nm suggesting the formation of the thermally stable a-Meta species[216]. However, slight changes can still be observed at later timescales, in particular at 520 nm. This could indicate a precursor state to the final a-Meta conformation as it has been suggested for octopus rhodopsin (t-Meta)[228]. In this case, photoactivation would take seconds to complete which is considerably slower than of any other reaction of mono- or bistable opsins. Alternatively, it may well be that produced thermally stable a-Meta and Rho states are excited by the probing light as observed for the long-lived P_4 state of channelrhodopsin-2 from *Chlamydomonas reinhardtii* (CrChR2)[203]. A global fit analysis, which omits the changes that occur after 20 ms, revealed a contribution of three intermediate states with a 3 ms rise time for a-Meta, similar to squid rhodopsin (fig. 5.36 **A** bottom panel)[229].

On the account of a same reaction path for Iso and Rho, the Iso → a-Meta reaction is considered to consist of the same intermediate states as the Rho → Meta transition and they will be termed accordingly[225,226,228]. The rise of an early red-shifted Batho intermediate is beyond the 50 ns time resolution of the experiment. Formation of an intermediate state is accompanied by simultaneous depletion of the initial state as recognized by the negative absorption at around 550 nm. Batho decays with a time constant of 200 ns into a new early blue-shifted Lumi intermediate indicated by the absorbance increase around 480 nm. In squid and octopus rhodopsin, Lumi is red-shifted with respect to the 11-*cis* state Rho. Such a pronounced blue-shift of Lumi is thus a unique feature of JSR1. However, it is not far enough blue-shifted to be indicative for a deprotonated Schiff base as it it the case for the M-intermediate in bacteriorhodopsin (bR) which absorbs at 412 nm (section 5.1). The decay of Lumi with a time constant of 80 µs is accompanied by the conversion to an intermediate with an absorption difference maximum around 520 nm called Meso. Finally, formation of a-Meta is achieved with a time constant of 3 ms illustrated by the absorbance decrease at 520 nm and the slight increase at 580 nm.

In bistable opsins, photon absorption by the all-*trans* a-Meta state recovers the 11-*cis* configuration corresponding to the native Rho state[217]. Unfortunately, the similar absorption characteristics of Rho and Meta prohibits accumulation of a-Meta by light. Instead, an a-Meta/Rho equilibrium is generated and pulsed laser excitation provokes therefore both reactions, the forward (Rho → a-Meta) and reverse (a-Meta → Rho) reaction (equilibrium reaction). These circumstances rendering the investigation of the photorecovery reaction a challenging task. However, the time-resolved absorbance changes of such an a-Meta/Rho equilibrium are depicted in fig. 5.36 **B**. The dataset also exhibits Batho (600 nm), Lumi (480 nm) and Meso states (510 nm) reasoning for the same reaction pathway of Iso and Rho. But there are also distinct differences as compared to the Iso → a-Meta reaction (fig. 5.36 **A**). Most strikingly, the dataset is not concluded by a pronounced positive absorption change. This illustrates

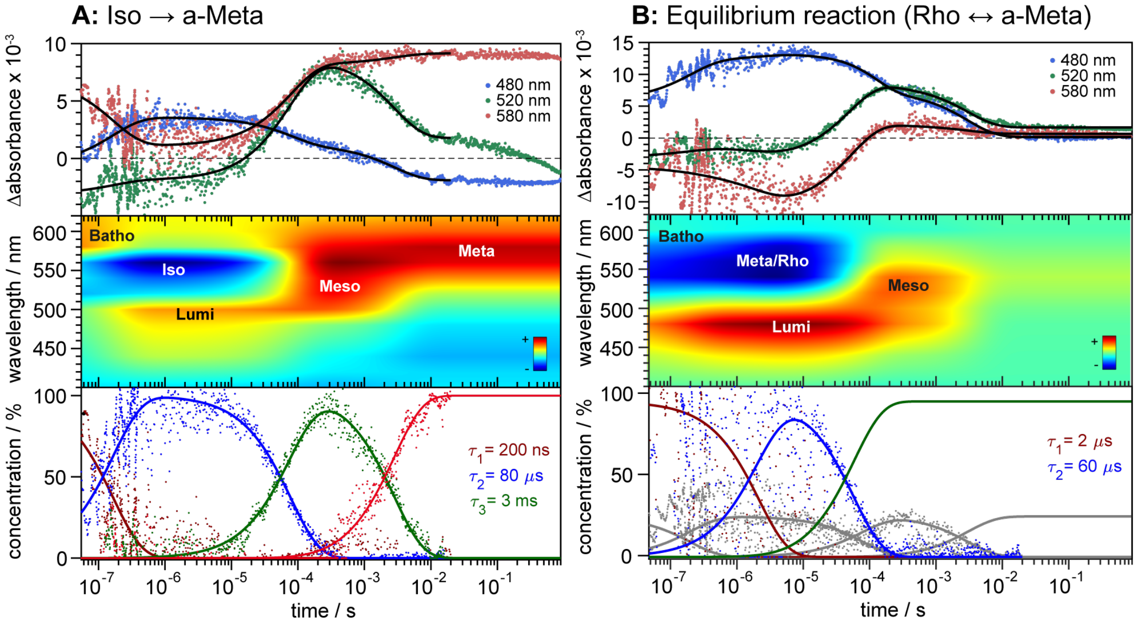

Figure 5.36: Time-resolved UV-Vis absorption changes of JSiR1 (JSR1 with 9-*cis* retinal) after excitation with 465 nm. Upper panels display three representative time traces at 480, 520 and 580 nm. Dots represent raw data while black lines are a result of a global fit. Middle panels show a contour plot of the photoreactions with intermediate states as indicated. Presented data is obtained by global fitting the raw data (bottom panels). **A:** Photoactivation of isorhodopsin. Model for the global fit were three sequential decay processes leading to a thermally stable state. Changes after 20 ms were neglected due to possible photolysis of produced stable Rho and Meta states provoked by the probing light. **B:** Interconversion between Rho and Meta states (equilibrium reaction). JSiR1 sample was pre-illuminated with 473 nm for 5 min depleting isorhodopsin into a stationary mixture of Rho and Meta states. Since the forward and the reverse reaction are induced by the exciting laser flash, the global fit is comprised of two processes. The forward reaction is fixed with the already obtained time constants (colored in grey) while the other reaction is subjected to the fitting procedure. The amplitude difference serves just as an accentuation of the Meta-to-Rho reaction and does not reflect actual concentrations.

the similar absorption profile of a-Meta and Rho which does not result in any change of absorbance if both are interconverted. Early negative signals of initial state depletion appears redshifted compared to Iso reflecting the spectral shift from 505 to 535 nm for a-Meta. Due to this shift, Lumi increases in absorbance while Meso is less pronounced and Batho is hardly observed. The characteristic kinetic trace for Lumi at 480 nm evidently shows a biphasic rise which is also apparent in the ground-state depletion signal at 520 nm. The simultaneous photoreactions of Rho and a-Meta overlay in the dataset and are certainly the origin of the biphasic rise and decay of Lumi. Contrary, Meso rises and decays in a monoexponential manner suggesting that this state exclusively belongs to the Rho/Iso → a-Meta photoactivation process.

To disentangle activation and recovery processes, the global fit routine was adopted to search for kinetic signatures that emerge on top of the activation process. This was realized by fixing one concentration profile with the already obtained time constants representing the forward reaction Rho → a-Meta (fig. 5.36 **A** bottom panel, colored in grey) while one simultaneous transition pathway was subjected to a fitting procedure. Combination of both reactions then yields the final dataset. For a satisfying global fit, two transitions with time constants of 2 and 60 µs were necessary for the

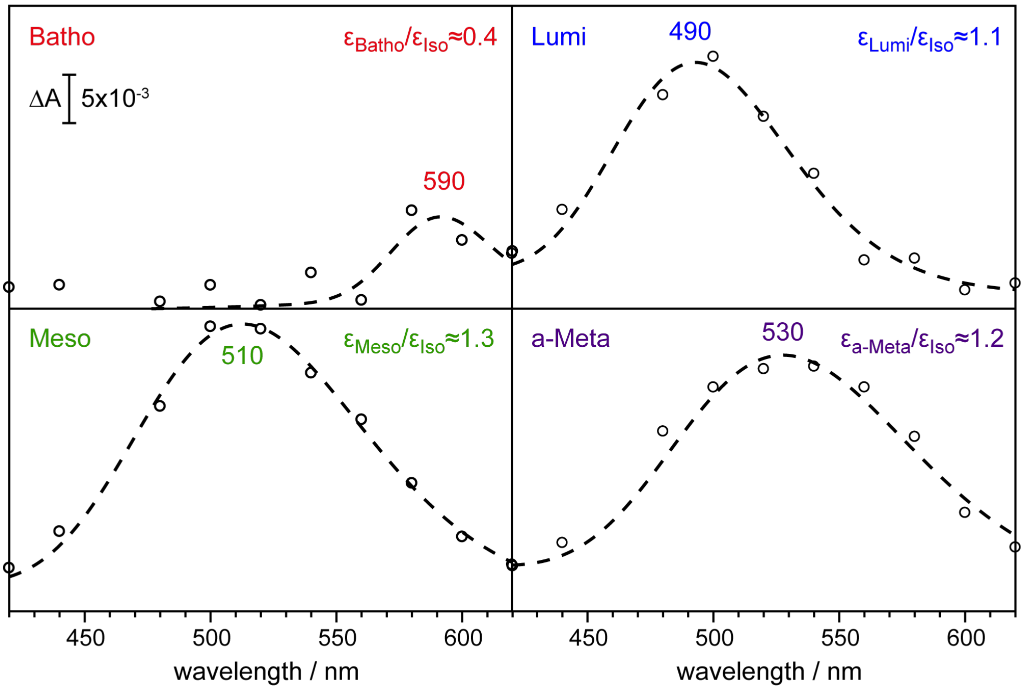

Figure 5.37: Calculated absolute spectra of JSR1 intermediate states compromising the photoactivation reaction. These were obtained by adding a steady state spectrum of isorhodopsin to the dataset of fig. 5.36 using a non-linear least squares regression. Absorption maxima and extinction coefficient ratios are indicated.

additional reaction pathway taking account of the biphasic rise and decay of Lumi. This suggests that the recovery of Rho from a-Meta is comprised of two intermediate states, further referred to as M_1 and M_2. With this, the photoreverse reaction of JSR1 is considerably faster than the activation process contrasted by the proposed octopus two-photon cycle where the opposite is observed[217]. Although both reactions are entangled in the contour plot, the absorption of M_1 and M_2 can be estimated to be similar to the redshift of Batho and the blueshift of Lumi, respectively, due to the lack of additional spectral features. In particular, a far blue-shifted intermediate indicative for a deprotonated Schiff base - as it was proposed for squid rhodopsin - can be excluded[219].

Maxima in difference signals might be shifted compared to the actual absolute absorption maximum of the intermediate species due to spectral overlap of the initial and photoproduct state. For determination of absolute absorption maxima, the difference dataset has to be converted to yield just positive signals. Elimination of the negative bleaching signal can be achieved by addition of a steady state spectrum of isorhodopsin to the forward reaction dataset of fig. 5.36 **A**. Since this problem has many solutions, three constraints were assumed:

1. Absolute absorption can not be negative
2. Absorption profiles of the intermediate states have a Gaussian shape in the energy domain
3. Dataset concludes with formation of a-Meta .

A non-linear least squares regression was performed complying these assumptions while trying to reproduce an a-Meta steady state spectrum at the end of the dataset. The resulting spectra of Batho, Lumi and Meso show absorption maxima at 590, 490 and 510 nm, respectively (fig. 5.37). Comparison of the absorption intensities of the obtained intermediate states spectra with the added isorhodopsin

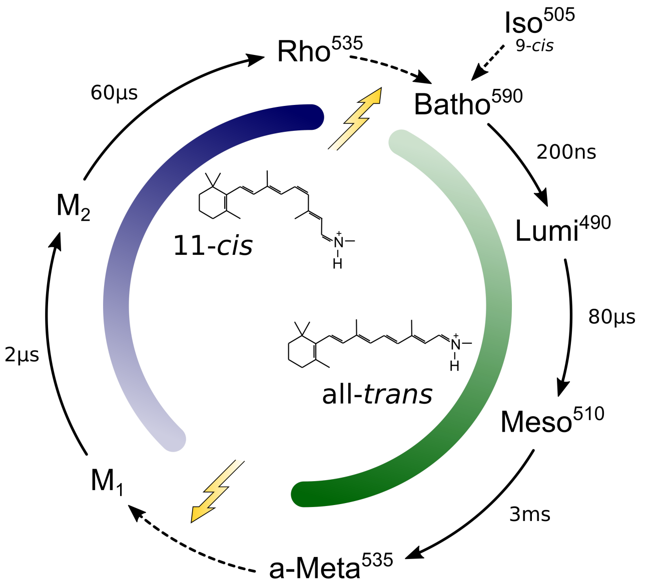

Figure 5.38: Proposed two-photon cycle of JSR1. Dashed arrows indicate light induced transitions. Transition time constants, isomeric state of the retinal and absorption maxima of the intermediate states are indicated.

spectrum yields extinction coefficient ratios which are typical for bistable pigments[230]. Exception is the low extinction coefficient for Batho which presumably is the result of its rise beyond the time resolution of the experiment. The extinction coefficient ratio of 1.2 for the active a-Meta state is in accordance with published spectra[223].

Based on the findings in this section, a model of the two-photon cycle of JSR1 is proposed (fig. 5.38). Absorption of a photon leads to photoactivation of Rho or Iso which both share the same reaction path consisting of three intermediate states (Batho, Lumi and Meso). Although Lumi is blueshifted in respect to the inactive state Rho, it is not indicative of a deprotonated Schiff base. Photoactivation is completed in 3 ms with the formation of a-Meta. Photorecovery on the other hand is considerably faster with a time constant of 60 µs and is composed of at least two intermediates. No additional blueshifted states were detected suggesting that the Schiff base stays also protonated during the reverse reaction.

5.5.3 Photostationary State Calculation

In light induced reactions, the population of a photoproduct depends on the photolysis k_{ph} and/or thermal decay k_{th} rate of its precursor, its own reaction upon absorption of a photon and its thermal lifetime. Exemplary for Meso:

$$^{d[Meso]}/_{dt} = -(k_{ph,Meso} + k_{th,Meso})[Meso]t + k_{th,Lumi}[Lumi]t \quad . \tag{5.4}$$

Here, square brackets denote concentrations and the thermal decay rates are the inverse of time constants ($k = 1/\tau$) obtained by the time-resolved UV/Vis absorption experiment from section 5.5.2. The photolysis rate is defined as

$$k_{ph,x} = ln(10) \cdot 10^3 \cdot \frac{\Phi_x \epsilon_x}{N_A h\nu} \cdot I \tag{5.5}$$

with Φ_x, ϵ_x, ν and I denote quantum efficiency, extinction coefficient in $\mathrm{M^{-1}\,cm}$, frequency and irradiance of the exciting light in $\mathrm{W\,cm^{-2}}$. These two equations permit to calculate concentrations of intermediates during illumination once the relevant bio- and photophysical properties are known. It was demonstrated with high-performance liquid chromatography (HPLC) that illumination of JSiR1 with 495 nm results in a mixture of 5 % Iso (9-*cis*), 19 % Rho (11-*cis*), 73 % a-Meta (all-*trans*) and a residual of 3 % 13-*cis*[3]. With this information, the proposed two-photon cycle depicted in fig. 5.38 can be validated. To do so, the resulting system of coupled ODEs (eq. (5.4)) was solved with a 5th order Runge-Kutta algorithm written in PYTHON. The algorithm had the following characteristics:

1. Isomeric composition of the JSiR1 sample is: 92 % Iso, 5 % Rho and 3 % a-Meta
2. For speeding up the calculation, a variable step size between 250 ns and 20 µs was chosen depending on the rate constant for the reverse reaction
3. As a result, Batho and M_1 were omitted in the calculations
4. Possible photolysis of non-stable intermediate states was neglected
5. In principle, Rho can photoconvert to Iso but just via the all-*trans* state Batho. This two-photon process has typically a low quantum efficiency and was therefore modeled with $\Phi_{Rho \rightarrow Iso} = 0.005$[226]
6. a-Meta has a low probability of photoisomerization to Iso
7. The 8 % photoconversion rate of Iso determined in section 5.5.2 translates into a quantum efficiency of 0.15 to 0.25 (depending on the actual laser spot size) in line with previous studies for mono- and bistable opsins (for the calculation 0.25 was used)[226,227]
8. An irradiance of $5\,\mathrm{W\,cm^{-2}}$ at 495 nm was chosen to simulate the conditions used in the retinal extraction experiments[3]
9. Time constants and extinction coefficients are taken from figs. 5.36 and 5.37
10. Calculations were run until equilibrium of a photostationary mixture was reached (convergence criteria) .

As a measure for accuracy, the mean absolute percentage error (MAPE) was used:

$$\begin{aligned} accuracy =& \frac{100}{3} \cdot \left(\left| \frac{[Meta]_{HPLC} - [Meta]_{Calc}}{[Meta]_{HPLC}} \right| \right. \\ &+ \left. \left| \frac{[Rho]_{HPLC} - [Rho]_{Calc}}{[Rho]_{HPLC}} \right| + \left| \frac{[Iso]_{HPLC} - [Iso]_{Calc}}{[Iso]_{HPLC}} \right| \right) \end{aligned} \tag{5.6}$$

This leaves just four variables undefined: quantum yields for Rho → Meta, Meta → Rho and Meta → Iso as well as the time constant for the reverse reaction to finally test the suggested photocycle model. Figure 5.39 **A** shows how a photostationary mixture evolves over time. As expected, the thermally stable states and intermediates with long lifetimes accumulate under continuous illumination, i.e. Rho, a-Meta and Meso. After the light is switched off, Meso will decay into a-Meta which is considered

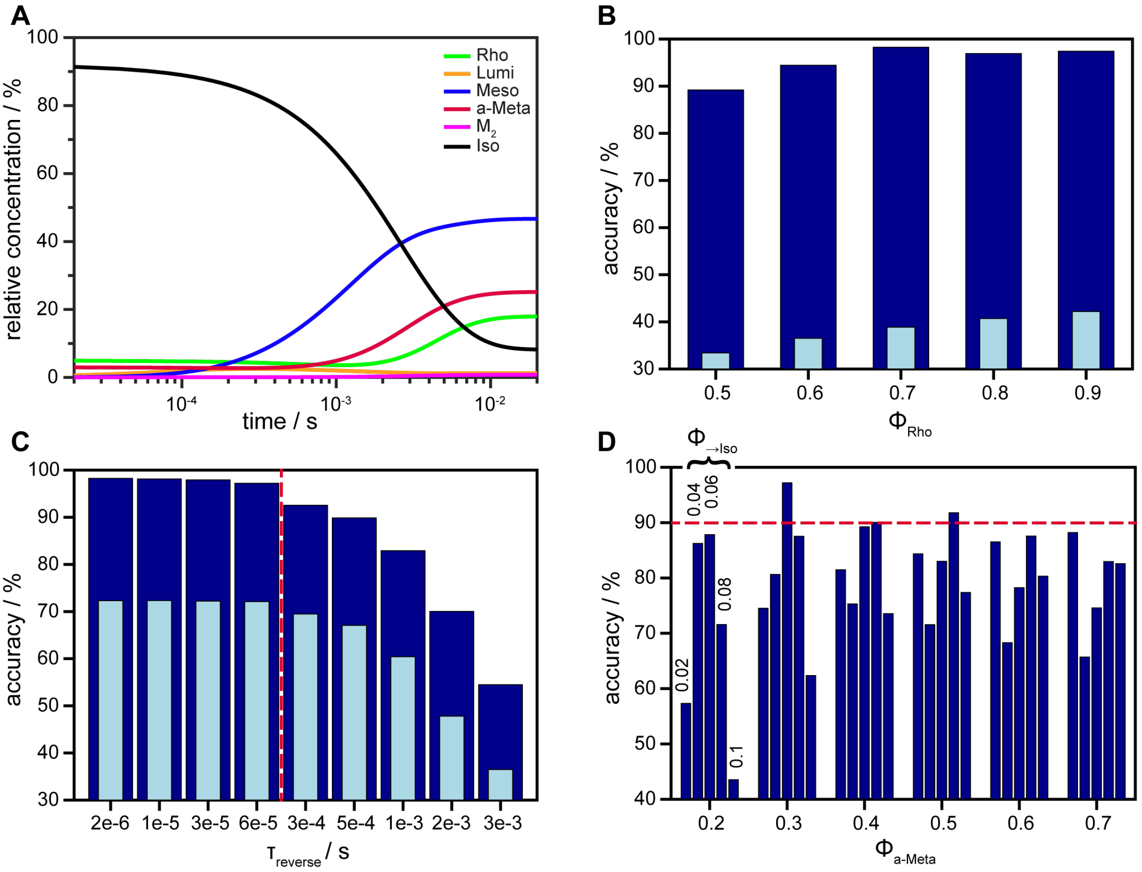

Figure 5.39: Photostationary state calculations modeling the proposed photocycle of fig. 5.38. **A:** Typical temporal evolution of the concentration profile of states ($\Phi_{Rho} = 0.7$, $\Phi_{Meta} = 0.3$, $\Phi_{Meta \to Iso} = 0.06$ and $\tau_{reverse} = 60\,\mu s$). **B:** Best achieved accuracy (dark blue) and overall performance (light blue) for all parameter combinations at a given quantum yield for Rho. **C:** Best achieved accuracy (dark blue) and overall performance (light blue) for all parameter combinations for $\Phi_{Rho} = 0.7$ at a given time constant for the reverse reaction a-Meta → Rho. **D:** Accuracies for $\Phi_{Rho} = 0.7$ and $\tau_{reverse} = 60\,\mu s$ for different quantum efficiencies of a-Meta. Individual bars represent values for the a-Meta → Iso transition of 0.02, 0.04, 0.06, 0.08, 0.1, respectively. An accuracy above 90% is considered to be in accordance with the HPLC data as indicated by the red dashed line.

in the analysis. First, all parameter combinations for a fixed quantum yield of Rho were analyzed (fig. 5.39 **B**). The dark blue bars represent the best achieved result while the thinner light blue bar indicate the overall performance (mean value of all parameter combinations). It is important to not just look at the best parameter scenario, because a low overall performance can point to just an exotic parameter combination. For quantum yields below 0.7 the accuracy starts to decline while above 0.7 the overall performance slightly increases indicating more parameter combinations with high accuracies. Actually, the best result is obtained with a quantum yield for the Rho → Meta reaction of 0.7 which is in accordance to many other rhodopsins[231]. Accordingly, this value is taken for further analysis on the influence of the time constant for photorecovery (fig. 5.39 **C**). Interestingly, the determined time constant for photorecovery of 60 µs marks a threshold. For faster time constants there is virtually no significant change in accuracy while it drops drastically for slower time constants.

This demonstrates that 60 µs is a reasonable time constant able to reproduce the HPLC results with the proposed two-photon reaction. It also illustrates that the reverse reaction has to be significantly faster than photoactivation so that a-Meta can accumulate.

Fixing a 0.7 quantum yield for Rho and 60 µs as the time constant for the reverse reaction permits insights about quantum efficiencies for a-Meta (fig. 5.39 **D**). An accuracy above 90 % is considered to be in accordance with the HPLC data due to the experimental error in determination of retinal isomers and uncertainties in exact light conditions. Individual bars represent values for the a-Meta → Iso transition of 0.02, 0.04, 0.06, 0.08, 0.1, respectively. Although the best accuracy is obtained with $\Phi_{a-Meta} = 0.3$ and $\Phi_{Meta \rightarrow Iso} = 0.06$, quantum yields of 0.4 and 0.5 for the reverse reaction and 0.08 for photoconversion to Iso also reach the 90 % accuracy mark. Overall, it becomes clear that a fast photorecovery in concert with a lower quantum yield for a-Meta compared to Rho are essential for a-Meta accumulation under continuous illumination. These findings support the proposed two-photon cycle of JSR1 of fig. 5.38.

5.5.4 Structural insights into photoswitching

Resonance Raman spectroscopy is a well suited technique to study the retinal and its electrostatic environment due to the chromophore selectivity. As demonstrated in section 5.5.3, JSiR1 establishes under continuous illumination a photostationary mixture consisting of mainly of Meso, a-Meta and Rho states. For resonance Raman spectroscopy, where a probing light inevitably photolyzes the sample, such a heterogeneous composition of states is challenging to analyze. After light exposure, Meso decays to a-Meta increasing its population and reducing the mixture to predominately a-Meta and less Rho states. A rotational cuvette filled with pre-illuminated JSiR1 solution provides always fresh sample in the probing laser spot permitting the spectroscopic investigation of the a-Meta/Rho mixture with a 532 nm laser (fig. 5.40 **A** green spectrum). One difference between a-Meta and Rho is the isomeric configuration of the retinal, i.e. all-*trans* and 11-*cis*, respectively. The fingerprint region, which is highly sensitive to the isomeric state of the retinal, exhibits a characteristic all-*trans* peak pattern around 1201 cm^{-1} with high similarity to the spectrum of the (light-adapted) ground state of bR[145]. Thus, a-Meta is indeed the predominant state in the sample. However, hydrogen-out-of-plane (HOOP) vibrations (900 to 1000 cm^{-1}) are usually weak for a thermally relaxed all-*trans* a-Meta state. Strong HOOP modes usually indicate a distorted polyene chain often found for *cis* isomers. On this basis, the band 967 cm^{-1} is assigned to Rho indicating its spectral presence but a contribution from a distorted all-*trans* retinal in a-Meta can not be excluded. The most intense C=C stretch band at 1536 cm^{-1} matches the correlation to the visible absorption and shows no asymmetric shape which reflects the same absorption maximum of a-Meta and Rho. Usually in a resonance Raman spectrum of rhodopsins, the C=N−H vibration of the protonated Schiff base (PSB) is the highest frequency band. Exchange of the proton to a deuterium (H/D exchange) shifts this band to lower wavenumbers (see section 5.2.1) allowing a clear assignment. Here, the band at 1644 cm^{-1} shifts to 1623 cm^{-1} upon deuteration while preserving the symmetric shape (fig. 5.40 **B**). This argues for the same isotope shift for a-Meta and Rho and thus points to a similar PSB hydrogen bond interaction in both states.

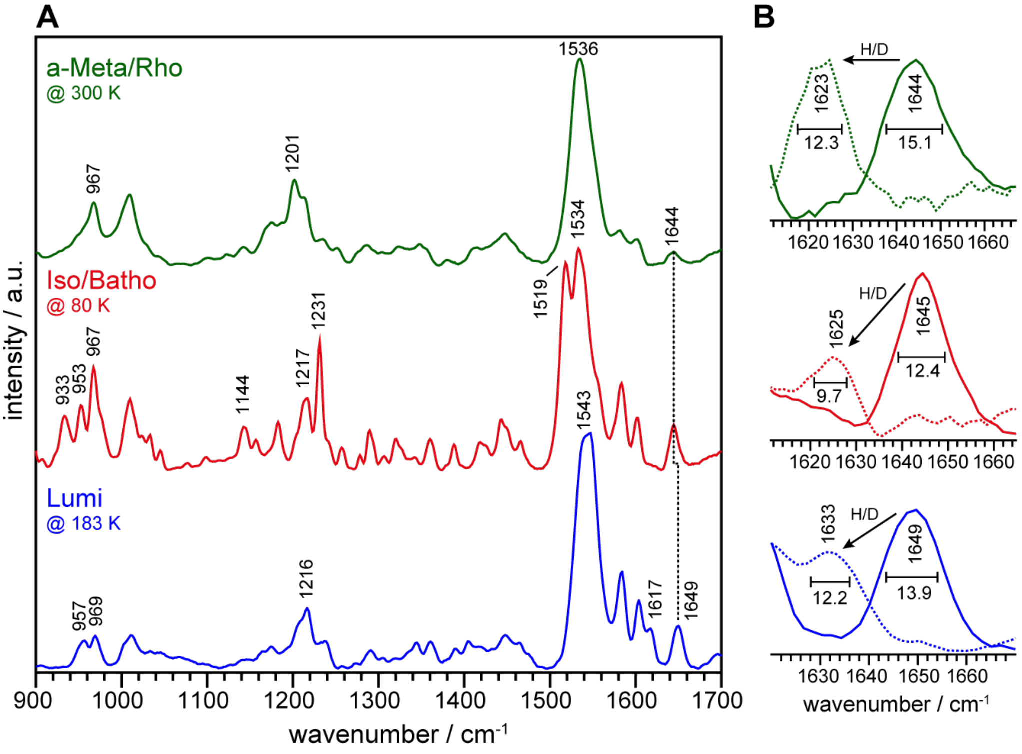

Figure 5.40: Resonance Raman spectroscopy on different states of JSR1. **A:** Top green spectrum refers to a-Meta/Rho mixture obtained at 300 K using a pre-illuminated JSiR1 solution in a rotational cuvette with Raman excitation at 532 nm. The red spectrum was recorded on a rehydrated JSiR1 film at 80 K with a probing wavelength of 532 nm. At this temperature thermal transitions are hindered resulting in a photostationary mixture of Iso and Batho. The blue Raman spectrum of Lumi was obtained at 183 K (−90 °C) with a Raman laser emitting at 457 nm. This blueshifted wavelength ensures an amplification of Lumi bands over other contributions. An additional laser at 532 nm initiated the photoconversion from Iso to Lumi. **B:** Enlarged Schiff base region. Dashed lines represent spectra taken in D_2O. H/D exchange was achieved by either washing the sample in D_2O or via vapor diffusion by glycerol/D_2O droplets placed in vicinity of a dried protein film. Peak positions and band widths were determined by band fitting with a Gaussian profile.

Cooling a rhodopsin to 80 K withdraws thermal energy needed for subsequent transitions after light absorption. In case of JSiR1, keeping the sample strictly in the dark while cooling it to cryogenic temperatures results in a photostationary mixture of Iso and Batho when subjected to the probing laser beam (fig. 5.40 **A** red spectrum). Spectroscopic studies on bovine, octopus and squid rhodopsin showed that intermediate states can be identified by their characteristic HOOP bands[232–235]. Accordingly, the band at 953 cm^{-1} can be assigned to isorhodopsin. The 9-*cis* configured retinal of Iso can be additionally identified by the fingerprint region band pattern with peaks at 1144, 1217 and 1231 cm^{-1} [232–234,236]. The C=C stretch region displays two pronounced bands at 1519 and 1534 cm^{-1}. Both frequencies does not fulfill the correlation to the visible absorption maximum of Iso at 505 nm. It can well be that this empirical correlation is not valid for 9-*cis* isomers. Although the band at 1519 cm^{-1} does not match the 590 nm visible absorption maximum of Batho either, it definitely indicate the presence of a redshifted intermediate state[148,237]. It seems that the ethylenic modes are split in Iso and Batho which gives rise to a more complex C=C band pattern. The spectral presence of Batho is further supported by the HOOP mode at 933 cm^{-1} which is at 940 cm^{-1} for Batho in octopus and squid rhodopsin[232,233]. The PSB mode is at 1645 cm^{-1} as identified by H/D exchange (fig. 5.40 **B**) with an isotope shift of 19 cm^{-1}. The same frequency along with the same isotope shift of the PSB as in the a-Meta/Rho mixture argues for an identical Schiff base environment for Iso, Rho, Batho and a-Meta which is in line with octopus and squid rhodopsin[232,236].

Increasing the temperature from 80 K permits thermal transitions to the following intermediate states. For octopus rhodopsin it was shown that Lumi is stable between −115 and −65 °C[238]. The blue spectrum in fig. 5.40 **A** was recorded at 183 K (−90 °C) while keeping the sample in the dark prior the measurement. A probing wavelength of 457 nm was chosen to selectively enhance signals of Lumi over other contributions. An additional laser emitting at 532 nm was focused on the sample spot to initiate the photoconversion of Iso to Lumi. The strongest C=C stretching vibration at 1543 cm^{-1} clearly reflects the blueshift in the visible absorption which is characteristic for Lumi. A HOOP mode at 957 cm^{-1} was shown to be a distinct feature of Lumi in bovine and octopus rhodopsin and evidently also for JSR1[233,239]. The Schiff Base region above 1600 cm^{-1} displays a small shoulder at 1617 and a pronounced band at 1649 cm^{-1}. A H/D exchange shifts the latter peak to lower wavenumbers by 16 cm^{-1} identifying it as a PSB vibration (fig. 5.40 **B**). This clearly demonstrates that the Schiff base is protonated in Lumi. The similar small deuterium isotope shift of 16 to 19 cm^{-1} in all investigated states, namely Iso, Rho, Meta, Batho & Lumi, implies a stable but rather weak hydrogen bond strength of the Schiff Base to its counterion system (see section 5.2.1). Yet, the C=N stretching frequency, which can be purely observed in D_2O, is higher in Lumi compared to the other states suggesting an increase in bond strength. Exactly the opposite was observed for bovine and octopus rhodopsin[240,241].

Analyzing the bandwidths of PSB vibrations in H_2O and D_2O permits to identify a water molecule to be part of the counterion complex[242]. Resonance energy transfer between the H_2O bending vibration of 1635 cm^{-1} and the C=N−H vibration shortens the lifetime of the PSB vibration. According to the uncertainty principle $\Delta E \Delta t \geq \hbar$, a lower lifetime broadens the energy distribution. This energy transfer is broken upon H_2O/D_2O exchange due to the shifted frequencies of heavy water vibrational modes resulting in a narrowed bandwidth in D_2O if a water molecule is in close vicinity to the PSB. The peaks presented in fig. 5.40 **B** were fitted with Gaussian profiles to determine peak positions and bandwidths. For Meta/Rho (from 15.1 ± 1.0 cm^{-1} to 12.3 ± 1.8 cm^{-1}) and Iso/Batho (from 12.4 ± 0.3 cm^{-1} to 9.7 ± 2.5 cm^{-1}) such a bandwidth narrowing is observed arguing for a neighboring water molecule. Indeed, a recently solved X-ray structure of JSiR1 shows a water molecule as part of the counterion complex[243]. In case of Lumi, the band narrowing is less pronounced and also more error prone (13.9 ± 0.5 cm^{-1} to 12.2 ± 3.7 cm^{-1}). Hence, the presence of a water molecule can not be unambiguously concluded in the Lumi state.

While the chromophore sensitivity of resonance Raman spectroscopy focuses on the retinal cofactor and its environment, infrared spectroscopy is not just sensitive to one part of the protein only. A difference FTIR spectrum of an illuminated minus dark JSiR1 sample at room temperature can reveal rearrangements of the protein backbone, protonation events of amino acid side chains and also vibrational changes of the retinal upon photoactivation. After recording a spectrum of dark 9-*cis* JSiR1, the sample was illuminated with a LED emitting at 470 nm converting it to a photostationary mixture consisting of predominately a-Meta and to lesser extent Rho states (see section 5.5.3). In the resulting difference spectrum, negative bands originate from JSiR1 while positive bands are associated with the transition to the photostationary mixture (fig. 5.41). Comparison of the retinal HOOP region with the Raman spectra of fig. 5.40 unveils the photoconversion from Iso to the photostationary mixture

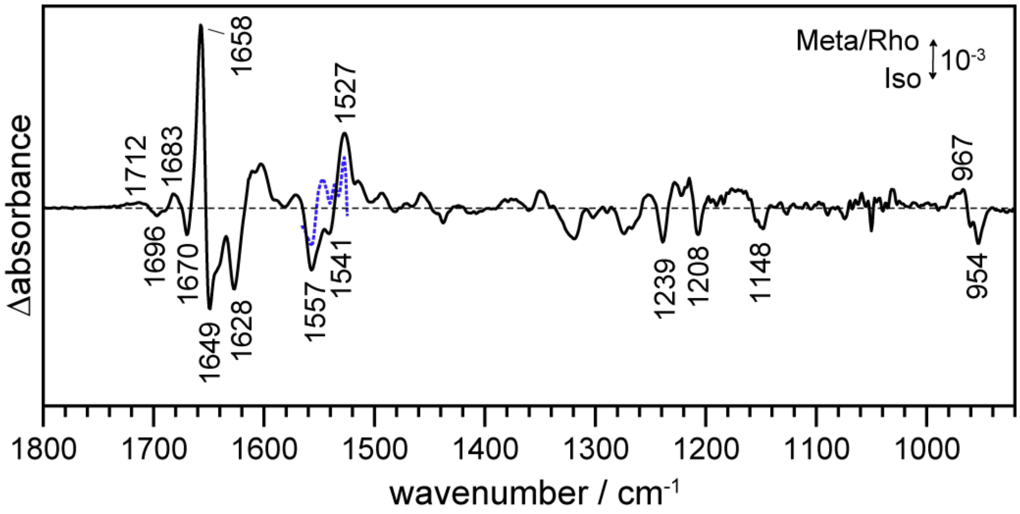

Figure 5.41: Light induced Fourier transform infrared (FTIR) absorbance difference spectrum of illuminated 9-*cis* JSiR1. Negative bands correspond to JSiR1 while positive bands are associated with the transition to the photostationary mixture a-Meta/Rho. Illumination was achieved with a light-emitting diode (LED) emitting at 470 nm. A constructed Raman difference spectrum in the C=C region is colored in blue and is scaled to match the FTIR data.

by the characteristic modes at 954(-) and 967(+)cm^{-1}, respectively. Further comparison shows that the 1559(-),1541(-)/1527(+)cm^{-1} feature can be attributed to the retinal C=C stretching vibrations of Iso and a-Meta/Rho, respectively. A constructed difference Raman spectrum of a-Meta/Rho minus Iso, colored in blue, solidifies this assignment (scaled to match the FTIR data). The absence of a negative band at 1519 cm^{-1} supports its previous assignment to a C=C mode of Batho which does not accumulate at room temperature. The fingerprint region exhibits three negative bands at 1148, 1208 and 1239 cm^{-1} which are characteristic for 9-*cis* isorhodopsin[234,241]. Direct comparison with the Raman spectra is not straight forward in this region due to other resonances of amino acid side chains. Furthermore, the positive bands, corresponding to Meta and Rho states, do not show explicit similarities to published spectra of bovine and octopus rhodopsin because of a different transition from Rho to a-Meta and not Iso to a-Meta[233,244].

Since both, Iso and Rho, are inactive states with different retinal isomers, it is expected that they predominantly just differ in the retinal moiety as it was shown for bovine and octopus rhodopsin[233,235]. Based on this, spectral changes above 1600 cm^{-1} can be attributed to the transition from Iso to the active state a-Meta. Contributions of PSB vibrations can be excluded due to identical frequencies in these states which in turn cancel in a difference spectrum (see fig. 5.40). The most pronounced amide I feature at 1649(-)/1658(+)cm^{-1} reflects that structural rearrangements of the protein backbone are associated with photoactivation. Protonation events and changes in hydrogen-bonding interactions of carboxylic residues can be monitored in the region above 1700 cm^{-1}. For JSiR1 no peaks in this region are detected for the transition from Iso to a-Meta, except from a weak band at 1712 cm^{-1}. This observation is in line with octopus rhodopsin where photoactivation also does not lead to changes in carboxylic bands[233,240]. In contrast, bovine rhodopsin exhibits strong bands in this region concurrently to a deprotonation of the Schiff base upon photoconversion from Rho to the signaling Meta-II state[244].

5.5.5 Conclusion

In this section, a first biophysical characterization of the bistable invertebrate rhodopsin JSR1 is presented. The methodical challenge of similar absorption profiles of the inactive Rho and active a-Meta state was addressed by reconstitution of JSR1 with 9-*cis* retinal (JSiR1). This leads to a blueshift of the visible absorption maximum and permits to resolve the formation of the thermally stable a-Meta conformation in a time-resolved UV/Vis difference experiment. Photoactivation of JSiR1 is completed with a time constant of 3 ms while passing three intermediate states, namely Batho ($\lambda_{max} = 590$ nm), Lumi ($\lambda_{max} = 490$ nm) and Meso ($\lambda_{max} = 510$ nm). Although kinetic data was only obtained for the Iso → Meta transition, it can be concluded from the measurement on pre-illuminated JSiR1 that Rho follows the same reaction path as Iso, as it is the case for other opsins[225,232]. A complex global fit analysis of the equilibrium reaction (Rho ↔ a-Meta) revealed a considerably faster photorecovery reaction with a time constant of 60 µs compromised of at least two intermediates. Based on these outcomes, a two-photon cycle model for JSR1 is proposed as shown in fig. 5.38.

Photostationary state calculations further solidified the derived reaction scheme of JSR1. Concentrations of thermally stable states after illumination obtained with HPLC could be quantitatively reproduced in the calculations. Under the assumption of a quantum yield of 0.7 for Rho, which is a common value among bistable opsins, it was demonstrated that a faster photoreverse reaction in concert with a lower quantum efficiency for a-Meta is a prerequisite for a predominant active state accumulation[231]. Best results were achieved with quantum yields between 0.3 and 0.5 for the reverse reaction in line with other bistable pigments[226,227].

Vibrational spectroscopy unveiled mechanistic details of photoactivation. Light-induced FTIR difference spectroscopy on JSiR1 demonstrated that formation of a-Meta is accompanied by structural rearrangements of the protein backbone presumably enabling G-protein binding. In contrast to bovine rhodopsin where the conversion from the inactive state to an active Meta-II conformation is characterized by a deprotonation of the Schiff base and pronounced carboxylic bands above 1700 $\mathrm{cm^{-1}}$, JSR1 does not exhibit any bands in this region upon photoactivation[244]. Furthermore, resonance Raman spectra in H_2O and D_2O clearly showed that a-Meta possesses a protonated Schiff base. The unique large blue shift of the Lumi state could hint to a deprotonation of the Schiff base during the forward reaction but is ruled out by the observed deuterium isotope shift in the Raman spectrum. In published crystal structures of squid rhodopsin, the glutamic acid counterion is too far away for a direct hydrogen bonding interaction to the PSB[245]. A water molecule between the PSB and the counterion may mediate the electrostatic interaction. Analysis of PSB bandwidths revealed a neighboring water molecule as part of the counterion complex in the thermally stable states in accordance to a recent X-ray structure of JSiR1[243]. A similar isotope shift in all investigated states suggests that the hydrogen bond interaction of the PSB remains constant throughout photoactivation. Taken together, the presented results strongly indicate that retinal isomerization induces structural changes in JSR1 eventually leading to the formation of a-Meta by rearrangements of the protein backbone without requiring the Schiff base to deprotonate.

6 SUMMARY & OUTLOOK

Interrogation of the energy landscape of (macro-)molecules can give insights into their structure and electrostatic environment. It further permits tracking protonation events or following changes of bond characteristics. Over the course of this work, several spectroscopic techniques were employed to investigate electronic and vibrational energy levels of the chromophore Zeaxanthin, as well as of a special class of chromophoric proteins, rhodopsins. Knowledge about structure and mechanistic details on the atomistic scale is crucial to utilize biological systems for technical applications such as optogenetics.

Organic voltage sensors are widely used to study neuronal activity or to characterize ion channels and pumps. Already in the 1970s, it was demonstrated that carotenoids embedded in a lipid membrane can serve as voltage sensors. Resonance Raman spectroscopy showed a voltage dependent and reversible intensity change between two major vibrational modes, the C=C stretch (ν_1) and a characteristic fingerprint vibration (ν_2)[21]. In chapter 4, surface-enhanced resonance Raman spectroscopy (SERRS) was used to study the voltage response of the carotenoid Zeaxanthin incorporated in a surface bound lipid bilayer. The combination of resonance and surface enhancement provides excellent sensitivity to investigate Zeaxanthin while applying an electric field across a single membrane. Unexpectedly, a change of the ν_1/ν_2 ratio was not observed, instead a new band at $1130\,\text{cm}^{-1}$ emerged in the fingerprint region (among other smaller spectral features) with higher electric field strengths. Further spectroscopic experiments and density functional theory (DFT) calculations revealed that this new band can be attributed to a 13-*cis* isomer of Zeaxanthin. Photoisomerization of carotenoids take place via a triplet excited electronic state. It seems that the electric field, if pointing along the polyene chain, increases the intersystem crossing probability between a singlet and a triplet which in turn also increases the rate of photoisomerization.

Rhodopsins are seven α-helical transmembrane proteins with a buried retinal chromophore attached to the protein backbone via a protonated Schiff base (PSB). Interestingly, these rhodopsins utilize the photoisomerization of retinal to trigger protein function. In the dark-adapted state of bacteriorhodopsin (bR), a microbial proton pump, the retinal is up to 60 % in an all-*trans* configuration while the remainder is 13-*cis*. This heterogeneity can be converted to a 100 % all-*trans* population upon illumination (light adaptation)[110,111]. Experiments shown in section 5.1 demonstrated that the same behavior is true for bR microcrystals. While light adaptation is a fast process (in the order of seconds), depending on the illumination intensity, the conversion back to the dark-adapted state has a determined time constant of 24 min. For a rehydrated purple membrane (PM) film a time constant of 28 min was obtained which suggests that differences in hydration level or a more rigid protein environment provided by the crystal lattice accelerates dark adaption in bR microcrystals.

A similar retinal configuration heterogeneity is observed in channelrhodopsin-2 from *Chlamydomonas reinhardtii* (CrChR2) with 30 % of 13-*cis* isomers in the ground state. CrChR2 is a microbial ion channel which is frequently used in optogenetics. Aside from the retinal heterogeneity, hybrid quantum mechanics/molecular mechanics (QM/MM) simulations revealed a flexible structure around the PSB permitting different hydrogen bond scenarios involving the amino acid side chains of E123 and D253[129]. A detailed analysis of the PSB vibrational band in the ground state of wild-type CrChR2 by resonance Raman spectroscopy conducted in section 5.2.1 revealed an asymmetric band shape which is strongly influenced upon variation of amino acid side chains. The low frequency component at 1661 cm^{-1} was identified to represent the PSB$\cdots$D253 motif while the band at 1665 cm^{-1} was assigned to a PSB$\cdots$E123 scenario. These different interactions of the PSB and E123 could be essential for a the voltage-dependent photocycle kinetics of ChR2[137]. In the T127A mutant, an isotope shift of 42 cm^{-1} in D_2O was obtained promoting it to the strongest hydrogen bond interaction between a PSB and an amino acid side chain observed so far. The increase of the hydrogen bond is not accompanied by shift in visible absorption[4]. This is particularly interesting because it is thought that the hydrogen bond interaction of the PSB plays a crucial role in the opsin shift in visible absorption[135].

Retinal heterogeneity is still a matter of debate for channelrhodopsin-1 from *Chlamydomonas augustae* (CaChR1). Studies suggested a pure all-*trans* ground state but controversially some others propose a 13-*cis* population of 30 %[140,144]. Among other things, these studies essentially relied on analysis of the C=C stretch vibration where a high frequency component around 1550 cm^{-1} was attributed to a 13-*cis* configuration. Section 5.2.2 presents a resonance Raman spectrum of the first intermediate P_1^{580} state after photoisomerization of the retinal from a predominantly all-*trans* isomeric state to 13-*cis*. The C=C in P_1^{580} exhibit distinct changes associated with a red shift in visible absorption. But the high frequency mode is nearly unaffected suggesting a more localized vibration which is not indicative for an isomeric configuration.

Section 5.3 illustrates how vibrational spectroscopy can reveal that distinct changes of the protein backbone induced by photoisomerization of the retinal are crucial for protein function. The high intensity output of quantum cascade lasers (QCLs) permitted recording an infrared absorption dataset from ns to s for halorhodopsin (hR) membrane patches with high hydration levels. Furthermore, it allowed the same experiment to be conducted on microcrystals. hR is a microbial chloride pump where the unidirectional ion transport requires some sort of back flow prevention, usually referred to as an ion accessibility switch. It can be suggested that this switch is associated with a rearrangement of the protein backbone observed as a negative amide I mode at 1660 cm^{-1} in the hL_2 intermediate. Microcrystals of hR lack this switch which indicates that the protein is non-functional in the crystal lattice. This result highlights the importance of a kinetic analysis of protein crystals prior to X-ray crystallography experiments.

The discovery of *Krokinobacter eikastus* rhodopsin 2 (KR2) was a surprise for the microbial rhodopsin community because it was thought that it is not possible for a rhodopsin to pump positively charged cations across the electrostatic repulsion at the PSB. However, investigation of the functional role of KR2 exposed it as a sodium (Na^+) pump. Several mechanistic models were proposed but proof for a transient ion binding site, which is needed for a switch to occur, was missing[182]. Together with the group of Jörg Standfuß from the Paul-Scherrer-Institut (PSI) in Switzerland, it was possible to shed light onto the mechanistic details of sodium pumping presented in section 5.4. Absorption spectroscopy on KR2 microcrystals showed that the protein is functional in the crystal lattice and highlighted important dynamic processes over the complete photoreaction which were further investigated by serial femtosecond X-ray crystallography. The combination of both techniques with atomistic resolution revealed a transient sodium binding site consisting of the amino acid side chains of N112 and D251. Furthermore, there are spectroscopic clues for a non ideal bidendate sodium coordination in agreement to the X-ray data. These insights about the sodium transport mechanism in KR2 will be helpful in the construction of protein variants for optogenetic applications.

In contrast to microbial rhodopsin, where the photoreaction eventually leads to the restoration of the ground state, invertebrate rhodopsins exhibit two thermally stable states. Photoisomerization of the retinal in the inactive form Rho converts it from an 11-*cis* configuration to all-*trans* in the active Meta conformation. A second photon finally restores the initial state, meaning that the protein can be switched between two conformations by light. Biophysical studies on invertebrate rhodopsins are scarce due to limitations in large-scale production. The group of Gebhard Schertler at the PSI succeeded to overcome these limitations permitting the first biological characterization of the invertebrate jumping spider rhodopsin-1 (JSR1) presented in section 5.5. A comprehensive scheme of the two-photon reaction could be constructed with time-resolved absorption spectroscopy in the visible despite the experimental challenge of a similar absorption profile of the active and inactive state. Vibrational spectroscopy further revealed that the PSB stays protonated throughout the whole photoreaction showing that a deprotonation, as in (monostable) bovine rhodopsin, is not a prerequisite for protein function in G-protein coupled receptors (GPCRs). Resonance Raman spectroscopy revealed a proposed water molecule as part of the counterion complex of the PSB which is in in agreement with data obtained with X-ray crystallography[243].

In conclusion, three achievements of this work will be highlighted. Zeaxanthin is a new promising organic voltage sensor which does not need to be attached to a more complex system and is thus easy to use. Its simple spectral profile and the commercial availability further underlines a possible wide-spread use. For a optogenetic application, the carotenoid can be harbored by another protein which then provides the specificity of genetic targeting[246]. JSR1 proved to be a candidate as a model system which can be used to deepen our understanding of bistability in GPCRs. Such a molecular switch will certainly find its use in optogentics. The synergy of time-resolved absorption spectroscopy on crystals with serial femtosecond X-ray crystallography is a powerful tool to scrutinize mechanistic details of protein function on a atomistic level. The pioneering work on KR2 is beyond doubt just a first stepping stone in this direction.

BIBLIOGRAPHY

1. Schnedermann, C. *et al.* Vibronic Dynamics of the Ultrafast all-trans to 13-cis Photoisomerization of Retinal in Channelrhodopsin-1. *Journal of the American Chemical Society* **138,** 1–8 (2016). doi: 10.1021/jacs.5b12251.
2. Kovacs, G. N. *et al.* Three-dimensional view of ultrafast dynamics in photoexcited bacteriorhodopsin. *Nature Communications* (2019). doi: 10.1038/s41467-019-10758-0.
3. **Ehrenberg, D.** *et al.* The two-photon reversible reaction of the bistable jumping spider rhodopsin-1. *Biophysical journal* **116,** 1248–1258 (2019). doi: 10.1016/j.bpj.2019.02.025.
4. **Ehrenberg, D.** *et al.* Atomistic insight into the role of threonine 127 in the functional mechanism of channelrhodopsin-2. *Applied Sciences* **9,** 4905 (2019). doi: 10.3390/app9224905.
5. Skopintsev, P. *et al.* Femtosecond to millisecond structural changes in a light-driven sodium pump. *Nature - under revision* (2020).
6. **Ehrenberg, D.** & Heberle, J. Voltage sensing by Raman Spectroscopy of Zeaxanthin. *Manuscript in preparation.*
7. Peterka, D. S., Takahashi, H. & Yuste, R. Imaging voltage in neurons. *Neuron* **69,** 9–21 (2011).
8. Deisseroth, K. Optogenetics. *Nature methods* **8,** 26 (2011).
9. Wang, C. & Tauber, M. J. High Yield Singlet Fission in a Zeaxanthin Aggregate Observed by Picosecond Time-Resolved Resonance Raman Spectroscopy. *Journal of the American Chemical Society* **132,** 1–17 (2010).
10. Müller, D. J., Wu, N. & Palczewski, K. Vertebrate membrane proteins: structure, function, and insights from biophysical approaches. *Pharmacological reviews* **60,** 43–78 (2008).
11. Rivalta, I., Nenov, A. & Garavelli, M. Modelling retinal chromophores photoisomerization: from minimal models in vacuo to ultimate bidimensional spectroscopy in rhodopsins. *Physical Chemistry Chemical Physics* **16,** 16865–16879 (2014).
12. Spira, M. E. & Hai, A. Multi-electrode array technologies for neuroscience and cardiology. *Nature nanotechnology* **8,** 83 (2013).
13. Alivisatos, A. P. *et al. Nanotools for neuroscience and brain activity mapping* 2013.
14. Yang, H. H. & St-Pierre, F. Genetically encoded voltage indicators: opportunities and challenges. *Journal of Neuroscience* **36,** 9977–9989 (2016).
15. Lin, M. Z. & Schnitzer, M. J. Genetically encoded indicators of neuronal activity. *Nature neuroscience* **19,** 1142 (2016).
16. Nagel, G. *et al.* Channelrhodopsin-1: a light-gated proton channel in green algae. *Science* **296,** 2395–2398 (2002).
17. Boyden, E. S., Zhang, F., Bamberg, E., Nagel, G. & Deisseroth, K. Millisecond-timescale, genetically targeted optical control of neural activity. *Nature neuroscience* **8,** 1263 (2005).
18. Baker, C. K. & Flannery, J. G. Innovative optogenetic strategies for vision restoration. *Frontiers in cellular neuroscience* **12** (2018).

19. Imai, Y. *et al.* Light-driven activation of mitochondrial proton-motive force improves motor behaviors in a Drosophila model of Parkinson's disease. *Communications Biology* **2,** 1–11 (2019).

20. Packer, A. M., Russell, L. E., Dalgleish, H. W. & Häusser, M. Simultaneous all-optical manipulation and recording of neural circuit activity with cellular resolution in vivo. *Nature methods* **12,** 140 (2015).

21. Szalontai, B., Bagyinka, C., Horvath, L. & Horváth, L. I. Changes in the Raman Spectrum of Frog Sciatic Nerve During Action Potential Propagation. *Biochemical and Biophysical Research Communications* **76,** 660–665 (1977).

22. Sathyanarayana, D. N. *Vibrational spectroscopy: theory and applications* (New Age International, 2015).

23. Leach, A. R. & Leach, A. R. *Molecular modelling: principles and applications* (Pearson education, 2001).

24. Bunker, P. R. & Jensen, P. *Molecular symmetry and spectroscopy* (NRC Research Press, 2006).

25. Ferraro, J. R. *Introductory Raman Spectroscopy* (Academic press, 2003).

26. Koleżyński, A. & Król, M. *Molecular Spectroscopy: Experiment and Theory: From Molecules to Functional Materials* (Springer, 1901).

27. Siebert, F. & Hildebrandt, P. *Vibrational spectroscopy in life science* (John Wiley & Sons, 2008).

28. Chalmers, J. & Griffiths, P. *Handbook of Vibrational Spectroscopy, 5 volumes set.* (Wiley, 2002).

29. Atkins, P., De Paula, J. & Friedman, R. *Quanta, matter, and change: a molecular approach to physical chemistry* (Oxford University Press, 2009).

30. Campbell, I. *Biophysical techniques* (Oxford University Press, 2012).

31. Bernath, P. *Spectra of Atoms and Molecules* (Oxford University Press, USA, 2005).

32. Aruldhas, G. *Molecular structure and spectroscopy* (PHI Learning Pvt. Ltd., 2007).

33. Griffiths, P. *Transform techniques in chemistry* (Springer Science & Business Media, 2012).

34. Hugi, A., Maulini, R. & Faist, J. External cavity quantum cascade laser. *Semiconductor Science and Technology* **25,** 083001 (2010).

35. Schultz, B.-J., Mohrmann, H., Lorenz-Fonfria, V. A. & Heberle, J. Protein dynamics observed by tunable mid-IR quantum cascade lasers across the time range from 10 ns to 1 s. *Spectrochimica Acta Part A: Molecular and Biomolecular Spectroscopy* **188,** 666–674 (2018).

36. Larkin, P. *Infrared and Raman spectroscopy; principles and spectral interpretation* (Elsevier, 2011).

37. Smith, E. & Dent, G. *Modern Raman spectroscopy: a practical approach* (John Wiley & Sons, 2005).

38. Aroca, R. *Surface-enhanced vibrational spectroscopy* (John Wiley & Sons, 2006).

39. Mayer, K. M. & Hafner, J. H. Localized surface plasmon resonance sensors. *Chemical reviews* **111,** 3828–3857 (2011).

40. Wiederrecht, G. *Handbook of nanoscale optics and electronics* (Academic Press, 2010).

41. Kneipp, K., Moskovits, M. & Kneipp, H. *Surface-enhanced Raman scattering: physics and applications* (Springer Science & Business Media, 2006).

42. Mueller, N. S., Heeg, S. & Reich, S. Surface-enhanced Raman scattering as a higher-order Raman process. *Physical Review A* **94,** 023813 (2016).

43. Sahni, V. in *Quantal Density Functional Theory* 67–133 (Springer, 2016).

44. Lewars, E. Computational chemistry. *Introduction to the theory and applications of molecular and quantum mechanics,* 318 (2003).

45. Capelle, K. A bird's-eye view of density-functional theory. *Brazilian Journal of Physics* **36,** 1318–1343 (2006).

46. Marques, M. *et al. Time-dependent density functional theory* (Springer Science & Business Media, 2006).
47. Chemla, S. & Chavane, F. Voltage-sensitive dye imaging: technique review and models. *Journal of Physiology-Paris* **104,** 40–50 (2010).
48. Xiong, H. *et al.* Stimulated Raman excited fluorescence spectroscopy and imaging. *Nature Photonics* **13,** 412 (2019).
49. Britton, G., Liaaen-Jensen, S. & Pfander, H. *Carotenoids, vol. 4: natural functions* (Springer Science & Business Media, 2008).
50. Kakitani, T., Honig, B. & Crofts, A. R. Theoretical studies of the electrochromic response of carotenoids in photosynthetic membranes. *Biophysical journal* **39,** 57–63 (1982).
51. Althaus, T., Eisfeld, W., Lohrmann, R. & Stockburger, M. Application of Raman spectroscopy to retinal proteins. *Israel journal of chemistry* **35,** 227–251 (1995).
52. Johnson, J. H., Lewis, A. & Gogel, G. Kinetic Resonance Raman Spectroscopy of Carotenoids: A Sensitive Kinetic Monitor of Bacteriorhodopsin Mediated Membrane Potential Changes. *Biochemical and Biophysical Research Communications* **103,** 182–188 (1981).
53. Koyama, Y., Long, R. A., Martin, W. G. & Carey, P. R. The resonance Raman spectrum of carotenoids as an intrinsic probe for membrane potential. Oscillatory changes in the spectrum of neurosporene in the chromatophores of Rhodopseudomonas sphaeroides. *Biochimica et biophysica acta* **548,** 153–160 (1979).
54. Paschenko, V. Z., Vershinin, A. O. & Churin, A. A. Electrochromic behaviour of carotenoid molecules in nerve cell membranes: a resonance Raman study. *Journal of Photochemistry and Photobiology B: Biology* **18,** 127–130 (1993).
55. Hoskins, L. The resonance Raman excitation profile of lutein. *Spectrochimica Acta Part A: Molecular Spectroscopy* **42,** 169–173 (1986).
56. Shaw, S. K., Lagutchev, A., Dlott, D. D. & Gewirth, A. A. Sum-frequency spectroscopy of molecular adsorbates on low-index Ag surfaces: Effects of azimuthal rotation. *Analytical chemistry* **81,** 1154–1161 (2008).
57. Schkolnik, G. *et al.* Vibrational Stark effect of the electric-field reporter 4-mercaptobenzonitrile as a tool for investigating electrostatics at electrode/SAM/solution interfaces. *International journal of molecular sciences* **13,** 7466–7482 (2012).
58. Slekiene, N., Ramanauskaite, L. & Snitka, V. Surface enhanced Raman spectroscopy of self-assembled layers of lipid molecules on nanostructured Au and Ag substrates. *Chemistry and physics of lipids* **203,** 12–18 (2017).
59. Saint-Pierre Chazalet, M. *et al.* Surface-enhanced Raman scattering studies of lipid planar bilayers in water. *Thin Solid Films* **244,** 852–856 (1994).
60. Krishnamurty, S. *et al.* Density functional theory-based conformational analysis of a phospholipid molecule (dimyristoyl phosphatidylcholine). *The Journal of Physical Chemistry B* **112,** 13433–13442 (2008).
61. Bunow, M. R. & Levin, I. W. Comment on the carbon-hydrogen stretching region of vibrational Raman spectra of phospholipids. *Biochimica et Biophysica Acta (BBA)-Lipids and Lipid Metabolism* **487,** 388–394 (1977).
62. Ye, Q., Fang, J. & Sun, L. Surface-enhanced Raman scattering from functionalized self-assembled monolayers. 2. Distance dependence of enhanced Raman scattering from an azobenzene terminal group. *The Journal of Physical Chemistry B* **101,** 8221–8224 (1997).
63. Spiker Jr, R. C. & Levin, I. W. Raman spectra and vibrational assignments for dipalmitoyl phosphatidylcholine and structurally related molecules. *Biochimica et Biophysica Acta (BBA)-Lipids and Lipid Metabolism* **388,** 361–373 (1975).

64. Stewart, S. & Fredericks, P. Surface-enhanced Raman spectroscopy of amino acids adsorbed on an electrochemically prepared silver surface. *Spectrochimica Acta Part A: Molecular and Biomolecular Spectroscopy* **55,** 1641–1660 (1999).
65. Wen, R. & Fang, Y. Adsorption of pyridine carboxylic acids on silver surface investigated by potential-dependent SERS. *Vibrational spectroscopy* **39,** 106–113 (2005).
66. MacDonald, R. C. *et al.* Small-volume extrusion apparatus for preparation of large, unilamellar vesicles. *Biochimica et Biophysica Acta (BBA)-Biomembranes* **1061,** 297–303 (1991).
67. Gruszecki, W. I. & Sielewiesiuk, J. Orientation of xanthophylls in phosphatidylcholine multibilayers. *Biochimica et Biophysica Acta (BBA)-Biomembranes* **1023,** 405–412 (1990).
68. Van de Ven, M., Kattenberg, M., Van Ginkel, G. & Levine, Y. Study of the orientational ordering of carotenoids in lipid bilayers by resonance-Raman spectroscopy. *Biophysical journal* **45,** 1203–1209 (1984).
69. Gruszecki, W. I. in *The photochemistry of carotenoids* 363–379 (Springer, 1999).
70. Johnson, Q. R., Mostofian, B., Gomez, G. F., Smith, J. C. & Cheng, X. Effects of carotenoids on lipid bilayers. *Physical Chemistry Chemical Physics* **20,** 3795–3804 (2018).
71. Cerezo, J., Zuniga, J., Bastida, A., Requena, A. & Ceron-Carrasco, J. P. Conformational changes of β-carotene and zeaxanthin immersed in a model membrane through atomistic molecular dynamics simulations. *Physical Chemistry Chemical Physics* **15,** 6527–6538 (2013).
72. Bando, Y., Sakamoto, M., Kim, S., Ayzenshtat, I. & Yuste, R. Comparative evaluation of genetically encoded voltage indicators. *Cell reports* **26,** 802–813 (2019).
73. Wang, C., Schlamadinger, D. E., Desai, V. & Tauber, M. J. Triplet excitons of carotenoids formed by singlet fission in a membrane. *ChemPhysChem* **12,** 2891–2894 (2011).
74. Köhn, S. *et al.* in *carotenoids* 53–98 (Springer, 2008).
75. Sujak, A., Okulski, W. & Gruszecki, W. I. Organization of xanthophyll pigments lutein and zeaxanthin in lipid membraned formed with dipalmitoylphosphadylcholine. *Biochimica et Biophysica Acta* **1509,** 255–263 (2000).
76. Billsten, H. H., Sundström, V. & Polıvka, T. Self-assembled aggregates of the carotenoid zeaxanthin: time-resolved study of excited states. *The Journal of Physical Chemistry A* **109,** 1521–1529 (2005).
77. Okulski, W., Sujak, A. & Gruszecki, W. I. Dipalmitoylphosphatidylcholine membranes modified with zeaxanthin: numeric study of membrane organisation. *Biochimica et Biophysica Acta (BBA)-Biomembranes* **1509,** 216–228 (2000).
78. Lettieri, R. *et al.* DPPTE Thiolipid Self-Assembled Monolayer: A Critical Assay. *Langmuir* **32** (2016).
79. Gruszecki, W. I. & Strzałka, K. Carotenoids as modulators of lipid membrane physical properties. *Biochimica et Biophysica Acta (BBA)-Molecular Basis of Disease* **1740,** 108–115 (2005).
80. Mabrey, S. & Sturtevant, J. M. Investigation of phase transitions of lipids and lipid mixtures by sensitivity differential scanning calorimetry. *Proceedings of the National Academy of Sciences* **73,** 3862–3866 (1976).
81. Wang, C., Berg, C. J., Hsu, C. C., Merrill, B. A. & Tauber, M. J. Characterization of carotenoid aggregates by steady-state optical spectroscopy. *Journal of Physical Chemistry B* **116,** 10617–10630 (2012).
82. Inagaki, F., Tasumi, M. & Miyazawa, T. Vibrational analysis of polyene chains. Assignments of the resonance Raman lines of poly (acetylene) and β-carotene. *Journal of Raman Spectroscopy* **3,** 335–343 (1975).
83. Mendelsohn, R. & Van Holten, R. W. Zeaxanthin as a resonance raman and visible absorption probe of membrane structure. **27,** 221–235 (1979).
84. Aslanian, D., Vainer, H. & Guesdon, J.-P. Thermotropic state transition in isolated platelet membranes studied by Raman spectroscopy. *European journal of biochemistry* **131,** 555–558 (1983).

85. Andreeva, A., Apostolova, I. & Velitchkova, M. Temperature dependence of resonance Raman spectra of carotenoids. *Spectrochimica Acta Part A: Molecular and Biomolecular Spectroscopy* **78,** 1261–1265 (2011).

86. Kuki, M., Koyama, Y. & Nagae, H. Triplet-Sensitized and Thermal Isomerization of All-Trans, 7-Cis, 9-Cis, 13-Cls, and 15-Cls Isomers of /9-Carotene: Configurational Dependence of the Quantum Yield of Isomerization via the T1 State.

87. Chen, B. & Huang, J. Degradation and isomerization of chlorophyll a and β-carotene as affected by various heating and illumination treatments. *Food Chemistry* **62,** 299–307 (1998).

88. Milanowska, J. & Gruszecki, W. I. Heat-induced and light-induced isomerization of the xanthophyll pigment zeaxanthin. *Journal of Photochemistry and Photobiology B: Biology* **80,** 178–186 (2005).

89. Macernis, M., Sulskus, J., Malickaja, S., Robert, B. & Valkunas, L. Resonance Raman spectra and electronic transitions in carotenoids: a density functional theory study. *The Journal of Physical Chemistry A* **118,** 1817–1825 (2014).

90. Frisch, M. J. *et al.* Gaussian˜09. Gaussian Inc. Wallingford CT (2009).

91. Koyama, Y., Takatsuka, I., Nakata, M. & Tasumi, M. Raman and infrared spectra of the all-trans, 7-cis, 9-cis, 13-cis and 15-cis isomers of β-carotene: Key bands distinguishing stretched or terminal-bent configurations form central-bent configurations. *Journal of Raman spectroscopy* **19,** 37–49 (1988).

92. Ceron-Carrasco, J., Bastida, A., Zuniga, J., Requena, A. & Miguel, B. Density functional theory study of the stability and vibrational spectra of the β-carotene isomers. *The Journal of Physical Chemistry A* **113,** 9899–9907 (2009).

93. Hashimoto, H. & Koyama, Y. Time-resolved resonance Raman spectroscopy of triplet. beta.-carotene produced from all-trans, 7-cis, 9-cis, 13-cis, and 15-cis isomers and high-pressure liquid chromatography analyses of photoisomerization via the triplet state. *The Journal of Physical Chemistry* **92,** 2101–2108 (1988).

94. Wormit, M. & Dreuw, A. Quantum chemical insights in energy dissipation and carotenoid radical cation formation in light harvesting complexes. *Physical Chemistry Chemical Physics* **9,** 2917–2931 (2007).

95. Andreussi, O., Knecht, S., Marian, C. M., Kongsted, J. & Mennucci, B. Carotenoids and light-harvesting: From DFT/MRCI to the tamm–dancoff approximation. *Journal of chemical theory and computation* **11,** 655–666 (2015).

96. Spezia, R., Knecht, S. & Mennucci, B. Excited state characterization of carbonyl containing carotenoids: a comparison between single and multireference descriptions. *Physical Chemistry Chemical Physics* **19,** 17156–17166 (2017).

97. Coccia, E., Varsano, D. & Guidoni, L. Ab initio geometry and bright excitation of carotenoids: quantum Monte Carlo and many body green's function theory calculations on peridinin. *Journal of chemical theory and computation* **10,** 501–506 (2014).

98. Dreuw, A., Fleming, G. R. & Head-Gordon, M. Charge-transfer state as a possible signature of a zeaxanthin- chlorophyll dimer in the non-photochemical quenching process in green plants. *The Journal of Physical Chemistry B* **107,** 6500–6503 (2003).

99. Yaroshevich, I., Krasilnikov, P. & Rubin, A. Functional interpretation of the role of cyclic carotenoids in photosynthetic antennas via quantum chemical calculations. *Computational and Theoretical Chemistry* **1070,** 27–32 (2015).

100. Shrestha, R., Anderson, C. M., Cardenas, A. E., Elber, R. & Webb, L. J. Direct measurement of the effect of cholesterol and 6-ketocholestanol on the membrane dipole electric field using vibrational stark effect spectroscopy coupled with molecular dynamics simulations. *The Journal of Physical Chemistry B* **121,** 3424–3436 (2017).

101. Rondonuwu, F. S., Watanabe, Y., Fujii, R. & Koyama, Y. A first detection of singlet to triplet conversion from the 11Bu- to the 13Ag state and triplet internal conversion from the 13Ag to the 13Bu state in carotenoids: dependence on the conjugation length. *Chemical physics letters* **376,** 292–301 (2003).

102. Hasson, K., Gai, F. & Anfinrud, P. A. The photoisomerization of retinal in bacteriorhodopsin: experimental evidence for a three-state model. *Proceedings of the National Academy of Sciences* **93,** 15124–15129 (1996).

103. Stoeckenius, W. & Rowen, R. A morphological study of Halobacterium halobium and its lysis in media of low salt concentration. *The Journal of cell biology* **34,** 365–393 (1967).

104. Oesterhelt, D. & Stoeckenius, W. Rhodopsin-like protein from the purple membrane of Halobacterium halobium. *Nature new biology* **233,** 149 (1971).

105. Lewis, A., Spoonhower, J., Bogomolni, R. A., Lozier, R. H. & Stoeckenius, W. Tunable laser resonance Raman spectroscopy of bacteriorhodopsin. *Proceedings of the National Academy of Sciences* **71,** 4462–4466 (1974).

106. Rothschild, K. J., Zagaeski, M. & Cantore, W. A. Conformational changes of bacteriorhodopsin detected by Fourier transform infrared difference spectroscopy. *Biochemical and biophysical research communications* **103,** 483–489 (1981).

107. Hampp, N. Bacteriorhodopsin as a photochromic retinal protein for optical memories. *Chemical Reviews* **100,** 1755–1776 (2000).

108. Borshchevskiy, V. I., Round, E. S., Popov, A. N., Büldt, G. & Gordeliy, V. I. X-ray-radiation-induced changes in bacteriorhodopsin structure. *Journal of molecular biology* **409,** 813–825 (2011).

109. Mizuide, N. *et al.* Structural changes in bacteriorhodopsin following retinal photoisomerization from the 13-cis form. *Biochemistry* **45,** 10674–10681 (2006).

110. Smith, S. 0., Pardoen, J. a., Lugtenburg, J. & Mathies, R. a. Vibrational Analysis of the 13-cis-Retinal Chromophore in Dark-Adapted Bacteriorhodopsin. *Journal of Physical Chemistry* **91,** 804–819 (1987).

111. Maeda, A., Iwasa, T. & Yoshizawa, T. Isomeric composition of retinal chromophore in dark-adapted bacteriorhodopsin. *Journal of Biochemistry* **82,** 1599–1604 (1977).

112. Bagley, K. *et al.* Fourier transform infrared difference spectroscopy of bacteriorhodopsin and its photoproducts. *Proceedings of the National Academy of Sciences of the United States of America* **79,** 4972–4976 (1982).

113. Maeda, A. Application of FTIR Spectroscopy to the Structural Study on the Function of Bacteriorhodopsin. *Israel Journal of Chemistry* **35,** 387–400 (1995).

114. Althaus, T., Eisfeld, W., Lohrmann, R. & Stockburger, M. Application of Raman spectroscopy to retinal proteins. *Israel Journal of Chemistry* **35,** 227 (1995).

115. Efremov, R. G., Gordeliy, V. I., Heberle, J. & Büldt, G. Time-resolved microspectroscopy on a single crystal of bacteriorhodopsin reveals lattice-induced differences in the photocycle kinetics. *Biophysical journal* **91,** 1441–51 (2006).

116. Scherrer, P., Mathew, M. K., Sperling, W. & Stoeckenius, W. Retinal Isomer Ratio in Dark-Adapted Purple Membrane and Bacteriorhodopsin Monomers. *Biochemistry* **28,** 829–834 (1989).

117. Alshuth, T. & Stockburger, M. Structural changes in the retinal chromophore of bacteriorhodopsin studied by resonance Raman spectroscopy. *Berichte der Bunsengesellschaft für physikalische Chemie* **85,** 484–489 (1981).

118. Horwitz, J. & Heller, J. Interactions of all-trans-, 9-, 11-, and 13-cis-retinal, all-trans-retinyl acetate, and retinoic acid with human retinol-binding protein and prealbumin. *Journal of Biological Chemistry* **248,** 6317–6324 (1973).

119. Ueki, N. *et al.* Eyespot-dependent determination of the phototactic sign in Chlamydomonas reinhardtii. *Proceedings of the National Academy of Sciences* **113,** 5299–5304 (2016).

120. Schneider, F., Grimm, C. & Hegemann, P. Biophysics of channelrhodopsin. *Annual review of biophysics* **44,** 167–186 (2015).

121. Lórenz-Fonfrıa, V. A. & Heberle, J. Channelrhodopsin unchained: structure and mechanism of a light-gated cation channel. *Biochimica et Biophysica Acta (BBA)-Bioenergetics* **1837,** 626–642 (2014).

122. Bruun, S. *et al.* Light–dark adaptation of channelrhodopsin involves photoconversion between the all-trans and 13-cis retinal isomers. *Biochemistry* **54,** 5389–5400 (2015).

123. Lórenz-Fonfrıa, V. A. *et al.* Pre-gating conformational changes in the ChETA variant of channelrhodopsin-2 monitored by nanosecond IR spectroscopy. *Journal of the American Chemical Society* **137,** 1850–1861 (2015).

124. Lórenz-Fonfría, V. a. & Heberle, J. Channelrhodopsin unchained: Structure and mechanism of a light-gated cation channel. *Biochimica et Biophysica Acta - Bioenergetics* **1837,** 626–642 (2014).

125. Nack, M., Radu, I., Bamann, C., Bamberg, E. & Heberle, J. The retinal structure of channelrhodopsin-2 assessed by resonance Raman spectroscopy. *FEBS Letters* **583,** 3676–3680 (2009).

126. Hegemann, P., Ehlenbeck, S. & Gradmann, D. Multiple Photocycles of Channelrhodopsin. *Biophysical Journal* **89,** 3911–3918 (2005).

127. Saita, M. *et al.* Photoexcitation of the P4480 state induces a secondary photocycle that potentially desensitizes channelrhodopsin-2. *Journal of the American Chemical Society* **140,** 9899–9903 (2018).

128. Kuhne, J. *et al.* Unifying photocycle model for light adaptation and temporal evolution of cation conductance in channelrhodopsin-2. *Proceedings of the National Academy of Sciences* **116,** 9380–9389 (2019).

129. Guo, Y. *et al.* Active site structure and absorption spectrum of channelrhodopsin-2 wild-type and C128T mutant. *Chem. Sci.* **7,** 3879–3891 (2016).

130. Lórenz-Fonfría, V. A. *et al.* Transient protonation changes in channelrhodopsin-2 and their relevance to channel gating. *Proceedings of the National Academy of Sciences of the United States of America* **110,** 73–81 (2013).

131. Volkov, O. *et al.* Structural insights into ion conduction by channelrhodopsin 2. *Science* **358** (2017).

132. Russell, T. S., Coleman, M., Rath, P., Nilsson, A. & Rothschild, K. J. Threonine-89 participates in the active site of bacteriorhodopsin: evidence for a role in color regulation and Schiff base proton transfer. *Biochemistry* **36,** 7490–7497 (1997).

133. Luecke, H., Richter, H.-T. & Lanyi, J. K. Proton transfer pathways in bacteriorhodopsin at 2.3 angstrom resolution. *Science* **280,** 1934–1937 (1998).

134. Aton, B. *et al.* Resonance Raman studies of the primary photochemical event in visual pigments. *Biophysical journal* **29,** 79–94 (1980).

135. Nielsen, M. B. Model systems for understanding absorption tuning by opsin proteins. *Chemical Society Reviews* **38,** 913–924 (2009).

136. Hu, J., Griffin, R. G. & Herzfeld, J. Synergy in the spectral tuning of retinal pigments: complete accounting of the opsin shift in bacteriorhodopsin. *Proceedings of the National Academy of Sciences* **91,** 8880–8884 (1994).

137. Berndt, A. *et al.* High-efficiency channelrhodopsins for fast neuronal stimulation at low light levels. *Proceedings of the National Academy of Sciences* **108,** 7595–7600 (2011).

138. Lin, J. Y. A user's guide to channelrhodopsin variants: features, limitations and future developments. *Experimental physiology* **96,** 19–25 (2011).

139. Hou, S.-Y. *et al.* Diversity of Chlamydomonas channelrhodopsins. *Photochemistry and photobiology* **88,** 119–128 (2012).

140. Muders, V. *et al.* Resonance Raman and FTIR spectroscopic characterization of the closed and open states of channelrhodopsin-1. *FEBS Letters* **588,** 2301–2306 (2014).

141. Sineshchekov, O. A., Govorunova, E. G., Wang, J., Li, H. & Spudich, J. L. Intramolecular proton transfer in channelrhodopsins. *Biophysical journal* **104,** 807–817 (2013).

142. Lórenz-Fonfría, V. A., Muders, V., Schlesinger, R. & Heberle, J. Changes in the hydrogen-bonding strength of internal water molecules and cysteine residues in the conductive state of channelrhodopsin 1. *The Journal of Chemical Physics* **141,** 22D507 (2014).

143. Stensitzki, T., Muders, V., Schlesinger, R., Heberle, J. & Heyne, K. The primary photoreaction of channelrhodopsin-1: wavelength dependent photoreactions induced by ground-state heterogeneity. *Frontiers in Molecular Biosciences* **2,** 1–10 (2015).

144. Ogren, J. I. *et al.* Proton transfers in a Channelrhodopsin-1 studied by fourier transform infrared (FTIR) difference spectroscopy and site-directed mutagenesis. *Journal of Biological Chemistry* **290,** 12719–12730 (2015).

145. Smith, S. O. *et al.* Vibrational analysis of the all-trans-retinal chromophore in light-adapted bacteriorhodopsin. *Journal of the American Chemical Society* **109,** 3108–3125 (1987).

146. Ogren, J. I. *et al.* Retinal Chromophore Structure and Schiff Base Interactions in Red-Shifted Channelrhodopsin-1 from Chlamydomonas augustae. *Biochemistry* (2014).

147. Bruun, S. *et al.* Light-Dark Adaptation of Channelrhodopsin Involves Photoconversion Between the all-trans and 13-cis Retinal Isomers. *Biochemistry* **54,** 150803134650002 (2015).

148. Braiman, M. & Mathies, R. Resonance Raman spectra of bacteriorhodopsin's primary photoproduct: evidence for a distorted 13-cis retinal chromophore. *Proceedings of the National Academy of Sciences* **79,** 403–407 (1982).

149. Yang, C. *et al.* FTIR spectral subtraction based on asymmetric least squares. *Proceedings - 2011 4th International Conference on Biomedical Engineering and Informatics, BMEI 2011* **3,** 1724–1728 (2011).

150. Ogren, J. I. *et al.* Comparison of the Structural Changes Occurring during the Primary Phototransition of Two Different Channelrhodopsins from Chlamydomonas Algae. *Biochemistry* **54,** 377–388 (2015).

151. Overman, S. A. & Thomas, G. J. Amide modes of the α-helix: Raman spectroscopy of filamentous virus fd containing peptide 13C and 2H labels in coat protein subunits. *Biochemistry* **37,** 5654–5665 (1998).

152. Wagner, G., Oesterhelt, D., Krippahl, G. & Lanyi, J. K. Bioenergetic role of halorhodopsin in Halobacterium halobium cells. *FEBS Letters* **131,** 341–345 (1981).

153. Engelhard, C., Chizhov, I., Siebert, F. & Engelhard, M. Microbial halorhodopsins: Light-driven chloride pumps. *Chemical reviews* **118,** 10629–10645 (2018).

154. Schobert, B., Lanyi, J. K. & Cragoe, E. Evidence for a halide-binding site in halorhodopsin. *Journal of Biological Chemistry* **258,** 15158–15164 (1983).

155. Walter, T. J. & Braiman, M. S. Anion-protein interactions during halorhodopsin pumping: halide binding at the protonated Schiff base. *Biochemistry* **33,** 1724–1733 (1994).

156. Lakatos, M., Groma, G. I., Ganea, C., Lanyi, J. K. & Váró, G. Characterization of the azide-dependent bacteriorhodopsin-like photocycle of salinarum halorhodopsin. *Biophysical journal* **82,** 1687–1695 (2002).

157. Kolbe, M., Besir, H., Essen, L.-O. & Oesterhelt, D. Structure of the light-driven chloride pump halorhodopsin at 1.8 Å resolution. *Science* **288,** 1390–1396 (2000).

158. Gmelin, W. *et al.* The crystal structure of the L1 intermediate of halorhodopsin at 1.9 angstroms resolution. *Photochemistry and photobiology* **83,** 369–377 (2007).

159. Schreiner, M., Schlesinger, R., Heberle, J. & Niemann, H. H. Crystal structure of Halobacterium salinarum halorhodopsin with a partially depopulated primary chloride-binding site. *Acta Crystallographica Section:F Structural Biology Communications* **72,** 692–699 (2016).

160. Varo, G. *et al.* Photocycle of halorhodopsin from halobacterium-salinarium. *Biophysical Journal* **68,** 2062–2072 (1995).

161. Hutson, M. S., Shilov, S. V., Krebs, R. & Braiman, M. S. Halide dependence of the halorhodopsin photocycle as measured by time-resolved infrared spectra. *Biophysical journal* **80,** 1452–1465 (2001).

162. Essen, L. O. Halorhodopsin: Light-driven ion pumping made simple? *Current Opinion in Structural Biology* **12,** 516–522 (2002).

163. Kouyama, T., Kawaguchi, H., Nakanishi, T., Kubo, H. & Murakami, M. Crystal structures of the L1, L2, N, and O states of pharaonis halorhodopsin. *Biophysical journal* **108,** 2680–2690 (2015).

164. Sass, H. *et al.* The tertiary structural changes in bacteriorhodopsin occur between M states: X-ray diffraction and Fourier transform infrared spectroscopy. *The EMBO journal* **16,** 1484–1491 (1997).

165. Hackmann, C. *et al.* Static and time-resolved step-scan Fourier transform infrared investigations of the photoreaction of halorhodopsin from Natronobacterium pharaonis: consequences for models of the anion translocation mechanism. *Biophysical journal* **81,** 394–406 (2001).

166. Chon, Y. S. *et al.* Existence of two L photointermediates of halorhodopsin from Halobacterium salinarum, differing in their protein and water FTIR bands. *Biochemistry* **38,** 9449–9455 (1999).

167. Váró, G. *et al.* Photocycle of halorhodopsin from Halobacterium salinarium. *Biophysical journal* **68,** 2062 (1995).

168. Váró, G. & Lanyi, J. Distortions in the photocycle of bacteriorhodopsin at moderate dehydration. *Biophysical journal* **59,** 313–322 (1991).

169. Zimányi, L. & Lanyi, J. K. Fourier transform Raman study of retinal isomeric composition and equilibration in halorhodopsin. *The Journal of Physical Chemistry B* **101,** 1930–1933 (1997).

170. Smith, S. O., Marvin, M. J., Bogomolni, R. A. & Mathies, R. a. Structure of the retinal chromophore in the hR578 form of halorhodopsin. *Journal of Biological Chemistry* **259,** 12326–12329 (1984).

171. Alshuth, T., Stockburger, M., Hegemann, P. & Oesterhelt, D. Structure of the retinal chromophore in halorhodopsin: a resonance Raman study. *FEBS letters* **179,** 55–59 (1985).

172. Diller, R., Stockburger, M., Oesterhelt, D., Tittor, J. & Titter, J. Resonance Raman study of intermediates of the halorhodopsin photocycle. *FEBS Letters* **217,** 297–304 (1987).

173. Ludmann, K., Ibron, G., Lanyi, J. K. & Váró, G. Charge motions during the photocycle of pharaonis halorhodopsin. *Biophysical journal* **78,** 959–966 (2000).

174. Kalaidzidis, I. V., Kalaidzidis, Y. L. & Kaulen, A. D. Flash-induced voltage changes in halorhodopsin from Natronobacterium pharaonis. *FEBS letters* **427,** 59–63 (1998).

175. Dioumaev, A. K. & Braiman, M. S. Nano-and Microsecond Time-Resolved FTIR Spectroscopy of the Halorhodopsin Photocycle. *Photochemistry and photobiology* **66,** 755–763 (1997).

176. Rothschild, K. J., Bousché, O., Braiman, M. S., Hasselbacher, C. A. & Spudich, J. L. Fourier transform infrared study of the halorhodopsin chloride pump. *Biochemistry* **27,** 2420–2424 (1988).

177. Mizuno, M., Nakajima, A., Kandori, H. & Mizutani, Y. Structural Evolution of a Retinal Chromophore in the Photocycle of Halorhodopsin from Natronobacterium pharaonis. *The Journal of Physical Chemistry A* **122,** 2411–2423 (2018).

178. Fujisawa, T., Kiyota, H., Kikukawa, T. & Unno, M. Low-Temperature Raman Spectroscopy of Halorhodopsin from Natronomonas pharaonis: Structural Discrimination of Blue-shifted and Red-shifted Photoproducts. *Biochemistry* (2019).

179. Braiman, M. S., Walter, T. J. & Briercheck, D. M. Infrared Spectroscopic Detection of Light-Induced Change in Chloride-Arginine Interaction in Halorhodopsin. *Biochemistry* **33,** 1629–1635 (1994).

180. Barth, A. & Zscherp, C. What vibrations tell about proteins. *Quarterly Reviews of Biophysics* **35** (2002).

181. Ames, J. B., Raap, J., Lugtenburg, J. & Mathies, R. A. Resonance Raman study of halorhodopsin photocycle kinetics, chromophore structure, and chloride-pumping mechanism. *Biochemistry* **31,** 12546–12554 (1992).

182. Kovalev, K. *et al.* Structure and mechanisms of sodium-pumping KR2 rhodopsin. *Science Advances* **5** (2019).

183. Inoue, K. *et al.* A light-driven sodium ion pump in marine bacteria. *Nature Communications* **4,** 1610–1678 (2013).

184. Kato, H. E. *et al.* Structural basis for Na+ transport mechanism by a light-driven Na+ pump. *Nature* **521,** 48–53 (2015).

185. Gushchin, I. *et al.* Crystal structure of a light-driven sodium pump. *Nature Structural and Molecular Biology* **22,** 390–396 (2015).

186. Vogt, A. *et al.* Engineered Passive Potassium Conductance in the KR2 Sodium Pump. *Biophysical Journal* **116,** 1941–1951 (2019).

187. Kaur, J. *et al.* Solid-state NMR analysis of the sodium pump Krokinobacter rhodopsin 2 and its H30A mutant. *Journal of structural biology* **206,** 55–65 (2019).

188. Hontani, Y. *et al.* The photochemistry of sodium ion pump rhodopsin observed by watermarked femto- to submillisecond stimulated Raman spectroscopy. *Phys. Chem. Chem. Phys.* **18,** 24729–24736 (2016).

189. Kato, Y., Inoue, K. & Kandori, H. Kinetic Analysis of H+/Na+ Selectivity in a Light-Driven Na+-Pumping Rhodopsin. *The Journal of Physical Chemistry Letters* **6,** 5111–5115 (2015).

190. Chen, H.-F., Ono, H., Inoue, K., Abe-Yoshizumi, R. & Kandori, H. Time-resolved FTIR study of light-driven sodium pump rhodopsins. *J. Phys. Chem. B, Article),* 17694–17704 (2018).

191. Nishimura, N., Mizuno, M., Kandori, H. & Mizutani, Y. Distortion and a Strong Hydrogen Bond in the Retinal Chromophore Enable Sodium-Ion Transport by the Sodium-Ion Pump KR2. *Journal of Physical Chemistry B* **123,** 3430–3440 (2019).

192. Asido, M. *et al.* Time-resolved IR spectroscopy reveals pump Krokinobacter eikastus rhodopsin 2 † (2019).

193. Shibata, M. *et al.* Oligomeric states of microbial rhodopsins determined by high-speed atomic force microscopy and circular dichroic spectroscopy. *Scientific reports* **8,** 8262 (2018).

194. Abe-Yoshizumi, R., Inoue, K., Kato, H. E., Nureki, O. & Kandori, H. Role of Asn112 in a light-driven sodium ion-pumping rhodopsin. *Biochemistry* **55,** 5790–5797 (2016).

195. Balashov, S. P. *et al.* Light-driven Na+pump from Gillisia limnaea: A high-affinity Na+binding site is formed transiently in the photocycle. *Biochemistry* **53,** 7549–7561 (2014).

196. Inoue, K. *et al.* Red-shifting mutation of light-driven sodium-pump rhodopsin. *Nature communications* **10,** 1993 (2019).

197. Mathies, R. & Stryer, L. Retinal has a highly dipolar vertically excited singlet state: implications for vision. *Proceedings of the National Academy of Sciences* **73,** 2169–2173 (1976).

198. Chen, H.-F. *et al.* Time-resolved FTIR study of light-driven sodium pump rhodopsins. *Physical Chemistry Chemical Physics* **20,** 17694–17704 (2018).

199. Kandori, H., Inoue, K. & Tsunoda, S. P. Light-Driven Sodium-Pumping Rhodopsin: A New Concept of Active Transport. *Chemical Reviews* (2018).

200. Haupts, U., Tittor, J., Bamberg, E. & Oesterhelt, D. General concept for ion translocation by halobacterial retinal proteins: the isomerization/switch/transfer (IST) model. *Biochemistry* **36,** 2–7 (1997).

201. Gushchin, I. *et al.* Structure of the light-driven sodium pump KR 2 and its implications for optogenetics. *The FEBS journal* **283,** 1232–1238 (2016).

202. Deacon, G. & Phillips, R. Relationships between the carbon-oxygen stretching frequencies of carboxylato complexes and the type of carboxylate coordination. *Coordination Chemistry Reviews* **33,** 227–250 (1980).

203. Resler, T., Schultz, B.-J. J., Lórenz-Fonfría, V. A., Schlesinger, R. & Heberle, J. Kinetic and Vibrational Isotope Effects of Proton Transfer Reactions in Channelrhodopsin-2. *Biophysical journal* **109,** 287–97 (2015).

204. Nara, M., Morii, H. & Tanokura, M. Coordination to divalent cations by calcium-binding proteins studied by FTIR spectroscopy. *Biochimica et Biophysica Acta (BBA)-Biomembranes* **1828,** 2319–2327 (2013).

205. Nara, M., Torii, H. & Tasumi, M. Correlation between the vibrational frequencies of the carboxylate group and the types of its coordination to a metal ion: an ab initio molecular orbital study. *The Journal of Physical Chemistry* **100,** 19812–19817 (1996).

206. Nara, M. *et al.* Infrared studies of interaction between metal ions and Ca2+-binding proteins Marker bands for identifying the types of coordination of the side-chain COO- groups to metal ions in pike parvalbumin (pI= 4.10). *FEBS letters* **349,** 84–88 (1994).

207. Furutani, Y., Murata, T. & Kandori, H. Sodium or lithium ion-binding-induced structural changes in the K-ring of V-ATPase from Enterococcus hirae revealed by ATR-FTIR spectroscopy. *Journal of the American Chemical Society* **133,** 2860–2863 (2011).

208. Noguchi, T., Ono, T.-a. & Inoue, Y. Direct detection of a carboxylate bridge between Mn and Ca2+ in the photosynthetic oxygen-evolving center by means of Fourier transform infrared spectroscopy. *Biochimica et Biophysica Acta (BBA)-Bioenergetics* **1228,** 189–200 (1995).

209. Govorunova, E. G., Sineshchekov, O. A., Li, H. & Spudich, J. L. Microbial rhodopsins: diversity, mechanisms, and optogenetic applications. *Annual review of biochemistry* **86,** 845–872 (2017).

210. Ernst, O. P. *et al.* Microbial and animal rhodopsins: Structures, functions, and molecular mechanisms. *Chemical Reviews* **114,** 126–163 (2014).

211. Smith, S. O. Structure and activation of the visual pigment rhodopsin. *Annual review of biophysics* **39,** 309–328 (2010).

212. Koyanagi, M. & Terakita, A. Diversity of animal opsin-based pigments and their optogenetic potential. *Biochimica et Biophysica Acta (BBA)-Bioenergetics* **1837,** 710–716 (2014).

213. O'Neill, P. & Gautam, N. Optimizing optogenetic constructs for control over signaling and cell behaviours. *Photochemical & Photobiological Sciences* **14,** 1578–1585 (2015).

214. Sulkes, M., Lewis, A. & Marcus, M. A. Resonance Raman spectroscopy of squid and bovine visual pigments: the primary photochemistry in visual transduction. *Biochemistry* **17,** 4712–22 (Oct. 1978).

215. Nishioku, Y., Nakagawa, M., Tsuda, M. & Terazima, M. Energetics and Volume Changes of the Intermediates in the Photolysis of Octopus Rhodopsin at a Physiological Temperature.

216. Nakagawa, M., Kikkawa, S., Iwasa, T. & Tsuda, M. Light-induced Protein Conformational Changes in the Photolysis of Octopus Rhodopsin. *Biophysical Journal* **72,** 2320–2328 (May 1997).

217. Inoue, K., Tsuda, M. & Terazima, M. Photoreverse reaction dynamics of octopus rhodopsin. *Biophysical journal* **92,** 3643–3651 (2007).

218. Suzuki, T., Sugahara, M. & Kito, Y. An intermediate in the photoregeneration of squid rhodopsin. *Biochimica et Biophysica Acta (BBA)-Bioenergetics* **275,** 260–270 (1972).

219. Tsuda, M. Kinetic study of photoregeneration process of digitonin-solubilized squid rhodopsin. *Biochimica et Biophysica Acta (BBA)-Bioenergetics* **502,** 495–506 (1978).

220. Palczewski, K. G protein–coupled receptor rhodopsin. *Annu. Rev. Biochem.* **75,** 743–767 (2006).

221. Shirzad-Wasei, N. & DeGrip, W. J. Heterologous expression of melanopsin: present, problems and prospects. *Progress in retinal and eye research* **52,** 1–21 (2016).

222. Murakami, M., Kitahara, R., Gotoh, T. & Kouyama, T. Crystallization and crystal properties of squid rhodopsin. *Acta Crystallographica Section F: Structural Biology and Crystallization Communications* **63,** 475–479 (2007).

223. Nagata, T. *et al.* Depth perception from image defocus in a jumping spider. *Science* **335,** 469–471 (2012).

224. Kliger, D. S. & Lewis, J. W. Spectral and kinetic characterization of visual pigment photointermediates. *Israel journal of chemistry* **35,** 289–307 (1995).

225. Kliger, D., Horwitz, J., Lewis, J. & Einterz, C. Evidence for a common BATHO-intermediate in the bleaching of rhodopsin and isorhodopsin. *Vision research* **24,** 1465–1470 (1984).

226. Suzuki, T. & Callender, R. Primary photochemistry and photoisomerization of retinal at 77 degrees K in cattle and squid rhodopsins. *Biophysical journal* **34,** 261–270 (1981).

227. Suzuki, T., Uji, K. & Kito, Y. Studies on cephalopod rhodopsin: photoisomerization of the chromophore. *Biochimica et Biophysica Acta (BBA)-General Subjects* **428,** 321–338 (1976).

228. Nishioku, Y., Nakagawa, M., Tsuda, M. & Terazima, M. A spectrally silent transformation in the photolysis of octopus rhodopsin: a protein conformational change without any accompanying change of the chromophore's absorption. *Biophysical journal* **80,** 2922–7 (2001).

229. Shichida, Y. & Imai, H. Visual pigment: G-protein-coupled receptor for light signals. *Cellular and Molecular Life Sciences CMLS* **54,** 1299–1315 (1998).

230. Yoshizawa, T. & Shichida, Y. in *Methods in enzymology* 333–354 (Elsevier, 1982).

231. Dixon, S. F. & Cooper, A. Quantum efficiencies of the reversible photoreaction of octopus rhodopsin. *Photochemistry and photobiology* **46,** 115–119 (1987).

232. Sulkes, M., Lewis, A. & Marcus, M. A. Resonance Raman spectroscopy of squid and bovine visual pigments: the primary photochemistry in visual transduction. *Biochemistry* **17,** 4712–4722 (1978).

233. Nishimura, S., Kandori, H., Nakagawa, M., Tsuda, M. & Maeda, A. Structural dynamics of water and the peptide backbone around the Schiff base associated with the light-activated process of octopus rhodopsin. *Biochemistry* **36,** 864–870 (1997).

234. Bagley, K. A., Eisenstein, L., Ebrey, T. G. & Tsuda, M. A comparative study of the infrared difference spectra for octopus and bovine rhodopsins and their bathorhodopsin photointermediates. *Biochemistry* **28,** 3366–3373 (1989).

235. Kandori, H. & Maeda, A. FTIR spectroscopy reveals microscopic structural changes of the protein around the rhodopsin chromophore upon photoisomerization. *Biochemistry* **34,** 14220–14229 (1995).

236. Huang, L. *et al.* A Resonance Raman Study of the CN Configurations of Octopus Rhodopsin, Bathorhodopsin, and Isorhodopsin. *Biochemistry* **35,** 8504–8510 (1996).

237. Huang, L. *et al.* A resonance Raman study of the C= C stretch modes in bovine and octopus visual pigments with isotopically labeled retinal chromophores. *Photochemistry and photobiology* **66,** 747–754 (1997).

238. Cooper, A., Dixon, S. & Tsuda, M. Photoenergetics of octopus rhodopsin. *European Biophysics Journal* **13,** 195–201 (1986).

239. Pan, D. & Mathies, R. A. Chromophore structure in lumirhodopsin and metarhodopsin I by time-resolved resonance Raman microchip spectroscopy. *Biochemistry* **40,** 7929–7936 (2001).

240. Masuda, S., Morita, E. H., Tasumi, M., Iwasa, T. & Tsuda, M. Infrared studies of octopus rhodopsin and lumirhodopsin. *Journal of molecular structure* **297,** 29–34 (1993).

241. Furutani, Y., Shichida, Y. & Kandori, H. Structural changes of water molecules during the photoactivation processes in bovine rhodopsin. *Biochemistry* **42,** 9619–9625 (2003).

242. Hildebrandt, P. & Stockburger, M. Role of water in bacteriorhodopsin's chromophore: resonance Raman study. *Biochemistry* **23,** 5539–5548 (1984).

243. Varma, N. *et al.* Crystal structure of jumping spider rhodopsin-1 as a light sensitive GPCR. *Proceedings of the National Academy of Sciences,* 201902192 (2019).

244. Siebert, F. Applications of FTIR spectroscopy to the investigation of dark structures and photoreactions of visual pigments. *Israel journal of chemistry* **35,** 309–323 (1995).

245. Murakami, M. & Kouyama, T. Crystal structure of squid rhodopsin. *Nature* **453,** 363 (2008).

246. Balashov, S. P. *et al.* Reconstitution of gloeobacter rhodopsin with echinenone: role of the 4-keto group. *Biochemistry* **49,** 9792–9799 (2010).

SELBSTSTÄNDIGKEITSERKLÄRUNG

Hiermit erkläre ich, daß ich die vorliegende Arbeit selbstständig angefertigt, nicht anderweitig zu Promotionszwecken vorgelegt und keine anderen als die angegebenen Hilfsmittel verwendet habe. Sämtliche wissentlich verwendete Textausschnitte, Zitate oder Inhalte anderer Verfasser wurden ausdrücklich als solche gekennzeichnet.

Berlin, den 17.03.2020

David Ehrenberg